The Solar Corona:
Modeled, Discretized, Visualized

vorgelegt von
M. Sc.
Marcel Padilla
ORCID: 0000-0001-8962-9355

von der Fakultät II - Mathematik und Naturwissenschaften
der Technischen Universität Berlin
zur Erlangung des akademischen Grades

Doktor der Naturwissenschaften
- Dr. rer. nat. -

genehmigte Dissertation

Promotionsausschuss:

Vorsitzender: Prof. Dr. Jörg Liesen
Gutachter: Prof. Dr. Ulrich Pinkall
Gutachter: Prof. Dr. Keenan Crane

Tag der wissenschaftlichen Aussprache: 25. September 2023

Berlin 2023

My life has been a wonderful roller coaster ride for which I can't limit my gratitude to those who are nearest to me at this moment in space and time. Everyone, intentionally or unintentionally, with whatever motive they had, has contributed to making my life what it is. I love it and want to express a deep thank you to anyone who in some way or another has become part of my life and left their signature in it:

Abdul, Adel, Adithya, Adytia, Aga, Agata, Ahmad, Ahmed, Aidan, Aigerim, Aimee, Akram, Alan, Albert, Alberto, Alejandra, Aleksandra, Alev, Alex, Alex, Alex, Alex, Alex, Alex, Alexander, Alexander, Alexander, Alexander, Alexandra, Alexandre, Alexandre, Alicja, Alina, Alis, Alison, Aljoscha, Alka, Alondra, Amal, Amandine, Amelia, Amir, Amir, Amos, Amy, Ana, Ana, Ana, Ancka, Andi, Andine, Andre, Andrea, Andrew, Andy, Aneesa, Angele, Angelica, Angelika, Aniruddha, Anja, Anja, Anja, Anna, Anna, Anna, Anne, Anne, Anne, Anneke, Anneke, Annette, Annika, Annika, Ariel, Arndol, Arne, Arnold, Arvy, Asol, Astrid, Auriel, Awa, Awsina, Bamboo, Bassili, Basta, Becky, Bee, Bella, Ben, Ben, Benedikt, Bettina, Blake, Blanca, Bonita, Boris, Bradley, Bree, Briana, Brunhilde, Bruno, Bruno, Bubi, Callum, Calvin, Can, Candan, Carla, Carla, Carlos, Carmen, Carnelian, Caro, Caro, Caro, Carolin, Carolin, Carsten, Cassandra, Castro, Ceci, Celia, Charlie, Charlotte, Charlotte, Charlotte, Chiara, Chris, Christian, Christoph, Christoph, Cindy, Clara, Clara, Clement, Cole, Colm, Constanze, Cosima, Cris, Cris, Daisy, Dan, Daniel, Daniele, Dasha, David, David, David, David, David, Davita, Dean, Deandra, Debora, Dennis, Devendra, Diana, Diego, Dilara, Dimitry, Domenico, Domi, Dominik, Dominik, Dominik, Donald, Dorit, Dorothea, Ecem, Eduardo, Ehab, Elena, Elena, Elena, Elena, Elena, Elisa, Ellie, Elmar, Elodie, Elodie, Elz, Emily, Emma, Enrique, Enrique, Erin, Estelle, Eva, Eva, Evelyn, Evelyn, Fabian, Fabian, Fabienne, Felix, Felix, Felix, Felix, Feliz, Ferdinand, Ferdinand, Fernando, Fethi, Filiz, Fiona, Florian, Florian, Florian, Florian, Floriane, Francesca, Francesca, Franco, Frank, Frank, Fransisco, Fransisco, Franz, Freya, Frida, Fritzi, Gabrielle, Galia, Gari, Georgia, Giacinta, Gitti, Glen, Gökhan, Gregor, Gur, Hadas, Haley, Hamid, Hanin, Hanka, Hanna, Hannes, Hariz, Haya, Haya, Hazem, Heiko, Helene, Helene, Helmut, Hülya, Humam, Humam, Iacopo, Iason, Ilse, Imelda, Ines, Ines, Ingelore, Isabel, Isabella, Isabelle, Isi, Issac, Iulia, Ivan, Jack, Jack, Jaime, Jakob, Jakob, James, James, James, Jan, Jan, Jan, Jan, Jan, Jana, Jana, Jarl, Jasper, Javier, Javier, Jazz, Jill, Jing, Jochen, Joey, Johan, Johan, Johanna, Johanna, Johanna, Johanna, Johannes, Johannes, Johannes, Johannes, Johannes, Jonas, Jonas, Jonas, Jonathan, Jonathan, Jörn, Jose, Jose, Jose, Joseph, Josephin, Josh, Joshua, Joshua, Joshua, Josi, Jovana, Jualian, Judith, Julia, Julian, Julian, Jürgen, Justin, Justin, Kai, Kai, Kamila, Karim, Karime, Karo, Karolin, Karolin, Kasia, Katarina, Katayoun, Kate, Kati, Katrin, Katrin, Kay, Kaydda, Keenan, Kerstin, Khaled, Kiki, Konsti, Kristina, Kyungmin, Lara, Lars, Laurie, Lea, Lea, Lea, Leadra, Leila, Leilani, Lena, Lena, Leo, Leo, Leonard, Leonardo, Leonhard, Leonie, Leslie, Libo, Lilly, Lina, Linda, Linea, Linell, Linnea, Lior, Lisa, Lisa, Livia, Liz, Lola, London, Louise, Louise, Lucian, Lucie, Luise, Lukas, Lulu, Lupita, Lutz, Lydia, Maha, Maik, Maike, Maike, Maiko, Manuel, Mara, Mara, Marat, Marc, Marc, Marcel, Marcela, Marco, Marco, Mareike, Maren, Mari, Maria, Maria, Marie, Marie, Marie, Mario, Marisol, Markus, Markus, Martha, Martin, Martin, Martina, Marv, Matea, Matheo, Mathias, Mathias, Mathis, Mats, Matthias, Max, Maxi, Maxime, Maya, Meegan, Megan, Mel, Melanie, Mercedes, Meredith, Mette, Michael, Michael, Michael, Michael, Michael, Michael, Michael, Michelle, Michelle, Miguel, Milan, Milan, Mirjam, Miro, Mischa, Mo, Mokka, Monica, Motaz, Nadia, Nadja, Nadjeli, Natalia, Natalia, Nathalia, Naza, Neville, Nick, Nick, Nick, Nihal, Nikio, Nikita, Niko, Niko, Nikolai, Nils, Nina, Noa, Noor, Nora, Olga, Olga, Oliver, Oliver, Olivia, Orlando, Oscar, Oswaldo, Owen, Öystein, Palid, Parsifal, Pascal, Pascal, Pati, Patricio, Patrick, Paul, Paula, Paula, Pauline, Pedram, Peeter, Peter, Peter, Philip, Phillip, Phillipp, Phoung Anh, Plom, Quetin, Rafael, Ramoni, Reda, Regina, Regina, Reinhold, Rhoslyn, Riccardo, Rich, Richard, Robert, Robert, Robert, Rochelle, Rodrigo, Ronja, Rouselle, Roxy, Sana, Sanaa, Sandra, Sandra, Sarah, Sarah, Sarah, Sasha, Sasha, Saskia, Satyanarayan, Sebastian, Sebastian, Sebastian, Sebastian, Sebstian, Selina, Selina, Selly, Shani, Silvia, Silvia, Silvio, Simon, Sina, Siri, Sissela, Socorro, Sophia, Sophia, Sophia, Sophia, Sophie, Sophie, Stephan, Sunhye, Sven, Sven, Svenja, Swenja, Tabea, Tacha, Tamar, Tamara, Tamara, Tamara, Tamino, Tanisa, Tanja, Tanya, Tara, Tatev, Teodor, Teresa, Teresa, Theo, Theo, Theresa, Thilo, Thilo, Thomas, Thomas, Thura, Tim, Tim, Tina, Tine, Tjioe, Tobias, Tobias, Torivan, Torsten, Tristan, Tuan, Tweneboah, Ugur, Ulrich, Ulricke, Uschi, Ushi, Vaan, Valentin, Valerie, Van Anh, Vanessa, Vanessa, Vera, Vero, Vesna, Victoria, Vida, Viktor, Viola, Violeta, Viry, Vittorio, Wai, Wejdan, Wella, Xinyu, Yashwant, Yousuf, Yuri, Yuval, Yuya, Ziv, Zoey, Zoey and many more I was unable to recall and many many more in the future that I have simply not yet met and many many many more that have indirectly contributed to my life.

Special loving thanks to Chiara for being such a wonderful partner in this time.

Abstract

In this dissertation, stellar atmospheres will be mathematically described together with the establishment of a discrete model for simulation purposes. Simulation of stellar atmospheres, such as that of our own sun, is a common task in CGI for scientific visualization, movies and games. A fibrous volumetric texture is the visually dominant feature of the solar corona—the plasma that extends from the solar surface into space. These coronal fibers can be modeled as magnetic filaments whose shape is governed by the magnetohydrostatic equation. The first goal of this dissertation is to rigorously establish and derive the mathematical model to solve this equation.

The second goal of this dissertation is the discretization of the established model and to derive an algorithm to solve the magnetohydrostatic equation computationally. The discrete magnetic filaments being introduced here provide a Lagrangian curve representation whose initial configuration can be prescribed or generated from magnetic flux surface maps given as scalar magnetic flux boundary data on the sun's surface. Subsequently, the shape of the filaments is determined based on a variational formulation.

Lastly, we apply the entire model to output visual renderings of the whole sun and put the output to various tests. The fidelity of the method is demonstrated by comparing the resulting renderings with actual images of our sun's corona. A pipeline for solar imagery creation is built.

Zusammenfassung

In dieser Dissertation werden Sternatmosphären mathematisch beschrieben und ein diskretes Modell für Simulationszwecke etabliert. Die Simulation von Sternatmosphären, wie z.B. das unserer eigenen Sonne, ist eine häufige Aufgabe in der Computergraphik für wissenschaftliche Visualisierung, Filme und Spiele. Eine faserige volumetrische Textur ist das visuell dominante Merkmal der Korona - das Plasma, das sich von der Sonnenoberfläche in den Weltraum erstreckt. Diese koronalen Fasern können als magnetische Filamente modelliert werden, deren Form durch die magnetohydrostatische Gleichung bestimmt wird. Das erste Ziel dieser Dissertation ist es, das mathematische Modell rigoros zu etablieren und herzuleiten, um diese Gleichung zu lösen.

Das zweite Ziel dieser Dissertation ist die Diskretisierung des etablierten Modells sowie die Ableitung eines Algorithmus zur computergestützten Lösung der magnetohydrostatischen Gleichung. Die hier eingeführten diskreten magnetischen Filamente bieten eine Lagrange-Kurvenrepräsentation, deren Anfangskonfiguration vorgegeben oder aus magnetischen Oberflächendaten generiert werden kann, die als skalare magnetische Daten auf der Sonnenoberfläche gegeben sind. Anschließend wird die Form der Filamente auf der Grundlage einer Variationsformulierung bestimmt.

Schließlich wenden wir das gesamte Modell an, um visuelle Darstellungen der gesamten Sonne zu erstellen und den Resultaten verschiedenen Tests zu unterziehen. Die Genauigkeit der Methode wird durch den Vergleich der resultierenden Darstellungen mit tatsächlichen Bildern der Korona unserer Sonne demonstriert. Eine Pipeline zur Erstellung von Sonnenbildern wird aufgebaut.

Contents

Figure 1: A procedurally generated solar atmosphere computed by the algorithm in this dissertation. The underlying boundary magnetic flux map was randomly generated and is shown in figure 2. This image appeared in the DFG-Calendar 2023 by winning a competition.
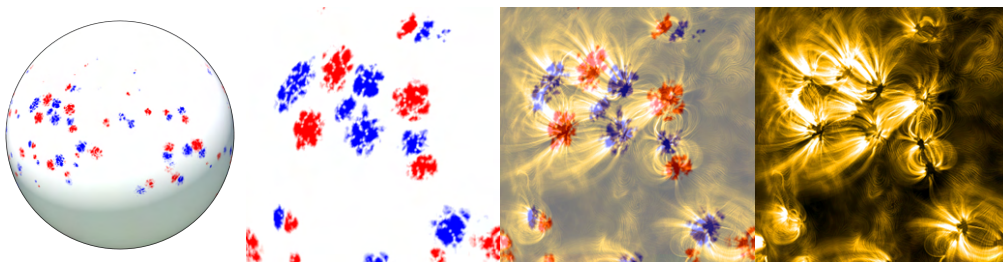
Figure 2: A procedurally generated magnetic flux map on the surface of the sun. The total flux cancels out. The generation involved sampling sun spot pairs and masking them with several levels of noise (explained in section 3.7.5). This dissertation will provide a full pipeline to create these images with only such a flux map as input.

Foreword

This work presented here is the result of several years of research together with my colleagues. The core of this work has been published at ACM SIGGRAPH 2022 [Padilla et al.(2022)] together with Oliver Gross, Felix Knöppel, Albert Chern, Ulrich Pinkall and Peter Schröder.

This dissertation expands on this publication and tells the whole story by going into the nitty-gritty mathematical, computational and practical details that the above mentioned publication could not hold due to page limitations and the style of the target conference.

Motivation

At the center of our solar system lies the sun providing us with all the energy necessary to sustain life. In the last century, solar physicists have begun to understand its processes, yet plenty of unanswered questions still remain. The solar atmosphere, known as the solar corona, displays emissions at wavelengths only possible at millions of degrees Kelvin in a poorly understood process that is addressed as the *coronal heating problem* [Aschwanden(2006)]. On top of that, the solar magnetic field displays turbulent changes in an 11 year cycle with active and quiet periods that are too poorly understood [Hathaway(2015)].
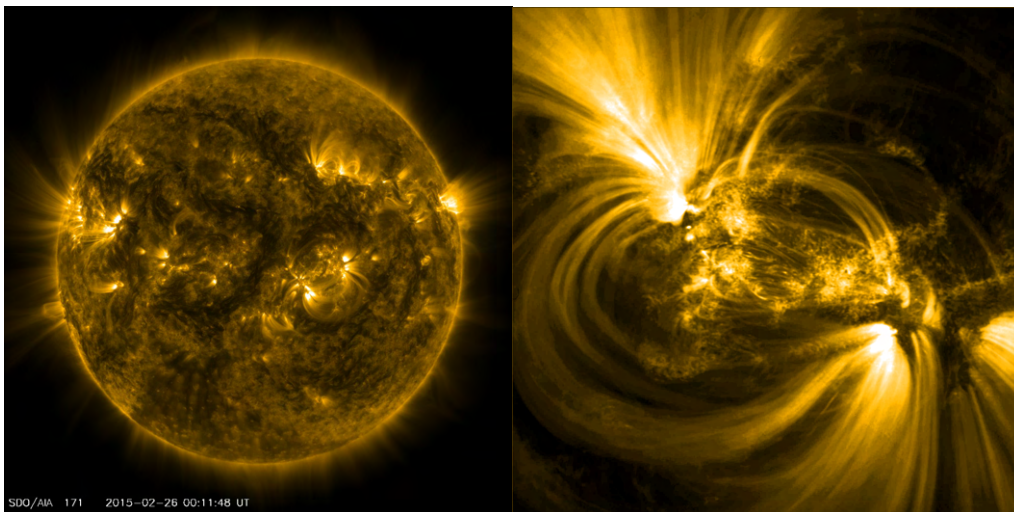
Figure 3: Image of the sun take by NASA's SDO mission by measuring the 17,1nm wavelength emissions and coloring the data by conventions. The fibred nature of the solar atmosphere becomes apparent. Left: the whole sun in Feburary 2015. Right: A close up on a sunspot pair taken in May 2018 during the Hi-C 2.1 mission.

When observed at extreme ultra violet (EUV) light (wavelength 17,1nm, see figure 3), the solar atmospheres reveals a plethora of structure. It is known that the visible fibrous structure is aligned with the sun's magnetic field that emerges from the magnetohydrodynamic (MHD) and magenetohydrostatic (MHS) equations, and that the emission properties are tightly linked to the temperature of the ionised gas, known as the solar *plasma*.

The desire to visualize astrophysical objects and phenomena is intricately linked with the early history of computer graphics [Gómez et al.(2017)] and continues today with landmark visualizations of the solar atmosphere [NASA Scientific Visualization Studio(2018), CADENS(2015), Borkiewicz et al.(2019)]. In particular, the arcs visible in our sun's atmosphere are some of the most awe-inspiring natural spectacles, making their visual depiction of great interest in scientific visualization, special effects, and games.

The goal of this dissertation is to shed light on the nature of the underlying phenomena that the extreme ultra violet images reveal. To accomplish this, this dissertation is broken down into three parts:

- **Part 1: The Mathematical modeling of the MHS equation** The topic is introduced together with related work. The Mathematical modeling of the MHS equation. A smooth differential geometric description of the magnetic field on the sun's surface is established.

- **Part 2: The Discretization of the MHS Equation**. A discrete approximation of the smooth differential geometric description will be developed that captures the smooth theory and enables computational approaches. An algorithm to solve the MHS equation based on a variational principle will be introduced.

- **Part 3: Validation and Image Generation**. The smooth description and discrete approximation undergo testing to be validated. The results are then applied for image generation together with some theory on the nature of these images.

Note that in this dissertation, the sun in our solar system will be the star of the show for being the main target application, as it is by far the most relevant example of a stellar object providing us with opportunities to validate this work. From the physical properties however, everything derived here applies to all stars by simply adjusting parameters. All stars are beautiful.

Part 1

The Mathematical Modeling of the MHS Equation
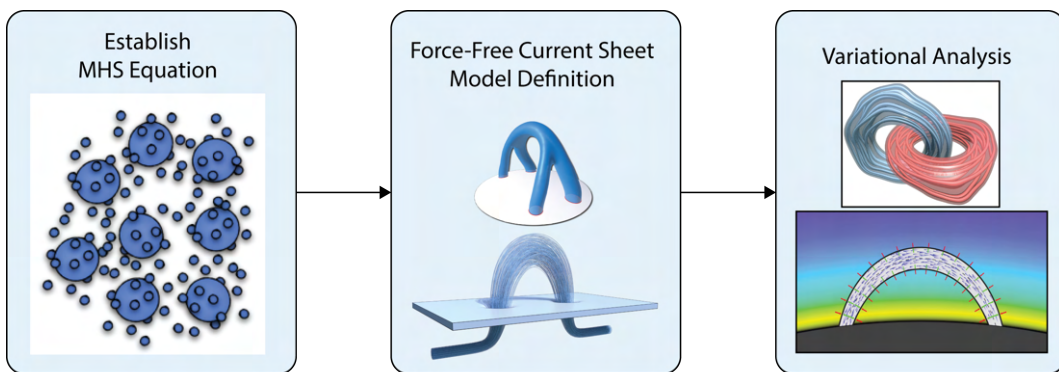
Figure 1.1: An overview of part 1 of this dissertation. Starting out with basic MHD theory we derive the MHS equation and then approach it with the FFCS model for which key theorems are presented through variational Analysis.

Many solar coronal properties are influenced by the underlying solar magnetic field, which aligns the fibrous visible features we are trying to understand and model. One must therefore dive into the theory of the solar magnetic field. In the first part of this dissertation will establish the following:

- Establish the fundamental equations governing the solar atmosphere.
- Review related work for various models to approach this equation.
- Introduce the central model in this work, the force-free current sheet (FFCS) model.
- Expand the FFCS model by introducing a differential geometric description.
- Derive and prove key equivalence conditions for the FFCS model to solve the MHS equation. These insights will then be the foundation for part 2 of this dissertation.

The main goals of this part of the dissertation is to establish the description of the

plasma state $(\mathbb{M}_\mathbf{B}, \mathbf{B})$ using the force-free current sheet model in a way that respects the exterior confining gas pressure and to then argue why solutions to the magnetohydrostatic equation can be found by minimizing the energy of these plasma states.

1.1 The Magnetohydrostatic (MHS) Equation

In this section we derive the main equation that describes the magnetic field in the solar corona. To do so, we will first discuss the medium of the atmosphere, the solar plasma to end up with the magnetohydrostatic equation shown below.

$$\mathbf{0} = \tfrac{1}{\mu_0}(\operatorname{curl}\mathbf{B}) \times \mathbf{B} - \operatorname{grad} p + \tfrac{m}{k_\mathrm{B}T}p\mathbf{g}. \tag{1.1}$$

1.1.1 Solar Plasma

Only three states of matter are usually taught to us. Their properties are determined by their inter atomic/molecular structure. The three common states are:

1. **Solid**. A crystalline structure characterised by strong bonds that leave large chunks of the structure rigid.
2. **Liquid**. A weakly bonding structure characterised by free motion of its components without changing volume much.
3. **Gas**. The bonds are too weak to keep the atoms/molecules in any structure. They move freely in the surrounding space.

This is however, not the complete story! There is a state that clearly distinguishes itself from the above that only occurs under special circumstances when ionization is possible inside a gas. An atom is ionized when it looses it's bonds to one or several electrons, which can then freely move inside the medium. A completely ionized gas is known as a *plasma*, and is usually formed when gas is exposed to strong electric currents or very high temperatures, the later being responsible for making plasma the most abundant state of matter in our universe due to its presence in stars like our sun.

In most stars, hydrogen is the most abundant substance, which is why we will from here on only refer to ionized hydrogen when speaking of plasma. Hydrogen plasma is basically a gas of protons and electrons moving freely in space. Because of this, plasma is very conductive, meaning that it can exhibit large electrical currents through itself, which then in turn couple its dynamics to the magnetic field. Thus, the description of the dynamics of plasma requires knowledge on the interaction between electric currents, magnetic fields and charged particles. See figure 1.2.

Liquids and non-ionized gases are classified as *fluids* and mathematically described (in the incompressible case) by the well known Navier-Stokes equations displayed here:

Positive ions   Electrons

Solid   Liquid   Gas   Plasma
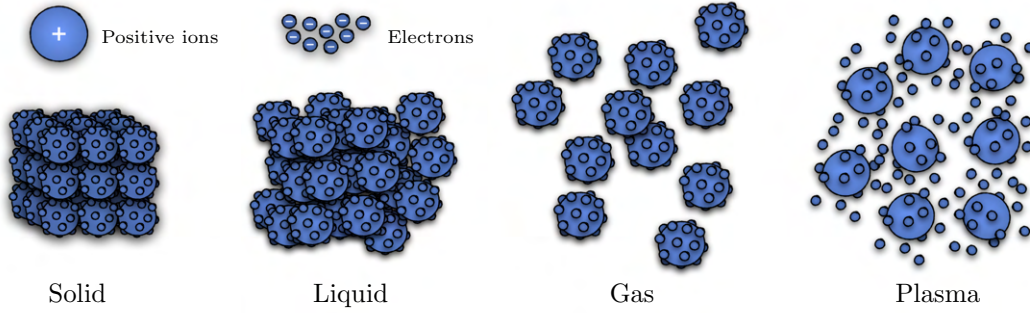
Figure 1.2: The four states of matter with a graphical display of structure between the particles involved. Plasma on the right is a gas of separated protons and electrons.

$$\frac{\partial}{\partial t}\mathbf{v} + \nabla_{\mathbf{v}}\mathbf{v} = -\frac{1}{\rho}\operatorname{grad} p + \mathbf{g} + \nu\Delta\mathbf{v} \tag{1.2a}$$

$$\frac{\partial}{\partial t}\rho + \operatorname{div}(\rho\mathbf{v}) = 0 \tag{1.2b}$$

Here, $\mathbf{v}$ represents the velocity vector field, $\nabla_{\mathbf{v}}\mathbf{v}$ the transport of the velocity field, ρ the fluid density, $\operatorname{grad} p$ the pressure, $\mathbf{g}$ the gravity and $\nu\Delta$ the viscosity effect. Equation 1.2a is known as the fluid momentum equation (*change in the velocity field*) and equation 1.2b is known as the incompressibility equation (mass preservation, *what goes in goes out*). Fluid dynamics is also referred to as *hydrodynamics*.

Plasma dynamics on the other hand, augment the Navier-Stokes equation with the coupled dynamics that come from electromagnetism, namely the induction of a magnetic field from current and its effects on charged particles. The resulting equations of plasma dynamics are commonly referred to as *magnetohydrodynamics* (MHD). The MHD equations are what we are going to study in detail in the next section.

1.1.2 The Magnetohydrodynamic (MHD) Equations

How exactly do Maxwell's equations from electromagnetism combined with hydrodynamics create *magnetohydrodynamics*? Let $\mathbb{M} = \mathbb{R}^3 \setminus \mathbb{B}$ denote the domain of the plasma. $\mathbb{B}$ represents the sun as a *ball* and then $\mathbb{R}^3 \setminus \mathbb{B}$ is the solar exterior[1] Since plasma is a gas too, we start out with the incompressibility equation with the plasma density $\rho\colon \mathbb{M} \to \mathbb{R}$ ᵏᵍ/ₘ³ and the plasma velocity field $\mathbf{v}\colon \mathbb{M} \to \mathbb{R}^3$ ᵐ/ₛ.

$$\frac{\partial}{\partial t}\rho + \operatorname{div}(\rho\mathbf{v}) = 0$$

Then we take the original fluid momentum equation 1.2a and add an additional electromagnetic force to it, namely the *Lorenz force* $\mathbf{J} \times \mathbf{B}$ created from the cross product of the

---

[1]We introduce $\mathbb{B}$ here because we later want to add boundary conditions to the surface of the sun. Generally, magnetohydrodynamics do not require the domain $\mathbb{M}$ to be restricted in such a way.

electric current $\mathbf{J}\colon \mathbb{M} \to \mathbb{R}^3$ C/m²s with the magnetic field $\mathbf{B}\colon \mathbb{M} \to \mathbb{R}^3$ kg/Cs. The Lorenz force acts on charged particles and diverts their trajectory (figure 1.3). The magnetohydrodynamics momentum equation looks like this:

$$\tfrac{\partial}{\partial t}\mathbf{v} + \nabla_{\mathbf{v}}\mathbf{v} = -\tfrac{1}{\rho}\operatorname{grad} p + \mathbf{g} + \nu\Delta\mathbf{v} + \tfrac{1}{\rho}\mathbf{J}\times\mathbf{B}.$$

Figure 1.3: Left: a current $\mathbf{J}$ through a wire induces a magnetic field $\mathbf{B}$, a basic fact from Electromagnetism. Right: In plasma dynamics, free electrons induce a current flux $\mathbf{J}$ which then creates a magnetic field $\mathbf{B}$. Moving charges inside a magnetic field are then affected by the Lorenz force, accelerating them in the direction $\mathbf{J}\times\mathbf{B}$.

Under the assumption of negligible electrical resistance (hydrogen plasma, a soup of protons and electrons, is a very very good conductor) we can express the electrical current by $\mathbf{B}$ alone thanks to Ampere's law:

$$\mathbf{J} = \tfrac{1}{\mu_0}\operatorname{curl}\mathbf{B},$$

where $\mu_0 = 1.25663706212\cdot 10^{-6}[\mathrm{NA}^{-2}]$ is the vacuum permeability (a universal constant). For the magnetic field $\mathbf{B}$, we track it's evolution by *Faraday's law* together with magnetic diffusivity.

$$\tfrac{\partial}{\partial t}\mathbf{B} = \operatorname{curl}(\mathbf{v}\times\mathbf{B}) + \mu\Delta\mathbf{B}$$

Later, in theorem 8, we show that in absence of the diffusion term (which we will later drop in section 1.1.3), this equation says that the magnetic field is passively transported by the plasma flow. Whenever the magnetic field shows up it always is accompanied by the

divergence free condition[2].

$$\mathrm{div}\,\mathbf{B} = 0$$

And lastly, since we are dealing with a gas that will vary in density, the ideal gas equation joins the party too:

$$\rho = \frac{m}{k_\mathrm{B}T}p,$$

where $m = 1.67262192{\cdot}10^{-27}$ [kg] is the mass of a proton, $k_\mathrm{B} = 1.380649{\cdot}10^{-23}$ [m^{2}kgs^{-2}K^{-1}] the Boltzmann constant and T the temperature in degrees Kelvin.

All of the equations above combined form the dissipative incompressible *magnetohydrodynamic (MHD)* equations are shown below grouped together.

$$\frac{\partial}{\partial t}\rho + \mathrm{div}(\rho\mathbf{v}) = 0 \tag{1.3a}$$

$$\frac{\partial}{\partial t}\mathbf{v} + \nabla_\mathbf{v}\mathbf{v} = -\frac{1}{\rho}\,\mathrm{grad}\,p + \mathbf{g} + \nu\Delta\mathbf{v} + \frac{1}{\rho}\,\mathbf{J}\times\mathbf{B} \tag{1.3b}$$
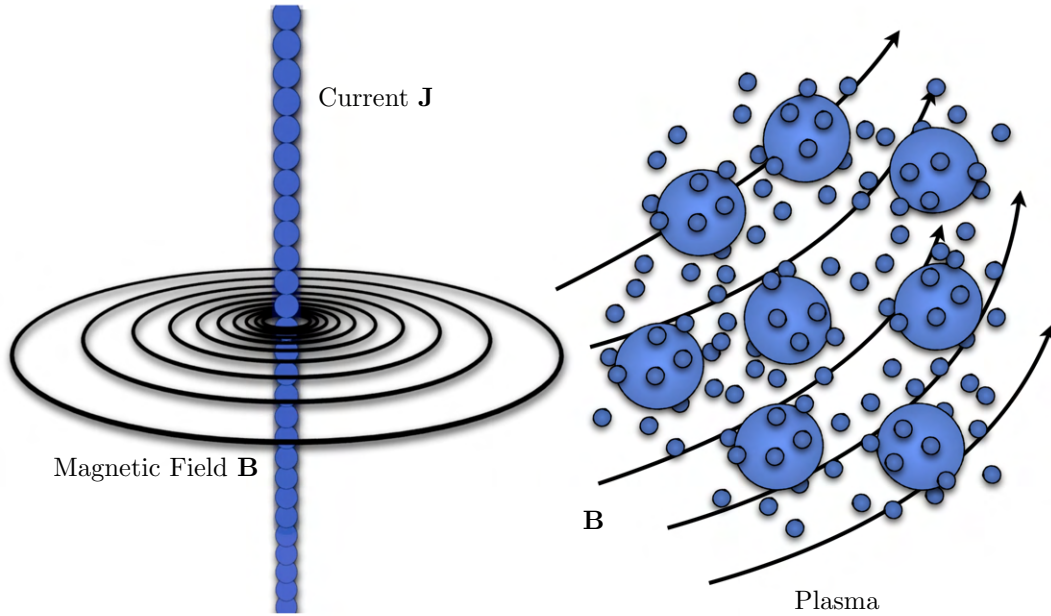
$$\frac{\partial}{\partial t}\mathbf{B} = \mathrm{curl}(\mathbf{v}\times\mathbf{B}) + \mu\Delta\mathbf{B} \tag{1.3c}$$

$$\mathrm{div}\,\mathbf{B} = 0 \tag{1.3d}$$

$$\mathbf{J} = \frac{1}{\mu_0}\,\mathrm{curl}\,\mathbf{B} \tag{1.3e}$$

$$\rho = \frac{m}{k_\mathrm{B}T}p \tag{1.3f}$$

When dealing with plasma dynamics, one would have to track all of these equations at once. Evidently, solving all these equations at once is difficult. We will simplify things tremendously by applying some observations about stellar atmospheres in the next section.

1.1.3 Deriving the MHS Equation

The sun is big. 1,391,400 km in diameter to be exact. That is more than 100 times wider than earth (12,756 km diameter). Thus the sun has 10,000 time more surface area and 1,000,000 times the volume. It is important to keep this sheer scale in mind when proceeding, as the visual features we are seeing on the extreme ultra violet images are beyond *earth sized* (see figure 1.4). At these massive scales, the MHD equations can be greatly simplified, as we will justify in this section.

We start *by neglecting the viscous/diffusive terms* $\nu\Delta\mathbf{v}$ and $\mu\Delta\mathbf{B}$. The reason behind this is the shear scale of the phenomena. Viscosity/diffusion are local effects that relate the values of neighbouring elements. When the simulation is large, these neighbouring effects are dwarfed in comparison to the large scale events, as the information travelled from neighbour

---

[2]This is a statement from Maxwell's equation, according to which magnetic monopoles do not exist
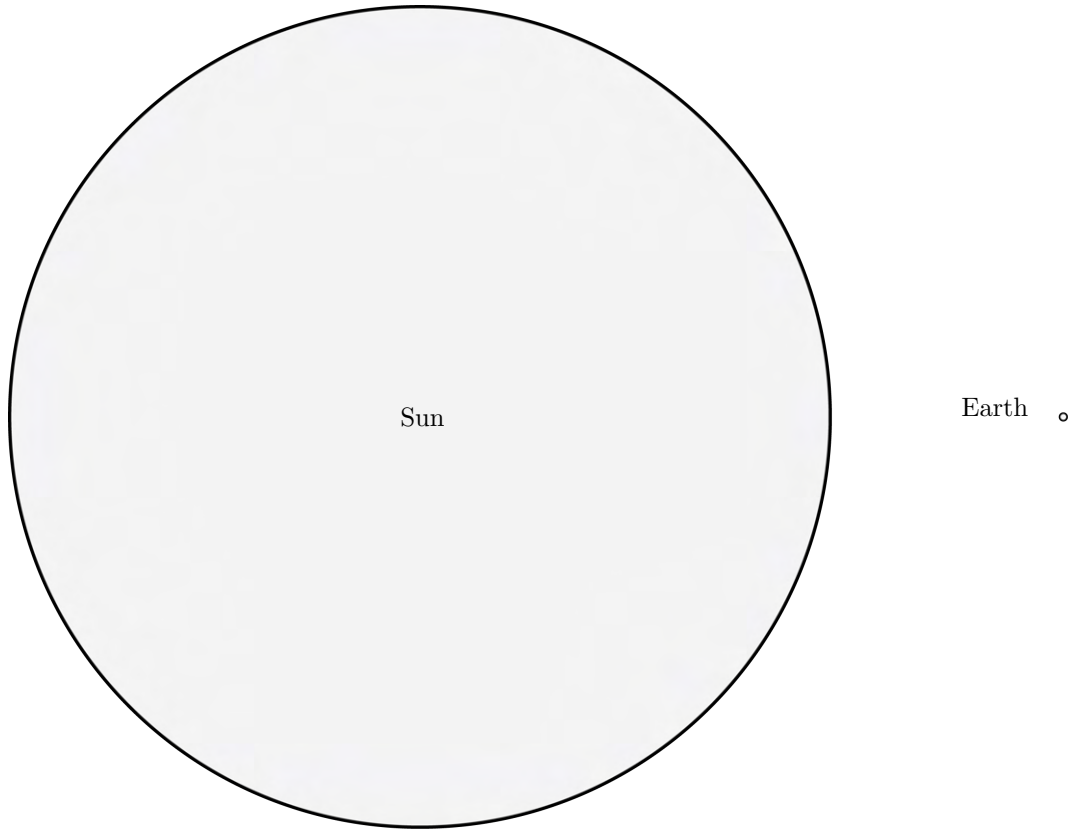
Figure 1.4: The sun and the earth to scale. The sun has a diameter of $\approx 1.390.000$km, while earth's diameter is ≈ 12.800km. The sun is ≈ 110 times bigger than earth. At this scale the magnetohydrodynamic equations can be safely simplified. Fun fact: Many volumetric grid methods in solar physics work with domain elements that are *earth-sized.*

to neighbour needs more and more time. Compare this to the following: water is often simulated to be inviscid (without viscosity), but for much smaller beings, such as bacteria, the flow of water is dominated by the viscous properties (see. Stokes flow)[Rieutord(2015), Ch. 4], meaning that friction is dominant and momentum build up is negligible. If a bacteria would perform fish like movements it would not be able to move forward. Instead, many bacteria use a rotating flagellum [Purcell(1997)], which is more akin to screwing oneself through a medium.

We apply the same domain scale argument to justify neglecting the terms involving the Laplacian, the viscous plasma term $\Delta \mathbf{v}$ and $\mu \mathbf{B}$. Viscous and diffusive effects can be important in plasma dynamics but not at the scale we are dealing with. Take note though that magnetic diffusivity is known to be the primary motor of so called *magnetic reconnection*, allowing topology changes of the magnetic field and perhaps being an important source of heat in the solar corona. Flares however, are rare eruption events, and most of the time the solar atmospheres displays stability over time, so at this stage, we discard the possibility to model magnetic reconnection by dropping the viscous/diffusive terms from the MHD

equations[3].

When we remove the viscosity/diffusivity terms form the MHD equations we are left with what is known as the *ideal MHD equations*. In many areas of plasma research, these are the common equations to start with. We display them here with the electrical current substituted by Ampere's law ($\mathbf{J} = {}^1\!/_{\mu_0} \operatorname{curl} \mathbf{B}$):

$$\frac{\partial}{\partial t}\rho + \operatorname{div}(\rho\mathbf{v}) = 0 \tag{1.4a}$$

$$\frac{\partial}{\partial t}\mathbf{v} + \nabla_\mathbf{v}\mathbf{v} = -\frac{1}{\rho}\operatorname{grad} p + \mathbf{g} + \frac{1}{\rho}\frac{1}{\mu_0}\operatorname{curl}\mathbf{B} \times \mathbf{B} \tag{1.4b}$$

$$\frac{\partial}{\partial t}\mathbf{B} = \operatorname{curl}(\mathbf{v} \times \mathbf{B}) \tag{1.4c}$$

$$\operatorname{div}\mathbf{B} = 0 \tag{1.4d}$$

$$\rho = \frac{m}{k_\mathrm{B}T}p \tag{1.4e}$$

Still, this set of equations is too messy. It is time to bring in the biggest help in simplifying these equations, which will remove the time dependent components. Observations on the sun reveal that the magnetic field is very stable apart from infrequent solar eruption events. Figure 1.5 shows how a single sunspot pair remains stable for at least multiple days.
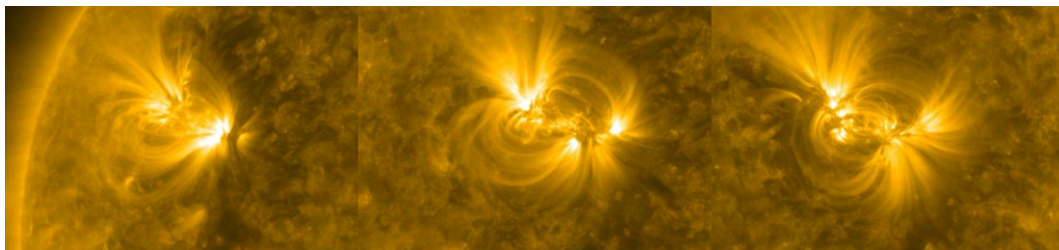
Figure 1.5: The magnetic field, seen through the aligned plasma filaments, displays a stability over days. These are three EUV AIA171 images taken from 27/05/18 until the 31/05/18. There is plenty variation in the glowing of the plasma as it rotates with the sun. However, the magnetic field structure, which can be guessed by tracing the plasma fibres, is pretty stable.

Since equation 1.4c shows that the magnetic field is transported by the plasma, combining this with the static observation reveals that the plasma velocity $\mathbf{v}$ must be negligible on the solar scale. Thus, we can drop $\mathbf{v} = \mathbf{0}$ into the ideal MHD equations above and see what happens:

---

[3]Note that in vortex filament dynamics [Weißmann and Pinkall(2010)], viscosity is also neglected in their fluid equations even though it then becomes a necessity to justify reconnecting vortex filaments. The situation here is very similar. The fluid field $\mathbf{v}$ and its vorticity share many parallels to magnetic fields $\mathbf{B}$ and their currents.

$$\frac{\partial}{\partial t}\rho = 0 \tag{1.5a}$$

$$\mathbf{0} = -\frac{1}{\rho}\operatorname{grad} p + \mathbf{g} + \frac{1}{\rho}\frac{1}{\mu_0}\operatorname{curl}\mathbf{B}\times\mathbf{B} \tag{1.5b}$$

$$\frac{\partial}{\partial t}\mathbf{B} = \mathbf{0} \tag{1.5c}$$

$$\operatorname{div}\mathbf{B} = 0 \tag{1.5d}$$

$$\rho = \frac{m}{k_{\mathrm{B}}T}p \tag{1.5e}$$

Grave collateral damage occurs. $\mathbf{v} = \mathbf{0}$ has also killed all time derivatives in the system. Thus, the *dynamic* system becomes *static*. If we now substitute ρ through the ideal gas law (1.4e) we arrive at the final *magnetohydrostatic equation* (MHS), the equation governing the solar atmosphere [Rosner et al.(1978)]:

$$\frac{1}{\mu_0}(\operatorname{curl}\mathbf{B})\times\mathbf{B} - \operatorname{grad} p + \frac{m}{k_{\mathrm{B}}T}p\mathbf{g} = \mathbf{0}. \tag{1.6}$$

Subject to $\operatorname{div}\mathbf{B} = 0$ and to a Neumann boundary flux condition on the surface of the sun. Let $\mathbb{B} \subset \mathbb{R}^3$ be a region representing the sun (a ball). Let $\mathbb{M} = \mathbb{R}^3 \setminus \mathbb{B}$ denote the exterior domain of the solar corona. The magnetic boundary flux is given on $\partial\mathbb{M}$ (such boundary flux data is called a magnetogram, see section 1.2.2). To maintain divergence freeness, the net boundary flux is zero (equal amount of outgoing and ingoing flux). The problem extensively discussed in the solar physics literature (see e.g. [Warren et al.(2018), Yeates et al.(2018)]) is the following:

> *Given a flux density on the surface of the sun, extend it to a magnetic field* $\mathbf{B}$ *in the solar atmosphere that, for suitable choice of gas pressure p and temperature distribution T, satisfies the MHS equation.*

How this problem was tackled before will be discussed in the related work section 1.3. The model used in this dissertation will then be introduced in section 1.4. When speaking of plasma pressure p, we will from now on refer to it as *gas pressure* due to the similarities of gas and plasma. In the next section, we will go into more detail about the sun and its magnetic field.

1.2   Properties of the Sun and the Magnetic Field

Without any further information, the MHS equation 1.6 has many possible solutions when given Neumann flux boundary conditions (e.g. a simple potential field). There are plenty of degrees of freedom to play around with. Some choices have to be made to approach this problem. Ideally, these choices come with rigorous physical motivation. To make more informed choices, lets mention some properties of the sun now.

1.2.1 Layers of the Sun

The solar radius $R_\odot$ is about 696,000km wide. The sun has many layers listed here and displayed in figure 1.6.
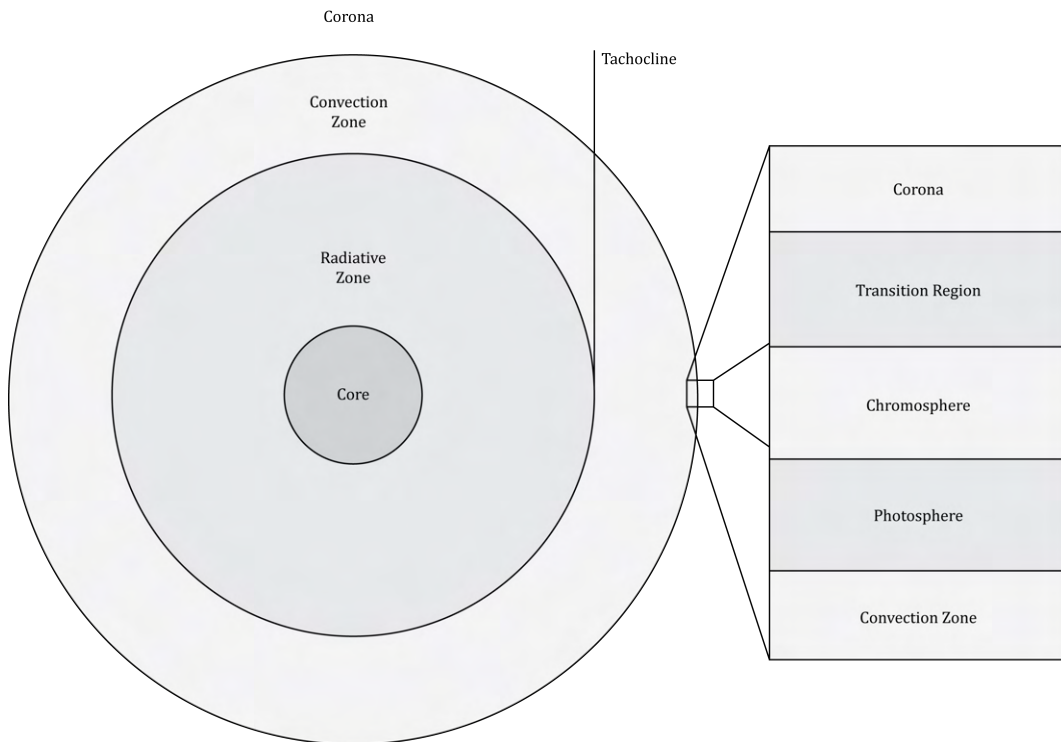
Figure 1.6: The many layers of the sun as explained in the text. It does not have a clear surface. Instead, there is a blurry transition between the inside and the outside involving multiple layers.

- **Core:**
  the extremely dense center where nuclear fusion takes place.
- **Radiative Zone:**
  where particles can't flow but heat travels by radiation.
- **Tachocline:**
  A brief transition layer where below everything rotates uniformly and above differential rotation (different speeds at different latitudes) begins.
- **Convective Zone:**
  The area where particles flow in complex ways due to differential rotation. This is where the magnetic field acquires its non-trivial structure as the magnetic field is transported by the plasma.
- **Photosphere:**
  Most visible light is emitted from this relatively thin layer through black body radiation at about 5800K. Due to the high amount of photon emission here, the magnetic field

strength measured in a magnetogram originates from here (more details later in this section 1.2.3).

- **Chromosphere:**

  A thin layer where the temperature cools down further. It is difficult to speak of a sharp *surface* of the sun as it is rather a soft transition of plasma density. Many visible surface features such as spicules (hair like plasma jets) are here.

- **Transition Region:**

  A thin layer where the temperature rises massively to 1 million K and density and pressure drops by similar orders of magnitude.

- **Solar Corona:**

  Finally, we arrive at the outer atmosphere. Temperatures are above 1 million K and to this day, it is unclear to solar physicists what mechanism drives this high level of heat (coronal heating problem). This is the area where our visible phenomena will take place, and where the MHS equation will be solved.

In this work, almost all of the attention will be directed at the solar corona. However, the publicly available boundary magnetic flux data, a.k.a. *magnetograms*, originate at the photosphere.

What do we mean when we speak of the *surface*? After all, with the layers shown the surface is rather blurry in nature with a continuous change in plasma density ρ. As a result, the answer is rather context dependent. When we speak of the magnetogram, the boundary flux data, we speak of the photosphere. When we talk about the footpoints of plasma filaments, we refer to the base of the corona. Physically, they are relatively speaking very close, yet they come with different pressures and densities. The exact distinction is important in the formulation of our glow model in section 3.1.2.

1.2.2   About the Magnetic Field of the Sun

To our comfort, the National Aeronautics and Space Administration (NASA) operates the Solar Dynamics Observatory (SDO) mission since 2010 which includes a satellite measuring various aspects of the sun. Most famously, it is responsible for taking extreme ultra violet images every 45 seconds which we have come to know as the golden images (*i.e.*figure 1.5). The SDO also takes images at various wavelengths and measures the doppler effects. Of great interest to us are the *magnetograms* captured by the SDO. As it turns out, the magnetic field has an effect on the polarisation of photons through the so called *Zeeman effect*, which in turn allows the measurement of the *line-of-sight component of the magnetic field* at the origin of the largest amount of emission, the photosphere. The data acquired this way are called magnetograms (figure 1.7).

Observations of the solar magnetic field reveal periodic transitioning between active and quiet periods in a cycle of 11 years. In the quiet periods, the magnetic field has a *familiar* dipole structure around the axis of rotation (like earth). Few local anomalies occur in this
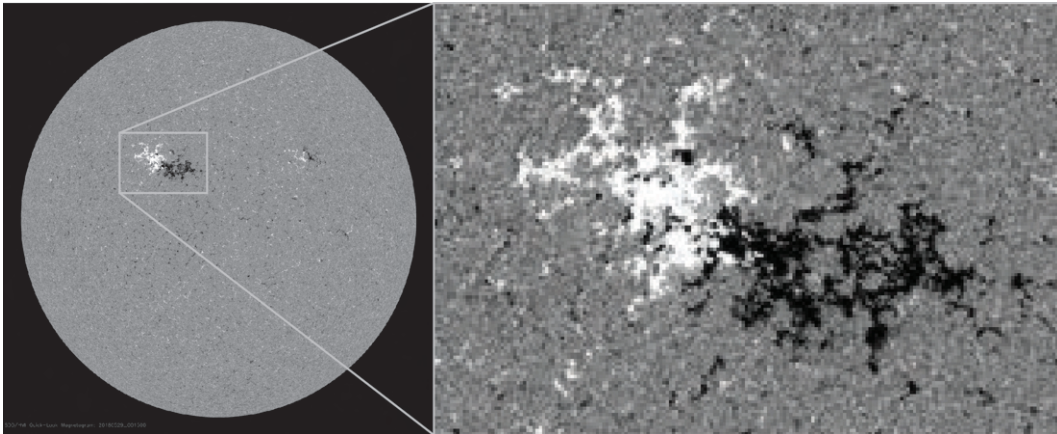
Figure 1.7: A magnetogram of the sun captured by NASA's Solar Dynamics Observatory mission. White areas indicate magnetic field coming out of the sun while black indicates the reverse. The image on the right shows a typical sunspot pair. This data was captured on 29/05/18, the same time as the center of figure 1.5.

period that would be responsible for plasma filaments. During the active period, the magnetic field becomes way more choatic, to the point that the polarity is completely flipped at the end of a full cycle.

Why exactly this cycle occurs is still unclear and the subject of *solar dynamo theory*. A major contribution seems to be the differential rotation, the distinct velocities at various latitudes in the convection zone cause by Coriolis forces. These can passively transport the magnetic field (see theorem 8) and thus cause large shearing over time, which deforms the magnetic field structure and builds up energy in it. See figure 1.8 for a visualization of differential rotation.
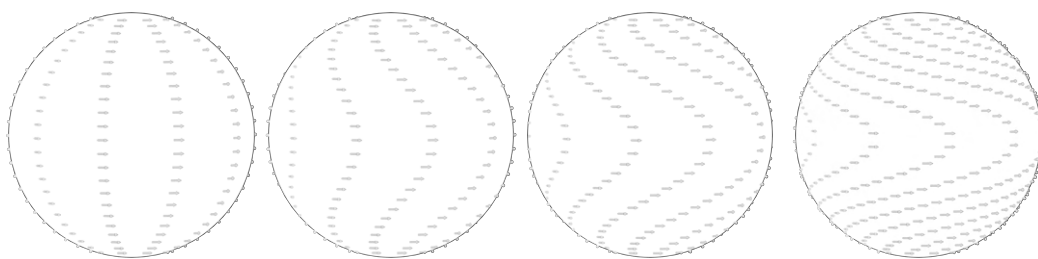
Figure 1.8: A demonstration of differential rotation. We track the motion of fixed points over time from left to right. The difference in axial rotation causes shearing, which in turn has a strong effect on the magnetic field that is transported by the plasma. The magnetic field builds up energy over time, and filaments are formed above and below the equator which will then rise above the surface.

This large shearing of the magnetic field under the surface is then responsible for the formation of *magnetic filaments*, strong bundles of magnetic field that usually occur away

from the poles. These magnetic filaments then rise above the surface due to buoyancy caused by a plasma density difference. Once above the surface, they form so called *sunspot pairs* (see figures 1.5, 1.7 and 1.9), above which plasma filaments occur [Priest(2014), Sec. 9.3] [Priest(2019), Sec. 3.2].
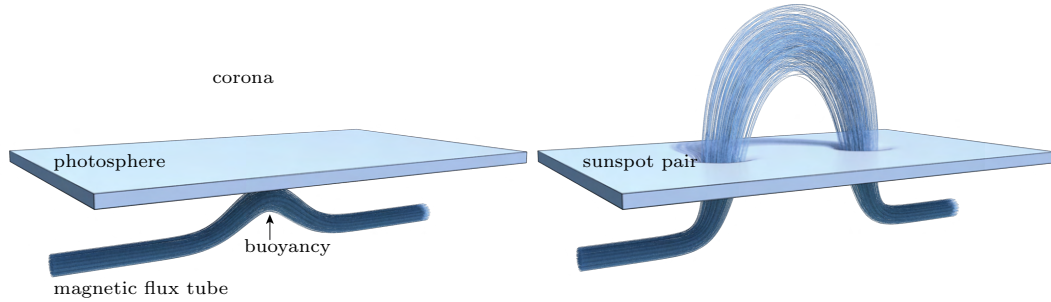
Figure 1.9: A magnetic filament forms under the surface of the sun. Through buoyant forces, it emerges to the surface as a sunspot pair which looks similar to the one seen in the magnetogram of figure 1.7.

Intuitively, a magnetic field is a smooth continuous structure. In the case of solar physics though, the above mentioned phenomena lead to the notion of the field being *fibered*, *i.e.*better described by a collection of filaments. Indeed, this description fits well with the strong concentration the magnetic field exhibits over sunspot pairs.

This dissertation will use the magnetic filament description as a baseline assumption to build a model to solve the MHS equation. We will call this model the *force-free current sheet (FFCS) model* (section 1.4). Later, the MHS equation will be solved computationally using filament based primitives to model the solution space. Before we start with our model, let us see what type of data is available and review some related work.

1.2.3   Available Magnetic Surface Data Types

Let's quickly mention the three main data types used in solar physics.

Magnetograms: The polarisation of the emission can be used to infer the magnetic field strength, which is stored in so called *magnetograms*. Around the viewing center of the sun, the magnetogram will provide accurate Neumann boundary flux data for our algorithm, as magnetograms do only provide the *line-of-sight* component of the magnetic field at the surface. The accuracy of magnetograms becomes weak at the limbs of the sun where the surface of the sun is bent away from us.

Vector Magnetograms: For the non-line-of-sight component of the magnetic field NASA also provides vector magnetogram data. However, these are known to involve large uncertainties [Klimchuk and Canfield(1994)]. For our approach Neumann boundary data theory is sufficient.

Synoptic Maps: Many visually striking features of the solar corona become apparent at the limb of the sun, which is precisely where the *line-of-sight* data provided by basic

magnetograms fails to deliver anything. This creates a general problem in comparing the results at the limbs with our output. What helps is the use of so called *synoptic maps*. These are the stitched result of a 26 days worth of magnetograms (the time it takes for a full rotation of the sun at the equator). From each magnetogram only the central latitude is recorded, and the rest discarded. The result is a flux map on the entire sun that looks coherent, but it has a strong discontinuity between the start and the end of the 26-day cycle, might not even have zero total flux and is sheared by differential rotation. Synoptic maps are nice to have approximative data on the limbs, but for any synoptic map there cannot exist a corresponding EUV measurement (photo) of the sun, as they are not happening at the same time. We will use synoptic maps when wanting to visualize the limbs, not when comparing the visualization output of our algorithm and the glow model with real footage.

1.3   Related Work

The MHS equation involves plasma (gas) pressure, the ideal gas law and gravity effects. The equation says that the Lorenz force contribution, gas pressure and gravitational effects are in balance.

$$\underbrace{\frac{1}{\mu_0}(\operatorname{curl}\mathbf{B})\times\mathbf{B}}_{\text{Lorenz force term}} \quad \underbrace{-\operatorname{grad}p}_{\text{gas pressure gradient}} \quad + \quad \underbrace{\frac{m}{k_{\mathrm{B}}T}p\mathbf{g}}_{\text{gravity term}} = \mathbf{0}. \tag{1.7}$$

In the following we review some previous work on approaching the modeling of the magnetic field of the solar corona.

1.3.1   Force-Free Fields

Many investigations on the solar magnetic field begin by arguing that the plasmatic effects are negligible ($p = 0$), meaning that the MHS equation collapses to a much simpler form:

$$(\operatorname{curl}\mathbf{B})\times\mathbf{B} = \mathbf{0}. \tag{1.8}$$

A magnetic field $\mathbf{B}$ fulfilling this equation is called a *force-free* field, due to the Lorenz force inducing term being zero. We can make the following statement about force-free fields.

> **Theorem 1 (Force-Free Fields Form).** For any non-zero force-free magnetic field there exists an $\alpha : \mathbb{M} \to \mathbb{R}$ such that
>
> $$\operatorname{curl}\mathbf{B} = \alpha\mathbf{B}.$$
>
> Additionally, α is constant along the field lines of $\mathbf{B}$.

Proof. Looking at the terms of equation 1.8, we see that a cross product of two non-zero

vectors is zero if and only if the two vectors are linearly dependent. Thus, for any solution of equation 1.8 on the plasma domain $\mathbb{M}$ there is a scalar function $\alpha : \mathbb{M} \to \mathbb{R}$ such that

$$\operatorname{curl} \mathbf{B} = \alpha \mathbf{B}. \tag{1.9}$$

This magnetic field $\mathbf{B}$ must be, as any magnetic field, compliant with the divergence free condition. By taking the divergence on both sides of the equation we see that

$$\underbrace{\operatorname{div}(\operatorname{curl} \mathbf{B})}_{\equiv 0} = \operatorname{div}(\alpha \mathbf{B}) = \alpha \underbrace{\operatorname{div} \mathbf{B}}_{\equiv 0} + \operatorname{grad} \alpha \cdot \mathbf{B}$$

From $\operatorname{grad} \alpha \cdot \mathbf{B} = 0$ we can deduce that the changes in α are always orthogonal to the field lines of $\mathbf{B}$. Thus α is constant along each field line.

$\square$

Notice that for force-free fields, the electric current $\mathbf{J} = \frac{1}{\mu_0} \alpha \mathbf{B}$ is aligned with the magnetic field $\mathbf{B}$. In the following we will mention three popular ways to solve this equation.

Potential Fields (PF)

Take equation 1.9 and set $\alpha = 0$ everywhere.

$$\operatorname{curl} \mathbf{B} = \mathbf{0}$$

The resulting equation is that of a curl-free condition on top of the divergence free magnetic field. By Helmholtz decomposition we know that such a field has to be a *potential field*, meaning that there exists a function $\phi : \mathbb{M} \to \mathbb{R}$ such that $\operatorname{grad} \phi = \mathbf{B}$.

This can be solved uniquely on the exterior of the sun $\mathbb{M}$ with appropriate Neumann boundary conditions. Looking for a field on the whole sun's exterior with prescribed flux through the sun's surface [Nabizadeh et al.(2021), Figs. 12, 13] gives unrealistic results far away from the sun (compare figure 3.18 in the results). Such a field can be computed ut using matrix solvers, iterative methods or boundary element methods.

Another popular approach is obtained if additional boundary conditions are prescribed on a fictional outer boundary about 2.5 sun radii away (compare figure 3.18, left), a so called *source surface*. This approach is known as the *Potential Field Source Surface* model (PFSS) [Altschuler and Newkirk(1969)]; [Sakurai(1982)] (see also [Priest(2014), Sec. 3.3]).

PFSS fields are published on a daily basis by NASA's solar dynamics observatory [NASA Solar Dynamics Observatory(2023)]. One such implementation is easily accesible in the *pfsspy* python package [Stansby et al.(2020)]. PFSS is still widely popular due to the its simplicity and the drawbacks from other methods. For this reason, the dissertation's output will compare its visual results to the PFSS method, as it is currently the go to method in solar physics.

Another important fact about potential fields is given by the *Minimum Energy Theorem for Potential Fields* [Priest(2014), p.98].

> *When the normal component of the magnetic field on a closed surface is given, the potential field in the volume enclosed by the surface has the minimum energy.*

Indeed, potential fields are thus the smoothest fields for the given conditions, something that contradicts the observation of strong concentrated magnetic filaments (section 1.2.2). One can see that potential fields are the smoothest fields by realizing that the magnetic energy minimum has the minimally integrated gradient of the potential ϕ.

$$\mathcal{E}(\mathbf{B}) := \int_{\mathbb{M}} \frac{|\mathbf{B}|^2}{2\mu_0} = \tfrac{1}{2\mu_0} \int_{\mathbb{M}} |\operatorname{grad} \phi|^2. \tag{1.10}$$

Potential field methods all require an *Eulerian grid* (voxel, tetrahedra) discretization of the space, which makes capturing high levels of details prohibitively expensive. On top of that, potential fields contain no helicity. More on that in the next subsection.

Linear Force-Free Fields (LFFF)

One can generalize the $\alpha = 0$ condition from equation 1.9 by setting $\alpha = \alpha_0 \in \mathbb{R}$ constant everywhere.

$$\operatorname{curl} \mathbf{B} = \alpha_0 \mathbf{B} \tag{1.11}$$

The resulting class of solutions are called *linear force-free fields*. These fields have the benefit of containing some helicty, a measure of how linked, twisted, writhed and knotted the magnetic field lines are. Helicity is defined by

$$\mathcal{H} := \int_{\mathbb{M}} \mathbf{A} \cdot \mathbf{B} \tag{1.12}$$

where $\mathbf{A}$ is the vector potential $\operatorname{curl} \mathbf{A} = \mathbf{B}$.

According to [Woltjer(1958)], the state of minimum magnetic energy for a given total magnetic helicity is a linear force-free field. Another benefit of the LFFF aproach is that when taking the curl of equation 1.9, we arrive at the well known Helmholtz equation

$$(\Delta + \alpha_0^2)\mathbf{B} = \mathbf{0} \tag{1.13}$$

It can be approached by a Fourier based method [Nakagawa and Raadu(1972)] [Alissandrakis(1981)] or by a Green's function method [Chiu and Hilton(1977)]. In either case, values for α_0 have to be guessed. One general problem is that solutions to the Helmholtz equation tend to oscillate towards infinity, making them non-zero towards infinity. As with the PF method, it requires a volumetric grid for computations.

Sadly, experiments show that the value of α_0 is highly non-uniformal [Wang(1993)] [Pevtsov et al.(1994)], revealing localized areas of strong field-aligned currents. Therefore, we now look over to the class of force-free fields that allow α to vary.

Non-Linear Force-Free Fields (NLFFF)

Take equation 1.9 and let α be anything it wants to be (while remaining constant along each field line) creates *non-linear force-free fields* (NLFFF). These methods tend to be a lot more complex and are less reliable.

The *Grad-Rubin* method is perhaps the most famous algorithm to compute NLFFF fields [Grad and Rubin(1958)] [Sakurai(1981)] [Wheatland(2004)]. This iterative volumetric method relies on vector magnetogram data and is, according to [Priest(2014), Sec. 3.4.5.2], the only method with a firm mathematical foundation. This method belongs to a separate class since we do not work with vector magnetogram data.

Other methods involve optimization of an energy, such as [Wiegelmann et al.(2006)] and [Sakurai(1979)]. There are also boundary element methods using Green's functions, which are usually too expensive for computing high detail [Yan(1995)] [Metcalf et al.(2008)]. Another class of methods requires adding a diffusion term and simulating relaxation [Low(1973)].

All of these methods require volumetric spatial discretization too, leading to the same issues with resolution and memory. For example, a 512^3 volume grid with three floating point values at each element representing **B** would take up about 1.6GB of data. On top of that 512^3 is far from enough to resolve the magnetogram surface, which is usually a 4096^2 array.

1.3.2   Clebsch Methods

There is also a small class of approaches using Euler potentials [Stern(1970)] (a.k.a. $\mathbb{R}^3$ valued Clebsch variables [Clebsch(1859)]). Clebsch methods have the benefit of encoding all field lines as level sets of a Clebsch map. However, $\mathbb{R}^3$-valued Clebsch methods are unable to encode any helicity (eq. 1.12).

Spherical valued Clebsch methods [Chern et al.(2017)] overcome these benefits, but as of the time of writing this dissertation, no $\mathbb{S}^3$ valued Clebsch method exists trying to deal with magnetic fields. Strong attempts have been made in the course of this dissertation, but the results were not as fruitful as the Lagrangian approach used in this dissertation and remain unpublished at the time of publication of this dissertation. A major drawback was again the requirement on the Eulerian volumetric spatial discritization making the desired target fidelity too costly and too slow to converge.

1.3.3   Lagrangian Methods

The alternative to Eulerian spatial discretization methods are Lagrangian methods, where the substance of interest itself is discretized. For example, for fluids the modeling primitive are small particles instead of tracking the fluid in a grid.

The approach in this dissertation is characterized by using Lagrangian curves to model a fibered volume. While applied to solar atmospheres here, such an approach is not new to many areas in computer graphics. It is also applied, for example, in hair modeling [Hadap and Magnenat-Thalmann(2001)], muscle modeling [Angles et al.(2019a)][Yu et al.(2021)], or for vorticity in fluids [Angelidis and Neyret(2005), Weißmann and Pinkall(2010), Padilla et al.(2019)].

In solar physics theory, magnetic filaments have been described mathematically as primitives without being applied for solving the MHS equation [Titov et al.(2018)]. [DeForest and Kankelborg(2007)] derived a Lagranian model for force-free fields. They do, however, rely strongly on an arbitrary initial topology, a problem that we will overcome in this dissertation (section 2.5.2 [Initial Curves and Matching by Optimal Transport]).

1.3.4 Other MHS Methods

All the methods mentioned above have in common that they attempt to solve the force-free field equation 1.8 with the argument that plasmatic effects in the MHS equation 1.6 are negligible. However, this negligibility is questionable, leading to the approaches as in [Rachmeler et al.(2009)], where in order to compensate for missing gas pressure artificial confining magnetic fields are deployed, something that is unphysical. As we will see in this dissertation, the gas pressure is necessary to confine/concentrate the magnetic field into strong bundles. This is why in this dissertation the full MHS equation is tackled.

Another approach is to run the full MHD simulation (equations 1.3) with dissipation together with fixed boundary conditions to let field dissipate into a static state [Mackay and Van Ballegooijen(2006)] [Contopoulos et al.(2011)] [Mikić et al.(1999)] or relaxation methods [Chodura and Schlüter(1981), Parker(1994), Janse et al.(2010)]. Each of these methods depends on an initial input field, which is often a potential field. Take note again that all of these mentioned methods operate on volumetric grids, not using Lagrangian primitives.

Making direct comparisons with the output of the above mentioned methods is difficult, and often these algorithms are inaccessible with standard hardware. Even if we had complete access to them, these methods have different requirements and objectives and thus fall into different categories than our approach. On top of that, section 1.3.5 shows how varying the output can be, which makes us believe that it would be very difficult to learn something from such direct comparisons. We therefore focus on comparing our results with the go-to method in solar physics, the PFSS method as mentioned in section (1.3.1).

One class of models which incorporates hydraulic gass pressure effects are the so-called *Current-Sheet* (CS) models (see e.g. [Moradi et al.(2010)]). In these, the magnetic field is confined in a domain bounded by a surface—the *current sheet*. Outside of this domain, in the gas domain, the magnetic field vanishes. This dissertation will enlarge the focus on these current-sheet models in section 1.4, where we will go into more detail.
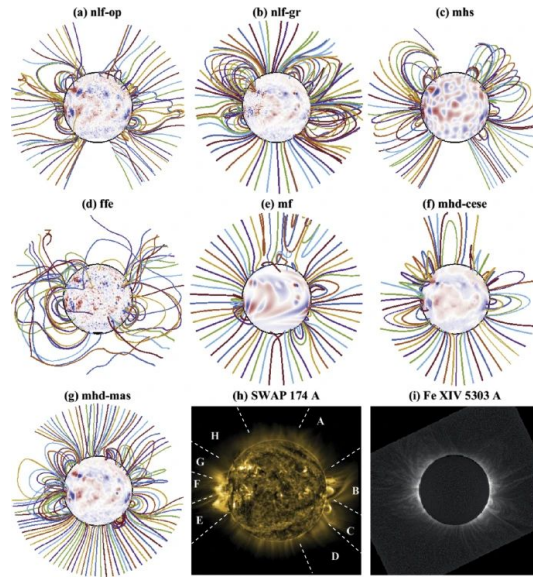
Figure 1.10: Image courtesy to [Yeates et al.(2018), Fig. 7]. Seven non-potential models are compared on the same dataset and some field lines are presented here. Due to the non-unique nature of the MHS equation, the resulting fields vary plentiful, making it hard, if not impossible, to point out which of these fields is "*correct*" in their fine structure.

1.3.5   About Comparisons

[Yeates et al.(2018)] provides a review of seven methods which vary greatly from each other. This comparison paper also shows how strongly the results vary depending on the chosen method, indicating that currently there is no reliable method for modeling the solar corona and comparisons [Yeates et al.(2018), Fig. 6, 7, 8](see figure 1.10). To facilitate further comparison, we often use the same data used by solar physicists as input to our method (e.g. figures. 3.21, 3.15, 3.17, 3.18 and 3.20).

However, we must note that solar physics has a major difficulty. When evaluating the quality of theoretical output, there simply is *no ground truth* available to compare with. The theory of the solar magnetic field is too complex to have evident answers and at the same time we are very limited to the data we can collect to compare with. Magnetograms and images of plasma filaments are basically the only data elements we have to estimate a flat projection of some part of a volumetric magnetic field. We will do our best to perform validations that are accessible in part 3 of this dissertation.

1.3.6   Visualization of Solar Atmospheres

The above mentioned related works deal with the magnetic field only, and not with the visualization of plasma filaments. Here we note some related work to the visualization effort.

Exemplary of the difficulty to match theory and real life are methods such as the *Aschwanden Vertical-current Forward Fit* (VCA) [Aschwanden et al.(2016)] method. It

employs magnetic modeling and additional image data as constraints to fit the result to the image. This means that the output of the theory is not enough to generate satisfying images. A photo of plasma filaments is used to correct the magnetic field.

For the purpose of rendering the solar atmosphere one needs to know how the computed magnetic field is related to emission (glow). Methods for the volumetric rendering of the solar atmosphere have been discussed in [Schrijver et al.(2005), Lionello et al.(2008), Machado et al.(2012), Peter et al.(2012), Naiman et al.(2017b)]. The physics of plasma glow is investigated in [Boerner et al.(2012), Zhuleku et al.(2020)]. As these methods depend on volumetric rendering, their level of detail is limited by the grid resolutions employed. This dissertation will establish a new glow model that is designed for the Lagrangian fibered nature of our approach.

Theory and visualization are often completely separated tasks. In this dissertation, we try to keep these separate too, although the theory was developed with visualization as a target application. Next, we introduce the smooth theory of force-free current sheets (part 1) that we then also discretize for computational purposes (part 2) and visualisation purposes (part 3).

1.4 Force-Free Current Sheet Model (FFCS)

As mentioned in section 1.3.4 there is a *current-sheet* (CS) model, where the magnetic field is confined in a domain bounded by a thin surface. This surface is called a current-sheet and is conceptually very similar to the vortex-sheet model in fluids [Fage and Johansen(1928)], used to describe discontinuous tangential vector field changes (figure 1.11). A vortex sheet describes a large concentration of vorticity where two regions with a large velocity field difference come into contact. Similarly, a current sheet describes a large concentration of current where two regions with a large magnetic field difference come into contact. Indeed, near the surface of the sun the magnetic field is strongly concentrated in a way that cannot be modeled with *smooth* fields such as potential fields, making the formation of current sheets inevitable at the boundary of this strong field region [Dixon et al.(1989)]. The normal component of $\mathbf{B}$ behaves continuously along the current sheet, while tangentially it does not have to, resulting in a large concentration of current $\mathbf{J} = \mathrm{curl}\,\mathbf{B}$ at the interface.

In this dissertation, the current-sheet model forms the basis of a new model that seeks to leverage the results from the force-free models without neglecting plasmatic gas effects. This model will be referred to as the *Force-Free Current-Sheet* (FFCS) model.

The core basis of the model is the observation of strongly concentrated magnetic filaments mentioned in section 1.2. The visually prominent features in the solar atmosphere do not form from processes in the corona itself. Instead, thin *flux tubes*—flux domains with cylindrical boundary—emerge from below the solar surface (Figure 1.9) (see also [Priest(2014), Sec. 9.3]; [Priest(2019), Sec. 3.2]). The pressure in the interior of these flux tubes is lower than the ambient gas pressure, raising the flux tubes above the solar surface due to buoyancy.
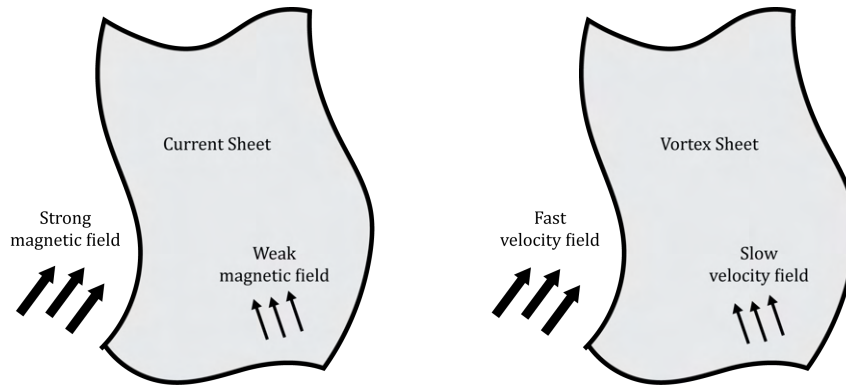
Figure 1.11: Left: The model of a current sheet separating an area of strong magnetic field with an area of weak magnetic field. Right: The model of a vortex sheet separating an area of fast velocity field with an area of slow velocity field. The concepts are the same.

While rising through the photosphere, the flux tube expands due to decreasing ambient gas pressure. By theorem 8, the magnetic field is transported by the same vector field as the gas, hence the amount of gas inside the tube remains unchanged. This leads to further decreasing gas density inside the expanding flux tube, leaving the gas pressure there at only a small fraction of the ambient gas pressure [Winebarger et al.(2008)].

This is close to the assumptions of the FFCS model when the current sheet is at the surface of the flux tubes. The approach lies in the following approximation: Instead of assuming a small fraction of plasma inside the flux tube, take the limit of assuming a *plasma-free* flux tube.

The flux tube's concentrated magnetic field creates a strong magnetic pressure that counters the gas pressure while creating a strong current sheet at the interface of the flux tube and the gas domain. Outside of the flux tube, we assume a weak magnetic field and hydrostatics that are dominated by the gaseous effects, while inside the flux tube we assume negligible gaseous effects where the force-free field theory applies in its limited domain. Let us now specify this decomposition mathematically in the next section.

1.4.1   Plasma Domain Decomposition

The solar corona (*plasma domain*) is decomposed into a *gas domain*, in which there is only gas but no magnetic field, and a *flux domain*, in which there is magnetic field but no gas. This model of separating the domains can also be found too in [Dixon et al.(1989)].

Definition 2 (**Domain Decomposition**)**.** Given the exterior domain of the stellar atmosphere $\mathbb{R}^3 \setminus \mathbb{B}$, we define the domain composition as follows:

$$\underbrace{\mathbb{R}^3 \setminus \mathbb{B}}_{\text{stellar exterior}} = \underbrace{\mathbb{M}}_{\text{plasma domain}} = \underbrace{\mathbb{M}_\mathbf{0}}_{\text{gas domain}} \cup \underbrace{\mathbb{M}_\mathbf{B}}_{\text{flux domain}} \tag{1.14}$$

with disjoint interiors

$$\mathbb{M}_\mathbf{0}^\circ \cap \mathbb{M}_\mathbf{B}^\circ = \emptyset. \tag{1.15}$$

We define the *interface* between the flux domain and the gas domain as

$$\mathcal{I} = \mathbb{M}_\mathbf{0} \cap \mathbb{M}_\mathbf{B}, \tag{1.16}$$

and define the *surface* of the sun

$$\partial\mathbb{M} = \partial\mathbb{B}, \tag{1.17}$$

and define the *magnetic surface* contact of the domain $\mathbb{M}_\mathbf{B}$ as

$$\Sigma_\mathbf{B} = \partial\mathbb{M} \cap \mathbb{M}_\mathbf{B}. \tag{1.18}$$

The index $\mathbf{0}$ on $\mathbb{M}_\mathbf{0}$ has been chosen to indicate the vanishing magnetic field $\mathbf{B} = \mathbf{0}$ in this domain. $\Sigma_\mathbf{B}$ will be the place where the Neumann boundary conditions are specified. See figure 1.12 for an illustration of the decomposition[4].

The state of the plasma is given by the domain decomposition together with the magnetic field $\mathbf{B}$. We call the pair $(\mathbb{M}_\mathbf{B}, \mathbf{B})$ the *plasma state.* In the FFCS model the plasma state will describe the entire state of the system.

1.4.2 Gas Domain

In the gas domain $\mathbb{M}_\mathbf{0}$ we have $|\mathbf{B}| = 0$ and the only relevant quantity is the gas pressure $p \colon \mathbb{M}_\mathbf{0} \to \mathbb{R}_{>0}$, which satisfies equation 1.6. Under mild topological assumptions (mentioned in the following theorem), p can be extended to a function $p \colon \mathbb{M} \to \mathbb{R}_{>0}$ depending on the height above the surface only.

The Gas Pressure of $\mathbb{M}_\mathbf{0}$ extended to $\mathbb{M}$

---

[4]This image was chosen to highlight that we never depended on the cylindrical shapes we used in out intuition. This theory works too for more complicated shapes.
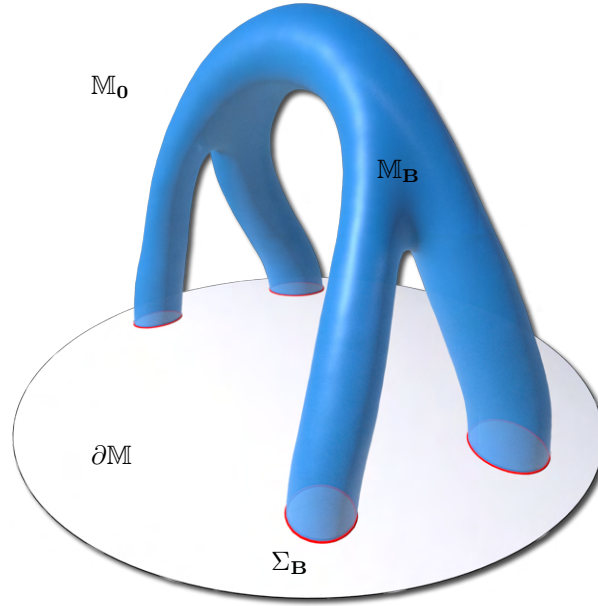
Figure 1.12: Domain decomposition of the sun's exterior $\mathbb{M}$ into a flux domain $\mathbb{M}_\mathbf{B}$ and a gas domain $\mathbb{M}_\mathbf{0}$. We write $\mathbb{M} = \mathbb{M}_\mathbf{B} \cup \mathbb{M}_\mathbf{0}$. $\partial\mathbb{M}$ is the surface of the sun and $\Sigma_\mathbf{B} = \mathbb{M}_\mathbf{B} \cap \partial\mathbb{M}$ is the domain of the sun's surface with magnetic flux.

Theorem 3 (**Gas Pressure Extension**). With the sun of radius $r_\odot$ centred at the origin, suppose that the level-sets $\{\mathbf{x} \in \mathbb{M}_\mathbf{0} \mid |\mathbf{x}| = r\}$ are connected for all $r \geq r_\odot$. Then, there exists a function $f \colon [r_\odot, \infty) \to \mathbb{R}_{>0}$ such that the gas pressure p is of the form

$$p(\mathbf{x}) = f(|\mathbf{x}|), \ p = p|_{\mathbb{M}_\mathbf{0}},$$

where $p \colon \mathbb{M} \to \mathbb{R}_{>0}$. In other words, p is a radial function.

Proof. By definition on $\mathbb{M}_\mathbf{0}$, $\mathbf{B} = \mathbf{0}$. Thus the MHS equation 1.6 becomes the equation of the hydrostatic equilibrium

$$\tfrac{m}{k_\mathrm{B} T} p \mathbf{g} - \operatorname{grad} p = \mathbf{0}.$$

Since the force of gravity is radial, then $\operatorname{grad} p$ is radially pointing inwards, as can easily be seen in the MHS equation 1.6. In the absence of magnetic field, we assume equal behaviour of temperature T in all directions. Thus, the level sets of p lie on concentric spheres. The extension is then obtained by extending these level sets to all connected concentric spheres.   □

What gas pressure model is relevant for the solar atmosphere? Let us specify this more.

The Gas Pressure Models

Consider a star with radius $r_\odot$ and centered at the origin. For $|\mathbf{x}| \geq r_\odot$ we assume a polynomial pressure model of the form

$$p(\mathbf{x}) = p_0 \left(\frac{|\mathbf{x}|}{r_\odot} \right)^{-\lambda}. \tag{1.19}$$

This choice is in reasonable agreement with measurements [Gent et al.(2013), Fig. 1] while having the huge benefit of allowing us to give an explicit description for the geodesics of the conformally changed metric (see section 2.2.3).

Under the assumption of constant temperature T, the gas pressure would be an exponential model looking like this:

$$p(\mathbf{x}) = p_0 e^{-\lambda \left(\frac{|\mathbf{x}| - r_\odot}{r_\odot} \right)}. \tag{1.20}$$

While this model is more common in solar physics and gives similar results in the area of interest near the sun's surface, it won't enable us to compute analytic solutions. Also, T is certainly not constant in reality. Using a polynomial barometric formula (equation 1.19) is a viable alternative in atmosphere physics.

1.4.3 Flux Domain

The flux domain is a manifold with corners—we allow for creases[5] on $\Sigma_\mathbf{B} := \mathbb{M}_\mathbf{B} \cap \partial\mathbb{M}$. Away from the creases the boundary $\partial\mathbb{M}_\mathbf{B}$ is smooth. The flux domain is by definition void of gas ($p = 0$) and thus the MHS equation 1.6 collapses to the well known force-free field equation (see section 1.3.1).

$$(\operatorname{curl}\mathbf{B}) \times \mathbf{B} = \mathbf{0}. \tag{1.21}$$

According to the FFCS model, $\mathbb{M}_\mathbf{B}$ is the support of a force-free divergence-free vector field $\mathbf{B}\colon \mathbb{M}_\mathbf{B} \to \mathbb{R}^3$. This field realizes the prescribed boundary flux on $\Sigma_\mathbf{B}$ (surface of the sun, flux going in and out) and is tangent to the boundary $\partial\mathbb{M}_\mathbf{B}$ elsewhere (zero Neumann boundary condition).

The Neumann Boundary Conditions of $\mathbb{M}_\mathbf{B}$

Let's get mathematically precise. For the boundary condition, we need to be given a map $\Phi : \partial\mathbb{M} \to \mathbb{R}$ from the surface of the sun to prescribed normal flux values.

---

[5]We notice that in our theory creases are no problem. We just wanted to mention this here although we do not intend to make any use of that.

Definition 4 (**Neumann Boundary Flux**)**.** Let $\Phi : \partial\mathbb{M} \to \mathbb{R}$. When the magnetic field $\mathbf{B}$ of the plasma state $(\mathbb{M}_\mathbf{B}, \mathbf{B})$ fulfils the following equations:

$$\Phi(\mathbf{x}) = \begin{cases} \langle \mathbf{B}(\mathbf{x}), N \rangle & \text{if } \mathbf{x} \in \Sigma_\mathbf{B} \\ 0 & \text{if } \mathbf{x} \in \partial\mathbb{M} \setminus \Sigma_\mathbf{B}. \end{cases}$$

$$\int_{\partial\mathbb{M}} \Phi(\mathbf{x}) = 0 \tag{1.22}$$

Then we say that $\mathbf{B}$ fulfils the *Neumann boundary conditions* set by the prescribed normal flux Φ on $\partial\mathbb{M}$.

The divergence freeness of the magnetic field $\mathbf{B}$ requires the total flux to be zero on the surface $\partial\mathbb{M}$ (magnetic monopoles are illegal).

The Force-Free Magnetic Field of $\mathbb{M}_\mathbf{B}$

Instead of deriving any explicit solution of the force-free and divergence-free field that fits the boundary conditions on $\mathbb{M}_\mathbf{B}$, we will for now derive theoretically its existence and some properties. The exact computation will be handled in part 2 of this dissertation once we introduced discrete magnetic filaments.

Theorem 5 (**B-Field Theorem**)**.** Given the FFCS model domain decomposition $\mathbb{M} = \mathbb{M}_\mathbf{0} \cap \mathbb{M}_\mathbf{B}$ and a boundary map $\Phi : \partial\mathbb{M} \to \mathbb{R}$, and the following conditions on a magnetic field $\mathbf{B} : \mathbb{M}_\mathbf{B} \to \mathbb{R}^3$:

1. Neumann boundary flux data Φ with zero total flux $(\int_{\partial\mathbb{M}} \Phi = 0)$.
2. Zero Neumann boundary flux on the gas and flux interface $\mathcal{I} = \mathbb{M}_\mathbf{0} \cap \mathbb{M}_\mathbf{B}$ $(\langle N, \mathbf{B} \rangle = 0)$.
3. $\mathbf{B}$ is divergence free $(\operatorname{div} \mathbf{B} = 0)$.
4. $\mathbf{B}$ is force-free $(\operatorname{curl} \mathbf{B} \times \mathbf{B} = \mathbf{0})$.

Then at least one such field $\mathbf{B}$ on $\mathbb{M}_\mathbf{B}$ always exists. One such magnetic field is the unique potential field.

Proof. What sounds so complex, is actually a basic result from PDE theory. Assume a function ϕ such that $\mathbf{B} = \operatorname{grad} \phi$ that satisfies condition 3 and 4. From the divergence free condition for the magnetic field we also get to write

$$\operatorname{div} \mathbf{B} = 0 = \operatorname{div} \operatorname{grad} \phi = \Delta\phi \tag{1.23}$$

which evidently show that this is just a basic Laplace equation $\Delta\phi = 0$ with a particular set of Neumann boundary condition to be solved. A basic task in PDE theory. Solving $\Delta\phi = 0$ also returns us a ϕ that really solves condition 3 and 4. The non uniqueness comes from the existence of other possible force free fields as mentioned in section 1.3.1.

$\square$

These fields don't have to be unique. Imagine a sunspot pair and potential field going through tube like structure connecting one to another. For a non-potential example, you could just evenly twist the field lines as shown in figure 1.13.
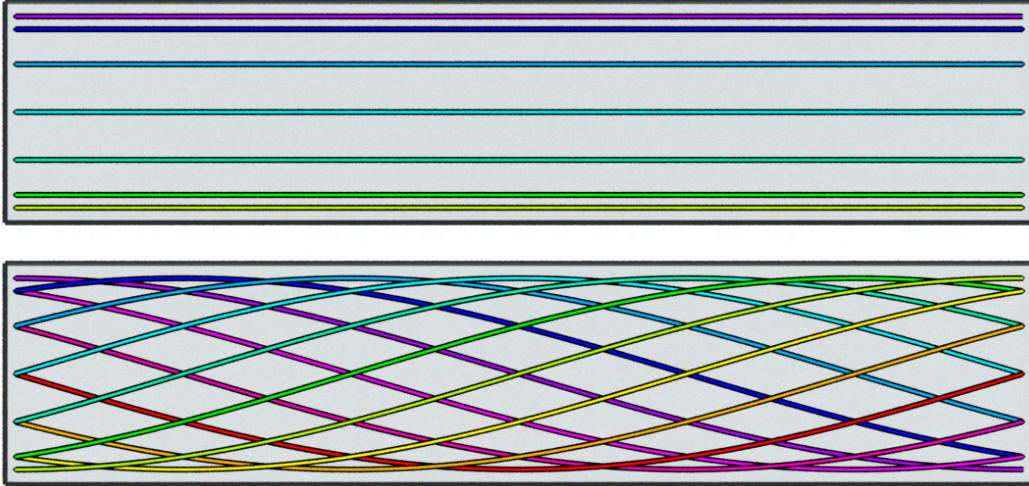
Figure 1.13: $\mathbb{M}_{\mathbf{B}}$ in an idealised setup as a perfect tube. Top: with a potential field. Bottom: with a twisted field. Both are force-free fields.

More importantly, a domain decomposition defined by $\mathbb{M}_{\mathbf{B}}$ together with a boundary flux map Φ will always guarantee us the existence of a plasma state $(\mathbb{M}_{\mathbf{B}}, \mathbf{B})$. In general, such plasma states do only solve the MHS equations on the interiors $\mathbb{M}_{\mathbf{0}}^{\circ}$ and $\mathbb{M}_{\mathbf{B}}^{\circ}$ of the domain composition, *but not necessarily at the interface $\mathcal{I}$*. Changing the potential field solution of $\mathbf{B}$ is equivalent to deforming the domain $\mathbb{M}_{\mathbf{B}}$. Generally, not every given $\mathbb{M}_{\mathbf{B}}$ can contain a valid solution $\mathbf{B}$ that satisfied the MHS equation on $\mathbb{M}_{\mathbf{B}}$ as well as on $\mathcal{I}$.

How does this differ from the potential field theory? The answer lies in the shape of $\mathbb{M}_{\mathbf{B}}$. If $\mathbb{M}_{\mathbf{B}} = \mathbb{M}$, ($i.e.\mathbb{M}_{\mathbf{0}} = \emptyset$, there is no gas) then we arrive at the same result as the potential field models (see theorem 40 in section 3.2.2). However, we will show in section 1.5 that in order for the MHS equation to be fulfilled on the interface $\mathcal{I}$, we need a special condition on the interface. We will come to understand that it is the gas pressure's influence that is concentrating the magnetic field into bundles by limiting $\mathbb{M}_{\mathbf{B}}$'s size.

In order to explore solutions of the FFCS model with a potential field inside, we could look at deformations of $\mathbb{M}_{\mathbf{B}}$. However, instead we are going to look at plasma states $(\mathbb{M}_{\mathbf{B}}, \mathbf{B})$ and figure out when the MHS equation is satisfied at the gas-flux interface $\mathcal{I}$.

1.4.4 FFCS Solutions of the MHS-Equation

Until now we have a domain decomposition model (section 1.4.1) that, with valid boundary conditions, guarantees to solve the MHS equation on the gas domain interior $\mathbb{M}_{\mathbf{0}}^{\circ}$ and flux

domain interior $\mathbb{M}_{\mathbf{B}}^{\circ}$. Since $\mathbb{M}_{\mathbf{0}}$'s purpose is to contain the gas pressure function p and $\mathbb{M}_{\mathbf{B}}$'s purpose is to carry the magnetic field $\mathbf{B}$, for the purpose of solving the MHS equation at the interface $\mathcal{I}$ we can expect to be some kind of relation between p and $\mathbf{B}$.

In this section we will prove that whatever force-free field $\mathbf{B}$ in $\mathbb{M}_{\mathbf{B}}$ is chosen, as long as it fulfils a basic *gas-flux pressure* balance, the MHS equation is solved everywhere, including the interface $\mathcal{I}$. But first, a mathematical remark.

Magnetic Tension and Pressure

The Lorenz force term can be decomposed into a *magnetic tension part* and a *magnetic pressure* part as follows:

$$\underbrace{\frac{1}{\mu_0}(\operatorname{curl}\mathbf{B})\times\mathbf{B}}_{\text{Lorenz force term}} = \underbrace{\frac{1}{\mu_0}(\mathbf{B}\cdot\nabla)\mathbf{B}}_{\text{magnetic tension}} - \underbrace{\operatorname{grad}\left(\frac{|\mathbf{B}|^2}{2\mu_0}\right)}_{\text{magnetic pressure}}. \tag{1.24}$$

In general, magnetic tension acts in the direction to reduce the field line's Euclidean lengths. Tension makes the field lines straighter and acts against curvature. On the other hand, magnetic pressure prevents the magnetic field lines from becoming too dense (large $\mathbf{B}$). Thus, a force-free field is a balance of magnetic tension and magnetic pressure. In the FFCS model the gas pressure in $\mathbb{M}_{\mathbf{0}}$ plays an important role on the force-free field of $\mathbb{M}_{\mathbf{B}}$, as we will establish next by a theorem.

FFCS-MHS Theorem

Now to a first key contribution of this research:

> **Theorem 6** (**FFCS MHS Theorem**). A state of the plasma $(\mathbb{M}_{\mathbf{B}},\mathbf{B})$ solves the MHS equation 1.6 (in a distributional sense) if and only if $\mathbf{B}$ is force-free and satisfies
>
> $$\frac{|\mathbf{B}|^2}{2\mu_0} = p$$
>
> on the gas-flux interface $\mathcal{I}$.

Proof. This proof will be rather technical. We will build a ε-*wide smooth transition region* between $\mathbb{M}_{\mathbf{0}}$ and $\mathbb{M}_{\mathbf{B}}$ and then take the limit $\varepsilon \to 0$. That is, we flatten the current sheet. We express $\mathbf{B}$ and p as the limit of a smooth magnetic field $\tilde{\mathbf{B}}$ and a smooth gas pressure $\tilde{p}$.

p is a known function, and $\mathbb{M}_{\mathbf{B}}$ is fixed. We are seeking a condition for a force-free $\mathbf{B}$ at the interface $\mathcal{I}$ as $\mathbf{B}$ is the degree of freedom we have. For that purpose, we will apply a variation on the MHS equation (1.6) with respect to $\mathbf{B}$ that keeps the stellar surface $\partial\mathbf{B}$ fixed due to the boundary condition.

Let $\varepsilon > 0$ be small and let $\mathbb{M}_{\mathbf{0}}^{\varepsilon}$ denote the ε-neighbourhood of $\mathbb{M}_{\mathbf{0}}$ (travelling ε in the normal direction). Now, let $\varphi_{\mathbf{B}}, \varphi_{\mathbf{0}} \colon \mathbb{M} \to [0,1]$ be smooth functions such that

$$\varphi_{\mathbf{B}}|_{\mathbb{M}_{\mathbf{B}}\setminus\mathbb{M}_{\mathbf{0}}^{\varepsilon}} = 1, \quad \varphi_{\mathbf{B}}|_{\mathbb{M}_{\mathbf{0}}} = 0, \quad \varphi_{\mathbf{0}}|_{\mathbb{M}_{\mathbf{0}}} = 1, \quad \varphi_{\mathbf{0}}|_{\mathbb{M}_{\mathbf{B}}\setminus\mathbb{M}_{\mathbf{0}}^{\varepsilon}} = 0.$$

These are continuous transition functions for the ε-neighbourhood. We create a new magnetic field $\tilde{\mathbf{B}}$ and a pressure function $\tilde{p}$ through these transition functions.

$$\tilde{\mathbf{B}} = \varphi_{\mathbf{B}}\mathbf{B}, \quad \tilde{p} = \varphi_{\mathbf{0}}p,$$

where p is the extension of the gas pressure function in theorem 3. In particular, we have

$$\operatorname{curl} \tilde{\mathbf{B}} = \varphi_{\mathbf{B}} \operatorname{curl} \mathbf{B} + \operatorname{grad} \varphi_{\mathbf{B}} \times \mathbf{B}$$

and

$$(\operatorname{curl} \tilde{\mathbf{B}}) \times \tilde{\mathbf{B}} = \varphi_{\mathbf{B}}^2 \operatorname{curl} \mathbf{B} \times \mathbf{B} + \tfrac{1}{2}(\operatorname{grad} \varphi_{\mathbf{B}}^2 \times \mathbf{B}) \times \mathbf{B}$$
$$= \varphi_{\mathbf{B}}^2 \operatorname{curl} \mathbf{B} \times \mathbf{B} + \tfrac{1}{2}(\mathbf{B}\langle \operatorname{grad} \varphi_{\mathbf{B}}^2, \mathbf{B}\rangle - \operatorname{grad} \varphi_{\mathbf{B}}^2 |\mathbf{B}|^2).$$

Instead of varying the entire MHS equation, we compute elements of it and bring the result together. We want to analyse how $\tilde{\mathbf{B}}$ differs from $\mathbf{B}$. Let Y be a vector field compactly supported away from the boundary $\partial\mathbb{M}$. Then, for $\varepsilon \to 0$, we get, using Stokes' Theorem, the following relation for the magnetic field $\mathbf{B}$:

$$\int_{\mathbb{M}} \langle (\operatorname{curl} \tilde{\mathbf{B}}) \times \tilde{\mathbf{B}}, Y\rangle - \int_{\mathbb{M}_{\mathbf{B}}} \langle (\operatorname{curl} \mathbf{B}) \times \mathbf{B}, Y\rangle$$
$$= \tfrac{1}{2}\int_{\mathbb{M}} \langle \operatorname{grad} \varphi_{\mathbf{B}}^2, \langle \mathbf{B}, Y\rangle \mathbf{B} - |\mathbf{B}|^2 Y\rangle + o(1)$$
$$= -\tfrac{1}{2}\int_{\mathbb{M}_{\mathbf{B}}} \operatorname{div}(\langle \mathbf{B}, Y\rangle \mathbf{B} - |\mathbf{B}|^2 Y) + o(1)$$
$$= \tfrac{1}{2}\int_{\partial\mathbb{M}_{\mathbf{B}}} |\mathbf{B}|^2 \langle Y, N\rangle + o(1).$$

In the last equation we used the fact that the normal unit vector N of $\mathcal{I}$ and $\mathbf{B}$ are perpendicular, $N \perp \mathbf{B}|_{\partial\mathbb{M}_{\mathbf{B}}}$ (see theorem 5), because the boundary condition was to have no normal flux at the interface $\mathcal{I}$. Similarly, the pressure gradient behaves the following way:

$$\int_{\mathbb{M}} \langle \operatorname{grad} \tilde{p}, Y\rangle = \int_{\mathbb{M}} \langle p \operatorname{grad} \varphi_{\mathbf{0}} + \varphi_{\mathbf{0}} \operatorname{grad} p, Y\rangle$$
$$= \int_{\mathbb{M}} \langle \operatorname{grad} \varphi_{\mathbf{0}}, pY\rangle + \int_{\mathbb{M}_{\mathbf{0}}} \langle \operatorname{grad} p, Y\rangle + o(1)$$
$$= -\int_{\mathbb{M}_{\mathbf{0}}} \operatorname{div}(pY) + \int_{\mathbb{M}_{\mathbf{0}}} \langle \operatorname{grad} p, Y\rangle + o(1)$$
$$= \int_{\partial\mathbb{M}_{\mathbf{B}}} p\langle Y, N\rangle + \int_{\mathbb{M}_{\mathbf{0}}} \langle \operatorname{grad} p, Y\rangle + o(1).$$

We now perform the entire MHS equation variation and plug in the $\tilde{\mathbf{B}}$ and $\tilde{p}$ results in

from above.

$$\int_{\mathbb{M}} \langle \tfrac{1}{\mu_0}(\operatorname{curl} \tilde{\mathbf{B}}) \times \tilde{\mathbf{B}} - \operatorname{grad} \tilde{p} + \tfrac{m}{k_B T} \tilde{p} \mathbf{g}, Y \rangle$$

$$= \tfrac{1}{\mu_0} \int_{\mathbb{M}_{\mathbf{B}}} \langle (\operatorname{curl} \mathbf{B}) \times \mathbf{B}, Y \rangle + \int_{\mathbb{M}_{\mathbf{0}}} \langle \tfrac{m}{k_B T} p \mathbf{g} - \operatorname{grad} p, Y \rangle$$

$$+ \int_{\partial \mathbb{M}_{\mathbf{B}}} (\tfrac{|\mathbf{B}|^2}{2\mu_0} - p)\langle Y, N \rangle + o(1)$$

If the MHS equation is solved by $\mathbf{B}$, then this integral expression needs to be zero for any variation Y (that is fixed at the surface). Since the domains are decomposed into $\mathbb{M}_{\mathbf{B}}$, $\mathbb{M}_{\mathbf{0}}$ and $\mathcal{I}$, we get three conditions:

1.

$$(\operatorname{curl} \mathbf{B}) \times \mathbf{B} = \mathbf{0}$$

on $\mathbb{M}_{\mathbf{B}}$, which is a given by the FFCS model, the force-free magnetic field.

2.

$$\tfrac{m}{k_B T} p \mathbf{g} = \operatorname{grad} p$$

on $\mathbb{M}_{\mathbf{0}}$, which is a given by the FFCS model, the hydrostatic equilibrium.

3.

$$\tfrac{|\mathbf{B}|^2}{2\mu_0} = p$$

on the interface $\mathcal{I}$, which is the new condition this theorem is about. Its requirement here is proof of the theorem.

$$\square$$

Theorem 6 provides us with an important condition for the core problem of solving the MHS equation on the entire domain $\mathbb{M}$ including the interface $\mathcal{I}$. $\mathbf{B}$ does not have to be a potential field inside $\mathbb{M}_{\mathbf{B}}$, as long as it fulfils the required boundary condition (section 1.4.3) and $|\mathbf{B}|^2/2\mu_0 = p$. See figure 1.14.

This theorem does only give us a valid condition required if $\mathbb{M}_{\mathbf{B}}$ is fixed. However, it is yet unclear what shape $\mathbb{M}_{\mathbf{B}}$ should have in the first place. Different shapes will give very different MHS solution plasma states $(\mathbb{M}_{\mathbf{B}}, \mathbf{B})$. What choice of plasma state $(\mathbb{M}_{\mathbf{B}}, \mathbf{B})$ is the *best*? In this dissertation, the choice of $\mathbb{M}_{\mathbf{B}}$ will be guided by an minimum energy principle. We define the required energy in the next section.

1.4.5   Magnetohydrostatic Energy

Theorem 6 gives us a valid criterion for solving the MHS equation using a given domain decomposition. However, it does not tell us what domain decomposition to go for, *i.e.*what should $\mathbb{M}_{\mathbf{B}}$ look like? In this section we will establish the physical energy of the plasma state $(\mathbb{M}_{\mathbf{B}}, \mathbf{B})$ to later explore its minima.
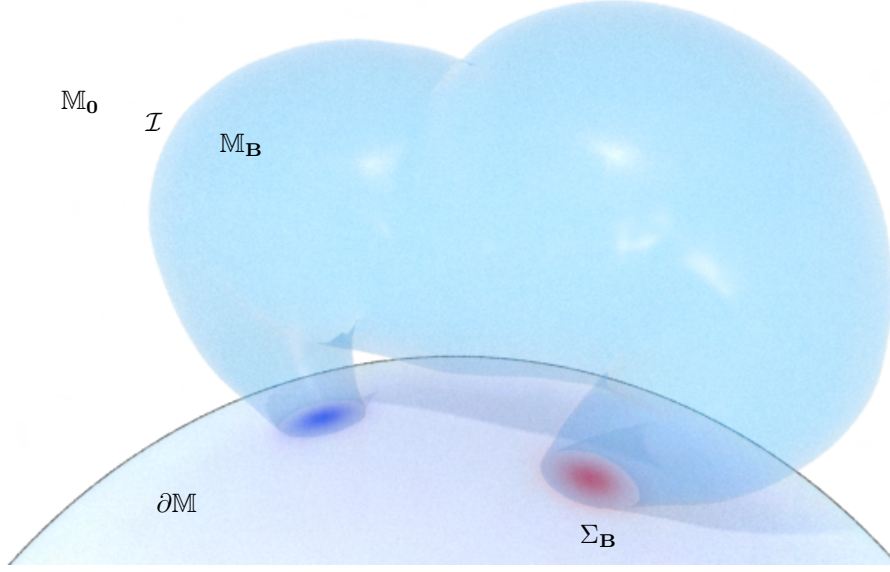
Figure 1.14: The flux map and the domain decomposition define a force-free field $\mathbf{B}$ inside of $\mathbb{M}_{\mathbf{B}}$, which solves the MHS equation on the interior of $\mathbb{M}_{\mathbf{B}}^{\circ}$, but not necessarily on the interface $\mathcal{I}$. Theorem 6 states that the required condition is the gas-flux pressure equilibrium $p = {}^{B^2}/_{2\mu_0}$ on $\mathcal{I}$. In $\mathbb{M}_{\mathbf{0}}^{\circ}$ we have $\mathbf{B} = 0$ and thus the hydrostatic pressure equilibrium. One could imagine $\mathbb{M}_{\mathbf{B}}$ to be like a balloon expanding against an exterior gas pressure.

Definition 7 (Magnetohydrostatic Energy). For a domain decomposition $\mathbb{M} = \mathbb{M}_{\mathbf{0}} \cup \mathbb{M}_{\mathbf{B}}$ with corresponding magnetic field $\mathbf{B}$ the *magnetohydrostatic energy is*

$$\mathcal{E}(\mathbb{M}_{\mathbf{B}}, \mathbf{B}) := \int_{\mathbb{M}_{\mathbf{B}}} \left(p + \tfrac{|\mathbf{B}|^2}{2\mu_0} \right) \tag{1.25}$$

where $p \colon \mathbb{M} \to \mathbb{R}_{>0}$ denotes the extension of the gas pressure on $\mathbb{M}_{\mathbf{0}}$ to a function on the whole of $\mathbb{M}$ (as established in theorem 3). We will refer to it as the *MHS energy*.

To see the physical meaning of this energy, imagine $\mathbb{M}$ initially without any magnetic field $\mathbf{B}$ and filled throughout with gas at pressure p. Growing a vacuum-filled hole—initially of zero volume—with shape $\mathbb{M}_{\mathbf{B}}$ involves doing work against the pressure p. The total energy (called enthalpy) needed for creating this vacuum will be $\int_{\mathbb{M}_{\mathbf{B}}} p$. Filling $\mathbb{M}_{\mathbf{B}}$ with the magnetic field $\mathbf{B}$ adds further magnetic energy, the amount being $\int_{\mathbb{M}_{\mathbf{B}}} |\mathbf{B}|^2/2\mu_0$. See figure 1.15.

$\mathcal{E}(\mathbb{M}_{\mathbf{B}}, \mathbf{B})$ is a physical energy quantity of the system we are dealing with. By the principle of minimum energy, we expect interesting properties of those plasma states $(\mathbb{M}_{\mathbf{B}}, \mathbf{B})$ that are minima of the MHS energy. We will show through variation, that these minima states are solutions on the MHS equation.
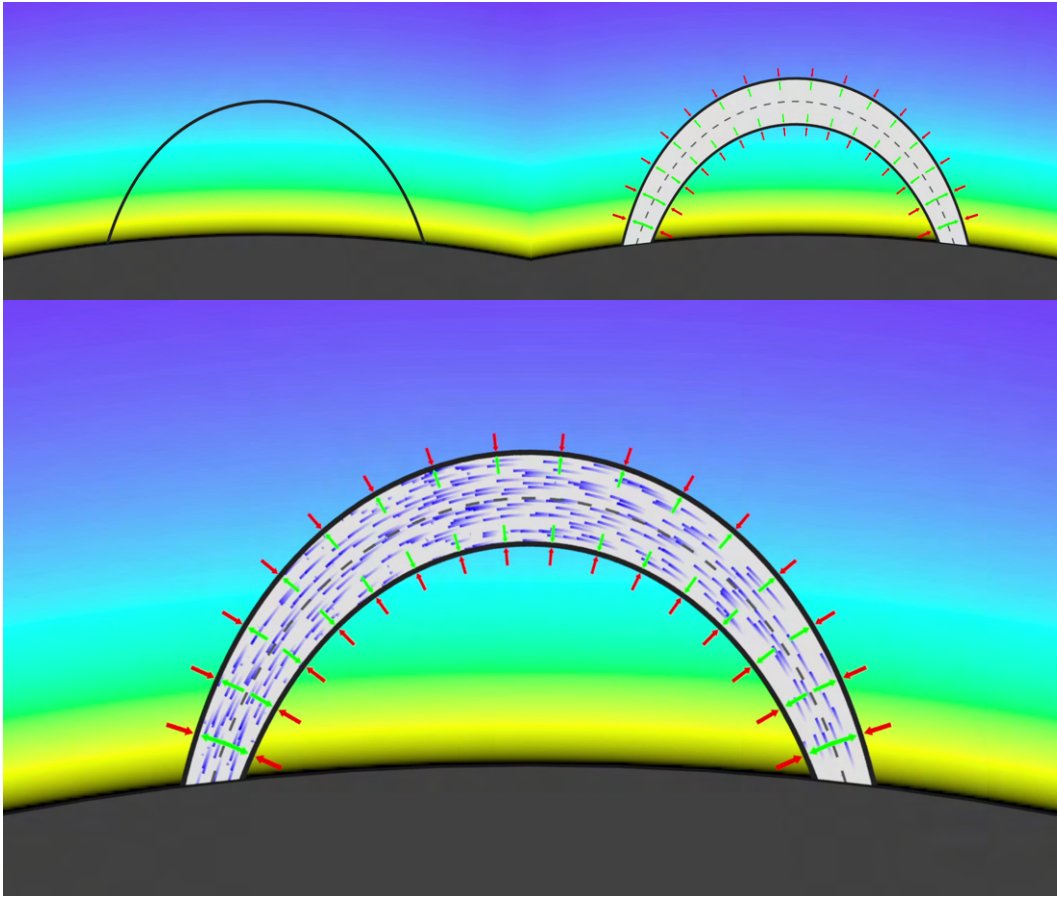
Figure 1.15: An illustration of the MHS energy. The background color gradient indicates the decreasing pressure by height. Top left: $\mathbb{M}_{\mathbf{B}}$ is infinitesimally thin. Equal flux in a small area makes $\int B^2/2\mu_0$ very large, thus leading to a high energy $\mathcal{E}$. Top right: Creating a vacuum in the interior requires the energy $\int p$. The exterior gas will push against it (red arrows) while an interior pressure needs to fight against it (green arrows). Bottom: The interior pressure is provided by the magnetic field flowing through $\mathbb{M}_{\mathbf{B}}$.

1.5   Variational Analysis

From the domain decomposition $\mathbb{M}_{\mathbf{B}}$ and boundary flux Φ we can always rely on the existence of a potential magnetic field $\mathbf{B}$ thanks to theorem 5. However, we can't yet guarantee that the gas-flux pressure equilibrium holds at the interface $\mathcal{I}$ to solve the MHS equation as demanded by theorem 6.

Since Φ is fixed input data, we know that deforming $\mathbb{M}_{\mathbf{B}}$ is the degree of freedom to point our attention to. Since we live with a boundary condition at the surface of the sun, the boundary $\Sigma_{\mathbf{B}}$ has to remain fixed at all times. The variation we choose should respect that. We will work with variations of the magnetic field $\mathbf{B}$, and when doing so, implicitly change the flux domain $\mathbb{M}_{\mathbf{B}}$ by shifting its support.

1.5.1 What Variation is Natural?

In this section, we establish what class of variations makes sense to consider given the magnetohydrostatic setting. The key observation is one we already touched upon in the introductory section 1.1.2. We mentioned that the magnetic field is passively transported by the gas in the ideal MHD theory. We establish this statement mathematically.

> **Theorem 8 (Frozen B-Field).** From the ideal MHD equations 1.4 it follows that the magnetic field **B** is passively transported by the gas motion **v**. In other words: **B** is frozen in the plasma.

Proof. Let $\mathbb{M}$ be a domain filled by plasma moving under the influence of arbitrary forces. Similarly to the differential geometric description of hydrodynamics as performed by [Arnold and Khesin(1998)], the motion of the gas can be described by a family of diffeomorphisms

$$t \mapsto \varphi_t \colon \mathbb{M} \to \mathbb{M}, \quad t \in (-\epsilon, \epsilon),$$

with $\varphi_0 = \mathrm{id}_{\mathbb{M}}$ and velocity field

$$\mathbf{v} = \frac{\partial}{\partial t}\big|_{t=0}\, \varphi_t = \mathring{\varphi}.$$

φ thus describes where the gas has moved after time t and its derivative describes the velocity. A piece of mass at $\mathbf{x} \in \mathbb{M}$ at $t = 0$ will be moved to $\varphi_{t_1}(\mathbf{x})$ at time $t = t_1$. We say that φ *transports* the gas. How does φ relate the initial magnetic field **B** with the magnetic field $\mathbf{B}_t$ at time t?

Faraday's law, as part of the ideal MHD equations (1.4), says that the time derivative of **B** can be expressed as

$$\mathring{\mathbf{B}} = \mathrm{curl}(\mathbf{v} \times \mathbf{B}).$$

We now switch to exterior calculus, in which we express the magnetic field **B** in terms of the two form $\beta_t = \iota_{B_t}\det$, which satisfies $d\beta_t = 0$ (always divergence fee), this equation can be written as

$$\mathring{\beta} = \iota_{\mathring{\mathbf{B}}}\det = \iota_{\mathrm{curl}(\mathbf{B}\times\mathbf{v})}\det = d(\iota_{\mathbf{v}}\iota_{\mathbf{B}}\det) = -d\left(\iota_{\mathbf{v}}\beta\right) - \iota_{\mathbf{v}}(d\beta) = -\mathcal{L}_{\mathbf{v}}\,\beta$$

where we use Cartan's magic formula for the Lie derivative

$$\mathcal{L}_X = d \circ \iota_X + \iota_X \circ d.$$

The resulting equation $\mathring{\beta} = -\mathcal{L}_{\mathbf{v}}\,\beta$ exactly implies that **B** is transported by the vector field **v**. In other words, the same diffeomorphisms φ also transports our magnetic field. Thus

$$\beta_t = (\varphi_t^{-1})^*\beta_0.$$

We visualize a magnetic field as a collection of field lines whose density indicates the field strength. Applying the diffeomorphisms φ_t to these field lines then acts as a deformation as seen in figure 1.16.
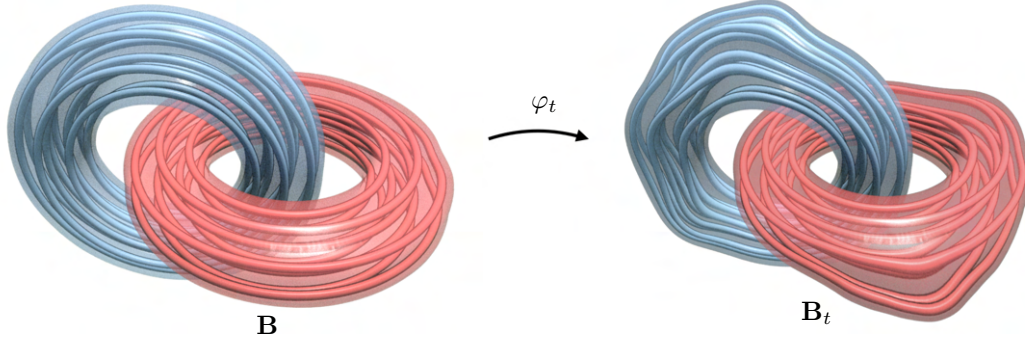
Figure 1.16: A magnetic field is transported by transporting its field lines.

$\square$

From theorem 8 we conclude: the only variations of a plasma state $(\mathbb{M}_\mathbf{B}, \mathbf{B})$ compatible with the laws of magnetohydrodynamics are those that come from diffeomorphisms of $\mathbb{M}$ shown in the above proof. These are the ones that transport $\mathbf{B}$ through Faraday's law. Thus, we can conclude:

> **Corollary 9** (**Natural Variation**). The natural class of variations of $\mathbf{B}$ in the ideal MHD setting are of the form
> $$\mathring{\mathbf{B}} = \mathrm{curl}(Y \times \mathbf{B}),$$
> induced by a vector field Y on $\mathbb{M}$.

Proof. From the ideal MHD equations 1.4 we know that

$$\tfrac{\partial}{\partial t}\mathbf{B} = \mathrm{curl}(\mathbf{v} \times \mathbf{B}).$$

Combine this with the statement that the magnetic field is frozen into the plasma (theorem 8) to see that setting $Y = v$ gives us all the varations that would occur in the ideal MHD setting. Any variation $\mathring{\mathbf{B}}$ of a different form would be incompatible with the ideal MHD equation.

$\square$

1.5.2   Variational Analysis of the MHS Energy

Let's perform the raw calculation of the variation on the MHS energy (def. 7) with the class of variations $\mathring{\mathbf{B}}$ mentioned in corollary 9.

Theorem 10 (MHS Variation). Let $\mathbb{M} = \mathbb{M_0} \cup \mathbb{M_B}$ be a domain decomposition with magnetic field $\mathbf{B}$ and N be the normal of the interface $\mathcal{I}$ pointing away from the flux domain $\mathbb{M_B}$. Then the MHS energy variation corresponding to a vector field Y on $\mathbb{M}$ such that $\mathring{\mathbf{B}} = \mathrm{curl}(Y \times \mathbf{B})$ is given by

$$\mathring{\mathcal{E}} = - \int_{\mathbb{M_B}} \langle \tfrac{1}{\mu_0} \mathrm{curl}\,\mathbf{B} \times \mathbf{B}, Y \rangle$$
$$+ \int_{\partial\mathbb{M_B}} \left(\left(p - \tfrac{|\mathbf{B}|^2}{\mu_0} \right) \langle Y, N \rangle + \tfrac{1}{\mu_0} \langle \mathbf{B}, Y \rangle \langle \mathbf{B}, N \rangle \right).$$

Proof. As a reminder, the MHS energy is written as

$$\mathcal{E}(\mathbb{M_B}, \mathbf{B}) := \int_{\mathbb{M_B}} \left(\underbrace{p}_{\text{gas pressure}} + \underbrace{\frac{|\mathbf{B}|^2}{2\mu_0}}_{\text{flux pressure}} \right)$$

We will separately compute the variation on the pressure term p and magnetic term $|\mathbf{B}|^2/2\mu_0$. Let $\mathring{\mathbf{B}} = \mathrm{curl}(Y \times \mathbf{B})$ be the variations of $\mathbf{B}$ given Y as motivated by corollary 9. Again, we need a family of diffeomorphisms $\varphi_t : \mathbb{M} \to \mathbb{M}$ just like in theorem 8's proof, with $\varphi_0 = \mathrm{id}_{\mathbb{M}}$ and $Y = \frac{\partial}{\partial t}\big|_{t=0} \varphi_t = \mathring{\varphi}$. We want to compute

$$\mathring{\mathcal{E}} = \frac{d}{dt}\bigg|_{t=0} \varphi_t^* \mathcal{E}$$

The change in the pressure contribution to the energy is given by the Lie derivative along Y because p does not change over time

$$\frac{d}{dt}\bigg|_{t=0} \int_{\mathbb{M_B}} \varphi_t^* p = \int_{\mathbb{M_B}} \mathcal{L}_Y p$$

We again use Cartan's magic formula from exterior calculus with basic calculus identities and get

$$\mathcal{L}_Y p = \iota_Y(dp) + d(\iota_Y p) = \langle \mathrm{grad}\, p, Y \rangle + p\,\mathrm{div}(Y) = \mathrm{div}(pY).$$

Integration by parts will then bless us with

$$\frac{d}{dt}\bigg|_{t=0} \int_{\mathbb{M_B}} \varphi_t^* p = \int_{\mathbb{M_B}} \mathrm{div}(pY)$$
$$= \int_{\partial\mathbb{M_B}} p\langle Y, N \rangle.$$

This concludes the pressure p part of the variation. The time derivative of the magnetic energy contribution is calculated similarly, but we have to keep in mind that instead of

the time-independent integrand p det we now are dealing with a time-dependent integrand $\frac{|\mathbf{B}|^2}{2\mu_0}$ det. Luckily for us, *Reynolds transport theorem* (see [Reddiger and Poirier(2020)] for more info) tells us exactly what to do. Reynolds transports theorem is written for time dependent domains $\Omega(t)$ and a time dependent scalar function f and says:

$$\frac{d}{dt}\Big|_{t=0} \int_{\Omega(t)} f = \int_{\Omega(t)} \partial_t f + \int_{\partial\Omega(t)} f\langle Y, N\rangle.$$

Instead of $\Omega(t)$ we have $\varphi_t(\mathbb{M}_\mathbf{B})$, and instead of integrating over $\varphi_t(\mathbb{M}_\mathbf{B})$ we integrate over $\mathbb{M}_\mathbf{B}$ and pullback the function by φ_t^*. Thus we get:

$$\frac{d}{dt}\Big|_{t=0} \int_{\mathbb{M}_\mathbf{B}} \varphi_t^*\left(\frac{|\mathbf{B}|^2}{2\mu_0}\right) = \int_{\mathbb{M}_\mathbf{B}} \frac{1}{\mu_0}\langle \mathring{\mathbf{B}}, \mathbf{B}\rangle + \int_{\partial\mathbb{M}_\mathbf{B}} \frac{|\mathbf{B}|^2}{2\mu_0}\langle Y, N\rangle.$$

The second summand we leave as it is. For the first summand we compute

$$\int_{\mathbb{M}_\mathbf{B}} \frac{1}{\mu_0}\langle \mathring{\mathbf{B}}, \mathbf{B}\rangle = \int_{\mathbb{M}_\mathbf{B}} \frac{1}{\mu_0}\langle \operatorname{curl}(Y\times\mathbf{B}), \mathbf{B}\rangle$$
$$= \int_{\mathbb{M}_\mathbf{B}} \frac{1}{\mu_0}\langle Y\times\mathbf{B}, \operatorname{curl}\mathbf{B}\rangle$$
$$\quad - \int_{\mathbb{M}_\mathbf{B}} \frac{1}{\mu_0}\operatorname{div}(|\mathbf{B}|^2 Y - \langle\mathbf{B}, Y\rangle\mathbf{B})$$
$$= -\int_{\mathbb{M}_\mathbf{B}} \langle \frac{1}{\mu_0}\operatorname{curl}\mathbf{B}\times\mathbf{B}, Y\rangle$$
$$\quad - \int_{\partial\mathbb{M}_\mathbf{B}} \left(\frac{|\mathbf{B}|^2}{\mu_0}\langle Y, N\rangle - \frac{1}{\mu_0}\langle\mathbf{B}, Y\rangle\langle\mathbf{B}, N\rangle\right),$$

where we used basic vector calculus operations and the divergence theorem. Putting now the pressure variation and magnetic energy variation together we obtain

$$\mathring{\mathcal{E}} = \frac{d}{dt}\Big|_{t=0}\varphi_t^*\mathcal{E}$$
$$= \frac{d}{dt}\Big|_{t=0} \int_{\mathbb{M}_\mathbf{B}} \varphi_t^* p + \frac{d}{dt}\Big|_{t=0} \int_{\mathbb{M}_\mathbf{B}} \varphi_t^*\left(\frac{|\mathbf{B}|^2}{2\mu_0}\right)$$
$$= -\int_{\mathbb{M}_\mathbf{B}} \langle \frac{1}{\mu_0}\operatorname{curl}\mathbf{B}\times\mathbf{B}, Y\rangle$$
$$\quad + \int_{\partial\mathbb{M}_\mathbf{B}} \left(\left(p - \frac{|\mathbf{B}_j|^2}{2\mu_0}\right)\langle Y, N\rangle + \frac{1}{\mu_0}\langle\mathbf{B}, Y\rangle\langle\mathbf{B}, N\rangle\right).$$

Which concludes the proof of the theorem.

$\square$

The variation allows us to directly work with the extrema of this energy, as we will see in the next section.

1.5.3 Extrema of the MHS Energy

Now that we know the variation of the MHS energy $\mathcal{E}$ by theorem 10, we formulate the following theorem about the nature of the critical points of this energy to investigate where the minimal energy principle will take us when applied to $\mathcal{E}$.

> **Theorem 11** (**MHS Solutions are MHS Energy Extrema**). In the FFCS model, $(\mathbb{M}_{\mathbf{B}}, \mathbf{B})$ is an extremum of the MHS energy $\mathcal{E}$ under variations that keep the boundary $\Sigma_{\mathbf{B}}$ fixed and are of the form $\mathring{\mathbf{B}} = \operatorname{curl}(Y \times \mathbf{B})$ if and only if $(\mathbb{M}_{\mathbf{B}}, \mathbf{B})$ solves the MHS equation everywhere.

Proof. The MHS energy $\mathcal{E}$ is critical if and only if $\mathring{\mathcal{E}}$ vanishes for all variation Y of the above mentioned form. From theorem 10 we know that

$$
\begin{aligned}
\mathring{\mathcal{E}} = &-\int_{\mathbb{M}_{\mathbf{B}}} \langle \tfrac{1}{\mu_0} \operatorname{curl} \mathbf{B} \times \mathbf{B}, Y \rangle \\
&+ \int_{\partial \mathbb{M}_{\mathbf{B}}} \left(p - \tfrac{|\mathbf{B}|^2}{2\mu_0} \right) \langle Y, N \rangle \\
&+ \int_{\partial \mathbb{M}_{\mathbf{B}}} \tfrac{1}{\mu_0} \langle \mathbf{B}, Y \rangle \langle \mathbf{B}, N \rangle.
\end{aligned}
$$

Note that $\partial \mathbb{M}_{\mathbf{B}} = \mathcal{I} \cup \Sigma_{\mathbf{B}}$. $\mathring{\mathcal{E}} = 0$ for all Y if and only if each of the three terms above vanish. For the respective summands, this happens under the following conditions:

- **First summand**: This term will vanish for force-free fields $\mathbf{B}$ in $\mathbb{M}_{\mathbf{B}}$. We can rely on the existence of such a field by theorem 5.
- **Second summand**: This term will vanish when the pressure equilibrium is reached at the interface $\mathcal{I}$. This is exactly the condition established in theorem 6 that is needed to solve the MHS equation. On $\Sigma_{\mathbf{B}}$, $Y = \mathbf{0}$ anyway due to the fixed boundary during variation.
- **Third summand**: This term vanishes always due to our boundary conditions. On $\mathcal{I}$, $\mathbf{B}$ is tangent to the boundary and thus $\langle \mathbf{B}, N \rangle = 0$. On $\Sigma_{\mathbf{B}}$. $Y = 0$ anyway due to the fixed boundary of the variation itself.

These conditions together are the same as the ones required to solve the MHS equation, thus ending this proof. At an extremum of the MHS energy, the MHS equation is thus solved everywhere: on $\mathbb{M}_{\mathbf{B}}{}^\circ$, $\mathbb{M}_{\mathbf{0}}^\circ$ and on $\mathcal{I}$.

$\square$

While theorem 5 only gave us a guarantee that each $\mathbb{M}_{\mathbf{B}}$ can have a force free field inside and theorem 6 gave us an interface $\mathcal{I}$ condition to solve the MHS equation, theses theorems actually did little to tell us how to find such a plasma configuration $(\mathbb{M}_{\mathbf{B}}, \mathbf{B})$. On the other hand, theorem 11 blesses us with something wonderful! An actual principle by which we can

find a solution to the MHS equation based on searching for an extremum of the MHS energy $\mathcal{E}$. The message is:

Corollary 12 (**Finding a MHS Solution**). Given an initial plasma state $(\mathbb{M}_\mathbf{B}, \mathbf{B})$ of an FFCS model with boundary flux conditions, one can find a solution to the MHS equation by minimizing the MHS energy $\mathcal{E}$ with the respect to the plasma state $(\mathbb{M}_\mathbf{B}, \mathbf{B})$ until an extrema is reached.

This corollary will be the basis of for the algorithm for the discretization of this theory in part 2 of this dissertation. By minimizing $\mathcal{E}$, we simultaneously solve for two things. We solve for ...

- ... a force free field $\mathbf{B}$, *i.e.*curl$(\mathbf{B}) \times \mathbf{B} = \mathbf{0}$.
- ... a domain $\mathbb{M}_\mathbf{B}$ with suitable gas-flux equilibrium $p = |B|^2/2\mu_0$ for the MHS equation to be solved on the gas-flux interface $\mathcal{I}$. This is possible as the support $\mathbb{M}_\mathbf{B}$ of the magnetic field $\mathbf{B}$ can be updated as $\mathbf{B}$ changes.

Also note, in the case of $\mathbb{M}_\mathbf{B} = \mathbb{M}$, *i.e.*no gas $\mathbb{M}_\mathbf{0} = \emptyset$, the global energy minimum of $\mathcal{E} = \int_{\mathbb{M}_\mathbf{B}} |\mathbf{B}|^2/2\mu_0$ is a potential field (see section 1.3.1), a fact known as *Minimum Energy Theorem for Potential Fields* (see e.g. [Priest(2014), Sec. 2.8]). Thus potential fields are a special case of our model (see theorem 40).

1.6   Magnetic Field Topology

It is time to talk more about the topology of the magnetic field $\mathbf{B}$. By *magnetic field topology* we refer to the internal structure of the field lines. Two magnetic fields have the same field topology if there exists a smooth family of diffeomorphisms transporting one field to the other without distorting the boundary.

1.6.1   Types of Field Topology

A magnetic field $\mathbf{B}$ going through a volume $\mathbb{M}_\mathbf{B}$ can be very smooth, the smoothest representation being the potential field (as explained in section 1.3.1). Alternatively, given the same boundary condition, one could also twist the magnetic field around an axis of a tube to receive another field that respects the boundary condition. Even more complex, one could braid the field lines like hair too, something that is also taken into consideration in solar physics [Prior and Yeates(2016a), Prior and Yeates(2016b)]. See figure 1.17 for illustrations of this as well as figure 3.27 for real life examples.

1.6.2   Invariance of Field Topology

In general magnetohydrodynamics, the field topology is not an invariant. However, in the case of ideal magneothydrodynamics where there is no plasma viscosity and magnetic diffusivity
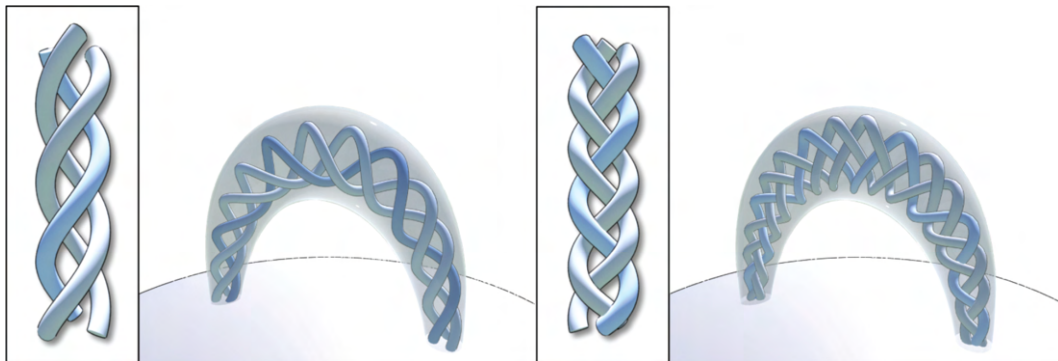
Figure 1.17: The volume $\mathbb{M}_{\mathbf{B}}$ of a tube like structure may have different magnetic fields **B** inside while maintaining the same boundary flux conditions. We display here a small selection of field lines. Left: twisted field lines. Right: braided field lines.

(see equations 1.4), the topology is an invariant, a direct consequence of the frozen **B**-field theorem 8 as the **B** is just transported by the gas.

The preservation of this topology in the discrete setting is generally not a given in volume based methods, but as we will later see, the Lagrangian approach in this dissertation will guarantee field topology preservation. This means that whatever initial magnetic field is chosen to minimize its MHS energy $\mathcal{E}$, as long as it runs into a local extrema, we know by theorem 11, that the resulting field solves the MHS equation with the initially prescribed topology. So a major question will be *what initial field topologies one should use in practice?* This question will be addressed in detail in section 2.5 [Initial Curves from Flux Density].

Summary of Part 1:
The Mathematical Modeling of the MHS Equation

This concludes the first part of the dissertation. Let's have a quick recap of what happened.

- **Section 1.1, The Magnetohydrostatic (MHS) Equation**
  We introduced the basics of solar physics and its observations we require. We also derived the magnetohydrostatic equation from the magnetohydrodynamic equations.
- **Section 1.3, Related Work**
  We discussed all matters of related work in section 1.3, in particular, the force-free field models and the current sheet model.
- **Section 1.4, Force-Free Current Sheet Model (FFCS)**
  We introduced the main model used in this dissertation: the FFCS model based on domain decompositions of the form $\mathbb{M} = \mathbb{M_0} \cup \mathbb{M_B}$. We then established a theorem about the condition by which this model solves the MHS equation everywhere. The MHS energy $\mathcal{E}$ was also introduced.
- **Section 1.5, Variational Analysis**
  We prepare and perform a variational analysis on the MHS energy $\mathcal{E}$ and learned that plasma configurations $(\mathbb{M_B}, \mathbf{B})$ that are extrema of $\mathcal{E}$ solve the MHS equation. This leads to a method to solve the MHS problem by energy minimization based on corollary 12 [**Finding a MHS Solution**].
- **Section 1.6, Magnetic Field Topology**
  We introduced the notion of magnetic field topology and discussed the invariance thereof.

The above sections create the smooth theory of the FFCS model. Next up, we will work towards the discretization of this model to enable computational methods.

Part 2

The Discretization of the MHS Equation
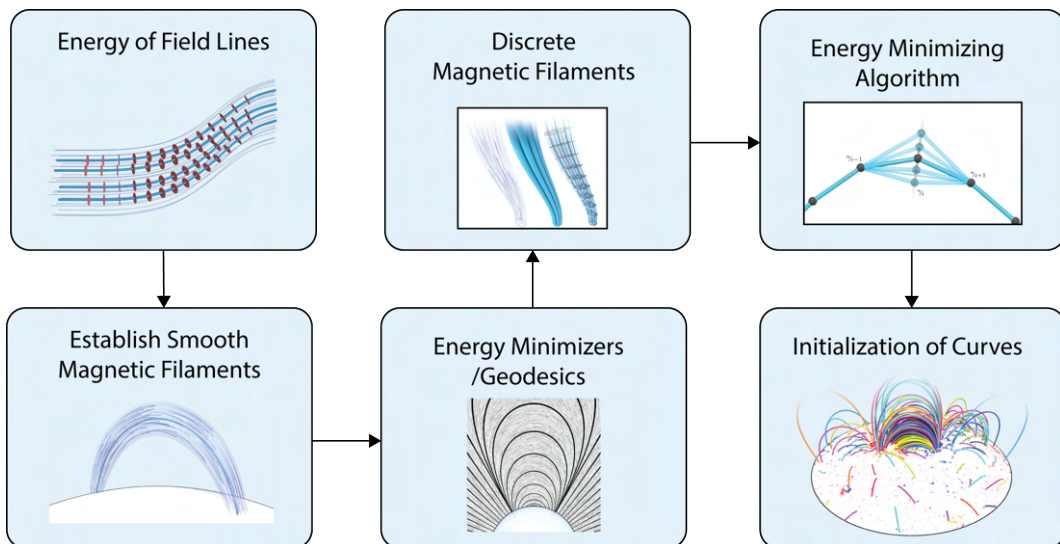
Figure 2.1: An overview of part 2 of this dissertation. We begin with field line energy and establish smooth magnetic filaments from them. We perform some analysis on smooth magnetic filaments before introducing the main discretization idea. We then establish an algorithm to minimize the energy and also tackle the initialization problem for the starting curve set given a magnetogram.

In part 1 we have derived a smooth theory of the FFCS model and analysed it to an extent that allows us to find a solution by minimizing the MHS energy $\mathcal{E}$. However, we have not established a computational entry point for the promised Lagrangian discretization for practical use. This part of the dissertation will provide a complete theory of discrete magnetic filaments. Here is the basic outline of this part:

- Establish a notion of the energy in terms of field lines.
- Discretize the field by approximating it with a finite set of thick field lines.
- Analyse the properties of these filaments and its discrete MHS energy.
- Develop an efficient algorithm for minimizing the discrete MHS energy based on notions of shortest curves.
- Introduce a method to initialize filaments as input for our algorithm using only a magnetogram.

The validation will then be covered in part 3 [Image Generation, Validation and Application] of this dissertation. We begin with a closer look at the field lines.

2.1   Field Line Energy

We will now establish a new viewpoint of the MHS energy in terms of field lines. The reward will be that in section 2.3 we will discretize our plasma configuration $(\mathbb{M}_\mathbf{B}, \mathbf{B})$ as a finite collection of field lines of the magnetic field $\mathbf{B}$ inside of $\mathbb{M}_\mathbf{B}$. See figure 2.2 for a teaser.

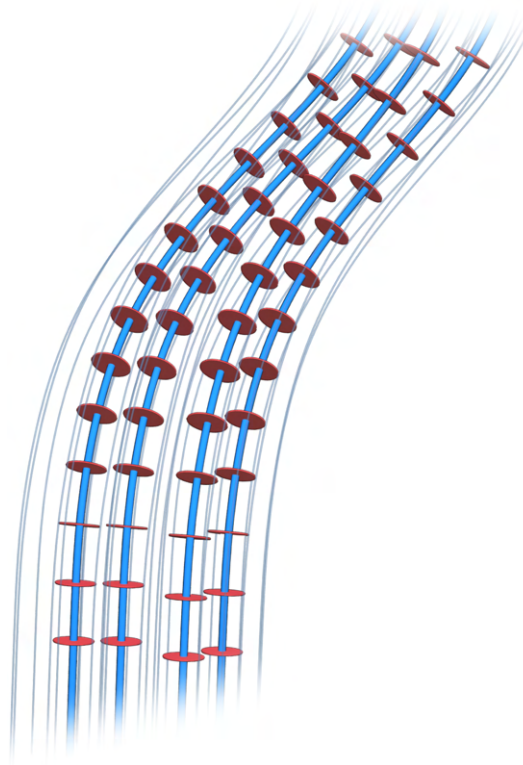**Figure 2.2**: An illustation of a magnetic field $\mathbf{B}$ (light gray) being represented by a finite set of thin tube-like field lines, each with thickness. This will be the core idea of our upcoming discretization.

2.1.1 Field Line Energy and MHS Energy

Field lines are infinitesimal small objects. We call the *set of all field lines* Γ. If we can express the magnetohydrostatic energy (definition 7) contribution of a single field line, we can then express the total MHS energy $\mathcal{E}$ by a simple integral over Γ.

We start with the domain decomposition $\mathbb{M} = \mathbb{M_0} \cup \mathbb{M_B}$ of the FFCS model (section 1.4). We can safely assume that $\mathbf{B}$ is nowhere zero on $\mathbb{M_B}$, because areas of $\mathbf{B} = \mathbf{0}$ belong to $\mathbb{M_0}$. Let $\gamma \in \Gamma$ be a curve that represent a field line, we can factor the volume element dV of $\mathbb{R}^3$ as the product of the Euclidean arclength measure ds along the field lines with orthogonal area measure dA

$$dV = ds \cdot dA \,.$$

On a infinitesimal cross section of a field line, we can assume the magnetic field strength $|\mathbf{B}|$ to be constant. The *flux measure* of the field line γ at a point on the curve is given by

$$d\gamma = |\mathbf{B}| dA$$

You can think of it this way: ds is the unit speed (arclength) measure while $|\mathbf{B}| = |\gamma'|$ is the curve speed dependent on how strong the magnetic field is. Field magnitude times area equals flux, captured by $d\gamma$. Consequently, we have

$$dV = \tfrac{1}{|\mathbf{B}|} ds \, d\gamma,$$

which is valid since $\mathbf{B}$ is non-zero in $\mathbb{M_B}$. Next, we can insert this factorisation into the formula of the MHS energy $\mathcal{E}$ (definition 7) and see what happens

$$\mathcal{E}(\mathbb{M_B}, \mathbf{B}) = \int_{\mathbb{M_B}} \left(p + \tfrac{|\mathbf{B}|^2}{2\mu_0} \right) dV.$$
$$= \int_{\mathbb{M_B}} \left(\tfrac{p}{|\mathbf{B}|} + \tfrac{|\mathbf{B}|}{2\mu_0} \right) ds \, d\gamma.$$

Now this is an interesting form! Given a plasma state $(\mathbb{M_B}, \mathbf{B})$, the magnetic field $\mathbf{B}$ and pressure p are known everywhere in space. The way $d\gamma$ is written at the end of the integral also allows us to express this integral in terms of field lines Γ rather than in terms of $\mathbb{M_B}$.

We need to understand that due to $\mathbf{B}$ being non-zero and divergence-free in $\mathbb{M_B}$, we can safely say that for every point $\mathbf{x} \in \mathbb{M_B}$ there exists exactly one field line $\gamma \in \Gamma$ that contains $\mathbf{x}$. Thus, the union of the images of all field lines γ combined must be equal to $\mathbb{M_B}$.

$$\bigcup_{\gamma \in \Gamma} \mathrm{img}(\gamma) = \mathbb{M_B}$$

For an individual field line $\gamma \colon [a, b] \to \mathbb{M_B}$ we can then write

$$\mathcal{E}(\mathbb{M}_{\mathbf{B}}, \mathbf{B}) = \int_\Gamma \left(\int_{\mathrm{img}(\gamma)} \left(\tfrac{p}{|\mathbf{B}|} + \tfrac{|\mathbf{B}|}{2\mu_0} \right) ds \right) d\gamma \tag{2.1}$$

$$= \int_\Gamma \underbrace{\left(\int_a^b \left(\tfrac{p}{|\mathbf{B}|} + \tfrac{|\mathbf{B}|}{2\mu_0} \right) \circ \gamma \, ds \right)}_{\text{field line } \gamma \text{ integral}} d\gamma. \tag{2.2}$$

where $\int_\Gamma$ is the integration over all field lines. We put the above form of the integral expression into the following definition:

Definition 13 (**Field Line MHS Energy**). Given the FFCS model, the *MHS energy of a mangetic field line* $\gamma \colon [a, b] \to \mathbb{M}_{\mathbf{B}}$ is given by

$$\mathscr{L}(\gamma) := \int_a^b \left(\tfrac{p}{|\mathbf{B}|} + \tfrac{|\mathbf{B}|}{2\mu_0} \right) \circ \gamma \, ds$$

This definiton enables us to write the energy as an integral of field line energies.

Theorem 14 (**MHS Energy Field Line Decomposition**). Given the FFCS model and letting Γ be the set of field lines making up $\mathbb{M}_{\mathbf{B}}$, then the MHS energy $\mathcal{E}$ can be decomposed into the integral of individual field line energies $\mathscr{L}(\gamma)$, $\gamma \in \Gamma$

$$\mathcal{E}(\mathbb{M}_{\mathbf{B}}, \mathbf{B}) = \int_\Gamma \mathscr{L}(\gamma) \, d\gamma,$$

Proof. Insert definition 13 into equation 2.2. $\qquad\qquad\qquad\qquad\qquad\qquad\square$

The letter $\mathscr{L}$ was chosen because of an insight that will be established in the next section linking this energy to *length*.

2.1.2 Field Line Energy as *Length*

Let us discuss the $\mathscr{L}(\gamma)$ term established in definition 13. At the first glance, it looks like a simple path integral. The great property of this integral is that the integrated value only depends on the spatial position, and not on any derivatives of the curve itself:

$$\mathscr{L}(\gamma) := \int_a^b \underbrace{\left(\tfrac{p(\gamma(s))}{|\mathbf{B}(\gamma(s))|} + \tfrac{|\mathbf{B}(\gamma(s))|}{2\mu_0} \right)}_{\text{only dependent on spatial position}} ds.$$

Minimizing this integral is a task that should interest us because corollary 12 [**Finding a MHS Solution**] tells us that finding an optimal path γ with minimal energy will also minimize the MHS energy and thus solve the MHS equation. Instead of using the Euclidean arclength metric ds, the spatial-only dependency allows us to create a new metric $d\tilde{s}$ that is non-Euclidean and that will help us approach this minimization problem. We will call this the *plasma metric* $d\tilde{s}$.

Definition 15 (Plasma Metric $d\tilde{s}$). Given the FFCS model with a domain decomposition $\mathbb{M} = \mathbb{M_0} \cup \mathbb{M_B}$ and a plasma state $(\mathbb{M_B}, \mathbf{B})$, we define its *plasma metric* $d\tilde{s}$, as the Euclidean metric ds multiplied by a conformal factor e^u.

$$
d\tilde{s} := e^u \, ds := \begin{cases} \sqrt{\frac{2p}{\mu_0}} \, ds & \text{in } \mathbb{M_0} \\ \left(\frac{p}{|\mathbf{B}|} + \frac{|\mathbf{B}|}{2\mu_0} \right) ds & \text{in } \mathbb{M_B}, \end{cases} \tag{2.3}
$$

$d\tilde{s}$ on $\mathbb{M}$ is a Remaniann metric.

The plasma metric is continuous under the same condition needed for the FFCS model to solve the MHS equation (theorem 6)[1].

Lemma 16 (Plasma Metric Continuity). The plasma metric is continuous if and only if the magnetohydrostatic equilibrium holds on the gas-flux interface $\mathcal{I}$, *i.e.*

$$
p = \frac{|\mathbf{B}|^2}{2\mu_0}
$$

Proof. Quick math. Set the two terms of the bracket in definition 15 equal and check what condition p has to fulfil for metric continuity.

$$
\sqrt{\frac{2p}{\mu_0}} = \frac{p}{|\mathbf{B}|} + \frac{|\mathbf{B}|}{2\mu_0}
$$

Then square both sides.

$$
\frac{2p}{\mu_0} = \frac{p^2}{|\mathbf{B}|^2} + 2 \frac{p}{|\mathbf{B}|} \frac{|\mathbf{B}|}{2\mu_0} + \frac{|\mathbf{B}|^2}{4\mu_0^2}
$$

Arrange for a quadratic polynomial structure in p.

$$
\underbrace{\frac{1}{|\mathbf{B}|^2}}_{a} p^2 + \underbrace{\left(-\frac{1}{\mu_0} \right)}_{b} p + \underbrace{\frac{|\mathbf{B}|^2}{4\mu_0^2}}_{c} = 0
$$

Like any quadratic polynomial, solve it using the *abc*-formula.

---

[1]In fact, the plasma metric $d\tilde{s}$ is defined as such to be compatible with the gas-flux pressure equilibrium. The choice of $\sqrt{\frac{2p}{\mu_0}}$ for $\mathbb{M_0}$ was exactly motivated to fulfil this criterion.

$$p_{\pm} = \frac{-b \pm \sqrt{b^2 - 4ac}}{2a}$$

$$= \frac{\frac{1}{\mu_0} \pm \sqrt{\frac{1}{\mu_0^2} - 4\frac{1}{|\mathbf{B}|^2}\frac{|\mathbf{B}|^2}{4\mu_0^2}}}{\frac{2}{|\mathbf{B}|^2}}$$

$$= \frac{\frac{1}{\mu_0} \pm 0}{\frac{2}{|\mathbf{B}|^2}}$$

$$= \frac{|\mathbf{B}|^2}{2\mu_0}$$

Since the square root in the *abs*-formula is zero, the continuity condition is unique.

$\square$

Let us also hold as a theorem the very reason we introduced the plasma metric: to express the MHS field line energy as *length*.

Theorem 17 (**MHS Field Line Energy as Length**). The MHS energy contribution of a field line is its length in the plasma metric $d\tilde{s}$, *i.e.*

$$\mathcal{E}(\mathrm{img}(\gamma)) = \mathscr{L}(\gamma) = \int_{\mathrm{img}(\gamma)} 1 d\tilde{s}.$$

The field lines of an FFCS model MHS solution are *geodesics* within the plasma metric.

Proof. Insert the definition 15 of $d\tilde{s}$ and compare it to the equation in theorem 14 to see that $\mathscr{L}(\gamma)$ is indeed the length γ with respect to the plasma metric.

Geodesics are extrema of length, so by theorem 11 [**MHS Solutions are MHS Energy Extrema**], extrema of this energy are solutions of the MHS equation in the FFCS model. $\square$

This leaves us in a great place for implementing a Lagrangian algorithm. Instead of minimizing the MHS energy of an entire field, the observations made in this section's theorem 14 allows us to minimize the MHS energy of field lines, and to do that theorem 17 says that this is equivalent to minimizing the length of the field lines as curves[2] in a non-Euclidean plasma metric $d\tilde{s}$. Let us take another look at the plasma metric. Let us rewrite it in a way that tells us a little more about it.

---

[2]We would like to clarify that until now we have not yet introduced curves as our computation elements. This statement will be justified in section 2.2.

Theorem 18 (Conformal Factor Splitting). For the plasma metric $d\tilde{s} = e^u ds$, the conformal factor in $\mathbb{M}_{\mathbf{B}}$ can be written as the product of a *gas factor* and a *magnetic pressure amplifier*

$$d\tilde{s} = e^u ds = \left(\frac{p}{|\mathbf{B}|} + \frac{|\mathbf{B}|}{2\mu_0} \right) ds = \underbrace{\sqrt{\frac{2p}{\mu_0}}}_{\text{gas factor}} \underbrace{\left(1 + \frac{\left(|\mathbf{B}| - \sqrt{2\mu_0 p}\right)^2}{2|\mathbf{B}|\sqrt{2\mu_0 p}} \right)}_{\text{mag. pressure amplifier}} ds. \qquad (2.4)$$

In terms of the logarithmic conformal factors u as in e^u, this allows the splitting on $\mathbb{M}_{\mathbf{B}}$ to be as follows:

$$u = u_{\text{gas}} + u_{\text{mag}}$$

$$u_{\text{gas}} := \ln\left(\sqrt{\frac{2p}{\mu_0}} \right)$$

$$u_{\text{mag}} := \ln\left(1 + \frac{\left(|\mathbf{B}| - \sqrt{2\mu_0 p}\right)^2}{2|\mathbf{B}|\sqrt{2\mu_0 p}} \right).$$

Proof. This is really just a job of rearranging the terms, but since the form looks so non-trivial, we will do it here step by step. We begin with the right hand side.

$$\sqrt{\frac{2p}{\mu_0}} \left(1 + \frac{\left(|\mathbf{B}| - \sqrt{2\mu_0 p}\right)^2}{2|\mathbf{B}|\sqrt{2\mu_0 p}} \right) = \sqrt{\frac{2p}{\mu_0}} + \sqrt{\frac{2p}{\mu_0}} \left(\frac{|\mathbf{B}|^2 - 2|\mathbf{B}|\sqrt{2\mu_0 p} + 2\mu_0 p}{2|\mathbf{B}|\sqrt{2\mu_0 p}} \right)$$

$$= \sqrt{\frac{2p}{\mu_0}} + \sqrt{\frac{2p}{\mu_0}} \left(\frac{|\mathbf{B}|}{2\sqrt{2\mu_0 p}} - 1 + \frac{\sqrt{2\mu_0 p}}{2|\mathbf{B}|} \right)$$

$$= \sqrt{\frac{2p}{\mu_0}} + \frac{|\mathbf{B}|}{2\mu_0} - \sqrt{\frac{2p}{\mu_0}} + \frac{p}{|\mathbf{B}|}$$

$$= \frac{p}{|\mathbf{B}|} + \frac{|\mathbf{B}|}{2\mu_0}$$

The relationship $u = u_{\text{gas}} + u_{\text{mag}}$ follows from basic exponential rules.

$$e^u = \left(\frac{p}{|\mathbf{B}|} + \frac{|\mathbf{B}|}{2\mu_0} \right) = \sqrt{\frac{2p}{\mu_0}} \left(1 + \frac{\left(|\mathbf{B}| - \sqrt{2\mu_0 p}\right)^2}{2|\mathbf{B}|\sqrt{2\mu_0 p}} \right) = e^{u_{\text{gas}}} e^{u_{\text{mag}}} = e^{u_{\text{gas}} + u_{\text{mag}}}$$

$$\square$$

u_{mag}'s second summand is strictly non-negative,

$$\frac{\left(|\mathbf{B}| - \sqrt{2\mu_0 p}\right)^2}{2|\mathbf{B}|\sqrt{2\mu_0 p}} \geq 0,$$

which is precisely why we call its effect *magnetic pressure amplifier*. Notice that if our famous gas-flux pressure equilibrium applies ($p = \frac{|\mathbf{B}|^2}{2\mu_0}$), that $u_{\text{mag}} = \ln(1) = 0$ vanishes, *i.e.* the magnetic pressure amplifier has no affect on the metric anymore.

$u_{\text{mag}} \geq 0$ in $\mathbb{M}_{\mathbf{B}}$ captures the effect of the magnetic pressure exceeding the gas pressure. We specify the situation of the absence of magnetic pressure amplification as a special case.

We call the emergent metric the *gas metric*.

Definition 19 (**Gas Metric**)**.** A special case of the plasma metric is the *gas metric*, given when $u_{\mathrm{mag}} \equiv 0$. It is of the form:

$$d\tilde{s} := e^{u_{\mathrm{gas}}} \, ds := \sqrt{\tfrac{2p}{\mu_0}} \, ds \qquad\qquad (2.5)$$

The length of a curve in the gas metric is noted by $\mathscr{L}_{\mathrm{gas}}(\gamma)$.

2.2 Smooth Magnetic Filaments

Recall that in section 1.2 we mentioned many solar field properties, one of which was the observation that the magnetic field is fibered into filaments that rise from below the surface (section 1.2.2). We will now study a special case of magnetic fields that will become the *building blocks* in our Lagrangian model.

2.2.1 Basics of Smooth Magnetic Filaments

The phenomenologically exciting parts of the solar corona happen above so called sunspot pairs. When a magnetic filament rises above the surface, it also marks its presence on the magnetogram through a positive flux and a negative flux pair known as a sunspot pair. We will now formally define a smooth magnetic filament (figure 2.3), an ideal configuration that represents the simplest field.
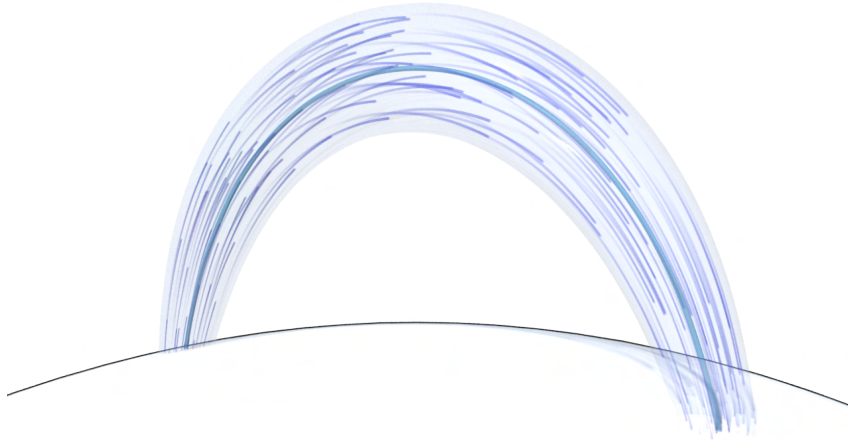

Figure 2.3: A smooth magnetic filament. A central curve γ together with a radius function r define a tubular volume $\mathbb{M}_{\mathbf{B}}$. The magnetic field $\mathbf{B}$ runs along the tube with with constant flux.

Definition 20 (**Smooth Magnetic Filament**). Let $\gamma : [0, L] \to \mathbb{M}$ be a curve with end points on the surface $\gamma(0), \gamma(L) \in \partial\mathbb{M}$. Let $r : [0, L] \to \mathbb{R}_+$ be a function defining a thin radius for every point of γ (thin w.r.t. the curvature, figure 2.4). Let $\mathbb{M}_\mathbf{B}$ have the shape of the tube with circular cross sections of variable thickness of radius r around the center curve γ. We say that $\mathbb{M}_\mathbf{B}$ has the *shape of a magnetic filament*.

$$\mathbb{M}_\mathbf{B} = \{\mathbf{x} \in \mathbb{M} : \exists\, s \in [0, L], \ |\mathbf{x} - \gamma(s)| < r(s)\,\}$$

Let Φ prescribe the boundary flux such that we have uniform incoming flux h around $\gamma(0)$ and equal uniform outgoing flux around $\gamma(L)$. Under the assumption that the tube is thin w.r.t. its curvature, we assume that $\mathbf{B}$ follows the tube and is constant on each cross section with flux-preserving magnitude

$$B := |\mathbf{B}| = \frac{h}{2\pi r^2}.$$

We call the resulting plasma state $(\mathbb{M}_\mathbf{B}, \mathbf{B})$ a *smooth magnetic filament* and denote it as $(\gamma, \mathbf{B})$. See figure 2.3 for an illustration.

Thin w.r.t. the curvature means that the tube won't buckle/overlap in a way that is an issue for the embedding of the parametric surface shown in figure 2.4. In the thin case, the approximation that B is constant and that p on the interface carries the same value as on the center curve is more applicable. We take sufficient thinness as a given as we will soon have many, many magnetic filaments bundled together. In any case, increasing the number of filaments improves the approximation while making filaments thinner. We will see what filament count is necessary in the validation section.
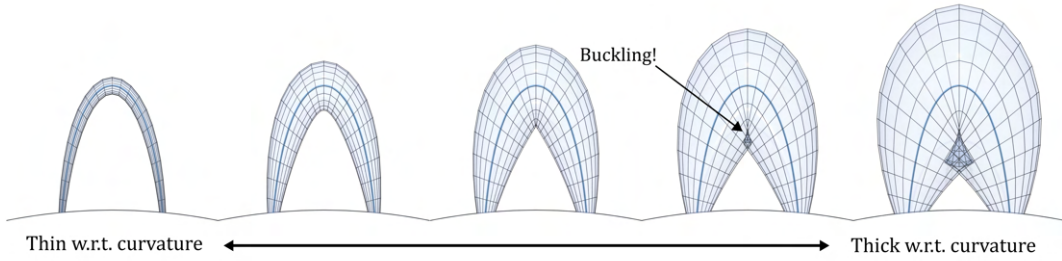
Figure 2.4: Smooth magnetic filaments with high curvature in their center curves γ and varying radii r. When the radii are too big relative to the curvature we start to get bad buckling behaviour, which will cause our magnetic field $\mathbf{B}$, which is tangential to γ, to be ill-defined and the parametric surface to not be embedded. Later we will see that we can circumvent having too thick filaments by replacing them with bundles of thinner filaments.

A smooth magnetic filament is the simplest case to study. For it, we can make some interesting statements. Later we will see that smooth magnetic filaments can be thought of

as *thick field lines.*

We will now derive some further statements about smooth magnetic filaments and will then show in section 2.5 that they are excellent approximation elements for the solar magnetic field when the gas pressure is high (or equivalently when the magnetic flux is weak, theorem 41).

Theorem 21 (Smooth Magnetic Filament Energy). The MHS energy of a smooth magnetic filament can be expressed as

$$\mathcal{E}(\gamma, \mathbf{B}) := h \int_0^L \left(\tfrac{p}{B} + \tfrac{B}{2\mu_0} \right) ds \approx \mathcal{E}(\mathbb{M}_{\mathbf{B}}, \mathbf{B})$$

Proof. This result makes direct use of the infinitesimal elements of the field line energy insight achieved in section 2.1.1. Previously though, γ described a single field line. Now, γ is the backbone describing the trajectory of all field lines in a smooth magnetic filament $(\gamma, \mathbf{B})$ with a non-vanishing volume. We can derive the result directly from the definition 7 of the MHS energy $\mathcal{E}$. Thanks to the constancy of B on each circular cross-section, we can easily integrate every cross-section.

$$
\begin{aligned}
\mathcal{E}(\mathbb{M}_{\mathbf{B}}, \mathbf{B}) :&= \int_{\mathbb{M}_{\mathbf{B}}} \left(p + \tfrac{|\mathbf{B}|^2}{2\mu_0} \right) dV \\
&= \int_{\mathbb{M}_{\mathbf{B}}} \left(p + \tfrac{B^2}{2\mu_0} \right) dA ds \\
&\approx \int_0^L \left(p + \tfrac{B^2}{2\mu_0} \right) 2\pi r^2 ds \\
&= \int_0^L \left(p + \tfrac{B^2}{2\mu_0} \right) \tfrac{h}{B} ds \\
&= h \int_0^L \left(\tfrac{p}{B} + \tfrac{B}{2\mu_0} \right) ds.
\end{aligned}
$$

$\square$

Theorem 21 provides basic understanding on smooth magnetic filaments. Next we will see some theoretical results about them.

2.2.2   Ideal Magnetic Filaments

We seek to now solve the MHS equation for smooth magnetic filaments. For terminology reasons, we establish the following definition:

Definition 22 (Ideal Magnetic Filament).

An *ideal magnetic filaments* is a smooth magnetic filament that solves the MHS equation everywhere and has minimal MHS energy.

One of the benefits of dealing with smooth magnetic filaments is the simplicity of the resulting conditions to solve the MHS equations. For example, we can exactly establish what the thickness distribution and shape should be like to solve the MHS equation according to the FFCS model. Let us first focus on the thickness through the following theorem:

Theorem 23 (Optimal Radius Theorem).

If a smooth magnetic filament with a center curve γ and flux h solves the MHS equation according to the FFCS model, then the radi are as follows:

$$r^2(s) = \frac{1}{2\pi}\frac{h}{\sqrt{2\mu_0 p(\gamma(s))}}$$

Proof. Since B is force-free by construction, we can just use theorem 6 [**FFCS MHS Theorem**] to solve for r^2 in the gas-flux pressure equilibrium condition

$$p = \frac{1}{2\mu_0}B^2 = \frac{1}{2\mu_0}\left(\frac{h}{2\pi r^2}\right)^2$$
$$\Leftrightarrow 2\mu_0 p_0 = \left(\frac{h}{2\pi r^2}\right)^2$$
$$\Leftrightarrow \sqrt{2\mu_0 p} = \frac{h}{2\pi r^2}$$
$$\Leftrightarrow 2\pi\frac{\sqrt{2\mu_0 p}}{h} = \frac{1}{r^2}$$
$$\Leftrightarrow r^2 = \frac{1}{2\pi}\frac{h}{\sqrt{2\mu_0 p}}.$$

Thus, a smooth magnetic filament with such an r will have the magnetic field strength $B = h/2\pi r^2$ that solves the MHS equation on the interface $\mathcal{I}$.

$\square$

Interestingly, one can also reach the same radii condition through energy minimization with the fixed curve γ (only varying radii). Is this a surprise? It should not be. After all, we have shown in theorem 11 that critical points of the MHS energy are solutions of the MHS equation. This is one such case.

Lemma 24. The optimal radius of theorem 23 also results from fixing γ and finding $r : [0, L] \to \mathbb{R}$ s.t. the MHS energy $\mathcal{E}(\gamma, \mathbf{B})$ is critical.

Proof. Derive the MHS energy term by r, set it to 0, and solve for r. We ignore the initial h term as it is constant.

$$\partial_r \left(\frac{p}{B} + \frac{B}{2\mu_0} \right) = \partial_r \left(\frac{p2\pi}{h} r^2 + \frac{h}{4\pi\mu_0} r^{-3} \right)$$

$$= \partial_r \left(\frac{2\pi p}{h} r^2 + \frac{h}{4\pi\mu_0} r^{-2} \right)$$

$$= \frac{4\pi p}{h} r - \frac{h}{2\pi\mu_0} r^{-3} \overset{!}{=} 0$$

$$\Leftrightarrow \quad \frac{4\pi p}{h} r = \frac{h}{2\pi\mu_0} r^{-3}$$

$$r^4 = \frac{1}{(2\pi)^2} \frac{h^2}{2\mu_0 p}$$

$$\Leftrightarrow \quad r^2 = \frac{1}{2\pi} \frac{h}{\sqrt{2\mu_0 p}}$$

$\square$

Let us define the *optimal radius* because we will reference it many times in the near future.

Definition 25 (**Optimal Radius**)**.** Given a pressure model p, define the *optimal radius* at $\mathbf{x} \in \mathbb{M}$ as

$$r_{\text{opt}}(\mathbf{x}) := \frac{1}{\sqrt{2\pi}} \frac{\sqrt{h}}{\sqrt[4]{2\mu_0 p(\mathbf{x})}} \tag{2.6}$$

Knowing the optimal radius of extremal smooth magnetic filament helps us a lot when we turn our attention to finding the optimal center curve γ in order to minimize the MHS energy $\mathcal{E}$ further. For instance, we can now express the energy of an ideal filament as a *length* too, just like we did with the field lines. We do this by bringing in the gas metric (definition 19).

Theorem 26 (**Ideal Filaments Energy as Length**)**.** The MHS energy of a smooth magnetic filament with center curve γ and flux h and optimal radius r_{opt} is proportional to the length of the center curve $\gamma : [0, L] \to \mathbb{M}$ in the gas metric.

$$\mathcal{E}(\gamma, \mathbf{B}) = h \mathscr{L}_{\text{gas}}(\gamma) = h \int_0^L \sqrt{\frac{2p}{\mu_0}} \, ds$$

Proof. Instead of inserting the optimal radii from theorem 23, we just plug in the gas-flux pressure equilibrium condition $p = \frac{B^2}{2\mu_0}$ since we know that this leads to the same result. By inserting the relation $B = \sqrt{2\mu_0 p}$ in the equation of theorem 21 we get:

$$\frac{1}{h}\mathcal{E}(\gamma, \mathbf{B}) = \int_0^L \left(\frac{p}{B} + \frac{B}{2\mu_0} \right) ds$$

$$= \int_0^L \left(\frac{p}{\sqrt{2\mu_0 p}} + \frac{\sqrt{2\mu_0 p}}{2\mu_0} \right) ds$$

$$= \int_0^L \left(\frac{\sqrt{p}}{\sqrt{2\mu_0}} + \frac{\sqrt{p}}{\sqrt{2\mu_0}} \right) ds$$

$$= \int_0^L 2\sqrt{\frac{p}{2\mu_0}} ds$$

$$= \int_0^L \sqrt{\frac{2p}{\mu_0}} ds$$

$$= \int_0^L e^{u_{\mathrm{gas}}} ds = \int_0^L 1 d\tilde{s} = \mathscr{L}_{\mathrm{gas}}(\gamma)$$

$$\square$$

Now we can proceed to look at the minimizing shapes of this energy.

2.2.3   Ideal Magnetic Filaments: The Minimizing Shape

Theorem 26 gives us a very easy computation of the energy which we will next use to compute analytically the global energy minimizers. The energy has now again been expressed as a *length*, which turns the *question of minimal energy into a question of finding geodesics*.

In section 1.4.2 [Gas Domain] we have mentioned the polynomial atmospheric pressure model we use

$$p(\mathbf{x}) = p_0 \left(\frac{|\mathbf{x}|}{r_\odot} \right)^{-\lambda}.$$

In the following theorem we will make good use of polynomial pressure form. Note that for the other popular atmospheric pressure model, the exponential model, we did not achieve an equivalent theorem. Close to the surface, the metric resulting from the polynomial pressure model is not so different to the one resulting from the exponential pressure model.

What should these geodesics look like? In the following, let $\mathbf{x}, \mathbf{y} \in r_\odot \mathbb{S}^2$ be two points on the surface of the sun such that they are separated by an angle θ relative to the sun's center (see figure 2.5):

$$\mathbf{x} = r_\odot \begin{pmatrix} -\sin\frac{\theta}{2} \\ 0 \\ \cos\frac{\theta}{2} \end{pmatrix}, \quad \mathbf{y} = r_\odot \begin{pmatrix} \sin\frac{\theta}{2} \\ 0 \\ \cos\frac{\theta}{2} \end{pmatrix}.$$
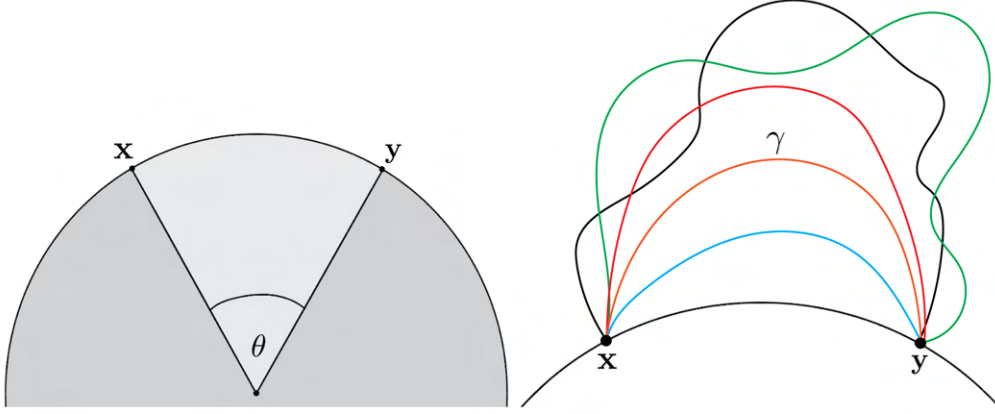
Figure 2.5: The points **x** and **y** lie on the surface of the sun $r_\odot \mathbb{S}^2$ with an angular distance of θ from each other. How does the energy minimizer / geodesic magnetic filament γ connecting these two points with extremal MHS energy look like?

Theorem 27 (**Energy Minimizer / Geodesics of Smooth Magnetic Filaments**).
We are given the polynomial pressure model on the exterior of the sun $\mathbb{M} = \mathbb{R}^3 \setminus \mathbb{B}_{r_\odot}$ with $\lambda \geq 4$. The gas metric geodesics between the two surface points **x** and **y** at an angle θ are of the following forms
Case $\theta < \frac{2\pi}{\lambda-2}$:

$$\gamma \colon [-\tfrac{\theta}{2}, \tfrac{\theta}{2}] \to \mathbb{M}, \ t \mapsto r_\odot \left(\frac{\cos\left(\frac{\lambda-2}{2}t\right)}{\cos\left(\frac{\lambda-2}{2}\frac{\theta}{2}\right)} \right)^{\frac{2}{\lambda-2}} \begin{pmatrix} \sin t \\ 0 \\ \cos t \end{pmatrix}. \tag{2.7}$$

Case $\theta \geq \frac{2\pi}{\lambda-2}$:
The length-minimizing geodesic with respect to $d\tilde{s}$ connecting **x** and **y** is given by the radial line going out from **x** to infinity followed by the radial line coming in from infinity to **y**.
These geodesics are also the center curves of the energy minimizers of smooth magnetic filaments with optimal radius.

Proof. For symmetry reasons, the geodesic in question has to lie in the plane containing the two surface points **x**, **y**, the xz-plane. Denoting $\mathbb{M}_{x,z} := \mathbb{M} \cap \mathrm{span}\{e_x, e_z\}$ and introducing polar coordinates (r, ϕ) on $\mathbb{M}_{x,z}$ we can use the transformation

$$f \colon \mathbb{M}_{x,z} \to \mathbb{R}^2 \tag{2.8}$$

$$r \begin{pmatrix} \sin \phi \\ 0 \\ \cos \phi \end{pmatrix} \mapsto \underbrace{\left(\frac{r}{r_\odot} \right)^{-\frac{\lambda-2}{2}}}_{R:=} \underbrace{\begin{pmatrix} \sin \left(\frac{\lambda-2}{2} \phi \right) \\ \cos \left(\frac{\lambda-2}{2} \phi \right) \end{pmatrix}}_{\mathbf{v}:=}$$

f

Figure 2.6: The mapping f of the xz-plane slice of $\mathbb{M}$ to multiple covers of a disc. f is not injective and wraps around the disc multiple times. The center of the disc is the image of the point at infinity. This is kind of like a helix pressed into a single plane. A *flat helix*.

in order to map $\mathbb{M}_{x,z}$ onto the interior of the unit disk in $\mathbb{R}^2$ (figure 2.6). f is not injective, as it maps onto the unit disk multiple times for $\lambda > 4$, kind of like a flat helix. Note that the polar metric and Euclidean metric relate through

$$ds^2 = dr^2 + r^2 d\phi^2.$$

We also have

$$\partial_r R = \left(-\frac{\lambda-2}{2} \right) \left(\frac{r}{r_\odot} \right)^{-\frac{\lambda-2}{2}-1} \frac{1}{r_\odot} dr$$
$$= \left(-\frac{\lambda-2}{2} \right) \left(\frac{1}{r_\odot} \right) \left(\frac{r}{r_\odot} \right)^{-\frac{\lambda}{2}} dr$$

and

$$\partial_\phi \mathbf{v} = \frac{\lambda - 2}{2} d\phi \underbrace{\begin{pmatrix} \cos\left(\frac{\lambda-2}{2}\phi\right) \\ -\sin\left(\frac{\lambda-2}{2}\phi\right) \end{pmatrix}}_{J\mathbf{v}=}.$$
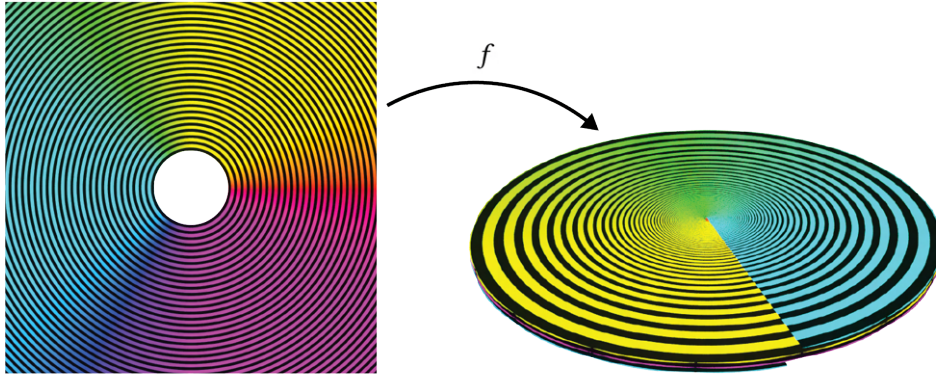
where J denotes the 90° anti-clockwise rotation, $\langle \mathbf{v}, J\mathbf{v} \rangle = 0$. Therefore

$$df = d(R\mathbf{v}) = (\partial_r R)\mathbf{v} + R(\partial_\phi \mathbf{v}) = (\partial_r R)\mathbf{v} + R\left(\frac{\lambda-2}{2}\right) d\phi J\mathbf{v}$$

and thus we can compute the induced metric of f directly:

$$\begin{aligned}
df^2 &= \langle df, df \rangle \\
&= \langle (\partial_r R)\mathbf{v} + R\left(\frac{\lambda-2}{2}\right) d\phi J\mathbf{v}, (\partial_r R)\mathbf{v} + R\left(\frac{\lambda-2}{2}\right) d\phi J\mathbf{v} \rangle \\
&= (\partial_r R)^2 \underbrace{\langle \mathbf{v}, \mathbf{v} \rangle}_{=1} + 2(\partial_r R)R\left(\frac{\lambda-2}{2}\right) d\phi \underbrace{\langle \mathbf{v}, J\mathbf{v} \rangle}_{=0} + \left(R\left(\frac{\lambda-2}{2}\right) d\phi\right)^2 \underbrace{\langle J\mathbf{v}, J\mathbf{v} \rangle}_{=1}
\end{aligned}$$

$$\begin{aligned}
&= (\partial_r R)^2 + R^2 \left(\frac{\lambda-2}{2}\right)^2 d\phi^2 \\
&= \left(\frac{\lambda-2}{2}\right)^2 \frac{1}{r_\odot^2} \left(\frac{r}{r_\odot}\right)^{-\lambda} dr^2 + \left(\frac{r}{r_\odot}\right)^{-(\lambda-2)} \left(\frac{\lambda-2}{2}\right)^2 d\phi^2
\end{aligned}$$

$$\begin{aligned}
&= \left(\frac{\lambda-2}{2}\right)^2 \frac{1}{r_\odot^2} \left(\frac{r}{r_\odot}\right)^{-\lambda} \underbrace{\left(dr^2 + r^2 d\phi^2\right)}_{=ds^2} \\
&= \left(\frac{(\lambda-2)^2}{4 r_\odot p_0}\right) \underbrace{p_0 \left(\frac{r}{r_\odot}\right)^{-\lambda}}_{=p} ds^2
\end{aligned}$$

$$\begin{aligned}
&= \underbrace{\left(\frac{\mu_0(\lambda-2)^2}{8 r_\odot p_0}\right)}_{\text{const. } c:=} \frac{2p}{\mu_0} ds^2 \\
&= c \left(\underbrace{\sqrt{\frac{2p}{\mu_0}} ds}_{=d\tilde{s}}\right)^2 \\
&= c\, d\tilde{s}^2.
\end{aligned}$$

To our extreme convenience, we see that the pullback under f of the Euclidean metric on the unit disk is a constant multiple of our gas metric $d\tilde{s} = \sqrt{\frac{2p}{\mu_0}} ds$. Let γ be our curve

and $\delta := f \circ \gamma$ the image of this curve. Then the Euclidean length of δ is a constant multiple of the gas metric length of γ:

$$
\begin{aligned}
\mathscr{L}_{\text{eucl}}(\delta) = \int |\delta'| \, ds = \int \left| \frac{d\delta}{ds} \right| ds \\
= \int \left| \frac{d(f \circ \gamma)}{ds} \right| ds \\
= \int \left| (df) \circ \gamma \, \frac{d\gamma}{ds} \right| ds \\
= \int \left| \sqrt{c} \, d\tilde{s} \, \frac{d\gamma}{ds} \right| ds \\
= \sqrt{c} \int \left| \frac{d\gamma}{ds} \right| d\tilde{s} = \sqrt{c} \int |\gamma'| \, d\tilde{s} = \sqrt{c} \, \mathscr{L}_{\text{gas}}(\gamma)
\end{aligned}
$$

If $\mathscr{L}_{\text{gas}}(\gamma)$ is a minimizer, then so is $\mathscr{L}_{\text{eucl}}(\delta)$ and vice versa. Thus, our search for gas metric geodesics γ leads us to look at Euclidean geodesics δ in the disc, which are simply straight lines!

But be careful! The phase of the mapping f is amplified by the factor $\frac{\lambda-2}{2}$. The exterior of the sun in $\mathbb{M}_{x,z}$ is mapped onto the sun's interior disc multiple times and is not injective. Topologically we can frame the image of f in useful ways to easier see what the geodesics should be like:

1. **Squeezed Disc:**

   Squeeze the multiple covers of the disc into a single cover of the disc like in figure 2.7. This of course distorts the Euclidean metric and is thus not the easier way to see the geodesics.
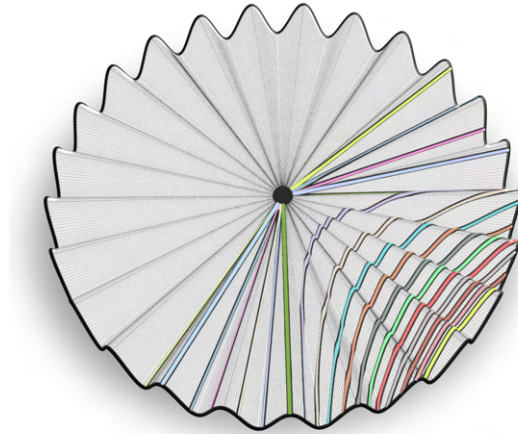

Figure 2.7: The map f from equation 2.8 which maps geodesics contained in a plane on the sun's exterior to geodesics in a squeezed cover of the unit disc in $\mathbb{R}^2$. Geodesics going through the midpoint of the disc represent geodesics going through infinity on the sun's exterior.

2. **Cut and Glued Helix:**

   Display the multiple covers of the disc as layers on top of each other that are glued together. Figure 2.8 shows this together with the geodesics. Due to the Euclidean metric the geodesics are either straight lines connecting the boundary points (right side middle), or go through the center in order to connect their targets with straight lines. Effectively, we track the polar angle beyond the usual domain $[0, 2\pi]$.
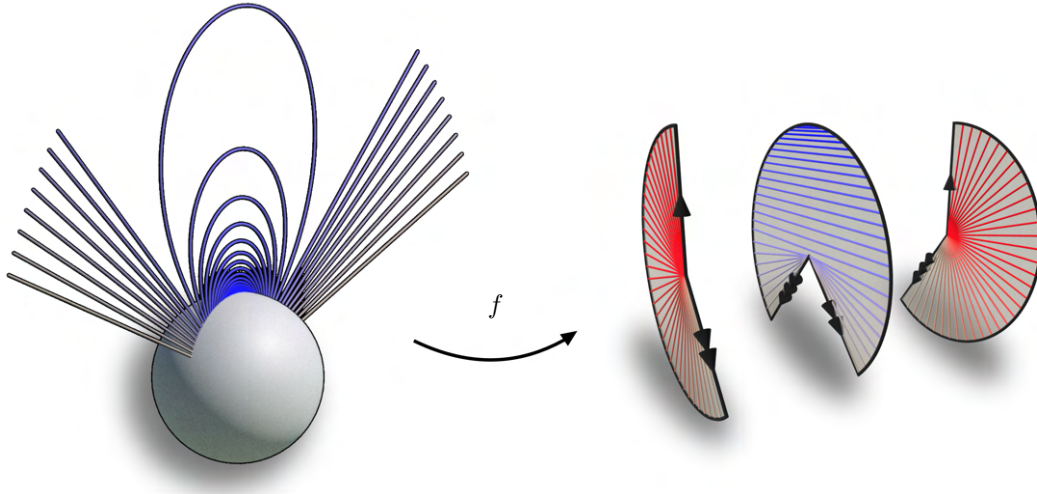
Figure 2.8: The map f from Eq. (2.8) which maps geodesics contained in a plane on the sun's exterior to geodesics in a multiple cover of the unit disc in $\mathbb{R}^2$.

3. **Stretched Helix:**

   Alternatively, one can take the flat helix seen in figure 2.6 on the right and stretch it upwards like a helix (figure 2.9). If we ignore the axial contribution to the Euclidean metric, we can directly see that geodesics between two boundary points are either directly connected by a straight line or have to wrap around the central axis in order to connect to their target.

f is not injective, but by augmenting f to track the polar angle as well, like in the stretched helix of figure 2.9, we do end up with an injective map. f on the flat helix it is even invertible now!

The Euclidean shortest paths in the image of f will directly map to the shortest paths of $\mathbb{M}_{x,z}$ through the now invertible map of f. Due to the helix-like structure we have to distinguish two cases for shortest paths between the two points at the outer boundary of the disc. In the flat helix image of f we will now discuss the Euclidean geodesics between the following two boundary points.

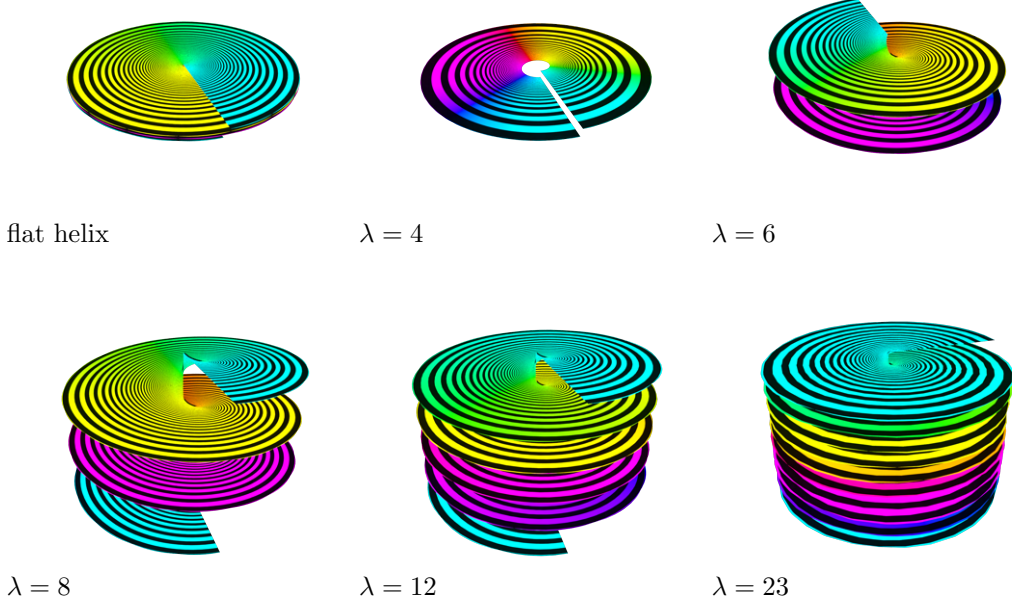flat helix $\lambda = 4$ $\lambda = 6$

$\lambda = 8$ $\lambda = 12$ $\lambda = 23$

Figure 2.9: The flat image of f (top left, $\lambda = 8$) artificially stretched out like a helix for various $\lambda \geq 4$. The polar coordinates ϕ are scaled by the factor $1/2(\lambda - 2)$, causing the helix to wrap around more and more times for higher values of λ.

$$f(\mathbf{x}) = \begin{pmatrix} -\sin\left(\frac{\lambda-2}{2}\frac{\theta}{2}\right) \\ \cos\left(\frac{\lambda-2}{2}\frac{\theta}{2}\right) \end{pmatrix} \quad \text{and} \quad f(\mathbf{y}) = \begin{pmatrix} \sin\left(\frac{\lambda-2}{2}\frac{\theta}{2}\right) \\ \cos\left(\frac{\lambda-2}{2}\frac{\theta}{2}\right) \end{pmatrix}.$$

The angle between these two points can be computed easily using a trigonometric sum identity

$$\cos^{-1}\left(\begin{pmatrix} -\sin\left(\frac{\lambda-2}{2}\frac{\theta}{2}\right) \\ \cos\left(\frac{\lambda-2}{2}\frac{\theta}{2}\right) \end{pmatrix} \cdot \begin{pmatrix} \sin\left(\frac{\lambda-2}{2}\frac{\theta}{2}\right) \\ \cos\left(\frac{\lambda-2}{2}\frac{\theta}{2}\right) \end{pmatrix}\right) = \cos^{-1}\left(\cos^2\left(\frac{\lambda-2}{2}\frac{\theta}{2}\right) - \sin^2\left(\frac{\lambda-2}{2}\frac{\theta}{2}\right)\right)$$

$$= \cos^{-1}\left(\cos\left(2\frac{\lambda-2}{2}\frac{\theta}{2}\right)\right)$$

$$= \frac{\lambda-2}{2}\theta.$$

The two cases of geodesics will distinguish themselves by the property of being directly connectible by a line segment on the flat helix. For that to happen we require

$$\frac{\lambda - 2}{2}\theta < \pi.$$

Case $\theta < \frac{2\pi}{\lambda-2}$:

$f(\mathbf{x})$ and $f(\mathbf{y})$ are close enough so that directly connecting lines are not affected by the helix-like topology because

$$\frac{\lambda - 2}{2}\theta < \pi.$$

Thus, the Euclidean geodesics here amount to drawing a straight line between these two points. Such a straight line can be parametrized by

$$\delta\colon [-\tfrac{\theta}{2}, \tfrac{\theta}{2}] \to \mathbb{R}^2,\ t \mapsto \underbrace{\frac{\cos\left(\frac{\lambda-2}{2}\frac{\theta}{2}\right)}{\cos\left(\frac{\lambda-2}{2}t\right)}}_{\tilde{R}:=} \underbrace{\begin{pmatrix} \sin\left(\frac{\lambda-2}{2}t\right) \\ \cos\left(\frac{\lambda-2}{2}t\right) \end{pmatrix}}_{\tilde{v}:=}.$$

To see that this is a straight line, just notice that the second component is constant in t (θ is fixed anyway)

$$\tilde{R}\cos\left(\tfrac{\lambda-2}{2}t\right) = \frac{\cos\left(\frac{\lambda-2}{2}\frac{\theta}{2}\right)}{\cos\left(\frac{\lambda-2}{2}t\right)}\cos\left(\tfrac{\lambda-2}{2}t\right) = \underbrace{\cos\left(\tfrac{\lambda-2}{2}\tfrac{\theta}{2}\right)}_{\text{constant in } t}.$$

We now just need to correctly invert δ through f. Thanks to the polar representations, this is fairly easy. $\tilde{v}$ gets mapped to $(\sin t, 0, \cos t)^\top$, which is easy to see from the definition of f. Inverting the radius $\tilde{R}$ leads to

$$R = \left(\frac{r}{r_\odot}\right)^{-\frac{\lambda-2}{2}}$$
$$\Leftrightarrow\quad r = r_\odot R^{\left(-\frac{2}{\lambda-2}\right)}.$$

Replacing R with the new $\tilde{R}$ will then give us the parametrization of the gas-metric geodesic in $\mathbb{M}_{x,z}$.

$$\gamma\colon [-\tfrac{\theta}{2}, \tfrac{\theta}{2}] \to \mathbb{M},\ t \mapsto r_\odot \left(\frac{\cos\left(\frac{\lambda-2}{2}t\right)}{\cos\left(\frac{\lambda-2}{2}\frac{\theta}{2}\right)}\right)^{\frac{2}{\lambda-2}} \begin{pmatrix} \sin t \\ 0 \\ \cos t \end{pmatrix}. \tag{2.9}$$

Case $\theta \geq \frac{2\pi}{\lambda-2}$:

$f(\mathbf{x})$ and $f(\mathbf{y})$ are now far away enough to be affected by the flat helix-like topology. The map f multiplies angles by a factor of $\frac{\lambda-2}{2} > 1$, so the conformally changed metric on the intersection of the exterior of the sun with the xz-plane has a cone point at infinity that is mapped to the center of the disc. Away from the cone singularity, the metric is flat (Euclidean). However there is negative curvature concentrated in the cone point and as a consequence, many length-minimizing geodesics are forced to pass through the cone point.

More intuitively, shortest paths have to *wind up* the helical structure of the flat helix image of f to reach the endpoints. The shortest way to do so is by wrapping around the central axis of the helix.

The Euclidean geodesic δ are thus two straight line segments, one from $f(\mathbf{x})$ to the disc center and another one back to $f(\mathbf{y})$. Each straight line segment has a constant polar coordinate and is thus mapped by the inversion of f to a straight line segment connecting $\mathbf{x}$ to the point at infinity and the point at infinity back to $\mathbf{y}$.

Since it was established that the length of γ is equivalent to the energy $\mathcal{E}$ of the smooth magnetic filament with center curve γ and optimal radius (theorem 26) we also know that these geodesics also describe the global minimal energy configurations of the filaments connecting $\mathbf{x}$ to $\mathbf{y}$.

$\square$
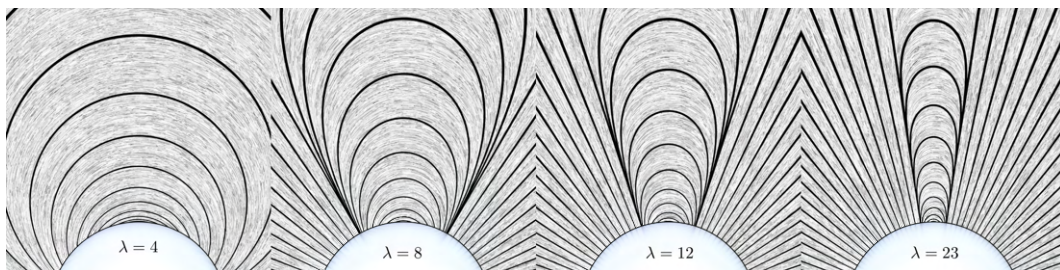
Figure 2.10: The shapes of all geodesics as analytically derived in theorem 27 for various λ when using the gas metric with $p = p_0 \frac{|x|}{r_\odot}^{-\lambda}$. When the angular distance θ between the footpoints is greater than $\frac{2\pi}{\lambda-2}$, the geodesics will go to the point at infinity and back.

Theorem 27 now gives us specific analytic solutions to energy minimizers for smooth magnetic filaments. Figure 2.10 displays these geodesics for different values of λ. The solutions will indeed be the global energy minimizers in the plasma metric if the filaments are so thin that they don't interact with each other. We will explain this in more detail in section 2.5.

2.2.4   Ideal Magnetic Filaments: The Minimizing Energy

A straight forward interest is now the energy such a geodesic has, which is equivalent to asking *how long* γ is in the plasma metric.

Corollary 28 (**Energy / Geodesic Distance of an Ideal Magnetic Filament**).
We are given the polynomial pressure model on the exterior of the ball $\mathbb{R}^3 \setminus \mathbb{M}$ with $\lambda \geq 4$. The geodesic between the two surface points $\mathbf{x}$ and $\mathbf{y}$ at an angle $0 < \theta < \pi$ from each other has the length

$$d(\mathbf{x}, \mathbf{y}) = \sqrt{\frac{2 p_0 r_\odot}{\mu_0}} \left(\frac{4}{\lambda - 2} \right) \cdot \sin\left(\min\{\theta, \tfrac{2\pi}{\lambda - 2}\} \cdot \tfrac{\lambda - 2}{4} \right).$$

This is also the global energy minimum of the smooth magnetic filament connecting $\mathbf{x}$ to $\mathbf{y}$.

Proof. Theorem 27 has provided us with the specific parametrization of the geodesics in the gas metric between the two points $\mathbf{x}$ and $\mathbf{y}$ at an angle θ from each other. We now just have to compute the geodesic length of this parametrization to get the distance $d(\mathbf{x}, \mathbf{y})$ between them. But wait, this would certainly lead us to an analytically messy integral expressions of the form

$$\int_\gamma |\gamma'|^2 ds = \int_\gamma 1 d\tilde{s} = \int_\gamma \sqrt{\frac{2p}{\mu_0}} ds = \sqrt{\frac{2p_0}{\mu_0 r_\odot^{-\lambda}}} \int_\gamma |\mathbf{x}|^{-\frac{\lambda}{2}} ds$$

to be integrated on a complicated parametrization. Instead, we take another look at the proof of theorem 27. In it, we established a mapping f for which the curve $\delta = f \circ \gamma$ has the following handy property:

$$d(\mathbf{x}, \mathbf{y}) = \mathscr{L}_{\text{gas}}(\gamma) = \underbrace{\sqrt{\frac{2p_0 r_\odot}{\mu_0}} \left(\frac{2}{\lambda - 2} \right)}_{c :=} \mathscr{L}_{\text{eucl}}(\delta) \tag{2.10}$$

Therefore, computing the gas-metric length only requires us to compute the Euclidean length. Because the geodesics appear in two distinct cases, we have to make a distinction here too.

Case $\theta < \frac{2\pi}{\lambda - 2}$:
δ is a straight line segment connecting

$$f(\mathbf{x}) = f\left(\gamma\left(-\tfrac{\theta}{2} \right) \right) = \underbrace{\left(\frac{\cos\left(\frac{\lambda - 2}{2} \frac{-\theta}{2} \right)}{\cos\left(\frac{\lambda - 2}{2} \frac{\theta}{2} \right)} \right)^{\frac{2}{\lambda - 2}}}_{=1} \left(\begin{array}{c} -\sin\left(\frac{\lambda - 2}{2} \frac{\theta}{2} \right) \\ \cos\left(\frac{\lambda - 2}{2} \frac{\theta}{2} \right) \end{array} \right) = \left(\begin{array}{c} -\sin\left(\frac{\lambda - 2}{2} \frac{\theta}{2} \right) \\ \cos\left(\frac{\lambda - 2}{2} \frac{\theta}{2} \right) \end{array} \right)$$

and

$$f(\mathbf{y}) = f\left(\gamma\left(\tfrac{\theta}{2}\right)\right) = \underbrace{\left(\frac{\cos\left(\frac{\lambda-2}{2}\frac{\theta}{2}\right)}{\cos\left(\frac{\lambda-2}{2}\frac{\theta}{2}\right)}\right)^{\frac{2}{\lambda-2}}}_{=1} \begin{pmatrix}\sin\left(\frac{\lambda-2}{2}\frac{\theta}{2}\right)\\ \cos\left(\frac{\lambda-2}{2}\frac{\theta}{2}\right)\end{pmatrix} = \begin{pmatrix}\sin\left(\frac{\lambda-2}{2}\frac{\theta}{2}\right)\\ \cos\left(\frac{\lambda-2}{2}\frac{\theta}{2}\right)\end{pmatrix}$$

The Euclidean distance is just the norm of the difference

$$\mathscr{L}_{\text{eucl}}\left(\delta\right) = |f(\mathbf{y}) - f(\mathbf{x})| = \left|\begin{pmatrix}2\sin\left(\frac{\lambda-2}{2}\frac{\theta}{2}\right)\\ 0\end{pmatrix}\right| = 2\sin\left(\frac{\lambda-2}{2}\frac{\theta}{2}\right)$$

were we dropped the $|\cdot|$ because $\sin \geq 0$ for $0 \leq \frac{\lambda-2}{2}\frac{\theta}{2} \leq \pi$. We combine this result with the relation from equation 2.10 and get

$$\mathscr{L}_{\text{gas}}(\gamma) = c\mathscr{L}_{\text{eucl}}\left(\delta\right) = \sqrt{\frac{2p_0 r_\odot}{\mu_0}}\left(\frac{4}{\lambda-2}\right)\sin\left(\frac{\lambda-2}{2}\frac{\theta}{2}\right)$$

Case $\theta \geq \frac{2\pi}{\lambda-2}$:

We could repeat the same computation as in the previous case. However, since we know that the geodesics in this case all go straight to infinity and back, they all have the same length. As we expect continuity in θ, we can also expect the previous case to result in the correct geodesic distance as θ approaches $\frac{2\pi}{\lambda-2}$.

In other words, the geodesics going to infinity and back have the length of the previous case when inserting $\theta = \frac{2\pi}{\lambda-2}$, *i.e.* at the peak of the sinus function.

$$\begin{aligned}\mathscr{L}_{\text{gas}}(\gamma) &= \sqrt{\frac{2p_0 r_\odot}{\mu_0}}\left(\frac{4}{\lambda-2}\right)\sin\left(\frac{\lambda-2}{2}\frac{1}{2}\frac{2\pi}{\lambda-2}\right)\\ &= \sqrt{\frac{2p_0 r_\odot}{\mu_0}}\left(\frac{4}{\lambda-2}\right)\end{aligned}$$

We can combine these two cases $\theta < \frac{2\pi}{\lambda-2}$ and $\theta \geq \frac{2\pi}{\lambda-2}$ into one handy formula with the minimum expression

$$d(\mathbf{x},\mathbf{y}) = \mathscr{L}_{\text{gas}}(\gamma) = \sqrt{\frac{2p_0 r_\odot}{\mu_0}}\left(\frac{4}{\lambda-2}\right)\cdot\sin\left(\min\{\theta,\tfrac{2\pi}{\lambda-2}\}\cdot\tfrac{\lambda-2}{4}\right).$$

Since theorem 27 also says that these geodesics are global minimizers of the energy $\mathcal{E}$ for smooth magnetic filaments, we know that this length energy must also be the global energy minima these filaments can obtain.

$\square$

At this point, an apology is due. The publication *Filament Based Plasma* [Padilla

et al.(2022)] had displayed the cost function to be $d(\mathbf{x}, \mathbf{y}) = \sqrt{p_0} \cdot 2 \sin\left(\min\{\theta, \frac{2\pi}{\lambda-2}\} \cdot \frac{\lambda-2}{4}\right)$, which is false due to the lack of scaling by $r_\odot$ and influences of λ. This error occurred because in the original calculation the solar radius was normalized and constant factors were neglected. The main application of this distance function lies in the optimal transport problem in section 7.1 [Matching Stipples], which is not affected by the constant factors. We show the energies/geodesic distances of the surface points for different values of λ in figure 2.11.
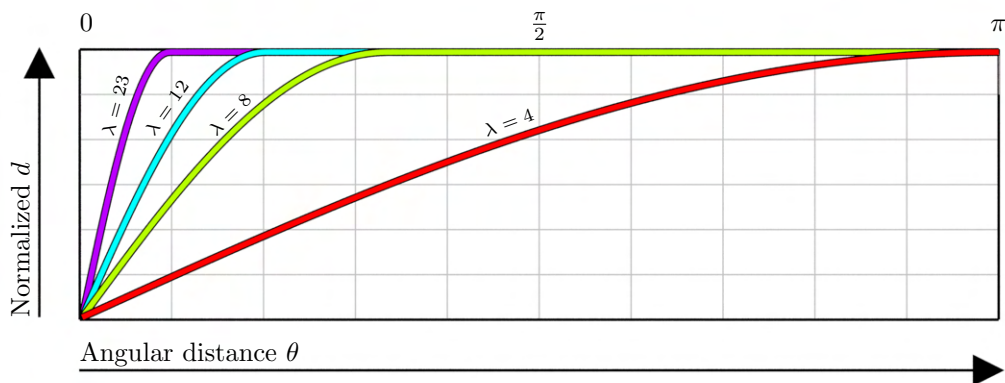

Figure 2.11: The normalized energy/geodesic distance functions as functions of the angular distance θ between the points on the surface of the sphere $\partial\mathbb{M}$. We show the resulting cost functions for different values of λ in the gas metric. The cost becomes constant as soon as the geodesics go through the point at infinity. These functions were derived in theorem 28 and are sine functions that become constant at their peaks.

2.2.5　Ideal Magnetic Filaments: Low's Geodesics

We take a small detour from our path to cover a side remark connecting our result to previous work in magnetohydrostatics. As mentioned at the beginning of section 2.2.3, the polynomial pressure model $p = p_0 \left(\frac{|\mathbf{x}|}{r_\odot}\right)^{-\lambda}$ enables explicit solutions of geodesics as seen in theorem 27, for the spherical sun. This remains the only way to archive an analytic solution known to us.

However, in the following we will show that an exponetial pressure model used in the limit of $r_\odot \to \infty$ leads to the global minimizers that are known to be analytic solutions of a special case derived by [Low(1982)]. The expression $r_\odot \to \infty$ is equivalent to going from a spherical setting to a flat setting. Therefore we reference this limit as the *flat sun*, modeled by the upper half space $\mathbb{M} = \mathbb{R}^3_{z+}$ (see figure 2.12).

For the pressure we choose a height-only dependent exponential model

$$p : \mathbb{M} \to \mathbb{R}$$

$$p(\mathbf{x}) = p_0 e^{-\lambda z}$$
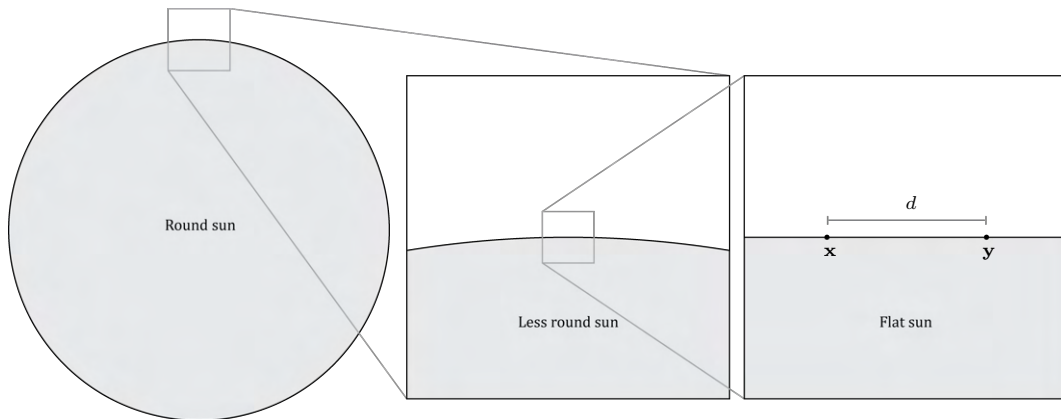
Figure 2.12: As the radius grows, locally, the sun is perceived as more flat. This does not prove that the sun is flat, even though it is considerably more flat than earth! The approximation works if the observed phenomenon is not significantly influenced by the curvature (*i.e.*small relative to $r_\odot$). **x** and **y** are now two points on the flat sun at a distance $d > 0$. How does the magnetic filament connecting these two points with extremal MHS energy look like?

We are interested in this setup to show that if we apply our model on these conditions, that we retrieve the special case of *Low's geodesics* as shown in [Low(1982)]. We capture this in the following theorem.

Theorem 29 (Low's Geodesics). We are given $\lambda > 0$ and two points on the surface of the flat sun at Euclidean distance $d > 0$ from another:

$$\mathbf{x} = \begin{pmatrix} -\frac{d}{2} \\ 0 \\ 0 \end{pmatrix} \quad \text{and} \quad \mathbf{y} = \begin{pmatrix} \frac{d}{2} \\ 0 \\ 0 \end{pmatrix}.$$

The geodesics in the gas metric $d\tilde{s} = \sqrt{\frac{2p}{\mu_0}}$ from an exponential pressure model are of the following form:

Case $d < \frac{2\pi}{\lambda}$:

$$\gamma \colon [-\tfrac{d}{2}, \tfrac{d}{2}] \to \mathbb{M}, \ t \mapsto \begin{pmatrix} t \\ 0 \\ \frac{2}{\lambda} \ln\left(\frac{\cos\left(\frac{\lambda}{2} t\right)}{\cos\left(\frac{\lambda}{2} \frac{d}{2}\right)} \right) \end{pmatrix}. \tag{2.11}$$

Case $d \geq \frac{2\pi}{\lambda}$:

Connect a vertical line from $\mathbf{x}$ to ∞ and return a vertical line from ∞ to $\mathbf{y}$.

These geodesics are also the center curves of the energy minimizers of smooth magnetic filaments with optimal radius. They global minimum energy can be expressed by the gas-metric geodesic distance

$$d(\mathbf{x}, \mathbf{y}) = \mathscr{L}_{\text{gas}}(\gamma) = \frac{4}{\lambda} \sqrt{\frac{\mu_0}{p_0}} \cdot \sin\left(\min\{d, \tfrac{2\pi}{\lambda}\} \cdot \tfrac{\lambda}{2}\right).$$

Proof. The proof will essentially be the same as the proof for theorem 27 with slightly modified calculations. For symmetry reasons we stick to the xz-plane, denoting it by $\mathbb{M}_{x,z}$. We define f as

$$f \colon \mathbb{M}_{x,z} \to \mathbb{R}^2$$

$$\begin{pmatrix} x \\ 0 \\ z \end{pmatrix} \mapsto \underbrace{e^{-\frac{\lambda}{2} z}}_{R:=} \underbrace{\begin{pmatrix} \sin\left(\frac{\lambda}{2} x\right) \\ \cos\left(\frac{\lambda}{2} x\right) \end{pmatrix}}_{\mathbf{v}:=}$$

We compute its derivative by the x and z component.

$$\partial_z f = -\frac{\lambda}{2} e^{-\frac{\lambda}{2}} \mathbf{v} ds = -\frac{\lambda}{2} R \mathbf{v} ds$$

$$\partial_y f = 0$$

$$\partial_x f = R \frac{\lambda}{2} \begin{pmatrix} -\cos\left(\frac{\lambda}{2}\phi\right) \\ \sin\left(\frac{\lambda}{2}\phi\right) \end{pmatrix} ds = \frac{\lambda}{2} R J \mathbf{v} ds$$

where J denotes the 90° anti-clockwise rotation, $\langle \mathbf{v}, J\mathbf{v} \rangle = 0$.

Thus we have

$$df^2 = (\partial_x f ds)^2 + (\partial_y f ds)^2 + (\partial_z f ds)^2$$

$$= \left(\left(-\frac{\lambda}{2}R\right)^2 \underbrace{|\mathbf{v}|^2}_{=1} + 0 + \left(\frac{\lambda}{2}R\right)^2 \underbrace{|J\mathbf{v}|^2}_{=1} \right) ds^2$$

$$= \left(\frac{\lambda}{2}\right)^2 2 \left(R ds\right)^2$$

$$= \frac{\lambda^2 \mu_0}{4 p_0} \left(\sqrt{\frac{2}{\mu_0}} \underbrace{\sqrt{p_0} e^{-\frac{\lambda}{2} z}}_{=\sqrt{p}} ds \right)^2$$

$$= \underbrace{\frac{\lambda^2 \mu_0}{4 p_0}}_{c:=} \left(\underbrace{\sqrt{\frac{2p}{\mu_0}} ds}_{=d\tilde{s}} \right)^2$$

$$= \frac{\lambda^2 \mu_0}{4 p_0} d\tilde{s}^2$$

By the same calculation as in the proof of theorem 27 we conclude that for $\delta = f \circ \gamma$ where γ is a curve connecting $\mathbf{x}$ to $\mathbf{y}$ we have

$$\mathscr{L}_{\text{eucl}}(\delta) = \sqrt{c}\, \mathscr{L}_{\text{gas}}(\gamma).$$

And again, this means that Euclidean geodesics δ will give us plasma-metric geodesics γ through the inversion of f. Due to the polar representation we will again have the flat-helix topology as the image of f. Figure 2.13 illustrates the function f and the Euclidean geodesics in the flat-helix topology and their preimages. The image of f is represented by glued together sections to form a flat helix. This is the same approach as performed in the proof of theorem 27 [**Energy Minimizer / Geodesics of Smooth Magnetic Filaments**]. The geodesic will connect the two boundary points

$$f(\mathbf{x}) = \begin{pmatrix} -\sin\left(\frac{\lambda}{2}\frac{d}{2}\right) \\ \cos\left(\frac{\lambda}{2}\frac{d}{2}\right) \end{pmatrix} \quad \text{and} \quad f(\mathbf{y}) = \begin{pmatrix} \sin\left(\frac{\lambda}{2}\frac{d}{2}\right) \\ \cos\left(\frac{\lambda}{2}\frac{d}{2}\right) \end{pmatrix}.$$

The angle between these two points can be computed easily using a trigonometric sum identity

$$\cos^{-1}\left(\begin{pmatrix} -\sin\left(\frac{\lambda}{2}\frac{d}{2}\right) \\ \cos\left(\frac{\lambda}{2}\frac{d}{2}\right) \end{pmatrix} \cdot \begin{pmatrix} \sin\left(\frac{\lambda}{2}\frac{d}{2}\right) \\ \cos\left(\frac{\lambda}{2}\frac{d}{2}\right) \end{pmatrix}\right) = \cos^{-1}\left(\cos^2\left(\frac{\lambda}{2}\frac{d}{2}\right) - \sin^2\left(\frac{\lambda}{2}\frac{d}{2}\right)\right)$$

$$= \cos^{-1}\left(\cos\left(2\frac{\lambda}{2}\frac{d}{2}\right)\right)$$

$$= \frac{\lambda}{2}d.$$

The two cases of geodesics will distinguish themselves by the property of being directly connectible by a line segment on the flat helix. For that to happen we require
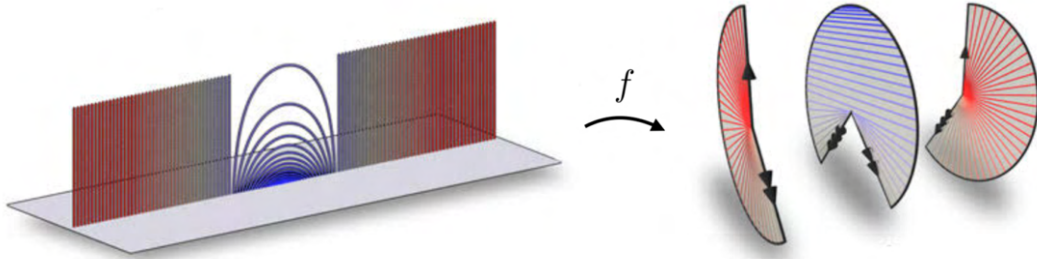
$$\frac{\lambda}{2}d < \pi.$$

Figure 2.13: Left: The flat sun represented as the upper half space with gas-metric geodesics γ. Right: The image of the upper half space mapped onto a limited part of a flat helix like topology using the function f, represented here by a cut and glued disc representation. The Euclidean geodesics $\delta = f \circ \gamma$ are displayed and are very similar as to the geodesics shown in figure 2.8.

Case $d < \frac{2\pi}{\lambda}$:

f maps $\mathbf{x}$ and $\mathbf{y}$ to a flat helix like structure. When $\frac{\lambda}{2}|x| < \frac{\pi}{2}$ then $f(\mathbf{x})$ and $f(\mathbf{y})$ will be connectible by a straight line δ on the flat helix as they share the same side of a disc. This straight line can be parametrized by

$$\delta \colon \left[-\frac{d}{2}, \frac{d}{2}\right] \to \mathbb{R}^2, \ t \mapsto \underbrace{\frac{\cos\left(\frac{\lambda}{2}\frac{d}{2}\right)}{\cos\left(\frac{\lambda}{2}t\right)}}_{\tilde{R}:=} \underbrace{\begin{pmatrix} \sin\left(\frac{\lambda}{2}t\right) \\ \cos\left(\frac{\lambda}{2}t\right) \end{pmatrix}}_{\tilde{v}:=}.$$

We now just need to correctly invert δ through f. Thanks to the polar representations, this is fairly easy. $\tilde{v}$ is responsible for the x component of the pre-image, which is easy to see from the definition of f. Inverting the magnitude $\tilde{R}$ leads to the z-component, for which we compute:

$$Z = e^{-\frac{\lambda}{2}z}$$
$$\Leftrightarrow \quad z = -\left(\tfrac{2}{\lambda}\right)\ln(Z).$$

Replacing Z with the new $\tilde{R}$ will then give us the parametrization of the gas-metric geodesic in $\mathbb{M}_{x,z}$.

$$\gamma\colon [-\tfrac{d}{2}, \tfrac{d}{2}] \to \mathbb{M},\ t \mapsto \begin{pmatrix} t \\ 0 \\ -\frac{2}{\lambda}\ln\left(\frac{\cos\left(\frac{\lambda}{2}\frac{d}{2}\right)}{\cos\left(\frac{\lambda}{2}t\right)}\right) \end{pmatrix} = \begin{pmatrix} t \\ 0 \\ \frac{2}{\lambda}\ln\left(\frac{\cos\left(\frac{\lambda}{2}t\right)}{\cos\left(\frac{\lambda}{2}\frac{d}{2}\right)}\right) \end{pmatrix}. \tag{2.12}$$

To compute the plasma-metric length of γ we compute the Euclidean length δ and use the relationship given in equation 2.12 to get the plasma-metric lenght of γ. For $d < \frac{\pi}{\lambda}$, the Euclidean length is simply the magnitude of the difference between $f(\mathbf{x})$ and $f(\mathbf{y})$.

$$d(\mathbf{x}, \mathbf{y}) = \mathscr{L}_{\text{gas}}(\gamma) = c^{-\frac{1}{2}}\mathscr{L}_{\text{eucl}}(\delta) \tag{2.13}$$
$$= c^{-\frac{1}{2}}|f(\mathbf{x}) - f(\mathbf{y})| \tag{2.14}$$
$$= c^{-\frac{1}{2}}\left|2\sin\left(\tfrac{\lambda}{2}\tfrac{d}{2}\right)\right| \tag{2.15}$$
$$= \frac{4}{\lambda}\sqrt{\frac{\mu_0}{p_0}}\sin\left(\tfrac{\lambda}{2}\tfrac{d}{2}\right) \tag{2.16}$$

Case $d \geq \frac{2\pi}{\lambda}$:

The images of $\mathbf{x}$ and $\mathbf{y}$ are not connectible by a simple straight line any more in the cut and glued helix image of f. Again, like in the proof of theorem 27, δ needs to pass straight through the center of the flat helix, the inversion of which are vertical lines to infinity and back. The length of these geodesics are all the same given by the equation 2.13 when $d = \frac{2\pi}{\lambda}$

$$d(\mathbf{x}, \mathbf{y}) = \frac{4}{\lambda}\sqrt{\frac{\mu_0}{p_0}}\underbrace{\sin\left(\tfrac{\lambda}{2}\tfrac{1}{2}\tfrac{2\pi}{\lambda}\right)}_{=1} = \frac{4}{\lambda}\sqrt{\frac{\mu_0}{p_0}}$$

We can combine these two cases $d < \frac{2\pi}{\lambda}$ and $d \geq \frac{2\pi}{\lambda}$ into one formula with the minimum expression

$$d(\mathbf{x}, \mathbf{y}) = \mathscr{L}_{\text{gas}}(\gamma) = \frac{4}{\lambda}\sqrt{\frac{\mu_0}{p_0}} \cdot \sin\left(\min\{d, \tfrac{2\pi}{\lambda}\} \cdot \tfrac{\lambda}{2}\right).$$

Since it was established that the length of γ is equivalent to the energy $\mathcal{E}$ of the smooth magnetic filament with center curve γ and optimal radius (theorem 26), we also know that this curve describes the global minimal energy configuration of the filament connecting $\mathbf{x}$ to $\mathbf{y}$.
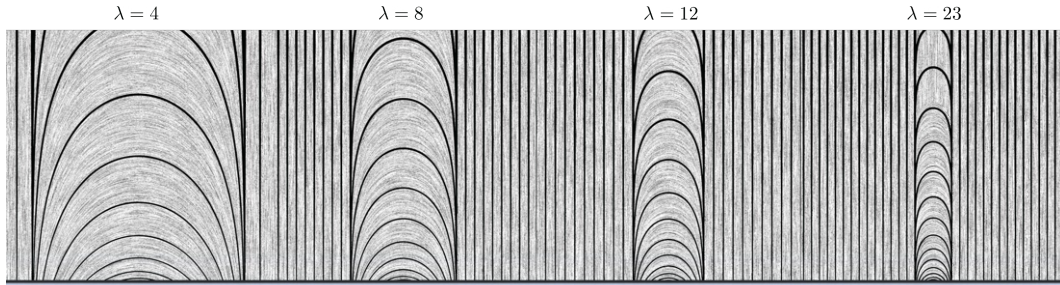
<div align="right">□</div>

Figure 2.14: The shapes of all Low's geodesics as analytically derived in theorem 29 for various λ. When the flat sun surface distance d between the footpoints is greater than $\frac{2\pi}{\lambda}$, the geodesics will go to the point at infinity and back. For $\lambda = 23$ the computation of the higher up vector field faced some numerical challenges due to the extreme small values of $e^{-\lambda}$.

Figure 2.14 shows all the geodesics from theorem 29. What makes this version for the flat sun so special? With a slight rewriting of the z-component we see

$$-\frac{2}{\lambda}\ln\left(\frac{\cos\left(\frac{\lambda}{2}\frac{d}{2}\right)}{\cos\left(\frac{\lambda}{2}t\right)}\right) = -\frac{2}{\lambda}\left(\ln\left(\cos\left(\frac{\lambda}{2}\frac{d}{2}\right)\right) - \ln\left(\cos\left(\frac{\lambda}{2}t\right)\right)\right) \tag{2.17}$$

$$= \frac{2}{\lambda}\ln\left(\cos\left(\underbrace{\frac{\lambda}{2}t}_{x:=}\right)\right)\underbrace{-\frac{2}{\lambda}\ln\left(\cos\left(\frac{\lambda}{2}\frac{d}{2}\right)\right)}_{c:=} \tag{2.18}$$

$$= \frac{2}{\lambda}\ln\left(\cos\left(x\right)\right) + c \tag{2.19}$$

Equation 2.17's *log-cosine-form* links our result to the analytic result of the MHS equation from [Low(1982)]. In Low's work, this shape of field lines was derived by deriving a solution for a coronal *arcade*. In our case, we derived this shape from our principles for a single plasma filament. Thus, the result of theorem 29 [**Low's Geodesics**] serve as a generalization of Low's solution. On top of that, this provides an important *validation* for our approach.

2.3   Discrete Magnetic Filaments

Time for some discretization! Up to now the entire theory was *smooth*, working with continuous objects only. We have prepared well for the upcoming transition, which in its
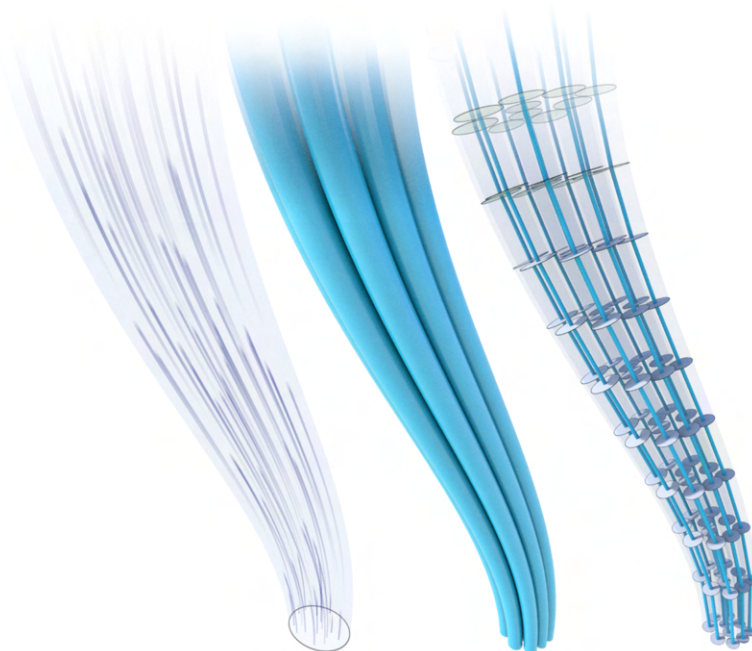
Figure 2.15: Discretization in a nutshell. A plasma state $(\mathbb{M}_{\mathbf{B}}, \mathbf{B})$ (left) is approximated by a finite collection of smooth magnetic filaments (middle) which are then represented by discrete curves with thickness (right).

basic feature will be the approximation of the flux domain $\mathbb{M}_{\mathbf{B}}$ through a collection of smooth magnetic filaments represented by discrete curves with thickness, as illustrated in figure 2.15. But first, we need to establish the no-overlap constraint.

2.3.1 Filaments Don't Overlap

In section 2.2 we extensively discussed smooth magnetic filaments which are defined by curves with variable cross-sectional radii. We also derived optimal conditions for the radii in theorem 23. However, this radii was only possible when the plasma-metric collapsed into the gas metric case, which is generally not the case. In fact, the gas metric is only relevant when the cross-sections do not overlap.

We motivate no-overlaping by the property that the filaments do not share the same points in $\mathbb{M}$. This is important due to the divergence-freeness of the magnetic field and the fact that we want to trace the magnetic field lines along the filaments in a well defined way. Let's establish what we mean by this in more detail.

Figure 2.16 illustrates the no-overlap constraint. The radii of two curves have to be limited to such an extent that the cross sections do not touch. The simplest, symmetrically fair way of doing so is to set the radii to half the distance to the other filament's center curve. We capture this as a definition, that also serves as an instruction on how to determine radii from a set of center curves Γ that guarantees no overlap.

<div align="center">unconstrained   constrained</div>
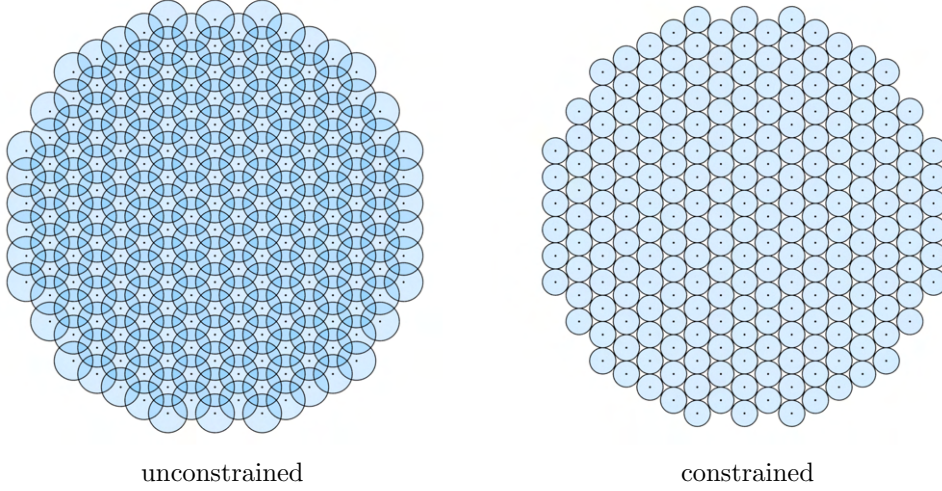
Figure 2.16: A slice of many filaments running in a parallel bundle. Left: the filaments if they were ignorant of each others. The magnetic filaments would overlap and the magnetic field becomes ill-defined at the overlap region. Right: the same filaments with the same flux and with a *no-overlap constraint*. The magnetic field is now more strongly concentrated and the magnetic field is well defined. Here, the radii are set to half the distance to their nearest neighbour.

Definition 30 (**Filament Radii, No Overlap Constraint**). Given a filament collection Γ of center curves (without raddi yet) and a flux parametrization $h > 0$, we define the local radii at $\gamma(s)$ of a center curve $\gamma \in \Gamma$ to be

$$r(s) := \min \left\{ \tfrac{1}{2}\mathrm{dist}(\gamma(s), \Gamma \setminus \gamma) \, , \, r_{\mathrm{opt}}(\gamma(s)) \right\}. \qquad (2.20)$$

Here, $\mathrm{dist}\,(\gamma(s), \Gamma \setminus \gamma)$ describes the minimum Euclidean distance between the point $\gamma(s)$ and all *other* center curves $\Gamma \setminus \gamma$. r_{opt} is directly taken from definition 25.

This definition *fulfils the no-overlap constraint by construction*. With it, no nieghbouring filament's cross sections can touch each other as their maximal expansion can only reach half the distance required to the other filament's center curves. The upper limit r_{opt} (definition 25) stems from the optimal radius as that is the energy minimum of a free (unconstrained) filament, and any further expansion would unnecessarily increase the MHS energy. r_{opt} is the maximum a filament can expand with its internal magnetic pressure $\frac{B^2}{2\mu_0}$ against the external gas pressure p.

Variable radii have important implications on the magnetic field magnitude B of the smooth magnetic filament. Given the flux h and the radius r, the magnetic field strength is approximately

$$B = \frac{\text{flux}}{\text{area}} = \frac{h}{2\pi r^2}$$

Given r_{opt}, we get a magnetic field strength that balances the gas-flux pressure equilibrium $p = \frac{B^2}{2\mu_0}$. If r decreases, B increases, and this will have an important effect on the plasma metric (definition 15) as it dependes on B. This will complicate things, but in a way that we will be able to handle later in section 2.4.

We can now begin the discretization with the flux domain $\mathbb{M}_{\mathbf{B}}$.
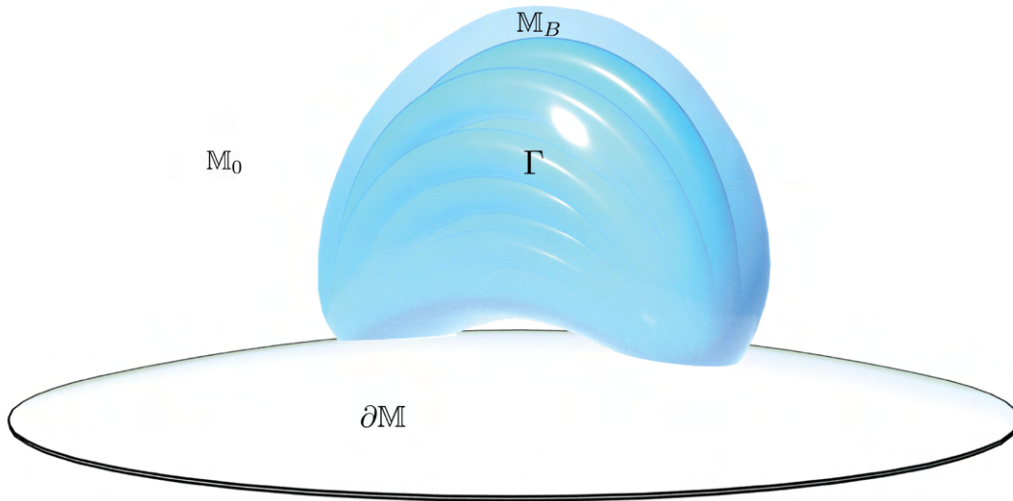

Figure 2.17: The core idea of the discretization. The plasma state $(\mathbb{M}_{\mathbf{B}}, \mathbf{B})$ is approximated by a collection of filaments Γ placed along the magnetic field lines. Each filament has the same amount of magnetic flux h. Tighter filaments with the same flux result in stronger fields.

2.3.2 Flux Domain $\mathbb{M}_{\mathbf{B}}$ to Smooth Magnetic Filaments Γ

The plasma state in the FFCS model is given by the flux domain $\mathbb{M}_{\mathbf{B}}$ together with a force-free magnetic field $\mathbf{B}$ inside of it which obeys the Neumann boundary flux condition Φ (definition 4). Until now this this theory has been handled in a smooth/continuous way. Time for discretization!

The discretization of the plasma state $(\mathbb{M}_{\mathbf{B}}, \mathbf{B})$ will now happen by a finite filament collection Γ, each with a fixed and equal magnetic flux h that serves as the discretization parameter. It determines how many smooth filaments are needed. A small h means that many weak filaments are deployed. A big h means that fewer, stronger filaments are deployed. The choice of h is equivalent to the choice of particle size in a Lagrangian fluid simulation. Smaller particles provide higher accuracy at the cost of computation and stability.

The choice of magnetic filaments as our discretization element should by no means be surprising. The solar magnetic field is fibred into areas of strong magnetic field, and the natural phenomena we are trying to model displays curve like features, as established in the solar physics review in section 1.2. Choosing filament as a modeling primitive is not uncommon. In the case of smoke rings and bubble rings, the underlying primitives used are vortex filaments that are structurally very similar [Angelidis and Neyret(2005)][Weißmann and Pinkall(2010)][Padilla et al.(2019)]. Hair and fur are modeled using curves too [Zhu et al.(2022)] and muscles too [Angles et al.(2019b)].

The discretization idea is displayed in figure 2.17. The core idea is as follows:

> *Replace the plasma state* $(\mathbb{M}_{\mathbf{B}}, \mathbf{B})$ *with a set of filaments* Γ *such that* $\mathbf{B}$ *is approximately preserved.*

In areas where $\mathbf{B}$ is stronger, the filaments become more abundant. They also become thinner in order avoid overlaps, which makes them sufficiently stronger in their $\mathbf{B}$ value. Figure 2.18 illustrates this process for various values of $h > 0$. The approximation is more accurate for smaller h.
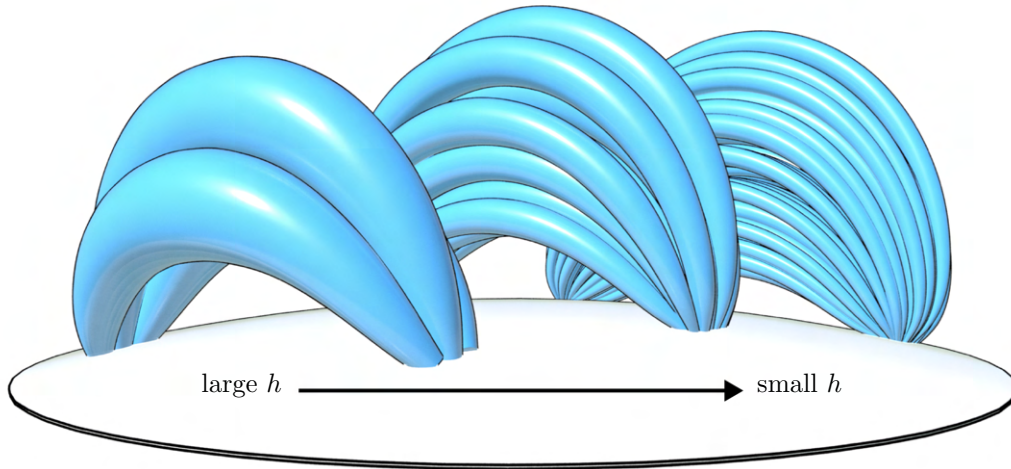
Figure 2.18: The discretization of the plasma state $(\mathbb{M}_{\mathbf{B}}, \mathbf{B})$ into filaments for various flux quantizations h. Smaller h leads to more filaments and higher accuracy at an increased computation cost. Left to right: decreasing value of h. The three bundles represent the same magnetic field at varying levels of detail determined by h.

Such a discretization is always possible. The guarantee comes from the divergence-freeness of any magnetic field $\mathbf{B}$. If the flux on the boundary $\partial \mathbb{M}$ is preserved, then any set of field lines expanding into $\mathbb{M}$ from the boundary preserve the flux along their entire path. A point $\mathbf{x} \in \mathbb{M}_{\mathbf{B}}$ belongs to a field line that touches the boundary $\Sigma_{\mathbf{B}}$ and is thus covered by some filament.

We will not provide a discretization approximation analysis due to the difficulty to quantify the efficacy of packing a space via circular tubes. We do however know that for sufficiently small h, the packing will be very dense and any magnetic field **B** in a finite domain $\mathbb{M}_\mathbf{B}$ will be well approximatable. We leave it to the validation section 3.3 to see that this approximation yields good results.

2.3.3 Discrete Magnetic Filaments

Until now every element we dealt with was smooth. It is time to switch to objects that computers can parse. Let us define the discrete analogue of the smooth magnetic filament.

> **Definition 31** (**Discrete Magnetic Filaments**). A *discrete magnetic filament* is a discrete curve of $n \in \mathbb{N}$ points $\gamma_1, \ldots, \gamma_n \in \mathbb{M}$ together with a radius on each point $r_1, \ldots, r_n \in \mathbb{R}_+$ and a flux parameter $h > 0$.
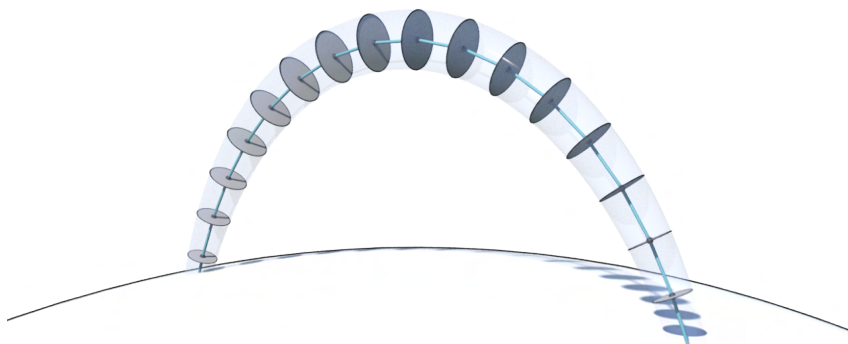

Figure 2.19: A discrete magnetic filament. It is represented by a discrete curve $\gamma_1, \ldots, \gamma_n \in \mathbb{M}$ with radii $r_1, \ldots, r_n \in \mathbb{R}_+$ and a constant flux $h > 0$. The magnetic field it represents runs tangentially along the curve.

Figure 2.19 shows a discrete filament and what it represents in detail. The magnetic field is always tangent to this discrete curve. During the later optimization we will have to update the curves and recompute the radii. This will be done exactly with the formula given in definition 30, which applies equally in the discrete setting

$$r_i := \min \left\{ \tfrac{1}{2} \mathrm{dist}(\gamma_i, \Gamma \setminus \gamma), \, r_{\mathrm{opt}}(\gamma_i) \right\}.$$

Figure 2.20 illustrates the difference the use of this formula makes rather than just using r_{opt}. In the discrete practice, we will compute the radius as performed in algorithm 1. That particular way of evaluating r_i guarantees no overlaps without actually giving the curves the

<div align="center">unconstrained   constrained</div>
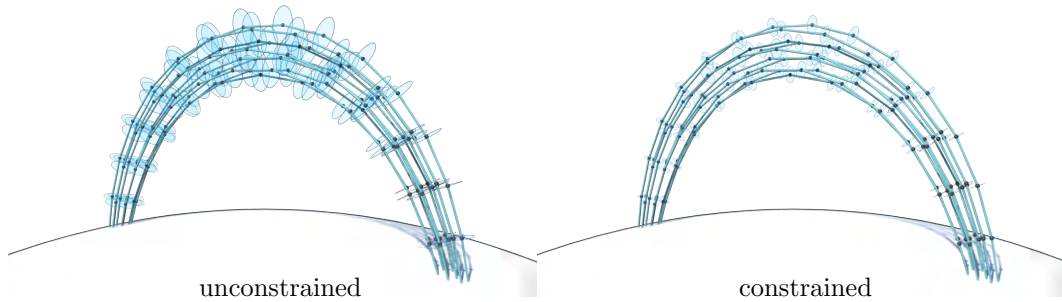
Figure 2.20: Left: A bundle of discrete magnetic filaments with $r \equiv r_{\text{opt}}$. The filaments naturally overlap. Right: The same bundle with the *no-overlap* constraint applied. No more overlapping. This concentrates the magnetic field more strongly in a smaller region.

biggest radii they could acquire. We argue that the slight difference between the maximally obtainable radii and the constrained r_i we compute does not matter much as the difference quickly dissipates away as the curves rearrange during optimization and gain roughly equal distances to each neighbouring curve. In practice, using a lot of curves we quickly reach a packing of the circular cross-sections that is roughly hexagonal, which is the optimal packing for circles.

Algorithm 1 ComputeRadius

Input: A point γ_i on a curve γ. The set of all curves Γ. Pressure function p.
Output: A radius r_i that is guaranteed to not overlap with any other filament.
  1: $P \leftarrow$ Closest point in $\Gamma \setminus \gamma$ of γ_i
  2: $d \leftarrow |P - \gamma_i|$
  3: $r_{\text{opt}} \leftarrow \frac{1}{\sqrt{2\pi}} \frac{\sqrt{h}}{\sqrt[4]{2\mu_0 p(\gamma_i)}}$
  4: $r_i \leftarrow \min\left\{ d/2, \ r_{\text{opt}} \right\}$

2.3.4   Discrete Energy and Length

How do we discretize the MHS energy $\mathcal{E}$ for discrete filaments? For that, we make direct use of theorem 26 [**Ideal Filaments Energy as Length**] giving us the energy of a smooth magnetic filament in terms of length in the plasma metric. As a reminder, the plasma metric $d\tilde{s}$ was given by the product of the Euclidean metric ds with a scalar function of p and B:

$$d\tilde{s} = e^u ds = \left(\frac{p}{B} + \frac{B}{2\mu_0} \right) ds.$$

Expressing the MHS Energy of a smooth magnetic filament is equivalent to expressing its

length in the plasma metric. We use the discrete notion of general metrics from [Luo(2004)] [Springborn et al.(2008)]. Let us define this properly:

Definition 32 (Discrete Metric). Given the conformal factor e^u, we define the *discrete metric* $d_u : \mathbb{M} \times \mathbb{M} \to \mathbb{R}$ as

$$d_u(\mathbf{x}, \mathbf{y}) := e^{\frac{u(\mathbf{x}) + u(\mathbf{y})}{2}} |\mathbf{x} - \mathbf{y}|$$

In the special Euclidean case $u \equiv 0$ we have the Euclidean metric and omit the subscript u

$$d(\mathbf{x}, \mathbf{y}) = |\mathbf{x} - \mathbf{y}|.$$

The discrete metric basically gives us the length between two points in $\mathbb{M}$. A closer look shows that the Euclidean edge lengths between two neighbouring points are multiplied by the geometric mean of the conformal factors of the two points. This notion is accurate when the conformal factor does not change much, *i.e.* when the points are close. We can now define the length for discrete curves by summing up distances of consecutive points.

Definition 33 (Discrete Conformal Length of γ). Given a discrete metric with the conformal factor e^u, the *discrete conformal length* for a discrete curve $\gamma = \gamma_1, \ldots, \gamma_n$ is given by

$$\mathscr{L}(\gamma) = \sum_{i=0}^{n-1} d_u(\gamma_i, \gamma_{i+1}). \tag{2.21}$$

In tandem with the smooth version's theorem 26 (**Ideal Filaments Energy as Length**) we define the discrete MHS energy.

Definition 34 (Discrete MHS Energy $\mathcal{E}(\gamma)$). The *MHS energy* $\mathcal{E}(\gamma)$ of a discrete magnetic filament γ and flux h is given by:

$$\mathcal{E}(\gamma) := h \mathscr{L}(\gamma)$$

We could from here on use the *energy* term $\mathcal{E}(\gamma)$ for the rest of the dissertation when describing the analysis and the algorithm, but we choose to continue to work with the *length* $\mathscr{L}(\gamma)$ because we are approaching the problems geometrically wherever we can, which makes our algorithm more intuitive. The results are equivalent as $h > 0$ is a uniformly fixed scalar factor and thus the minimization results are the same. For discrete curves with points $\gamma_1, \ldots, \gamma_n$, we introduce the shorthands

$$l_{i,i+1} := d(\mathbf{x}, \mathbf{y})$$
$$u_i := u(\gamma_i).$$

The discrete metric approximates the geodesic metric as $|\mathbf{x} - \mathbf{y}| \to 0$. Similarly, the discrete length of the curve approximates the smooth length of the curve as $|\gamma_{i+1} - \gamma_i| \to 0$ on the curve interior.

The most straight forward way to shorten a curve is by looking at the gradient of the discrete conformal length.

Lemma 35 (Gradient of $\mathscr{L}(\gamma)$). Deriving $\mathscr{L}$ by the Euclidean gradient with respect to the point γ_i on the interior of the curve γ yields

$$(\operatorname{grad}\mathscr{L}(\gamma))_i = \tfrac{1}{2}(\operatorname{grad} u)_i e^{\frac{u_i+u_{i+1}}{2}} l_{i,i+1} + e^{\frac{u_i+u_{i+1}}{2}} \frac{\gamma_i - \gamma_{i+1}}{l_{i,i+1}} +$$
$$\tfrac{1}{2}(\operatorname{grad} u)_i e^{\frac{u_i+u_{i-1}}{2}} l_{i,i-1} + e^{\frac{u_i+u_{i-1}}{2}} \frac{\gamma_i - \gamma_{i-1}}{l_{i,i-1}}$$

Proof. Straightforward calculus. Since γ_i is an interior point, there are only two consecutive terms in the sum that have γ_i and don't vanish when deriving by γ_i

$$(\operatorname{grad}\mathscr{L}(\gamma))_i = (\operatorname{grad} d_u(\gamma_{i-1},\gamma_i))_i + (\operatorname{grad} d_u(\gamma_i,\gamma_{i+1}))_i .$$

Since the pairs $i, i+1$ and $i, i-1$ are interchangeable, it suffices to only compute the derivative of one of these two terms.

$$\begin{aligned}(\operatorname{grad} d_u(\gamma_i,\gamma_{i+1}))_i &= \left(\operatorname{grad}\left(e^{\frac{u_i+u_{i+1}}{2}} l_{i,i+1}\right)\right)_i \\ &= \left(\operatorname{grad}\left(e^{\frac{u_i+u_{i+1}}{2}}\right)\right)_i l_{i,i+1} + e^{\frac{u_i+u_{i+1}}{2}} (\operatorname{grad}(l_{i,i+1}))_i \\ &= \tfrac{1}{2}(\operatorname{grad} u)_i e^{\frac{u_i+u_{i+1}}{2}} l_{i,i+1} + e^{\frac{u_i+u_{i-1}}{2}} \frac{\gamma_i - \gamma_{i-1}}{l_{i,i-1}}\end{aligned}$$

Replace $i+1$ with $i-1$ to receive the second term and sum them together to finish the proof.

$\square$

The above definition 33 [**Discrete Conformal Length of** γ] was written for general metrics. In our case, the logarithmic conformal factor expressed in theorem 18 [**Conformal Factor Splitting**] has to be inserted, making the expression a bit messy.

Keep in mind that this expression of length $\mathscr{L}$ in the plasma metric is equivalent to the magnetohydrostatic energy $\mathcal{E}$ of the smooth and discrete filament. Minimizing $\mathcal{E}$ is equivalent to minimizing $\mathscr{L}$, *i.e.* shortening curves.

2.4   Energy/Length Minimization

A look at the plasma metric in definition 15 shows that the plasma metric itself depends on the plasma state $(\mathbb{M}_{\mathbf{B}}, \mathbf{B})$ due to the appearance of B in the metric. For the discrete

filaments, the value of B is determined by the flux quantization constant h and the variable radii r. This will complicate things, as the radii will change during the energy minimization, thus changing **B** and the metric itself. Whatever minimization method is chosen, the plasma metric will have to be updated repeatedly.

2.4.1   Minimizing Length

We want to minimize the MHS energy $\mathcal{E}$ which is equivalent to the length $\mathscr{L}$ in the plasma metric (theorem 21). Thus, we can focus our attention on length minimizing strategies until we hit an extremum. The moment we hit an extremum, by theorem 11 [**MHS Solutions are MHS Energy Extrema**] we know that we have a valid solution of the MHS equation.

Where do we begin? In section 2.3 we established a discrete expression for the length $\mathscr{L}$ and its gradient $\operatorname{grad}\mathscr{L}$. Can we just directly solve $\operatorname{grad}\mathscr{L}(\gamma)_i = 0$? Unfortunately is analytically inaccessible. It is even locally difficult to solve analytically for γ_i as u_i depends on γ_i too and appears in an exponent.

The approach used in this dissertation will focus on a *quasi-Newton* approach to solve this equation iteratively[3]. The approach begins by choosing an interior point γ_i of the curve and writing down its gradient as seen in Lemma 35 and setting it to zero. Additionally, we highlight γ_i in red and it's dependent values u_i, $(\operatorname{grad} u)_i$, $l_{i,j}$ in blue.

$$(\operatorname{grad}\mathscr{L}(\gamma))_i \overset{!}{=} 0 = \tfrac{1}{2}(\operatorname{grad} u)_i e^{\frac{1}{2}u_i}e^{\frac{1}{2}u_{i+1}}l_{i,i+1} + e^{\frac{1}{2}u_i}e^{\frac{1}{2}u_{i+1}}\frac{1}{l_{i,i+1}}\left(\gamma_i - \gamma_{i+1}\right) + \quad (2.22)$$

$$\tfrac{1}{2}(\operatorname{grad} u)_i e^{\frac{1}{2}u_i}e^{\frac{1}{2}u_{i-1}}l_{i,i-1} + e^{\frac{1}{2}u_i}e^{\frac{1}{2}u_{i-1}}\frac{1}{l_{i,i-1}}\left(\gamma_i - \gamma_{i-1}\right) \quad (2.23)$$

Expressing u_i, $(\operatorname{grad} u)_i$, $l_{i,j}$ explicitly in terms of γ_i and solving for γ_i is impossible. To our rescue comes the *quasi-Newton* method with the following approach:

$$\text{Fix } u_i, \ (\operatorname{grad} u)_i, \ l_{i,j} \ \text{and solve only for } \gamma_i.$$

It does sound like a bad idea to solve an equation wrongly, but let's just wait and see what happens before judging. We can start by dropping all common factors $e^{\frac{1}{2}u_i}$ by dividing by them on both sides of the equation.

$$0 = \tfrac{1}{2}e^{\frac{1}{2}u_{i+1}}l_{i,i+1}(\operatorname{grad} u)_i + \frac{e^{\frac{1}{2}u_{i+1}}}{l_{i,i+1}}\left(\gamma_i - \gamma_{i+1}\right) + $$

$$\tfrac{1}{2}e^{\frac{1}{2}u_{i-1}}l_{i,i-1}(\operatorname{grad} u)_i + \frac{e^{\frac{1}{2}u_{i-1}}}{l_{i,i-1}}\left(\gamma_i - \gamma_{i-1}\right)$$

$$\Leftrightarrow 0 = \tfrac{1}{2}e^{\frac{1}{2}u_{i+1}}l_{i,i+1}(\operatorname{grad} u)_i + \frac{e^{\frac{1}{2}u_{i+1}}}{l_{i,i+1}}\gamma_i - \frac{e^{\frac{1}{2}u_{i+1}}}{l_{i,i+1}}\gamma_{i+1} + $$

$$\tfrac{1}{2}e^{\frac{1}{2}u_{i-1}}l_{i,i-1}(\operatorname{grad} u)_i + \frac{e^{\frac{1}{2}u_{i-1}}}{l_{i,i-1}}\gamma_i - \frac{e^{\frac{1}{2}u_{i-1}}}{l_{i,i-1}}\gamma_{i-1}$$

---

[3]Initially, we did not know the term *quasi-Newton method*. So at first we called it the *dirty direct method* because we solve the wrong equation repeatedly until we converge to a true solution

$$\Leftrightarrow -\left(\frac{e^{\frac{1}{2}u_{i+1}}}{l_{i,i+1}} + \frac{e^{\frac{1}{2}u_{i-1}}}{l_{i,i-1}}\right)\gamma_i = \frac{1}{2}e^{\frac{1}{2}u_{i+1}}l_{i,i+1}(\operatorname{grad} u)_i - \frac{e^{\frac{1}{2}u_{i+1}}}{l_{i,i+1}}\gamma_{i+1} +$$

$$\frac{1}{2}e^{\frac{1}{2}u_{i-1}}l_{i,i-1}(\operatorname{grad} u)_i - \frac{e^{\frac{1}{2}u_{i-1}}}{l_{i,i-1}}\gamma_{i-1}$$

$$\Leftrightarrow \left(e^{\frac{1}{2}u_{i+1}}l_{i,i-1} + e^{\frac{1}{2}u_{i-1}}l_{i,i+1}\right)\gamma_i = -\frac{1}{2}e^{\frac{1}{2}u_{i+1}}l_{i,i-1}l_{i,i+1}^2(\operatorname{grad} u)_i + e^{\frac{1}{2}u_{i-1}}l_{i,i+1}\gamma_{i-1} +$$

$$-\frac{1}{2}e^{\frac{1}{2}u_{i-1}}l_{i,i+1}l_{i,i-1}^2(\operatorname{grad} u)_i + e^{\frac{1}{2}u_{i+1}}l_{i,i-1}\gamma_{i+1}$$

$$\Leftrightarrow \gamma_i = -\frac{1}{2}\underbrace{\left(\frac{e^{\frac{1}{2}u_{i+1}}l_{i,i-1}}{e^{\frac{1}{2}u_{i+1}}l_{i,i-1}+e^{\frac{1}{2}u_{i-1}}l_{i,i+1}}\right)}_{\omega_+:=}l_{i,i+1}^2(\operatorname{grad} u)_i - \frac{1}{2}\underbrace{\left(\frac{e^{\frac{1}{2}u_{i-1}}l_{i,i+1}}{e^{\frac{1}{2}u_{i+1}}l_{i,i-1}+e^{\frac{1}{2}u_{i-1}}l_{i,i+1}}\right)}_{\omega_-:=}l_{i,i-1}^2(\operatorname{grad} u)_i$$

$$+ \underbrace{\left(\frac{e^{\frac{1}{2}u_{i-1}}l_{i,i+1}}{e^{\frac{1}{2}u_{i+1}}l_{i,i-1}+e^{\frac{1}{2}u_{i-1}}l_{i,i+1}}\right)}_{\omega_-:=}\gamma_{i-1} + \underbrace{\left(\frac{e^{\frac{1}{2}u_{i+1}}l_{i,i-1}}{e^{\frac{1}{2}u_{i+1}}l_{i,i-1}+e^{\frac{1}{2}u_{i-1}}l_{i,i+1}}\right)}_{\omega_+:=}\gamma_{i+1}$$

$$\Leftrightarrow \gamma_i = \omega_-\gamma_{i-1} + \omega_+\gamma_{i+1} - \frac{1}{2}\left(\omega_-l_{i,i-1}^2 + \omega_+l_{i,i+1}^2\right)(\operatorname{grad} u)_i$$

Notice that $\omega_- + \omega_+ \equiv 1$ always and $\omega_-, \omega_+ > 0$. Essentially, $\omega_\pm$ are weights. What we get is not a correct solution to the problem, as the blue terms depend on γ_i. What we rather get is an update rule for an iterative scheme with some interesting interpretation

$$\gamma_i^{\text{new}} \leftarrow \underbrace{\omega_-\gamma_{i-1} + \omega_+\gamma_{i+1}}_{\text{weigthed midpoint}} - \underbrace{\frac{1}{2}\left(\omega_-l_{i,i-1}^2 + \omega_+l_{i,i+1}^2\right)(\operatorname{grad} u)_i}_{\text{gradient correction}}. \tag{2.24}$$

The sneaky thing about turning this derivation into an update rule (equation 2.24) is that if this iteration converges, *i.e.*it reaches a fix-point γ_i, then γ_i *will solve the equation 2.22 fully*, and thus we found a local extremum for the length between the points $\gamma_{i-1}, \gamma_i, \gamma_{i+1}$ when adjusting γ_i.

$$\gamma_i^{\text{new}} = \omega_-\gamma_{i-1} + \omega_+\gamma_{i+1} - \frac{1}{2}\left(\omega_-l_{i,i-1}^2 + \omega_+l_{i,i+1}^2\right)(\operatorname{grad} u)_i$$
$$\Leftrightarrow (\operatorname{grad}\mathscr{L}(\gamma))_i = 0$$

In a nutshell, we are performing repeated updates locally, fixing two points and trying to move the one in the middle to be locally more geodesic than before. This is depicted in figure 2.21.

The update rule 2.24 performs an energy minimization on a single point relative to its
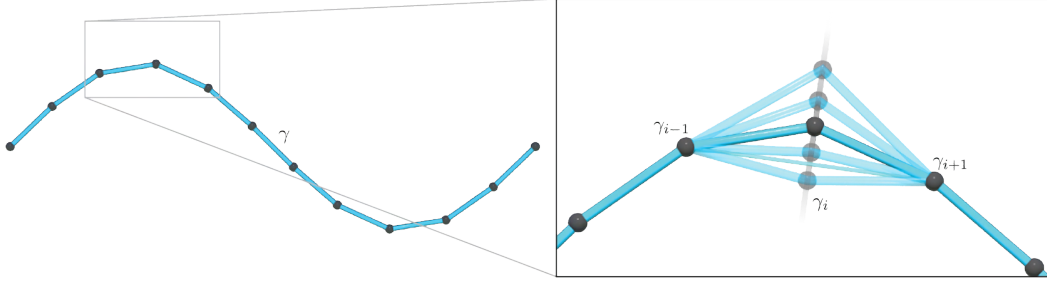
Figure 2.21: The quasi-Newton method we use to locally optimize for geodesy. Left: The input is a discrete curve γ. Right: we locally fix the two points $\gamma_{i-1}, \gamma_{i+1}$ and adjust the position of γ_i such that the 3 points together are shorter than before according to their discrete metric. We iterate this method for all interior points until convergence.

neighbours. In order to minimize the energy of the entire curve we perform the same update rule on all interior points repeatedly until convergence. Let's define this:

Definition 36 (**Quasi-Newton Method for Geodesics**). Given a discrete metric with conformal factor e^u and a discrete curve $\gamma_1, \ldots, \gamma_n$ with fixed endpoints, the *quasi-Newton method* to reduce the length of the curves is as follows:

- for each $i \in \{2, \ldots, n-1\}$

    1. compute u_{i-1}, u_i, u_{i+1}, $l_{i,i-1}$, $l_{i,i+1}$, $(\operatorname{grad} u)_i$ with the current values of γ.
    2. compute the weights

    $$\omega_- := \frac{e^{\frac{1}{2} u_{i-1}} l_{i,i+1}}{e^{\frac{1}{2} u_{i+1}} l_{i,i-1} + e^{\frac{1}{2} u_{i-1}} l_{i,i+1}} \text{ and } \omega_+ := \frac{e^{\frac{1}{2} u_{i+1}} l_{i,i-1}}{e^{\frac{1}{2} u_{i+1}} l_{i,i-1} + e^{\frac{1}{2} u_{i-1}} l_{i,i+1}}.$$

    3. apply the update rule

    $$\gamma_i^{\text{new}} \leftarrow \ \omega_- \gamma_{i-1} + \omega_+ \gamma_{i+1} - \tfrac{1}{2} \left(\omega_- l_{i,i-1}^2 + \omega_+ l_{i,i+1}^2 \right) (\operatorname{grad} u)_i.$$

- Repeat the above step until convergence.

At this point, an apology is due. The paper *Filament Based Plasma* [Padilla et al.(2022)] has an error in the appendix describing the above formula. The weights $\omega_\pm$ equation (23) on page 14 in the paper are missing the $\frac{1}{2}$ factors in the exponent. The code in the supplement material of that publication did not miss this factor.

Algorithm 2 [**CurveShorteningStep**] represents a single quasi-Newton step from definition 36 in pseudo code form. Algorithm 3 [**CurveShorteningFlow**] then repeatedly applies these steps until convergence on a whole discrete curve γ. This is the form it is used for all the upcoming examples in section 2.4.2 [Examples of Length Minimizations].

Algorithm 2 CurveShorteningStep

Input: Three adjacent points $\gamma_{i-1}, \gamma_i, \gamma_{i+1}$ on a curve. A logarithmic conformal factor u function.

Output: γ_i position update with lower length $\mathscr{L}$ according to the metric $e^u ds$.

1: compute u_{i-1}, u_i, u_{i+1}, $l_{i,i-1}$, $l_{i,i+1}$, $(\operatorname{grad} u)_i$

2: compute ω_-, ω_+

3: $\gamma_i \leftarrow \ \omega_- \gamma_{i-1} + \omega_+ \gamma_{i+1} - \frac{1}{2} \left(\omega_- l_{i,i-1}^2 + \omega_+ l_{i,i+1}^2 \right) (\operatorname{grad} u)_i$

Algorithm 3 CurveShorteningFlow

Input: Initial discrete curve $\gamma = \gamma_1, \ldots, \gamma_n$, logarithmic conformal factor u.

Output: A discrete curve $\gamma_1, \ldots, \gamma_n$ with extremal lower length $\mathscr{L}$ according to the metric $e^u ds$, if convergent.

1: **while** not converged **do**

2:     **for each** $i \in \{2, \ldots, n-1\}$ in parallel **do**

3:         $\gamma_i \leftarrow$ CurveShorteningStep$(\gamma_{i-1}, \gamma_i, \gamma_{i+1}, u)$.

4:     **end for**

5: **end while**

About the Quasi-Newton Method

Can we say something about the convergence of the quasi-Newton method for geodesics? In equation 2.24 we saw that the update rule can be split into a *weighted midpoint* part and a *gradient correction* part. We discuss them separately

- **Weighted midpoint part:**

$$\omega_- \gamma_{i-1} + \omega_+ \gamma_{i+1}$$

  By the definition of the weights $\omega_\pm$, the midpoint part will forever be on the line segment between the adjacent points. Therefore, the midpoint part is stable. Also, for uniformly sampled curves ($l_{i,i-1} = l_{i,i-1}$) with increasing resolution the values of u_{i-1}, u_{i+1} approach each other and thus $\omega_\pm \to \frac{1}{2}$.

- **Gradient correction part:**

$$-\frac{1}{2} \left(\omega_- l_{i,i-1}^2 + \omega_+ l_{i,i+1}^2 \right) (\operatorname{grad} u)_i$$

  The behaviour of this term is more dependent on the curve resolution. $(\operatorname{grad} u)_i$ is locally bounded in a well defined metric, and the magnitude of this part can be reduced by selecting a curve resolution fine enough that compensates the magnitude of $(\operatorname{grad} u)_i$. This can make the gradient correction part arbitrarily small and thus stable. The gradient term points in the direction of lower values of u, in an attempt to move the curve to a place where the "*length cost*" is reduced.

So given a high enough curve resolution, the quasi-Newton method seems stable. However, the higher the resolution the slower the convergence will be. Evidently, the information only travels between neighbours at each iteration. Its convergence behaviour is therefore similarly slow as that of a 1 dimensional heat flow with local averaging.

In practice, the component of the update that is parallel to the line segment connecting γ_{i-1} and γ_{i+1} is worthless to track, as changes along the tangential direction do not change the curve's shape and disappear by reparametrization. Actually, poor sampling of the curve can even cause numerical instabilities by distributing points very unevenly. This will be addressed in algorithm 5 [**Energy Minimization**] in section 2.4.4 where the curves are evenly resampled regularly.

Note also that in the process of length minimization, scaling a conformal factor globally won't change the geodesics. This is because the weighted midpoint and gradient correction part remain invariant. If we scale the conformal factor by a constant A, $e^u \leftarrow Ae^u$, then the logarithmic conformal will transform as $u \to u + \ln(A)$. One can then easily see that the new term cancelled out in the computation of $\omega_\pm$ and adds nothing to the gradient.

2.4.2 Examples of Length Minimizations

To evaluate the quasi-Newton method for minimizing the energy/length we take a look at examples where the solutions are known. In our case we will look at the Euclidean plane, the hyperbolic Poincaré-disc, the Poincaré half-plane model and the gas metric geodesics as seen in theorem 27 in section 2.2.3 [Ideal Magnetic Filaments: The Minimizing Shape].

Euclidean Geodesics

$$u : \mathbb{R}^3 \to \mathbb{R}$$
$$u(\mathbf{x}) = 0$$
$$(\operatorname{grad} u)(\mathbf{x}) = \mathbf{0}$$

This is the most trivial case. All geodesics are straight lines. The update rule collapses to a local averaging of the position values $\gamma_i^{\text{new}} \leftarrow \frac{1}{2}\gamma_{i-1} + \frac{1}{2}\gamma_{i+1}$. Figure 2.22 displays an example of the flow.
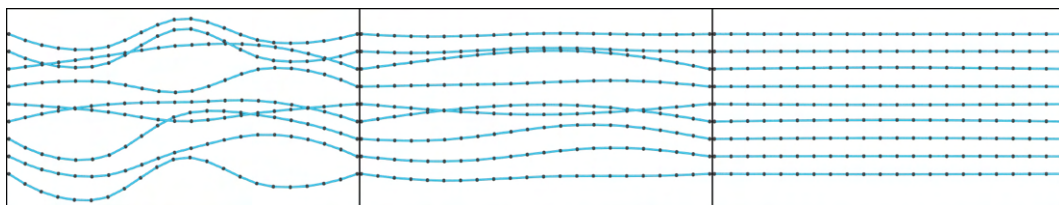

Figure 2.22: The quasi-Newton method for length shortening applied on a set of wavy curves in an Euclidean metric in $\mathbb{R}^2$. Left to right: After a few iterations, the curves become Euclidean geodesics: straight lines.

Poincaré-Disc Model Geodesics

$$u : \mathbb{D} \to \mathbb{R}$$

$$u(\mathbf{x}) = \ln(2) - \ln\left(1 - |\mathbf{x}|^2\right)$$

$$(\operatorname{grad} u)(\mathbf{x}) = \frac{2}{|1-|\mathbf{x}|^2|}\mathbf{x}$$

Poincaré-disc geodesics are known to be arcs of circles that intersect the unit disc orthogonally. Figure 2.23 shows how this shape is reproduced when the endpoints are held near the unit circle. To show the robustness of this algorithm, we initialized the curves with an suboptimal arrangement.
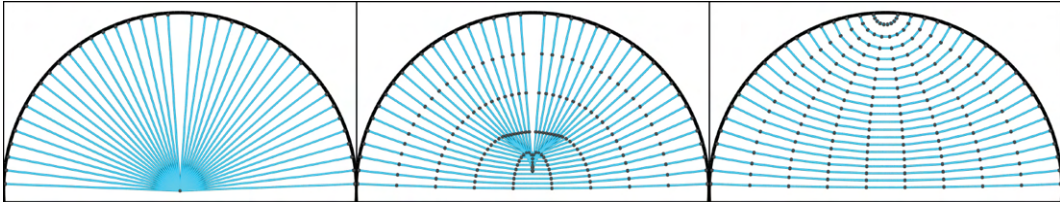

Figure 2.23: The quasi-Newton method for length shortening applied on a set of suboptimally initialized curves in the Poincaré-disc metric. Left to right: After a few iterations, the curves become Poincaré geodesics: arcs of circles intersecting the unit disc orthogonally.

Poincaré Half-Plane Model Geodesics

$$u : \mathbb{R}^2_{y>0} \to \mathbb{R}$$

$$u(\mathbf{x}) = -\ln\langle \mathbf{x}, e_2 \rangle$$

$$(\operatorname{grad} u)(\mathbf{x}) = -\frac{1}{\langle \mathbf{x}, e_2 \rangle}e_2\mathbf{x}$$

Poincaré half-plane geodesics are known to be arcs of circles that intersect the x-axis orthogonally. Figure 2.24 shows how this shape is reproduced when the endpoints are held slightly above the x-axis. To show the robustness of this algorithm, we initialized the curves with a subpar arrangement.

Gas Metric Geodesics For Polynomial Pressure Model

$$u : \mathbb{M} \to \mathbb{R}$$

$$u(\mathbf{x}) = -\ln\sqrt{\frac{2p}{\mu_0}}$$

$$(\operatorname{grad} u)(\mathbf{x}) = -\frac{1}{2p}\operatorname{grad} p$$

To which we insert $p(\mathbf{x}) = p_0 \left(\frac{|\mathbf{x}|}{r_\odot}\right)^{-\lambda}$, giving us
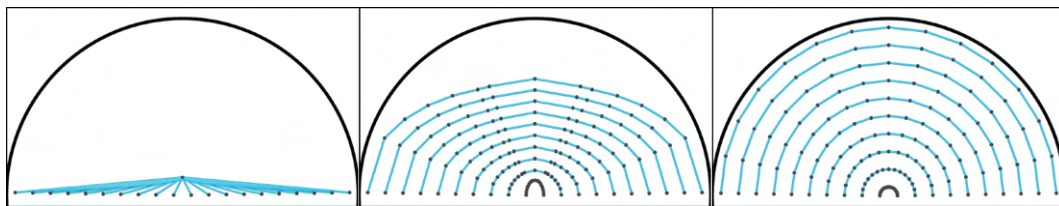
Figure 2.24: The quasi-Newton method for length shortening applied on a set of subparly initialized curves in the Poincaré half-plane metric. Left to right: After a few iterations, the curves become Poincaré half-plane geodesics: half circles intersection the x-axis orthogonally.

$$u(\mathbf{x}) = -\tfrac{\lambda}{2} \ln \left(\sqrt{\tfrac{2p_0}{\mu_0}} \tfrac{|\mathbf{x}|}{r_\odot} \right) \tag{2.25}$$

$$(\operatorname{grad} u)(\mathbf{x}) = -\tfrac{\lambda}{2} \tfrac{\mathbf{x}}{|\mathbf{x}|^2}. \tag{2.26}$$

The gas metric (definition 19) geodesics for the polynomial pressure model where derived in theorem 27 and shown in figure 2.10. Figure 2.25 shows how these shapes are reproduced by the quasi-Newton method. To show the robustness of this algorithm, we initialized the curves with a bad arrangement.
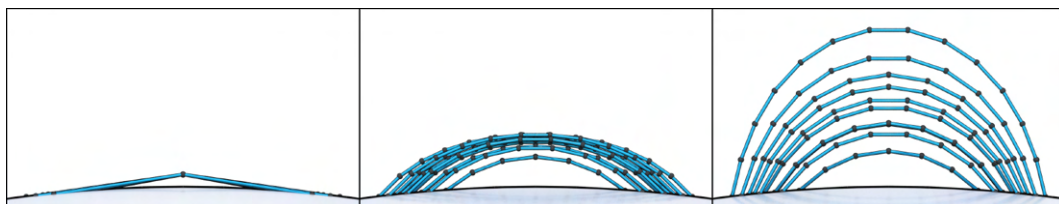

Figure 2.25: The quasi-Newton method for length shortening applied on a set of badly initialized curves in the gas metric from definition 19. Left to right: After a few iterations, the curves become plasma metric geodesics: the exact parametrization which was analytically derived in theorem 27.

The geodesics examples above give us good validation that the quasi-Newton length minimizing scheme does its job well while also verifying that the analytic geodesics we derived were true. In order to apply this scheme to the full plasma metric (definition 15) we need to explicitly compute $u = u_{\text{gas}} + u_{\text{mag}}$ and its gradient first.

2.4.3 Computing the Plasma Metric and its Gradient

For the energy minimization of the quasi-Newton method we need to insert the logarithmic conformal factor and its gradient into the formula of definition 36. In this section, we will specify how we compute these values for the plasma metric, the essential metric to solve the MHS equation as established in section 2.1.2. The conformal factor is written as

$$d\tilde{s} = e^u ds = \left(\frac{p}{|\mathbf{B}|} + \frac{|\mathbf{B}|}{2\mu_0} \right) ds = \sqrt{\frac{2p}{\mu_0}} \left(1 + \frac{(|\mathbf{B}| - \sqrt{2\mu_0 p})^2}{2|\mathbf{B}|\sqrt{2\mu_0 p}} \right) ds. \tag{2.27}$$

Theorem 18 [**Conformal Factor Splitting**] then showed us that we can also split the logarithmic conformal factor into two parts:

$$u = u_{\mathrm{gas}} + u_{\mathrm{mag}}$$

$$u_{\mathrm{gas}} := \ln \left(\sqrt{\frac{2p}{\mu_0}} \right)$$

$$u_{\mathrm{mag}} := \ln \left(1 + \frac{(|\mathbf{B}| - \sqrt{2\mu_0 p})^2}{2|\mathbf{B}|\sqrt{2\mu_0 p}} \right).$$

We can thus focus on computing u_{gas}, $\mathrm{grad}\, u_{\mathrm{gas}}$, u_{mag} and $\mathrm{grad}\, u_{\mathrm{mag}}$ separately.

Computing $u_{\mathbf{gas}}$ and $\mathrm{grad}\, u_{\mathbf{gas}}$

This was already done in section 2.4.2 equation 2.25. The gas metric is the special case when $u = u_{\mathrm{gas}}$, $u_{\mathrm{mag}} = 0$ (definition 19). Given the polynomial pressure model we obtain the following:

$$u_{\mathrm{gas}}(\mathbf{x}) = -\frac{\lambda}{2} \ln \left(\sqrt{\frac{2p_0}{\mu_0}} \frac{|\mathbf{x}|}{r_\odot} \right) \tag{2.28}$$

$$(\mathrm{grad}\, u_{\mathrm{gas}})(\mathbf{x}) = -\frac{\lambda}{2} \frac{\mathbf{x}}{|\mathbf{x}|^2}. \tag{2.29}$$

To compute the gas metric's logarithmic conformal factor u_{gas} and its gradient $\mathrm{grad}\, u_{\mathrm{gas}}$ for a discrete magnetic filament at a point $\gamma_i \in \mathbb{M}$, we only have to insert γ_i into the above equation. Once our filament configuration is updated in a step of the energy minimization, we have to recompute these values at every point because the point positions γ_i have been updated. The u_{gas} part of the plasma metric $u = u_{\mathrm{gas}} + u_{\mathrm{mag}}$ is *a function of space*. It does not depend on other filaments of the configuration Γ.

Computing $u_{\mathbf{mag}}$ and $\mathrm{grad}\, u_{\mathbf{mag}}$

Here things get trickier. u_{mag} has a dependence on B which is ever changing with the filament configuration Γ. This is due to the varying radii r_i in the no overlap constraint (definition 30). Given a constant flux h we have

$$B_i = \frac{h}{2\pi r_i^2}.$$

Thus, the u_{mag} part of the plasma metric $u = u_{\mathrm{gas}} + u_{\mathrm{mag}}$ is *not a function of space* only, after every step of the energy minimizing algorithm we have to recompute this part of

the metric by looking at all filaments Γ. We recompute the radii r_i at each point of the filaments, as in definition 30, and then compute B_i through the given flux h and can then plug this B_i together with the computed gas pressure $p_i = p(\gamma_i)$ into the formula for u_{mag}:

$$(u_{\text{mag}})_i = \log\left(1 + \frac{\left(B_i - \sqrt{2\mu_0 p_i}\right)^2}{2B_i\sqrt{2\mu_0 p_i}}\right). \tag{2.30}$$

Now we need the gradient of u_{mag}, so we simply take the derivative of this, right? There is a problem! In the discrete setting we have no analytic expression for the gradient of B because it is constant along the cross section of each filament and then drops to zero at the filament boundary. For discrete magnetic filaments, $(u_{\text{mag}})_i$ is not a smooth function and we can't really compute $(\text{grad}\, u_{\text{mag}})_i$, or can we?

To overcome this issue, we make use of a sampling technique to approximate the gradient. Under ideal conditions with infinite infinitesimal filaments this would result in an accurate solution if sampled enough in direct vicinity of where we evaluate $\text{grad}\, u_{\text{mag}}$. With a finite amount of filaments, we sample values $(u_{\text{mag}})_j$ of neighbouring filaments and estimate the gradient in the following way:

$$(\text{grad}\, u_{\text{mag}})_i \approx \frac{1}{|\mathcal{N}(\gamma_i)|} \sum_{\gamma_j \in \mathcal{N}(\gamma_i)} \left((u_{\text{mag}})_j - (u_{\text{mag}})_i\right) \frac{\gamma_j - \gamma_i}{|\gamma_j - \gamma_i|^2}. \tag{2.31}$$

Here, $\mathcal{N}(\gamma_i)$ is a set of points in the vicinity of γ_i that are not on the same curve. In the implementation, we searched for the 100 closest points in a $10r_i$ radius around γ_i. These search parameters are arbitrary as they depend on the resolution of the curves and the number of filaments. The choice of $\mathcal{N}$ and the weights used in the averaging in equation 2.31 resemble a constant averaging scheme.

Reducing Bias of $\text{grad}\, u_{\text{mag}}$ Computation

Sampling u_{mag} where nearby filaments are creates a bias in the direction of present filaments in equation 2.31. This will be a problem for filaments at the boundary of a bundle. Identifying which filaments are on the boundary is a difficult task, so we propose an approach that does not require us to identify this.

For each γ_i we search for neighbouring points γ_j. Now, for each neighbouring point γ_j we will assume the existence of a *virtual point* γ_{ij}^v on the exact opposite side of γ_j

$$\gamma_{ij}^v := \gamma_i - 2(\gamma_j - \gamma_i). \tag{2.32}$$

This virtual point will represent a discrete magnetic filament that is *out in the open*, meaning that it has full spatial extension

$$r_{ij}^v := r_{\text{opt}}.$$

By doing so, it represents the contribution of the exterior gas onto the filament. The effect of the gas pushing into the domain $\mathbb{M}_{\mathbf{B}}$ is captured by this virtual point. The virtual point is then sampled for our sum like any other point into equation 2.31. This process will only really make a difference for filaments at the boundary. For inner filaments, this extra sum will cancel out in all directions. This reduces the bias at the boundary that is present in the absence of these virtual points. Interestingly, setting $r_{ij}^v = r_{\text{opt}}$ also results in $(u_{\text{mag}})_{ij}^v = 0$, which eases the computation a bit in the section 2.4.4.

Summary of Plasma Metric Computation

In our experience, as demonstrated in part 3 of this dissertation, our way of computing the plasma metric and in particular u_{mag} and $\operatorname{grad} u_{\text{mag}}$ is sufficient. We do however admit the lack of mathematical rigour here regarding $\operatorname{grad} u_{\text{mag}}$. A value that is not accessible in the discretization is being approximated by a smoothed out version. We assume that the resulting gradient direction is correct, but we can't really make any statement about its magnitude because we have nothing to compare its quality to.

We capture the computation of $\operatorname{grad} u$ of the plasma metric in algorithm 4 [**ComputePlasmaMetric**].

Algorithm 4 ComputePlasmaMetric

Input: A point γ_i on a curve γ. The set of all curves Γ. A pressure function p.
Output: u_i and $(\operatorname{grad} u)_i$ for each point.
1: **for each** point index i in parallel **do**
2:     $p_i \leftarrow p(\gamma_i)$
3:     $u_{\text{gas}} \leftarrow \ln\left(\sqrt{\frac{2p_i}{\mu_0}}\right)$
4:     $(\operatorname{grad} u_{\text{gas}})_i \leftarrow -\frac{\lambda}{2}\frac{\gamma_i}{|\gamma_i|^2}$ ▷ equation 2.28.
5:     $r_i \leftarrow \text{ComputeRadius}(\gamma_i, \Gamma, p_i)$ ▷ algorithm 1.
6:     $B_i \leftarrow \frac{h}{2\pi r_i^2}$
7:     $(u_{\text{mag}})_i \leftarrow \log\left(1 + \frac{\left(B_i - \sqrt{2\mu_0 p_i}\right)^2}{2B_i\sqrt{2\mu_0 p_i}}\right)$ ▷ equation 2.30
8:     $\mathcal{N}_i \leftarrow$ point indices of neighbours $\Gamma \setminus \gamma$ in a $10 \cdot r_i$ search radius around γ_i.
9: **end for**
10: **for each** point index i in parallel **do**
11:     $(\operatorname{grad} u_{\text{mag}})_i \leftarrow 0$
12:     **for each** $j \in \mathcal{N}_i$ **do**
13:         $(\operatorname{grad} u_{\text{mag}})_i \leftarrow (\operatorname{grad} u_{\text{mag}})_i + \frac{1}{|\mathcal{N}_i|}\left((u_{\text{mag}})_j - (u_{\text{mag}})_i\right)\frac{\gamma_j - \gamma_i}{|\gamma_j - \gamma_i|^2}$ ▷ equation 2.31.
14:         $\gamma_{ij}^v \leftarrow \gamma_i - 2(\gamma_j - \gamma_i)$ ▷ equation 2.32.
15:         $(\operatorname{grad} u_{\text{mag}})_i \leftarrow (\operatorname{grad} u_{\text{mag}})_i + \frac{1}{|\mathcal{N}_i|}\left(0 - (u_{\text{mag}})_i\right)\frac{\gamma_{ij}^v - \gamma_i}{|\gamma_{ij}^v - \gamma_i|^2}$
16:     **end for**
17:     $u_i \leftarrow (u_{\text{gas}})_i + (u_{\text{mag}})_i$
18:     $(\operatorname{grad} u)_i \leftarrow (\operatorname{grad} u_{\text{gas}})_i + (\operatorname{grad} u_{\text{mag}})_i$
19: **end for**

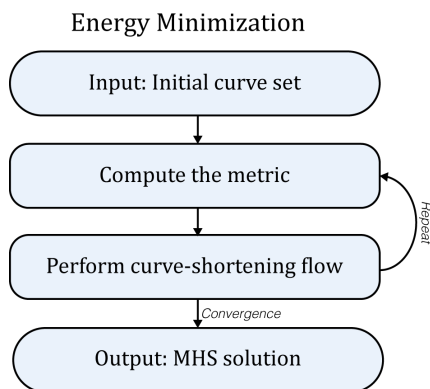### 2.4.4 Final Energy Minimization Algorithm

Figure 2.26: The energy minimization algorithm in a nutshell. An initial set of curves is the input. We loop the plasma metric computation at the points of each curve and then shorten these accordingly. Once we converge sufficiently, we exit the loop as the output.

It is time to set up the energy minimizing algorithm. The previous chapters were all about setting up the necessary computations for this moment. Algorithm 5 [**Energy Minimization**] (and figure 2.26) combines everything in a while loop that continues until sufficient convergence. We evenly resample the curves regularly in order to avoid numerical issues when the points on the curve are unevenly distributed.

Algorithm 5 Energy Minimization

Input: Initial curve set Γ, pressure function p, flux quantization h.
Output: Γ with a local extrema MHS energy $\mathcal{E}$.

 1: **while** not converged **do**
 2:     **for each** $\gamma \in \Gamma$ in parallel **do**
 3:         **for each** index i on γ in parallel **do**
 4:             $u_i, (\text{grad } u)_i \leftarrow \text{COMPUTEPLASMAMETRIC}(\gamma_i, \gamma, \Gamma, p);$ ▷ section 2.4.3.
 5:             $\gamma_i \leftarrow \text{CURVESHORTENINGSTEP}(\gamma_{i-1}, \gamma_i, \gamma_{i+1}, u);$ ▷ section 2.4.
 6:         **end for**
 7:         $\gamma \leftarrow \text{RESAMPLE}(\gamma);$
 8:     **end for**
 9: **end while**

The resulting configuration of discrete magnetic filaments then represents the magnetic field which solves the MHS equation. Figure 2.27 shows a set of discrete magnetic filament bundles and their radii minimizing their energy at increasing magnetic flux h per filament.

This completes the main algorithm for the computation of the MHS equation solutions in this dissertation. Until now, we have however neglected the question of initialization, the initial topological input used in the algorithm. We will focus on this in the next section.
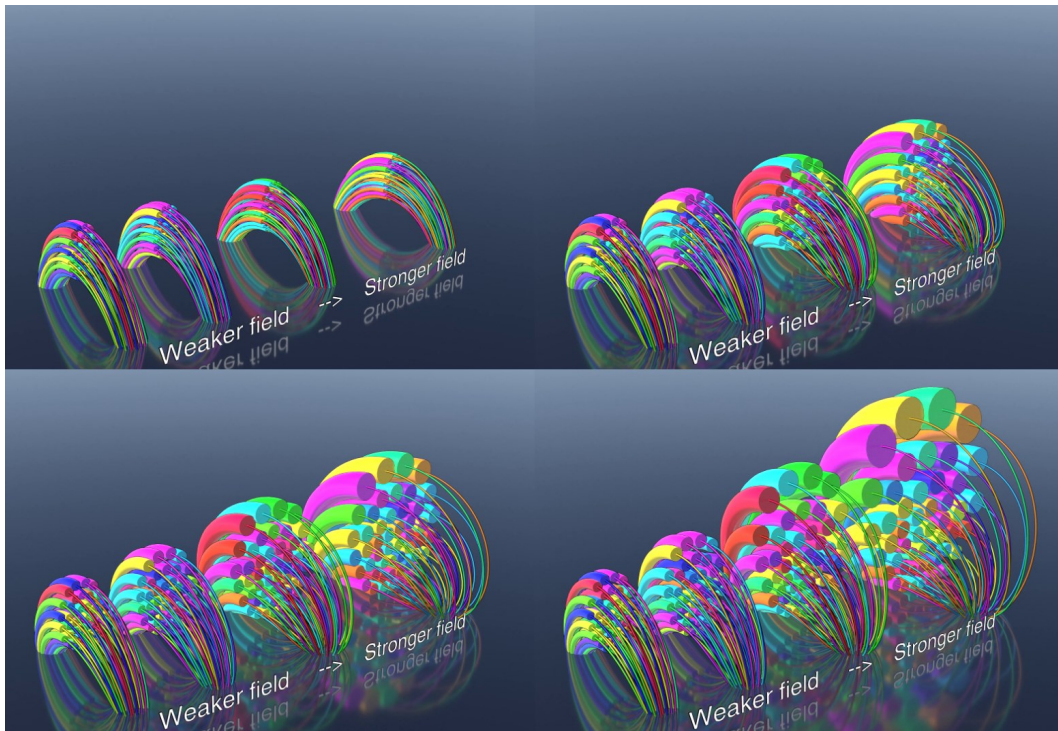
Figure 2.27: The energy minimization algorithm 5 [**Energy Minimization**] in action. Multiple bundles of varying magnetic field strength (h increasing from left to right) are used as initial input. The energy minimization progressively shortens the curves in the h dependent plasma metric. The no-overlap constraint amplifies the magnetic field B, which then changes the metric. (Sequence: left to right, top to bottom). Without the no-overlap constraint all geodesic would have the shape of the left most bundle while the tubes are significantly thicker for increasing h. The filament colors were randomly assigned for visibility.

2.5   Initial Curves from Flux Density

As brought forth in section 1.6, the topology of the magnetic field in the plasmatic setting is invariant. In the ideal MHD setting, the frozen **B**-field theorem 8 showed us that **B** is just transported by the gas. So any volumetric representation of the magnetic field **B** would also preserve its topology in an ideal MHD simulation unless lost by numerical dissipation.

In our case, using our magnetic filaments, the established constraint that filaments don't overlap (see section 2.3.1) perfectly prevents topological changes. We guarantee the preservation of the topology by limiting the updates of each filament to not move beyond their respective radii in a single step in algorithm 2 [**CurveShorteningStep**].

This also means that whatever topology is chosen as input to our MHS energy minimization algorithm 5, that exact topology is maintained in the final solution. What initial topology should we select and how reasonable would that selection be? And on top of that, how do we convert magnetic surface flux data of the sun into a discrete filament compatible representation?

We will begin by stippling the continuous magnetic surface flux data into a discrete representation (section 2.5.1), for which we then solve an optimal transport problem (section 2.5.2) that gives us a good initial guess to place our ideal filaments on.

2.5.1 Stippling the Flux Density

The initial input data we want to respect is the Neumann boundary condition determining the magnetic surface flux as established in section 1.4.3. We call these magnetic flux maps $\Phi : \partial\mathbb{M} \to \mathbb{R}$ *magnetograms*, as they are called by NASA, the provider of such data from the sun on their SDO archive.

Our algorithm input is most of the time not a bundle of filaments, but rather a magnetogram Φ from which we want to generate an initial bundle of filaments, such that their flux at the surface is approximately equal to the magnetogram's surface flux.

Initial Number of Filaments

In our algorithm, we want to give each filament equal flux h. The first thing we have to do is to select a flux quantization value $h > 0$, which automatically determines the resolution *i.e.* number of filaments we will have. This is because the magnetogram determines the *total absolute flux*

$$T_{\partial\mathbb{M}}(\Phi) := \int_{\partial\mathbb{M}} |\Phi|.$$

Note that this is different from the zero total flux $\int_{\partial\mathbb{M}} \Phi = 0$ that the magnetogram has to fulfil anyway (magnetic monopoles are illegal). We split the surface $\partial\mathbb{M}$ into a *positive flux part* $\partial\mathbb{M}_+$ and a *negative flux part* $\partial\mathbb{M}_-$ and a *no flux part* $\partial\mathbb{M}_0$.

$$\partial\mathbb{M} = \partial\mathbb{M}_+ \cup \partial\mathbb{M}_- \cup \partial\mathbb{M}_0$$
$$\partial\mathbb{M}_+ := \{x \in \partial\mathbb{M} : \Phi(x) > 0\}$$
$$\partial\mathbb{M}_0 \ := \{x \in \partial\mathbb{M} : \Phi(x) = 0\}$$
$$\partial\mathbb{M}_- := \{x \in \partial\mathbb{M} : \Phi(x) < 0\}$$

In practice, $\partial\mathbb{M}_0$ does not really matter as any minuscule amount of flux will disqualify a point x to be inside of it. Because nature is noisy, pretty much no points are in $\partial\mathbb{M}_0$ (never *exactly* zero).

The question now is: How many magnetic filaments should be used? The answer ties together the total flux $T_{\partial\mathbb{M}}$ to h. Let $N \in \mathbb{N}$ be the number of filaments. If each filament brings a positive flux h and a negative flux $-h$ into the surface, then the following relation should hold:

$$2Nh = T_{\partial\mathbb{M}}.$$

Only if this relation holds, can we expect the surface flux to be consistent with that of the magnetogram Φ. Thus we conclude:

$$N = \left\lfloor \frac{T_{\partial\mathbb{M}}}{2h} \right\rfloor$$

This determines the number of footpoints the filaments have, but it is yet entirely unclear how to place them.

Stippling the Footpoints of the filaments

We now proceed to discretize Φ by a process we call *stippling*. The magnetogram is a continuous object, which in practice is provided by NASA as a matrix data type which projects onto the visible part of the sun orthogonally. In practice, we literally project magnetic flux data onto a fine spherical mesh and then perform the stippling.

> **Definition 37 (Stippling).** Given a magnetogram $\Phi : \partial\mathbb{M} \to \mathbb{R}$, a flux quantization $h > 0$ and $N = \lfloor T_{\partial\mathbb{M}}/2h \rfloor$, we define a normalized density function
>
> $$\phi : \partial\mathbb{M} \to \mathbb{R}_{\geq 0}$$
> $$\phi(x) \mapsto \frac{1}{\int_{\partial\mathbb{M}} |\Phi(y)| dy} |\Phi(x)|.$$
>
> ϕ is then used to sample N points $P \subset \partial\mathbb{M}$. P is the *stippling* of Φ.

In practice, we stipple $\partial\mathbb{M}_+$ and $\partial\mathbb{M}_-$ separately with half the points to ensure equal number of stipples on each region (which is the expected outcome when the total flux is zero). We write the stipples of $\partial\mathbb{M}_+$ as P_+ and the stipples of $\partial\mathbb{M}_-$ as P_-. Additionally, we make use of Houdini's scatter point relaxation method to avoid points being sampled extremely close to each other. This enables higher representation fidelity of the stippling with less points. Figure 2.28 shows an example of stippling in practice.

When we consider these stipples to be footpoints of vertical magnetic filaments and compute their radii r according to the no-overlap constraint established in section 2.3.1, then we can expect the magnetic field strength B to be approximately that of the magnetogram.
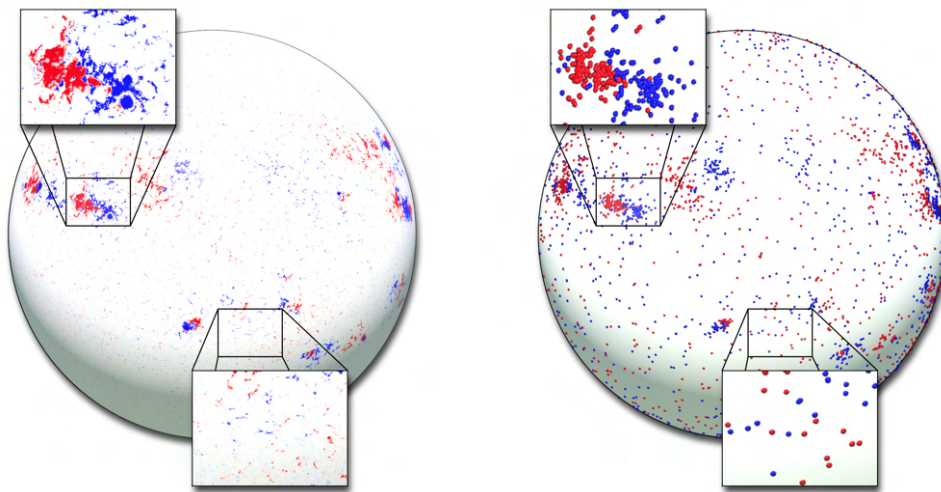
$$|\Phi| \approx B = \frac{h}{2\pi r^2}$$

Figure 2.28: A magnetogram (left) and its stippled version (right). Each dot represents the same amount of magnetic flux h. Areas of stronger magnetic field have tightly packed stipples (top left) while areas of low flux are sparsely populated with stipples (bottom). The underlying magnetogram was captured by NASA's SDO mission on Oct. 21st, 2011.

2.5.2 Initial Curves and Matching by Optimal Transport

We just converted a magnetogram Φ into a stippling. The stippled points will now be our footpoints for our magnetic filaments. As mentioned in the beginning of section 2.5, the topology of the filaments remain preserved during the progress of the energy minimization when solving for an MHS field. In other words, chaotic entanglements, delicate braidings and twists cannot be undone, even if the energy of the system would be reduced if they were to untangle. We will now formulate the *filament matching problem:*

> *Given a the stippling $P = P_+ \cup P_-$ of a magnetogram $\Phi : \partial \mathbb{M} \to \mathbb{R}$ on the surface of the sun, what is a reasonable initialization of filaments connecting points from P_+ to points from P_- for the MHS energy minimization algorithm to reach a good minimum?*

Since we are attempting to minimize energy, it is sensible to select an initial topology that minimizes energy in some simplified way that is easier to solve exactly. We want low/minimum twisting and avoid large filaments at the beginning. See figure 2.29 to quickly see that this is a hard combinatorial challenge. This also means that the problem is in general computationally very expensive to solve, if we consider potentially matching every point to each other point with any possible shape. Therefore, we need to make some choices.

Our approach is based on attempting to minimize the total energy sum of an initial ideal filament population. In section 2.2.3 figure 2.10 we have derived the exact shape and energy/length of ideal filaments, which are exactly the global energy minimizers if the magnetogram would only consist of two stipples or if the gas pressure is very high (theorem
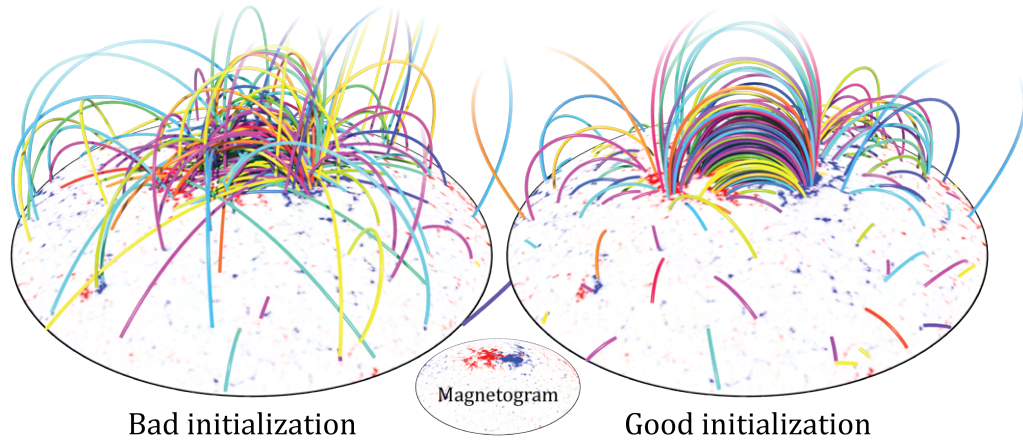
Figure 2.29: The initialization problem. Given a magnetogram (middle bottom) that we stipple, how should we populate the solar corona with initial magnetic filaments that pay respect to the magnetogram while being a good guess for our algorithm? More precisely: what shapes should the initial curves have and what points should they connect with each other? A bad initialization results in topological chaos and high energy (left), while good initialization has lower energy and far less linking.

38 below). If we choose to only populate the initial filament set with the shapes of ideal filaments, then the question now becomes purely combinatorial as shown in figure 2.30.

Mathematically, we attempt to build a special bipartite graph connecting points in P_+ to points in P_-. In the initial graph G, every point $p_i^+ \in P_+$ shares an edge (i, j) connection with every point in $p_j^- \in P_-$. From these edges, we attempt to select a subgraph G_M of edges such that all points in P_+ are uniquely matched with points in P_-. We define the energy of this matching as

$$\mathcal{E}(G_M) := \sum_{(i,j)\in G} d(p_i^+, p_j^-)$$

Where $d(\,\cdot\,,\,\cdot\,)$ is the energy of the ideal filament connecting p_i to p_j and also the distance between these two points in the gas metric as established in corollary 28. The combinatorial goal is now to find a matching G_M that minimizes $\mathcal{E}(G_M)$. Solving for such a G_M is known as a *linear sum assignment problem*, which can also be seen as a discrete version of an *optimal transport problem*.

Populating the initial filaments with ideal filaments is a good idea because of the following theorem:
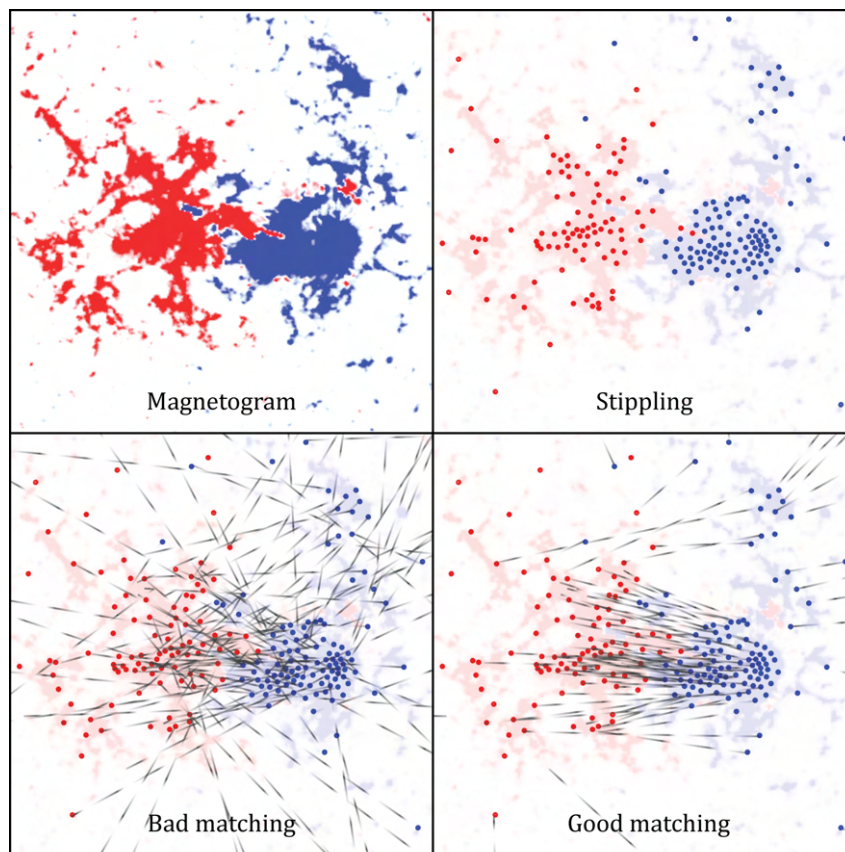
Figure 2.30: The matching problem. A magnetogram (top left) is stippled into a set of points with equal flux (top right). If we choose to populate the solar atmosphere with ideal filaments and want to minimize the MHS-energy of the sum of these filaments, then which points should be connected with each other by these filaments? A *bad* matching would create in a chaotic topology and a high initial energy (bottom left), while *good* matching should create a topology with minimal linking and have minimal energy for the problem statement. This is a combinatorial problem.

Theorem 38 (**Minimal Initialization**). Placing ideal filaments between points by solving the linear sum assignment problem between stipples P_+ and P_- according to the energy $\mathcal{E}(G_M)$ will return the *global MHS energy minimizer* (no energy minimization algorithm needed) in the special case when the pressure p is very high (which is equivalent to a weak magnetic flux Φ).

Proof. In the limit of high pressure, we know that the values of r_{opt} (definition 25) approaches zero:

$$\lim_{p \to \infty} r_{\text{opt}}(\mathbf{x}) = \lim_{p \to \infty} \frac{1}{\sqrt{2\pi}} \frac{\sqrt{h}}{\sqrt[4]{2\mu_0 p(\mathbf{x})}} = 0.$$

The radii r_i we compute on the curves thus never overlap (definition 30), and thus each filament's energy is completely independent. To minimize the MHS energy it is sufficient to simply minimize the energy of each filament individually. This means that we can write $\mathcal{E}(\Gamma) = \mathcal{E}(G_M)$. From theorem 27 [**Energy Minimizer / Geodesics of Smooth Magnetic Filaments**] we know that the chosen ideal filaments are *exactly* those global minimizers.

$\square$

Theorem 38 shows us that the topology we propose to use for our optimal matching has the same topology as that of the global minimal MHS energy configuration in the high pressure limit $\lim_{p\to\infty}$, which also means that the choice of topology is ideal in that particular case and that the energy can't be reduced further using topological changes. We thus believe that preserving that topology is the reasonable, probably the best possible, choice for our algorithm input to archive minimal final energy.

Linear sum assignment problem solvers are available to us in the SciPy library. They typically require a *cost matrix* C that in our case will be populated with the pairwise ideal filament energy between P_+, represented in the rows, and P_-, represented in the columns.

$$C := \underbrace{\begin{bmatrix} d(p_1^+, p_1^-) & \cdots & d(p_1^+, p_N^-) \\ \vdots & \ddots & \vdots \\ d(p_N^+, p_1^-) & \cdots & d(p_N^+, p_N^-) \end{bmatrix}}_{(\#P_+)\times(\#P_-) \text{ matrix}}$$

There is however, a problem! The matrix C is *very dense* in our case, and thus the computation time for the matching becomes too long. What can we do to ease the computation?

2.5.3   Sparsity Thanks to Infinity

From theorem 28 (**Energy / Geodesic Distance of an Ideal Magnetic Filament**) we know that the maximum energy/distance/cost an ideal filament can have is limited by $d_{\max} := \sqrt{\frac{2p_0 r_\odot}{\mu_0}\left(\frac{4}{\lambda-2}\right)}$ which is reached when the angle θ between the points p_i^+ and p_j^- is greater or equal than $\theta_{\max} := {}^{2\pi}/_{\lambda-2}$. According to theorem 27, all ideal filaments connecting points beyond a distance $\theta_{\max}$ will be vertical lines from the surface going through the point at infinity.

This allows us to greatly simplify things. In the case of the sun, $\lambda \approx 23$ and thus $\theta_{\max} \approx {}^{2\pi}/_{21} \approx 17°$ (reaching less than than 10% of the sun's circumference), which means that only points p_j^- which are relatively close to p_i^+ points on the surface of the sun are eligible to match with a non-trivial (not going through infinity) ideal filament connection. Beyond that, we don't need to know exactly which stippled points in P_+ match with what other stippled points in P_-, since they all go through infinity (see figure 2.31).

We can leverage this indiscrimination to transition our optimal matching problem into a sparse version of the linear sum assignment problem. For this to work it suffices to modify
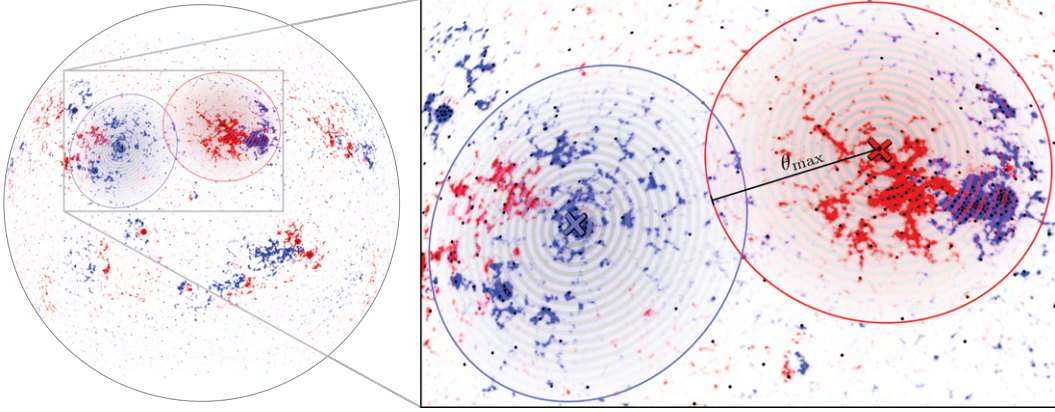
Figure 2.31: For ideal filaments, if the foot points have an angular distance $\theta \geq \theta_{\max} = \frac{2\pi}{\lambda - 2}$, then the parametrization derived in theorem 27 shows that the filament will go straight through the point at infinity. This means that beyond a distance of $\theta_{\max}$, we become indifferent about the exact matching of stipples. Thus, we only really have to consider matching points that are closer than $\theta_{\max}$ to each other, which greatly simplifies the linear sum assignment problem and allows us to leverage sparse matrix implementations. The positive and negative points highlighted by an $\times$ will not include each other in their matching considerations.

the input without having to adjust the SciPy solver. We create a sparse matrix C^{s} by only allowing entries between points who's angular distance is below $\theta_{\max}$. However, this alone would create ill defined problem as some points in P_+ might not have any point to match to or unfairly reserve points to themselves when they should rather match with a far away point in P_- by going through the point at infinity. We circumvent these issues by adding points to the initial bipartite graph G to form a new graph G^∞. Each point $p_i^+ \in P_+$ receives a dedicated point (no other point shares an edge to it) at infinity $p_i^\infty \in P_-$ with a cost of $d(p_i^+, p_i^\infty) = d_{\max}$. In practice, we can set $p_i^\infty := -p_i^+$ (antipodal point). The resulting cost matrix C^∞ is a concatenation of C^{s} with a diagonal matrix C^*. In SciPy, a zero cost means that the bipartite graph is assumed to have no edge between the corresponding points.

$$C^\infty := \underbrace{\left[\; C^{\mathrm{s}} \; \middle| \; C^* \; \right]}_{(\#P_+) \times (\#P_- \; + \; \#P_+) \; \text{matrix}}$$

$$C_{ij}^{\mathrm{s}} := \begin{cases} d(p_i^+, p_j^-) & \text{if } d(p_i^+, p_j^-) < d_{\max} \\ 0 & \text{else.} \end{cases}$$

$$C_{ij}^* := \begin{cases} d_{\max} & \text{if } i = j \\ 0 & \text{else.} \end{cases}$$

The linear sum assignment problem solver can now act on G^∞ and if p_i^+ is matched

to p_i^∞, then we know that the required ideal filament is just a vertical line. Vice versa we know that any point $p_i^- \in P_-$ that received no matching must also require an ideal filament reaching out to the point at infinity.

To our blessing, SciPy has this sparse linear sum assignment solver implemented and it can be called via this simple command:

$$\texttt{scipy.sparse.csgraph.min\_weight\_full\_pipartite\_matching}(C^\infty)$$

2.5.4   Initialization Algorithm

Let's place what we learned into algorithm 6 [**Initialize Filaments**] to make it clear what is happening. We also show how the sparse matrix is built in SciPy.

Algorithm 6 Initialize Filaments

Input: Magnetogram Φ, flux quantization h.
Output: Initial filament set Γ.
 1: $P_+ \leftarrow$ sample N points by density function $|\Phi|$ on $\partial\mathbb{M}_+$
 2: $P_- \leftarrow$ sample N points by density function $|\Phi|$ on $\partial\mathbb{M}_-$
 3: compute $d_{\max}$
 4: compute $\theta_{\max}$
 5: create empty lists col, row, c, Γ
 6: **for each** $p_i^+ \in P_+$ **do**
 7:     $T_i \leftarrow$ all $p_j^- \in P_-$ at an angular distance $< \theta_{\max}$ to p_i^+
 8:     add $p_i^\infty = -p_i^+$ to T_i
 9:     **for each** $p_j^- \in T_i$ **do**
10:         $col \leftarrow \text{append}(col, i)$
11:         $row \leftarrow \text{append}(row, j)$
12:         $c \leftarrow \text{append}\big(c, d(p_i^+, p_j^-)\big)$
13:     **end for**
14: **end for**
15:     $C^\infty \leftarrow \texttt{scipy.sparse.csr\_matrix}(c, (row, col)), (|\#P_+|, |\#P_-| + |\#P_+|)$ ▷ create sparse matrix
16:     $row, col \leftarrow \texttt{scipy.sparse.csgraph.min\_weight\_full\_pipartite\_matching}(C^\infty)$
     ▷ solve linear sum assignment problem
17: **for each** $i \in \{1, \ldots, \text{length}(row)\}$ **do**
18:     **if** $d(p_{col[i]}^+, p_{row[i]}^-) < d_{\max}$ **then**
19:         add an ideal filament γ connecting $p_{col[i]}^+$ with $p_{row[i]}^-$ to Γ
20:     **else**
21:         add a long vertical filament γ to Γ starting at $p_{col[i]}^+$.
22:     **end if**
23: **end for**
24: **for each** $p_j^- \in P_-$ that was not matched **do**
25:     add a long vertical filament γ to Γ starting at p_j^-.
26: **end for**

When placing long vertical filaments γ we cut of their height at about twice the solar radius. At that distance, filaments are not visible anyway and their influence on the rest of the system is negligible. On top of that, the assumptions of our model might not even apply much this far away from the sun. In practice, filament initialization is computationally quick

and far from being the bottleneck (more on this in section 3.6.2 [Performance and Refinement Thereof].

Note that our stippling is not time coherent, meaning that if we had a time dependent sequence of magnetograms Φ_t, every sampling would be quiet different. It was not an aim to create *quasi-static evolution* by stringing together solutions with varying input, but if the sampling coherence issue where to be solved, this could easily be an option. In fact, frame-coherent stippling has already been developed as a rendering technique [Pastor et al.(2003)].

Summary of Part 2:
The Discretization of the MHS Equation

This concludes the second part of the dissertation. Let's have another recap of what happened.

- **Section 2.1, Field Line Energy**
  Starting with the FFCS model, we analysed the energy of singular magnetic field lines and established the relationship between their energy and their *length* in the *plasma metric*.
- **Section 2.2, Smooth Magnetic Filaments**
  We introduced *smooth magnetic filaments* as a special primitive of a tube like magnetic structure. We also characterized ideal filaments and their exact shape and thickness by computing geodesics in the *gas metric*, a special case of the plasma metric.
- **Section 2.3, Discrete Magnetic Filaments**
  We introduced *discrete magnetic filaments* as a direct discretization of smooth magnetic filaments. We established the no-overlap constraint between filaments and described their energy and length.
- **Section 2.4, Energy/Length Minimization**
  We established how we reduce the energy of the discrete magnetic filament set Γ using a quasi-Newton method. We show how the plasma metric is computed and gave algorithms for the energy minimization.
- **Section 2.5, Initial Curves from Flux Density**
  We approached the problem of the initial discrete filament input set. We introduced magnetogram *stippling* and solved a linear sum assignment problem to select established sensible ideal filament placements. We also sparsified the problem and built an algorithm to create the optimal matching between stipples.

The above sections transitioned the smooth FFCS model into the discrete magnetic filament model and established the algorithms to deal with it. Next up, we will work towards the visualization and validation of these results.

Part 3

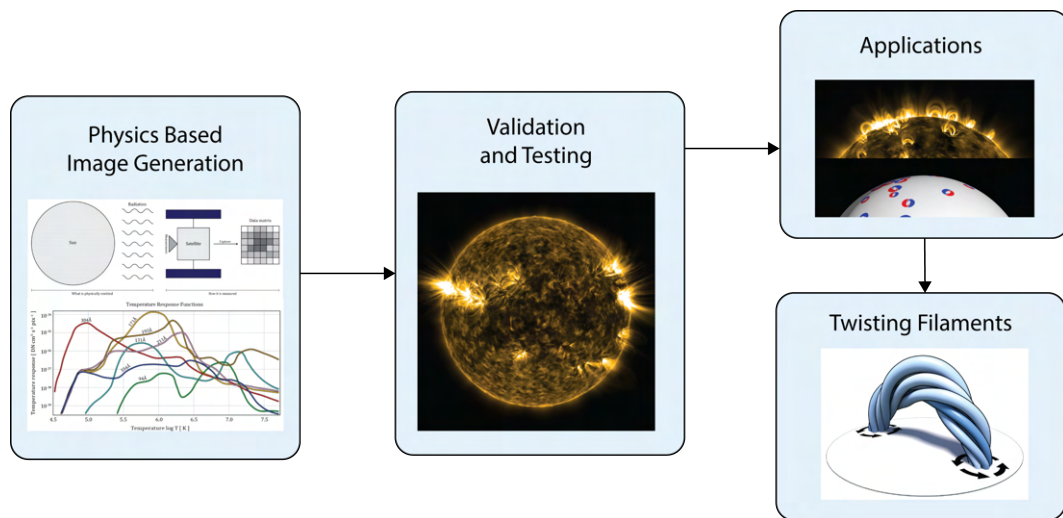# Image Generation, Validation and Application

Figure 3.1: An overview of part 3 of this dissertation. We establish a model for physical based image generation. We then validate various claims of the entire dissertation through tests. We list some applications and focus especially on one application regarding the twisting of filaments.

We have now established the smooth theory, its discretization, and an approach to solve the MHS problem and provided algorithms to do so. Thus we have covered the computational part of this dissertation. Was any of this any good in practice? Is this all a hoax? This part of the dissertation will answer this question.

From here on, we will *discuss the algorithm output and processing*. We will deal with . . .

- . . . the *generation* of images from the discrete magnetic filaments.
- . . . the *validation* of the output by comparison with real life data.

- ... the *application* in research and image generation.
- ... the *experimental results* when adding twist to our filaments.

3.1   Physics Based Image Generation

One of our initial goals was to generate images of the sun that look like the real life extreme ultra violet data captured from NASA. To do so, we have to establish a processing method that takes our output and creates these images. The theory behind this processing should be physics based and mimic what NASA's observatory equipment went through in order to generate these images.

The visualization problem is separate from the computation problem. In our case, we use many inspirations from our model together with some facts from solar physics literature to propose a new visualization model presented here.

3.1.1   Basic Physics and Measurements: The What and How

What are we actually seeing and how is this happening? The *what* is the *physical* aspect of the problem, mainly dealing with the emission from the sun. The *how* is the *measurement* aspect of what the equipment will pick up and how the data is being presented to us. Figure 3.2 shows these two stages. If we want to create realistic results based on a physical model, we need to predict the emission of the sun through our model and simulate the measuring and capturing of that data.
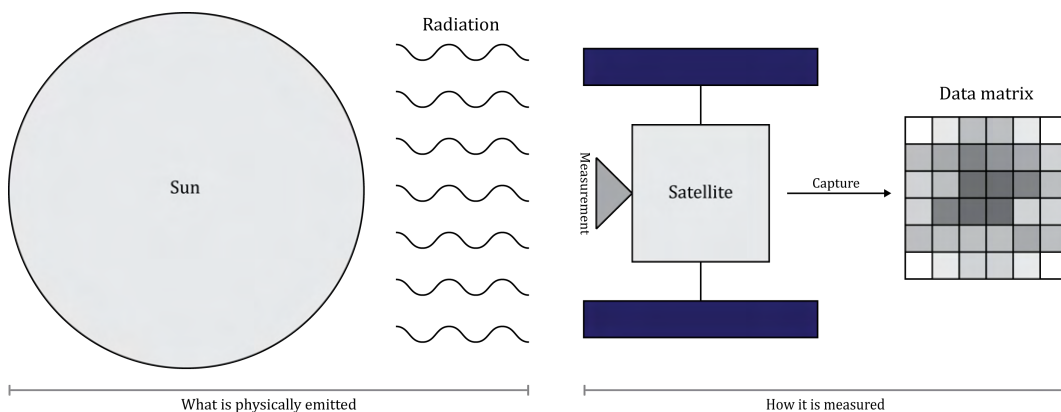

Figure 3.2: The *what* and *how* of what is measured. Left: the sun is emitting a lot of radiation at different wavelengths. Right: A professionally drawn satellite measures parts of the radiation and captures it in data matrices that are then visualized. If we want to create realistic images from our model, we need to understand both parts of this process. We need to predict the emitted radiation and simulate its measurement.

The Physical: The What

The elements being measured are the photons emitted by the sun. These come in a huge spectrum of different wavelengths/frequencies. Depending on which wavelengths you register you can get vastly different images. Human eyes for example, perceive only the visible light radiation with the sensitivity so high that our vision of the sun is blinded from seeing any finer structure.

Instead of visible light, we focus our attention on specific wavelengths, the most prominent being 171Å=17,1nm (Ånström, nanometer) radiation. The reason this wavelength is regarded as the best to observe solar plasma is that it produces the sharpest images due to a radiation spike in the emission spectrum which we will explain more in detail later. The *what* question then becomes: *How many 171Å photons does the solar corona emit at each point?* We answer this question when dealing with our glow model in section 3.1.2.
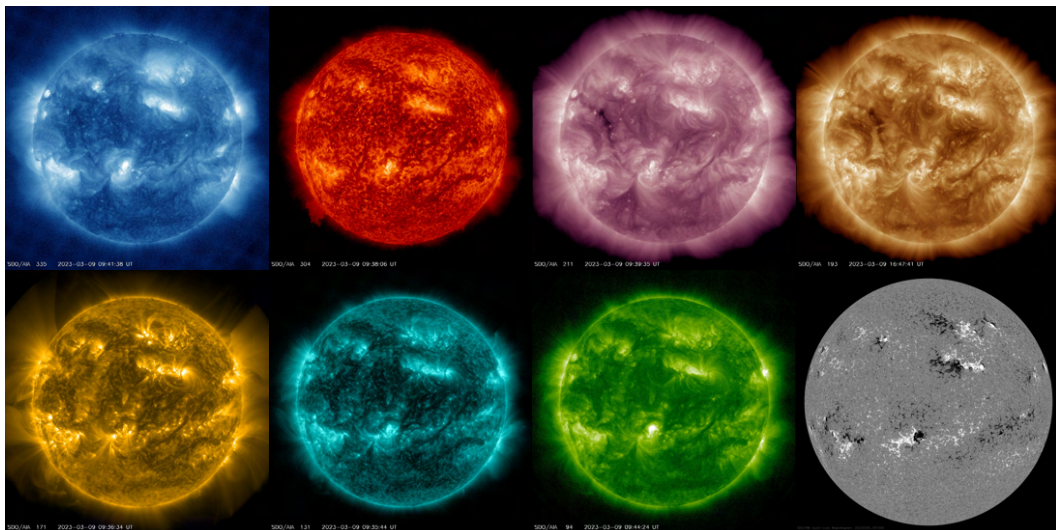

Figure 3.3: NASA Solar Dynamics Observatory Data taken on the 09/03/2023. From left to right and top to bottom these depict: 335Å emission, 304Å emission, 211Å emission, 183Å emission, 171Å emission (the most prominent that we attempt to recreate), 131Å emission, 94Å emission and the HMIB magnetogram. These images are taken every 45 seconds and published by [NASA Solar Dynamics Observatory(2023)].

The Measurement: The How

Photons of a certain wavelength meet the observatory equipped. What happens then? The equipment placed on NASA's Solar Dynamics Observatory basically resembles a camera with a 2D matrix of detectors. Within a specified measurement time window (exposure), whenever a photon hits one of these detectors and is successfully registered, a +1 is added to the corresponding location in an array. For the golden EUV images only photons at a wavelength of around 171Å are registered. The result is a data matrix of integers.

In the solar atmosphere, we can assume the medium to be *optically thin*, meaning that

Channel	Color	Primary Source	Region of Atmosphere
335Å	blue	Fe XVI	active-region corona
304Å	red	He II	chromosphere, upper transition region
211Å	purple	Fe XIV	active-region corona
193Å	bronze	Fe XII, XXIV	corona and hot flare plasma
171Å	gold	Fe IX	quiet corona, upper transition region
131Å	teal	Fe VIII, XX, XXIII	flaring regions
94Å	green	Fe XVIII	flaring regions

Table 3.1: A table of the major emission bands measured by the NASA Solar Dynamics Observatory together with their respective color convention, primary emission sources and regions [NASA Atmospheric Imaging Assembly(2023)].

the gas does not absorb any significant amount of emissions and allows all emissions to go through the medium. Due to the immense distance between the sun and the camera, the resulting image is an orthogonal projection. Thus, the measured value resembles the emission of the solar plasma integrated over the orthogonal line of sight. See figure 3.2 right.

The final integer array is then artificially coloured and interpreted as an image according to NASA's conventions to easily identify the measured wavelength. The colors are mapped linearly from black to a specified color and to white. See figure 3.3 to see the color standardized conventions. Each wavelength captures different radiation distributions. Table 3.1 displays the main AIA bands being measured.

3.1.2   What? The Glow Model

This section will answer how we take the filament bundle Γ output of our algorithm and turn it into rendered images. The first big question is: what is actually glowing? This is where we have to loosen up a bit the strict conditions of our Force-Free Current Sheet model (section 1.4). After all, the magnetic field is invisible and cannot glow by any means. In this discussion, we allow some gas to be trapped by the magnetic filaments. The fact that filaments contain very little gas is known, and the little gas that remains is sometimes estimated by a *loop filling factor* [Reale(2014)][Winebarger et al.(2008)]. We assume that it is not enough gas for our model to become inaccurate.

The measured emission comes from the mass in the solar atmosphere and on the surface. The most basic source of solar radiation is black body radiation, which is determined by the surface temperature being 5200 Kelvin at which mostly visible and ultra violet light is emitted (see figure 3.4 left). As the solar surface has a lot more mass then the atmosphere, this is by far the most dominant source of radiation.

However, further up in the atmosphere the temperature quickly rises to a million Kelvin and more while the density drops drastically. At those temperatures, specific emissions from electron shell transitions occur, most notably from heavier isotopes. These produce much more concentrated spikes in the emission spectrum which can be measured by the observatory
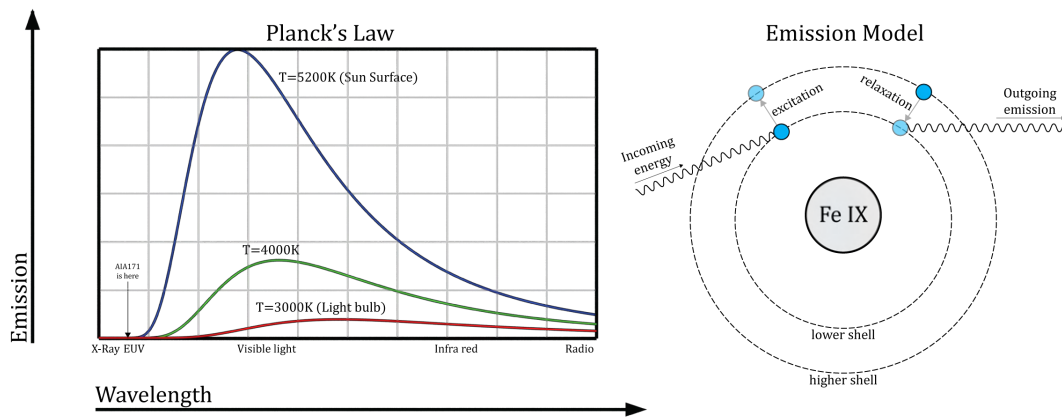
Figure 3.4: Left: Planck's law on black body radiation. The amount of emission at different wavelengths is determined by the temperature. Most of the sun's radiation is black body radiation and has lower energy. However, it does not account for the EUV and X-Ray emissions we are interested in. Right: Emission model for electrons hopping between energy levels shown here using Bohr's model. When an electron jumps down an energy level, the energy difference is being emitted. This causes emission spikes at shorter wavelenghts. In our case, the isotope Fe IX is responsible for the 171Å EUV emission.

equipment (see figure 3.4 right).

Temperature Response Functions

The wavelength 171Å, the most prominent one responsible for NASA's iconic gold images, is the result of the emission that occurs at the higher shell's of the heavy iron isotope *Fe IX* at a characteristic temperature of around $6.3 \cdot 10^5$K. The coronal plasma's emission responses for the SDO measurement wavelengths from the solar atmosphere at various temperatures have been captured in the graph of figure 3.5 [Boerner et al.(2012)]. These functions are called *temperature response functions*. For the wavelength $l > 0$, we note the corresponding response function as f_l.

Thus, it becomes clear that if we want to physically estimate how much radiation is emitted, we also have to estimate the temperature of the plasma filaments in the solar atmosphere. The measurements in figure 3.5 are independent of density. The greater the density, the greater the emission. A proposed radiation model is the following:

> **Definition 39 (Filament Glow).** At any point $x \in M$ in the solar atmosphere, the emission of the wavelength l at temperature T and density ρ is given by
>
> $$\mathrm{em}(l, T, \rho) = f_l(T) \cdot \rho^a$$
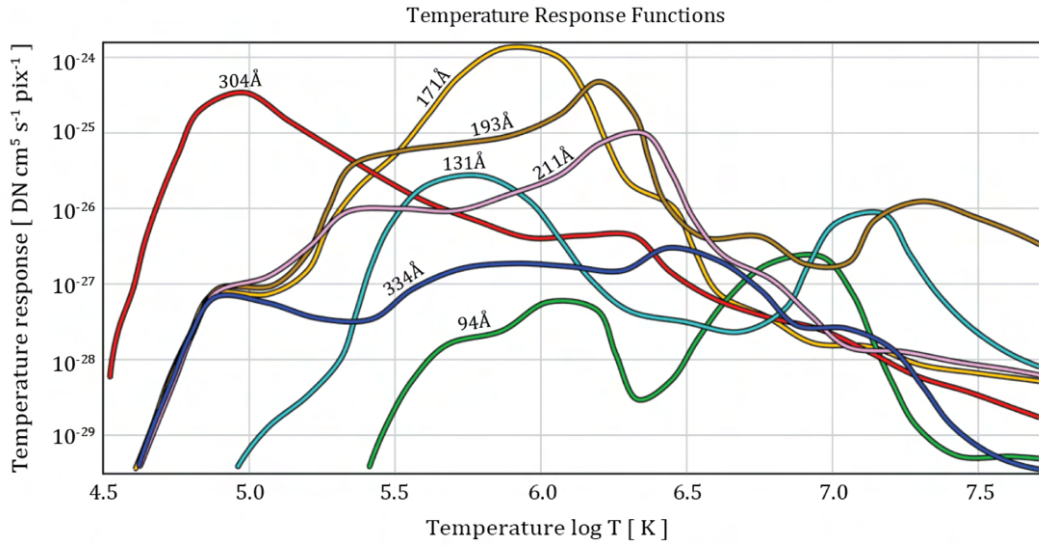>
> where a indicates how much density scales.

Figure 3.5: The temperature response functions of the solar coronal plasma for the wavelengths 334Å, 304Å, 211Å, 193Å, 171Å, 131Å, 94Å colored by their respective conventions in the NASA SDO publications (see figure 3.3). These functions reveal how much radiation is emitted at what temperatures independently of density. 171Å stands out as being the wavelength that has the most concentrated response, which is why it creates the sharpest images. 94Å on the other hand, responds weaker at a much larger temperature range.

This formula was used with the parameter $a = 2$ in [Wilmot-Smith(2015)]. In order to use this formula, we have to now make statements to estimate the temperature T and the density ρ.

Choice of wavelength: Which of the wavelengths plotted in 3.5 should we care about the most? As one can now recognize from the plot, the EUV 171Å wavelength stands out as being the *sharpest*, meaning that it has a rather unique peak response near its characteristic temperature and little responses elsewhere. This in turn makes the measurements much sharper, unlike the X-ray 94Å measurements which have two distinct peaks. This is why EUV 171Å is the solar physicists' favourite band.

The other wavelengths measured by NASA's SDO mission do also give valuable information. However, apart from being less sharp, their responses are also suboptimal to study the solar corona for other reasons. The wavelengths that are longer than 171Å mostly occur at lower characteristic temperatures, which then in turn entangles the measured emission with the emission emitted by the surface of the sun and not of the solar corona. Measuring smaller wavelengths than 171Å creates blurrier and noisier images, as the response functions are less sharp and there is generally less emission to measure. Let us not forget that the measurements are a statistical sampling result of photons reaching the observatory measuring device in a 45 second time window. Lower emission also means more noisy measurements.

Sensitivity of Temperature Response: What is particularly tricky about the

temperature response functions in figure 3.5 is that they also show us that having the right temperature is really important to see anything at all. If the plasma is *too cool*, then it won't respond with any 171Å emission. However, if the plasma is *too hot* it also won't respond much too. There is a sweet spot in between and getting an estimate for the temperature that is good enough in various places of the sun is a difficult task, but it is our best lead for a physically based glow model so we have to try it anyway.

Estimating Temperature T and density ρ

Essentially, in order to do this right we would have to solve the complicated *coronal heating problem* [Aschwanden(2006)], which is still unsolved (see section 1.2.1). The next best thing we can do is to take some approximative insight regarding the temperature distribution in our area of interest. We make use of multiple assumptions inspired by solar physics literature.

Assumption 1: The temperature at the foot points is given by the ideal gas law, where the gas pressure is equal to the magnetic pressure. ρ_0 is the density at a foot point and m is the mass of a hydrogen atom, the by far most abundant element dominating the thermodynamics. We assume ρ_0 to be constant on the entire sun's surface and that the temperature at a footpoint can be estimates as follows:

$$T_i = \frac{mp}{k_B \rho_0} = \frac{mB_i^2}{2\mu_0 k_B \rho_0}$$

Assumption 2: We follow [Reale(2014), Reale and Peres(1999)] in assuming that *the temperature along a magnetic field line is constant and determined at the footpoints.* The idea being that the strong magnetic field locks plasma flow along the field lines and thus heat conductivity is rapid parallel to the field lines but relatively slow across neighbouring field lines. Additionally, most of the filament mass is at the foot points, giving them strong weight in the temperature determination. For a filament with two foot point temperatures T_1 and T_2 we assume the maximal temperature to dominate the filament temperature T_γ.

$$T_\gamma = \max(T_1, T_2)$$

Assumption 3: The ideal gas law still holds in the entire filament. Given the temperature T_γ and the magnetic field strength B, we estimate the density again through the ideal gas law with the magnetic pressure:

$$\rho_i = \frac{mB_i^2}{2\mu_0 k_B T_\gamma}$$

A Grain of Salt: Straightforwardly, the assumptions made on the temperature T and density ρ for this glow model can easily be challenged. Can we really assume T_γ to be constant while estimating ρ_i? We need to stress that there is no coherent model to compute temperature and density and that we were limited by the currently available theories regarding the coronal heating problem. This is an attempt to combine observations from

multiple sources in solar physics to a model. We tried out models until we found one that worked best, not perfectly. We think that the results give this temperature model some merit.

The Glow Model Algorithm

We condense the glow model of section 3.1.2 into algorithm 7 [**ComputeEmission**].

Algorithm 7 ComputeEmission

Input: A point γ_i on a curve γ. A wavelength l. Base density ρ_0
Output: An estimation of the emission $\text{em}(l, T, \rho)$ around γ_i.
 1: Get foot points γ_-, γ_+ of the filament γ
 2: $T_{\gamma_-} \leftarrow {mB^2_{\gamma_-}}/{2\mu_0 k_B \rho_0}$
 3: $T_{\gamma_+} \leftarrow {mB^2_{\gamma_+}}/{2\mu_0 k_B \rho_0}$
 4: $T_\gamma \leftarrow \max(T_{\gamma_-}, T_{\gamma_+})$
 5: $\rho_i \leftarrow {mB^2_{\gamma_i}}/{2\mu_0 k_B T_\gamma}$
 6: $\text{em}(l, T_\gamma, \rho_i) \leftarrow f_l(T_\gamma)\rho_i^a$

This emission is then computed for each point of Γ. In practice we set $a = 1/3$ and $\rho_0 \approx 20 \cdot 10^{-9}$. Before we can evaluate the results of this glow model in section 3.4 we must first talk about the image generation from this glow.

3.1.3   How? The Measuring Model

Now that we have a model on how much a magnetic filament will glow at each point, it is time to use that model to generate images. We remember from section 3.1.1 that the solar plasma is optically thin, meaning that its emission is not hindered by its own presence (not reabsorbed). Thus, the registered emission between the measurement device and the sun should be the sum of all the emissions in the path the device was pointing at. This is effectively an integral of emissions as seen in figure 3.6.

Such integrals are usually not simple to compute, but we have a nice trick up our sleeves to leverage existing software. State of the art render engines use ray tracing to create realistic images. We assign to every filament an invisible and light emissive material with emission intensity proportional to the glow model emission $\text{em}(l, T, \rho)$. The resulting ray traced pixel color values will then be the integration results along the line of sight of the camera that mimics a measurement device. On top of that, by rendering high dynamic range images (HDR) we can even capture the emissions in floating point values (not limited to [0,1] range) for easier post-processing (coloring).

The output is then an array of integrated emission values. This can be seen as a black and white image to which we introduce colors by NASA's usual conventions mentioned in section 3.1.1. For the extreme ultra violet images at 171Å, these come with a golden hue. Figure 3.7 shows the color mappings.

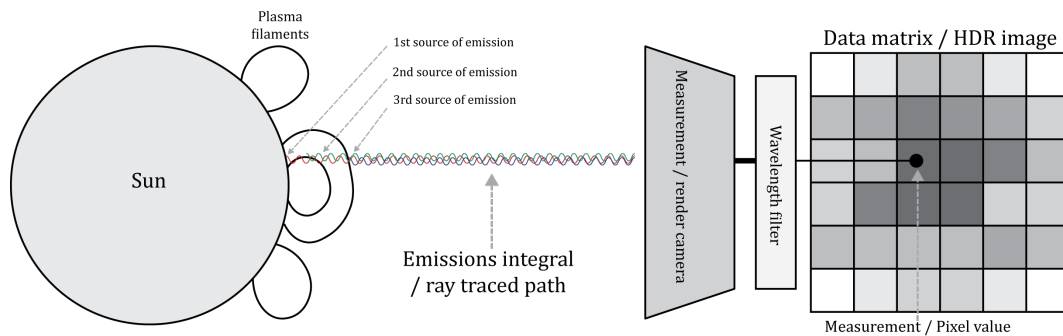**Figure 3.6**: The measurement / render setup. The emissions of the optically thing medium sum up over the line of sight of the measurement device. The total emission reaching the device is the integral of the emission on the line of sight times the area of the measuring device. The specific wavelengths are measured separately and the intensity of the measurement is the emission integral. In the render setup, this amounts to layering invisible and emissive objects on top of each other and evaluating the resulting color in a ray-tracer. The pixels then become the measurement, and the HDR image is the simulated emission data capture.

3.1.4 Upsampling of Filaments

The truth is: the number of magnetic filaments we handle in the final computation is rather rough for visualization purposes. But let us not forget: each filament represent a bundle of field lines and is thus a reduction of the actual detail it represents. We will now extract that detail for visual purposes.

Upping the number of filaments would greatly enhance the visual details but at too high of a computational cost to be feasible. Also, upping the number of filaments does not substantially change the structure of the output. Therefore, we propose a post processing step to upsample the filaments for rendering purposes.

For a thick discrete magnetic filament γ we seed new points in the circular disc of radius r_0 around one footpoint γ_0 of the filament. These new points are then parallely transported along γ while respecting the change in radii. The result is a replacement of the original filament γ with lots of tiny filaments with smaller radii. We chose parallel transport to minimize any artificial twist introduction. Figure 3.8 shows how this happens in practice.

3.1.5 Glow Variation

Upsampling itself does not however increase the visual fidelity much in the glow model, as all subsampled filaments would glow exactly the same. Can a natural phenomenon help us out here?

To our help comes the *thermal instability and non-equilibrium in solar coronal loops* [Antolin(2020)]. It describes cycles of heat and plasma flow along the filaments in a condensation, evaporation and rain-like cycle process. This is of course beyond the scope of
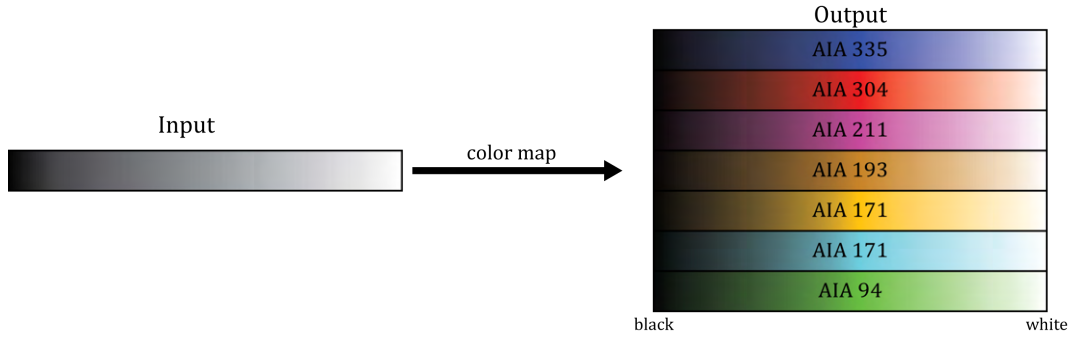
Figure 3.7: The color mapping convention as established by the NASA SDO AIA mission. The input data are just intensity maps of photon registrations. In order to easily identify the measured wavelengths a convention has been introduced to simply color these images with distinct hues. The values are mapped linearly onto a gradient going from black to a specific color to white.
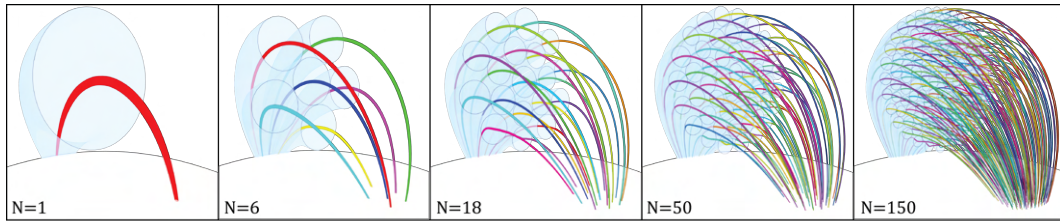

Figure 3.8: Our upsampling scheme. A single filament γ is replaced with N smaller filaments. They are created by parallely transporting seeded points in the circular disc of radius r_0 at a footpoint γ_0. This increases detail without the high computational cost of running the algorithm with such a high number of filaments. Here we show the upsampling scheme for various $N \in \mathbb{N}$ starting from a single thick filament.

this dissertation to model accurately, but we mention it because it explains the variation of the glow between neighbouring filaments. To approximate this glow variation, we sprinkling some noise patter (we chose simplex noise) on the footpoints of filaments which we then use to scale the glow intensity of the filaments. This has two benefits:

- **Filament structure**
  A fine fibrous texture is created that compares much better to NASA's captured data. This also makes the magnetic field lines far more visible. The subsampling of filaments really helps making this step much finer.

- **Animated glow**
  The above mentioned thermal instability is also responsible for glow variations in time-lapse footage. The majority of these variations only affect the emission-intensity and not the magnetic field structure. By simply animating/perturbing the simplex

noise at the footpoints over time we achieve similar glow variation.

The upsampling of filaments and glow variation increase the visual information output of our glow model. The magnetic filaments themselves are just primitives representing a bundle of magnetic field lines. These methods help to show these internal field lines better when generating solar images through our glow model. See figure 3.26 to see the glow variation and upsampling scheme in practice.

3.1.6 Adding Some Background Details

We have only focused on the glow of the filaments until now. Comparing our output to images from NASA would not yet be fair because there are a lot more emissions influencing their measurements. A lot of emissions still come from the solar surface in non-trivial ways. Simulating this physically correct too is far beyond the theory in the scope of this dissertation. However, since it does play a role in the presentation and comparison it is also fair that we add some background effects and explain how we do so.

The results of the filament glow are entangled with emissions from sources which are not filaments. The integrative nature of these emissions along the line of sight means that the composition of these layers happens by summation too. The additivity happens before the images are coloured by NASA conventions. The four layers we use are:

- **Filament layer**
  This is the output of our glow model algorithm. This is the only layer we do not count as a background layer.
- **Surface layer**
  The color of the surface. We model it by masking multiple levels of simplex noise at different scales on a high resolution mesh of a sphere while biasing the poles to be less noisy. See figure 3.9.
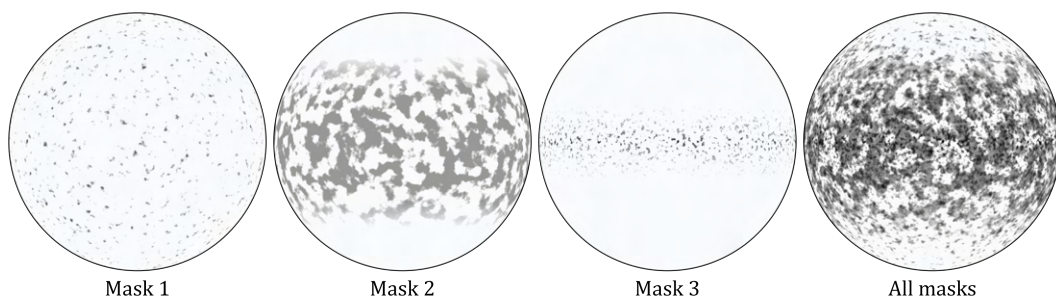

Mask 1   Mask 2   Mask 3   All masks

Figure 3.9: For the surface details of the sun we multiply a constant field with three masks made from simplex noise, each having a different element size. Mask 2 and 3 are more focused on the equator, as that is where more solar activity is expected. These masks were simply estimated from looking at data.

- **Spicules layer**

  The surface does have a vector field like structure that are described as spicules (hair-like jets of plasma). We model spicules by generating hair with the color of the surface layer and combing it along a random tangent vector field.

- **Fog layer**

  Around the sun there is a foggy halo. We model this halo by an emissive gas with exponential density drop off with height. The values are then also integrated through the line of sight. The noise of the surface layer is used as well to make the fog less regular.

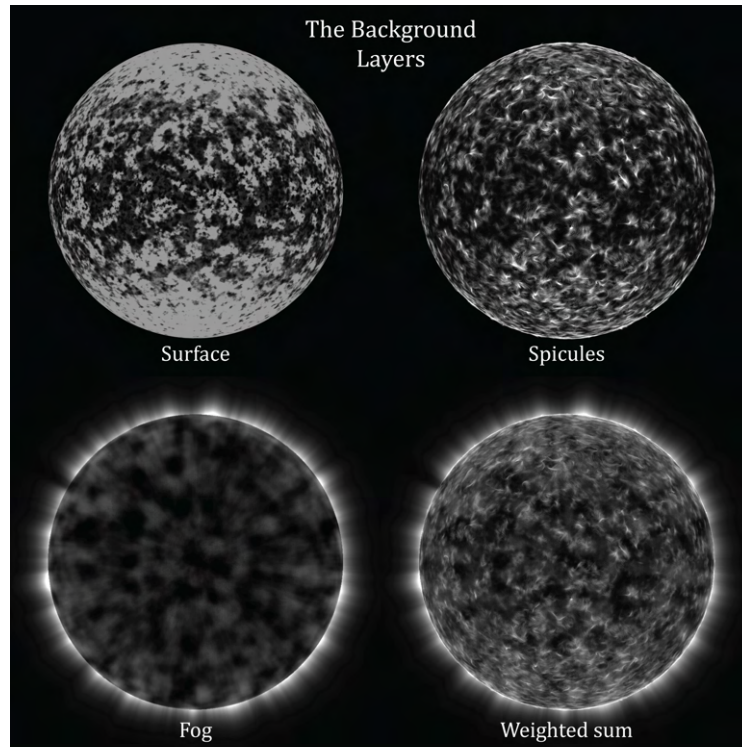Figure 3.10 shows how the background layers look individually and what their weighted sum looks like.

Figure 3.10: The three background layers used in our final composition. The surface layer is created by masking a white sphere with noise. The spicules layer is randomly combed hair colored by the surface layer. The fog is a volume render with variations linked to the surface layer. The emissions of all background layers together can be achieved by simply taking a weighted sum.

The background layers are then summed with the filament layer and then colored by the usual conventions where the *saturation value* has to be specified, the threshold value at which the array elements reach the white color (figure 3.11). A higher saturation value leads

to a darker image, while a lower saturation value can make some regions too bright (see figure 3.12). For raw emission data, such a choice has to be made when a measurement is interpreted as a pixel color. This is a normal process for any camera.
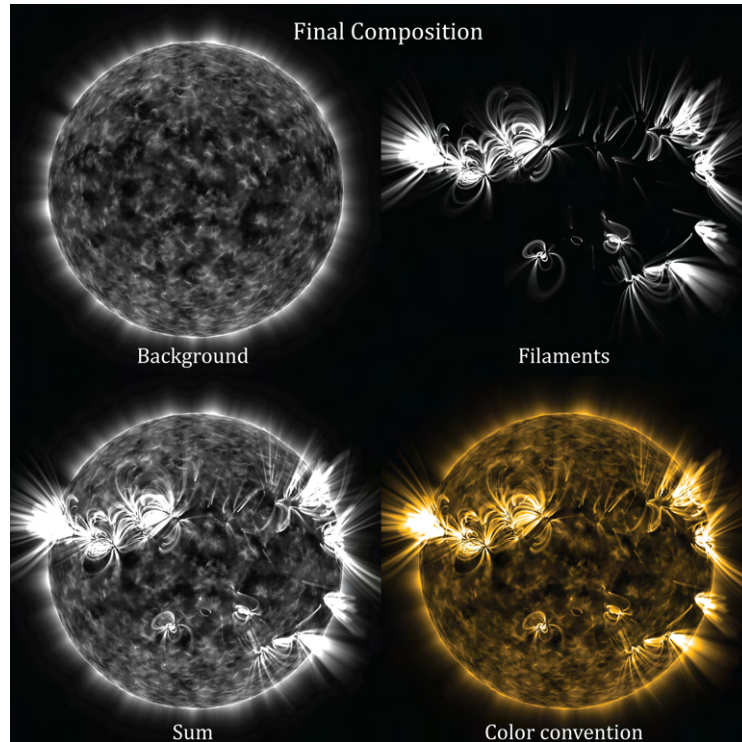

Figure 3.11: The final composition. The background layer is summed with the filament glow layer into a black and white image representing the raw emission data. This final image is then color mapped according to NASA color conventions.

Now that we have set up a way to render the output into images, we can fully dedicate ourselves to the discussion of our output. We begin with the validation of the numerics.

3.2 Validation of Numerics

How can we be sure that our output has any validity? This is a fundamental problem in solar physics as there is no available ground truth data to compare to. The measurements we have from the sun lack so much detail. We are limited to photon counting from which we can make statements about the quantity at different wavelengths and the magnetic field strength on the surface

Even worse is the fact that all captured data is captured from one perspective. In doing so, the spherical sun is orthogonally projected to a disc and the magnetic surface data on the limb is completely unknown while it is very relevant for the prominent visible features around the limb. This is why the glow model matters in the validation. Plasma filaments align with
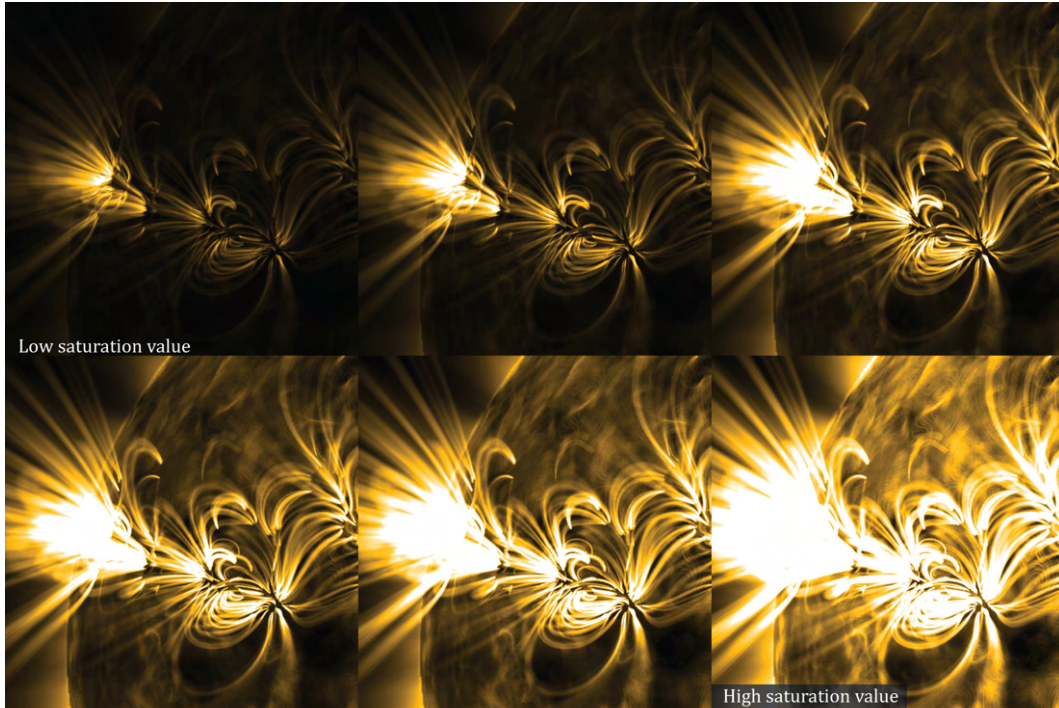
Figure 3.12: Varying the saturation value. The raw emission data is just an intensity map. Similarly to regular cameras, a choice has to be made about the color interpretation. This also applies for the visualization of the output of our images and their subsequent color mappings. Here, we increase the saturation level from top left to right, bottom left to right.

the magnetic field and by comparing our glow model output with EUV images of filaments we can make statements about the quality of the magnetic field we computed.

An opportunity for validation of the numerics arises when we have some theoretical predictions that we can then test if they indeed come true in our output. We will focus on the numerics of the curve shortening flow (section 3.2.1), the FFCS to PFSS limiting case (section 3.2.2) and the boundary flux region validation (section 3.2.3).

3.2.1   Validation of the Curve Shortening Flow

The validation of the curve shortening flow as an energy minimization for varying metrics independently of the rest of the magnetic filament theory was already performed in section 2.4.2 [Examples of Length Minimizations]. There, the quasi-Newton method established in definition 36 was tested if it can successfully reproduce the well known geodesics of the Euclidean space, the Poincaré-disc model and the Poincaré half-plane model, which it faithfully did.

Additionally, the quasi-Newton method also correctly reproduced the analytically derived geodesics of the gas metric for polynomial pressure model (definition 19), which additionally

verifies our analytic solutions of theorem 27.

Note again that as discussed in section 2.4.3, we do not posses an entry point to evaluate the quality of the plasma metric u computation due to the unavailability of a ground truth for the magnetic field. This also makes it impossible for us to numerically evaluate the output of the grad u_{mag} computation.

3.2.2 Potential Field Limiting Case

A strength of our approach is that we deal with the entire MHS equation. As mentioned in the related work section many solar magnetic field methods neglect the influence of the gas pressure in favor of only having to solve for a force-free field (curl $\mathbf{B} \times \mathbf{B} = 0$). What happens in our model when we reduce the influence of the gas pressure? It should approach the force-free results! The following theorem captures this.

> **Theorem 40 (FFCS to PF limit at low pressure p).** In the limit of $p \to 0$, the magnetic field established by the FFCS model collapses to the magnetic field of the PF model.

Proof. Our definition of the FFCS model's domain decomposition (definition 2) involves the *gas domain* $\mathbb{M_0}$ and the *flux domain* $\mathbb{M_B}$:

$$\mathbb{M} = \mathbb{M_0} \cup \mathbb{M_B}.$$

We will now show that when $p \to 0$, that the gas domain will vanish in the FFCS model during the energy minimization. When that happens, only $\mathbb{M} = \mathbb{M_B}$ remains with a potential field inside of it which then has to be the PF field.

From theorem 6 we know that we require a gas-flux pressure equilibrium at the interface $\mathcal{I} = \mathbb{M_0} \cap \mathbb{M_B}$ in order to have a valid MHS solution. From theorem 11 we know that extrema of the MHS energy $\mathcal{E}$ determine MHS solutions in the FFCS model. For $p \to 0$ the gas-flux equilibrium and the MHS energy $\mathcal{E}$ behave as follows:

$$\lim_{p \to 0} \left[p = \frac{B^2}{2\mu_0} \right] \quad \Leftrightarrow \quad [0 = B], \quad \text{on } \mathcal{I} \tag{3.1}$$

$$\lim_{p \to 0} \mathcal{E}(\mathbb{M_B}, \mathbf{B}) = \lim_{p \to 0} \int_{\mathbb{M_B}} \left(p + \frac{B^2}{2\mu_0} \right) = \frac{1}{2\mu_0} \int_{\mathbb{M_B}} B^2 \tag{3.2}$$

Since B won't ever be 0 in $\mathbb{M_B}$, equation 3.1 can only be dealt with if $\mathcal{I}$ vanishes, which is the case when $\mathcal{I}$ is at infinity, which is equivalent to saying that the gas domain does not exist, *i.e.* $\mathbb{M_0} = \emptyset$.

The energy minimization of equation 3.2 is familiar from section 1.3.1. There we already established that the minimizers given a Neumann boundary condition are potential fields

(PF) of the form $\mathbf{B} = \operatorname{grad} \phi$. Since $\mathbb{M} = \mathbb{M}_{\mathbf{B}}$ and the boundary condition comes from the surface of the sun this is the solution of the PF model. This concludes the proof.

<div align="right">□</div>

In our practice, weak pressure p means that our discrete magnetic filaments can expand without external resistance. The radii r_{opt} a filament would have to be in balance with the gas pressure (definition 25) becomes infinite as $p \to 0$

$$\lim_{p \to 0} r_{\text{opt}}(\mathbf{x}) = \lim_{p \to 0} \frac{1}{\sqrt{2\pi}} \frac{\sqrt{h}}{\sqrt[4]{2\mu_0 p(\mathbf{x})}} = \infty$$

This will cause our magnetic filaments to keep expanding forever and it will also create issues with radii being too large relative to the filaments' curvatures. As a reminder: smooth magnetic filaments (definition 20) have small radii w.r.t. their curvature to avoid buckling. The radii even become so big that their overlap with the sun's surface itself becomes an issue. This is also why in the $p \to 0$ limit, our analytic geodesic solutions are not applicable. As mentioned earlier in theorem 38 (**Minimal Initialization**), our analytic geodesics are solutions in the *high pressure limit $p \to \infty$*.

Remember that for the discretized case the topology remains fixed. For our given Neumann boundary condition Φ the potential field is the global energy minimizer as mentioned in the related work section 1.3. Because the PF topology might differ from our initial topology, we might actually not be able to reach the global energy minimizer during the energy minimization process, even when $p \to 0$. Thankfully, the initialization method we provided in section 2.5 mitigates this problem as the initial matching already has low (maybe minimal) topological twists and inter-linkages.

FFCS to PF Limit Experiment

Nevertheless, even without proper convergence due to the infinity radii expansion magnetic filaments would have in the $p \to 0$ limit we can still plug some filaments into our machinery and see what happens at extremely small values of p_0 in the polynomial pressure model

$$p(\mathbf{x}) = p_0 \left(\frac{|\mathbf{x}|}{r_\odot} \right)^{-\lambda}.$$

As the input we take a simple magnetogram of a sun spot pair and compute the PFSS field from it using the python *pfsspy* package. We then compute our discrete magnetic filaments using a very small value for p_0. From the midpoints of our discrete magnetic filaments we then volume trail field lines in the PFSS field so that we can directly compare the outputs.

The result of this experiment is shown in figure 3.13. Qualitatively, the field lines match pretty well. We take the result as evidence that the numerics of our filament FFCS model is correct enough to reproduce this theoretically predicted example. An issue arises near the surface were the overlap with the sun itself becomes a problem since we don't have good rules

regarding the filament-surface interaction. For now, we only constrain the filament's central curves to not cross the surface.
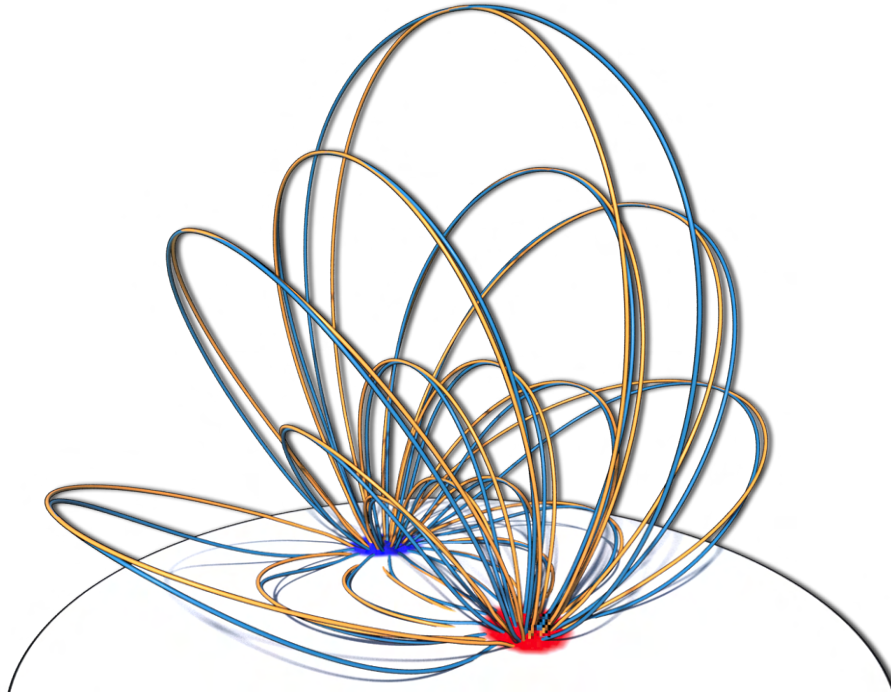

Figure 3.13: The result of our experiment to compare the output of our discrete magnetic filament model in the low pressure limit (blue) with trace field lines of a potential field model volume grid (yellow). As predicted theoretically, they exhibit qualitatively the same shapes with the only exception being the discrete filaments that are too close to the sun's surface where we prevent the filaments center curves from touching the surface.

3.2.3 Boundary of Flux Region Validation

Let us study how thick our discrete magnetic filaments become. The interface $\mathcal{I}$ between the gas domain $\mathbb{M_0}$ and the flux domain $\mathbb{M_B}$ is where our discrete magnetic filaments need to satisfy the gas-flux pressure equilibrium $p = {}^{B^2}\!/2\mu_0$. The thickness of the outer layer of filaments should be determined by the exterior pressure p.

Away from the interface, the filaments prevent each other from becoming thicker through the no-overlap constraint. At the interface, the filaments should reach their maximally achievable size. Let us design an experiment to verify the thickness computation of our filaments:

Filament Ring Link Experiment

We build a setup with constant pressure $p \equiv p_0$. In that case, given a constant flux h the optimal radius r_{opt} is constant everywhere. To avoid any boundary effects, we initialize the

experiment without any boundary at all by initializing closed magnetic filaments.

A single closed magnetic filament with constant magnetic pressure will shrink under the energy minimization, so far that its curvature becomes too high *w.r.t.* its length and our model of smooth magnetic filaments becomes invalid (see definition 20). Evidently, without a fixed boundary, shorter filament carry less energy while having the same flux. Therefore filaments would completely collapse under the energy minimization.

In our experiment we avoid the filament collapse by initializing two interlinked flux tori of filaments. Due to the preservation of topology in our algorithm (see Section 2.5), these rings can't ever collapse to a point like a single ring would. Due to the constancy of r_{opt}, we predict that in the energy minimization of the linked flux tori should results in an outer layer of filaments with constant thickness. Figure 3.14 shows our experiment that successfully reproduces this prediction. We show a slice of the interlinked flux tori to make this more clearly visible.
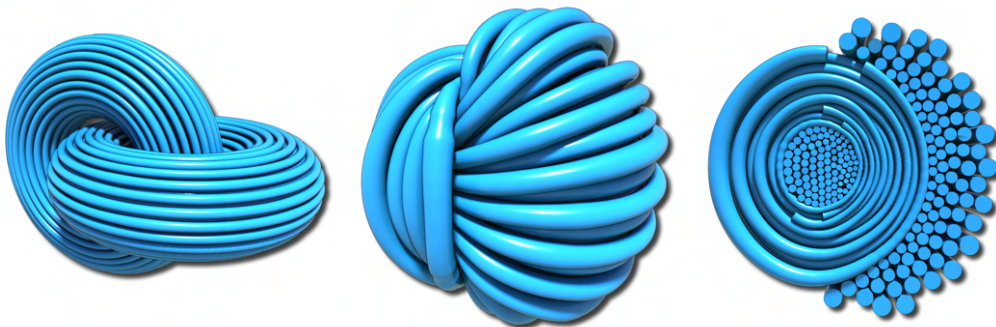

Figure 3.14: In a setting with constant pressure $p \equiv p_0$ we initialize two linked flux tori (left). After energy minimization we successfully see filaments of constant thickness on the outer layer as predicted (middle, right).

Conclusion About the Validation of Numerics

We have established some test cases and made predictions on their outcomes. We saw that these theoretically predicted outcomes agreed with the output of our algorithm in various situations, giving us confidence in the validity of the output in the more complex situations.

Due to the inaccessibility of a comparable ground-truth for magnetic fields, we are not able to just straight forwardly compare the outputs for numerical error. Another untestable output is the approximation error of the computation of the gradient of u_{mag}. We believe to have conducted the best tests available given these circumstances.

3.3 Validation of FFCS Model Applicability

Starting with a magnetogram of the sun, we would like to verify if the output after stippling, matching, initializing and energy minimization is valid. This again comes with the issue of

not having a ground truth magnetic field available to directly compare with. Thus, instead of directly comparing the magnetic fields, we rely on comparing visualizations of the magnetic field, which allows us to compare the output with other research. In the case of clearly visible plasma filaments in the EUV spectrum, we can also check if the traced magnetic field lines follow these filaments.

Additionally, thanks to the glow model established in section 3.1.2, we can also validate the magnetic field output by applying the glow model on it and then comparing the glow model output to NASA's EUV footage of the sun. In this section, we will focus on validations prior to the application of the glow model and leave those comparisons to section 3.4 [Validation of the Glow Model].

3.3.1 Comparison with PFSS

PFSS is the most used method for solar magnetic field visualization and still used by NASA's SDO mission as the primary magnetic field visualizer. In their daily uploads they also include images with overlays of PFSS traced field lines. We will now compare visualizations as such of the PFSS field with our output. As a reminder, PFSS computes the potential field (PF) using an outer source surface.

In section 3.2.2 [Potential Field Limiting Case], we saw that as the pressure p goes to zero, the FFCS model output will resemble that of a PF [theorem 40, **FFCS to PF limit at low pressure** p]. We are going to make the same statement for fixed pressure and rising magnetic field strength.

> **Theorem 41** (**FFCS to PF limit for strong magnetic fields** B)**.** In the limit of scaling $B \to \infty$ while p is held fixed, the magnetic field established by the FFCS model collapses to the magnetic field of the PF model.

Proof. We will show that scaling B is equivalent to a reduction of p, and then apply the already established theorem 40 [**FFCS to PF limit at low pressure** p] to draw the same conclusion of the collapse of the FCSS model to a PF model.

Scaling $B \to \infty$ means that we define $\tilde{B} := B_0 \cdot B$ and let $B_0 \to \infty$. In practise, this means that the magnetogram on the surface of the sun becomes stronger with increasing values of $B_0 > 0$. The minimization of the MHS energy $\mathcal{E}$ reaches a valid solution of the FFCS model if the gas-flux pressure equilibrium is met (theorem 11), which we can rewrite:

$$p = \frac{\tilde{B}^2}{2\mu_0} = \frac{(B_0 B)^2}{2\mu_0} = B_0^2 \frac{B^2}{2\mu_0}$$

$$\Leftrightarrow \quad \underbrace{\left(\frac{p}{B_0^2} \right)}_{\tilde{p}:=} = \frac{B^2}{2\mu_0}.$$

Thus, the coeeficient B_0 can be entirely absorbed in the pressure. $B_0 \to \infty$ with fixed

pressure is then equivalent to $\tilde{p} \to 0$ with fixed magnetic field for the gas-flux pressure equilibrium. Stating this, we have arrived at the conditions of theorem 40 from which we can now directly infer the statement of this theorem.

$\square$

Theorem 41 is interesting because it tells us how gas pressure scaling and magnetic flux scaling are equivalent for the structure of our solution. In solar physics literature, the ratio between gas pressure and magnetic pressure is referred to as the β-number [Gary(2001)]. A low β-number corresponds to relatively weak gas pressure. We note the following observations:

- Decreasing gas pressure.
  - $\Rightarrow$ Decreased resistance of the gas domain $\mathbb{M_0}$ pushing against the flux domain $\mathbb{M_B}$.
  - $\Rightarrow$ The flux domain M_B expands while the gas domain $\mathbb{M_0}$ shrinks.
- Increasing magnetic flux.
  - $\Rightarrow$ Increase strength of the flux domain $\mathbb{M_B}$ pushing against the gas domain $\mathbb{M_0}$.
  - $\Rightarrow$ The flux domain M_B expands while the gas domain $\mathbb{M_0}$ shrinks.
- Increasing gas pressure.
  - $\Rightarrow$ Increased resistance of the gas domain $\mathbb{M_0}$ pushing against the flux domain $\mathbb{M_B}$.
  - $\Rightarrow$ The flux domain M_B shrinks while the gas domain $\mathbb{M_0}$ expands.
- Decreasing magnetic flux.
  - $\Rightarrow$ Decreased strength of the flux domain $\mathbb{M_B}$ pushing against the gas domain $\mathbb{M_0}$.
  - $\Rightarrow$ The flux domain M_B shrinks while the gas domain $\mathbb{M_0}$ expands.

Evidently, increasing B_0 is equivalent to decreasing p_0 when dealing with the gas-flux pressure equilibrium. The resulting field structures are the same, with a difference in the magnitude of B. The glow model however would react differently with changing values of B.

3.3.2   Direct Comparisons

Let us look closer at the magnetic field line outputs in various settings.

Comparison with PFSS Traced Field Lines at Strong Flux Areas

Theorem 41 tells us that in the case of strong magnetic flux on the surface of the sun, we can expect the output of the FFCS model to be similar to that of a potential field. This motivates us to compare the magnetic filaments output by our algorithm with the traced field lines produced by PFSS in other people's works when they attempted to overlay PFSS field lines on footage. Figure 3.15 shows this comparison. Qualitatively, we think that our field lines do a better job at following the field lines of the footage.

Comparison with PFSS Traced Field Lines at Moderate Flux Areas

We define areas of moderate magnetic flux as areas where the magnetic field is not dominant enough for the FFCS model to collapse into a potential field model and also where the
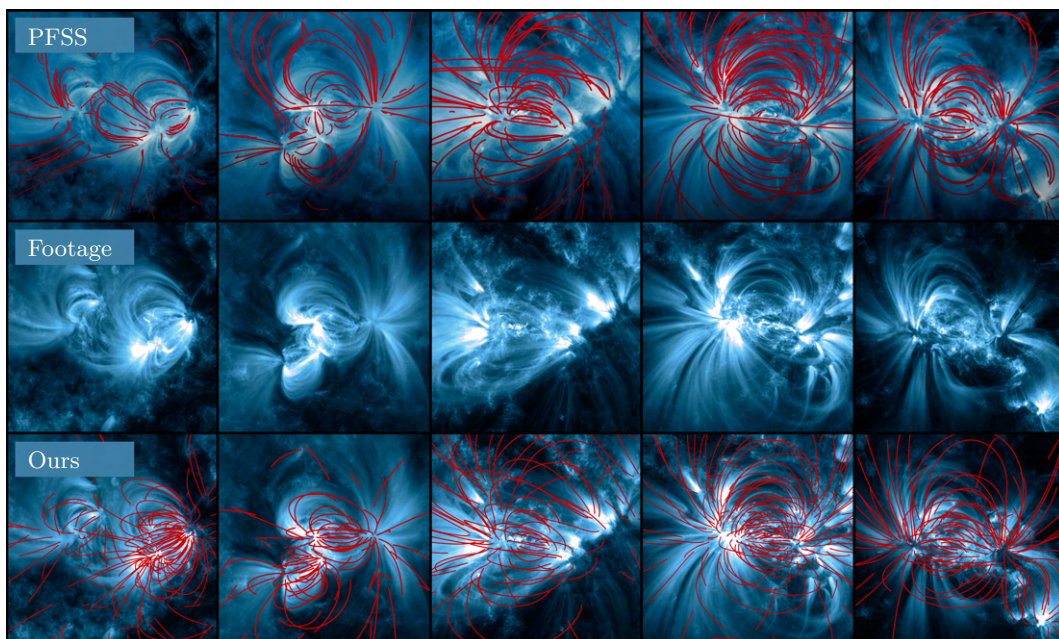
Figure 3.15: PFSS field lines [Warren et al.(2018), Fig. 9] (top) compared to NASA SDO's AIA171 footage (middle) and our magnetic filaments (bottom). We chose the blue color for the background footage because it was the choice in the above mentioned publication.

magnetic flux is not so weak that the pressure becomes completely dominant and the magnetic field solution collapses into the ideal filaments matching result established in theorem 38 [**Minimal Initialization**].

An intrinsic problem of trying to validate moderate magnetic field structures is that these are rarely visible in the EUV footage precisely because they are not strong. The emissions of EUV photons are determined by the density and the temperature of the plasma trapped by the filaments as explained in section 3.1.2. For moderate magnetic fields, our glow model predicts far weaker emission too. Therefore, it is hard to make a visual comparison, the field is barely visible.

However, we can still make a qualitative statement about the structure of the field lines in the medium flux case. In the potential field model we have $\mathbb{M}_{\mathbf{B}} = \mathbb{M}$ and $\mathbb{M}_{\mathbf{0}} = \emptyset$, and thus the whole exterior of the sun is filled with field lines. This also means that field lines with footpoints on the sun that are significantly far away from each other can still be connected. In contrast, our FFCS model predicts that $\mathbb{M}_{\mathbf{B}} \subset \mathbb{M}$ and $\mathbb{M}_{\mathbf{0}} \neq \emptyset$, meaning that certain areas simply won't have a magnetic field. This enables our magnetic field to have shorter field lines that are closer to the surface, a prediction that is indeed realistic according to [Wiegelmann and Solanki(2004b), Wiegelmann and Solanki(2004a)].

Figure 3.16 compares the near surface PFSS field with the near surface magnetic filaments. For the sake of compariswe translated the PFSS grid into a filament field by tracing field lines and computing their radii. The fields are cut off at a certain height for visual insight

purposes. We can clearly see that in our model, the magnetic field stays closer to the surface of the sun in weak or moderate flux regions. The PFSS field does indeed maximally expand and spread/smooth out wherever it can while our FFCS model field is far more concentrated. This concentration of field lines is then responsible too for the visual glowing features and the *fibered* nature of the solar magnetic field.
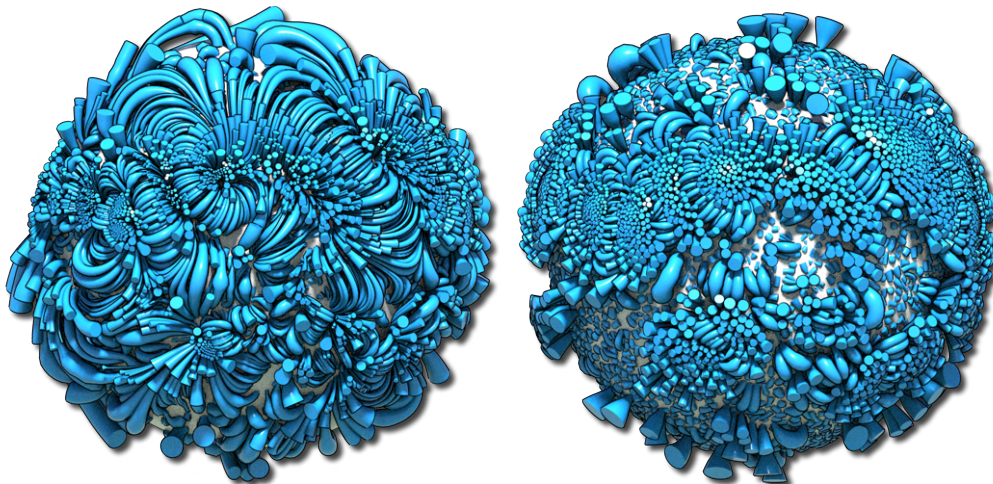

Figure 3.16: Comparison of the near surface fields in the PFSS model (left) and our FFCS model (right). On the left, an equal number of field lines were traced and visualized like thick filaments. We notice that the PFSS field has a strong tendency to spread/smooth out far into space also in areas of weak flux. In contrast, our FFCS model allows more concentrated fields, yielding a more *fibered* magnetic field as observations suggest. The underlying magnetogram was captured on the 21st of October, 2011.

Filaments Higher Up from the Surface

Let us turn an eye on our FFCS model's behaviour in the higher up regions. In order to save computational costs, our algorithm treats very far regions as negligible, and thus cuts/deletes filaments sections that stray too far away. The motivation to do so is that these regions are not visible in any emission spectrum and their magnetic field is too weak to meaningfully interact with the visible features near the surface. Let us now closer observe how the field behaves higher up from the surface before our model becomes invalid.

We compare our results from the FFCS model with the PFSS model and another non-PFSS model in the style of the authors of a comparative study [Yeates et al.(2018)]. Their visualisation traces the field lines of points close to the limb of the viewing point only. For our model, we delete all the filaments that are not near the limb.

Figure 3.17 shows this comparison and illustrates how the PFSS model, as implemented in the *pfsspy* package, makes the active regions far more expansive. In contrast, our model has a lot more activity concentrated close to the surface, an observation that goes well with the

NLF-OP method that we compare with too. The NLF-OP method is a volumetric non-linear force-free field method based on local optimizations and requires vector magnetogram data (which is more than just the flux data we require as input, thus putting this method in a different class) [Tadesse et al.(2014), Wiegelmann(2007)]. The data used by all three examples are the vector flux synoptic map and the normal flux synoptic maps during a total eclipse in early 2015.
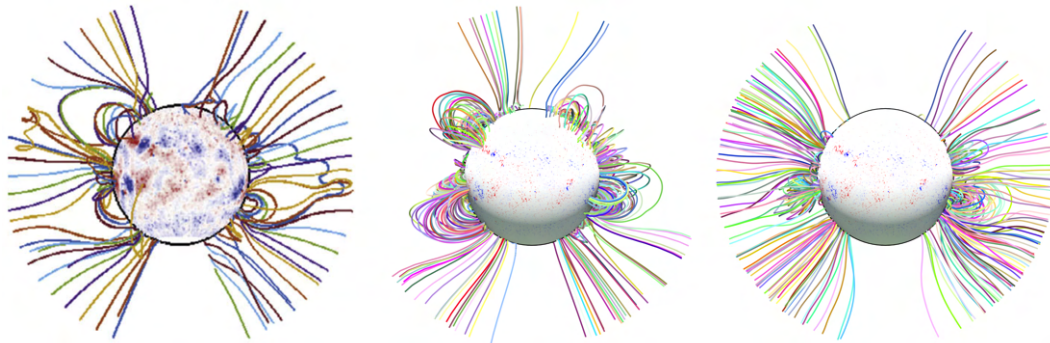

Figure 3.17: The far magnetic field during the eclipse on Mar. 15th, 2015 reconstructed by the NLF-OP model (left, courtesy: [Yeates et al.(2018), Fig. 7]), the PFSS model (middle) and our model (right). The flux data used here comes from the synoptic map CR2161 that was stitched together by 26 days worth of magnetograms.

Additionally, we primitively visualize the far field using a simplified variant of the glow model where the visibility does not drop away from the sun. This enables us to compare the basic structure of the magnetic field with the structure seen on a photo taking during a total solar eclipse. Figure 3.18 compares a solar eclipse photo with our FFCS version and the PFSS version where we added the moon to simulate an eclipse and to focus on the comparison.

Note that for figures 3.18 we focused on having decent data at the limbs. This is not possible to have from magnetogram data as they only provide the *line-of-sight* component of the surface field. To circumvent this issue, we used the synoptic map CR2161 and rotated it to fit the image. This also means that the comparison with the original image is not entirely fair. See section 1.2.3 where we discussed this issue.

Conclusion About the Validation of FFCS Model Applicability

We have now tested the FFCS model with our discrete magnetic filament application in several occasions and witnessed that it behaves as predicted. We think that it provides plenty of evidence for the correctness of our model in these situations. We confess that we wish to provide stronger evidence than this, but the inaccessibility of a comparable ground-truth denies this. Hopefully, future research and solar physics satellites such as NASA's *Parker Solar Probe Mission* can provide us with such data.
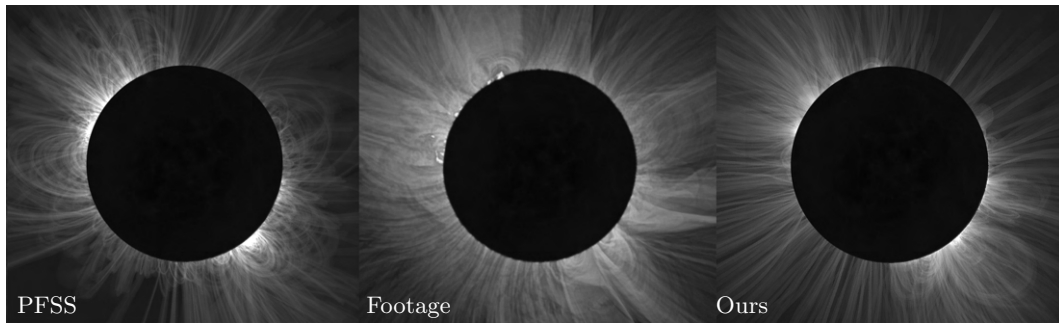
Figure 3.18: The far magnetic field (middle, Image by Miroslav Druckmüller, Shadia Habbal, Peter Aniol, Pavel Štarha) during the total solar eclipse on Mar. 15th, 2015 reconstructed and rendered by our model (right) and the PFSS model (left). Potential fields as in the PFSS model have a tendency to spread out in large arcs, unlike the actual field in the footage. The computation was conducted on the synoptic map CR2161 to get more or less a valid flux data on the limbs. To compare this output with figure 3.17 this needs to be adjusted for photographic rotation.

3.4   Validation of the Glow Model

The only way to really validate the glow model is to compare our output with the data measured by NASA's SDO mission. As mentioned in section 3.1.1, the most common wavelength used to observe the plasma filament structure is 171Å, which is thus chosen to be our default wavelength for our algorithm output.

3.4.1   Comparing with NASA's SDO Footage

The main objective of the glow model is to create similar footage to the one that is captured by NASA's Solar Dynamics Observatory (SDO). To this end, we take a particularly feature rich image and compare its output in figure 3.19. We begin with the magnetogram, stipple the surface, initialize curves, minimize the energy, and apply the glow model on the output.

The PFSS method, as an Eulerian volumetric grid method, is not suitable for our Lagrangian filament based glow model. We again translated the PFSS grid into a filament field by tracing field lines and computing their radii, essentially pretending that they are the output of some other Lagrangian filament model and treating it equally in the eyes of our glow model.

We think that our output does a better job in capturing the visual features of the solar activity of the original footage. While we acknowledge that the PFSS field and our output are at least similar regarding the field line structure in the areas of glow. We see that the glow model does not work very well with the PFSS output.

Note again that in this example, the magnetogram provides only the *line-of-sight* magnetic surface flux. This is why our model breaks down near the limbs of the footage, where we simply have no flux data available. Both the PFSS version and our version use the
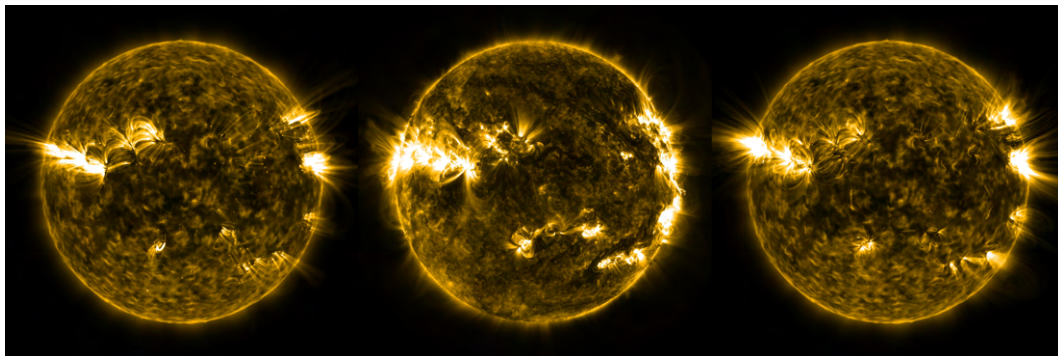
Figure 3.19: Real footage of the solar atmosphere on Oct. 21st, 2011 (middle) compared to the output from our rendering method applied on the PFSS model (left) and our algorithm (right) computed from the corresponding frontal flux map.

same parameter ρ_0 in the glow model.

3.4.2 Comparing Temperature Response Functions

The temperature response function of the wavelength 171Å is the sharpest, which is great to identify finer details. Looking again at the temperature response functions for different wavelengths in figure 3.5, we see that many other response functions have similar peaks and/or are much more smudged out. For our purposes, 171Å is the best, but observing the sun using other wavelengths reveals other information that is also valuable. In particular, the X-Ray 94Å wavelength responses to extremely high temperatures, thus showing where extreme heat is concentrated.
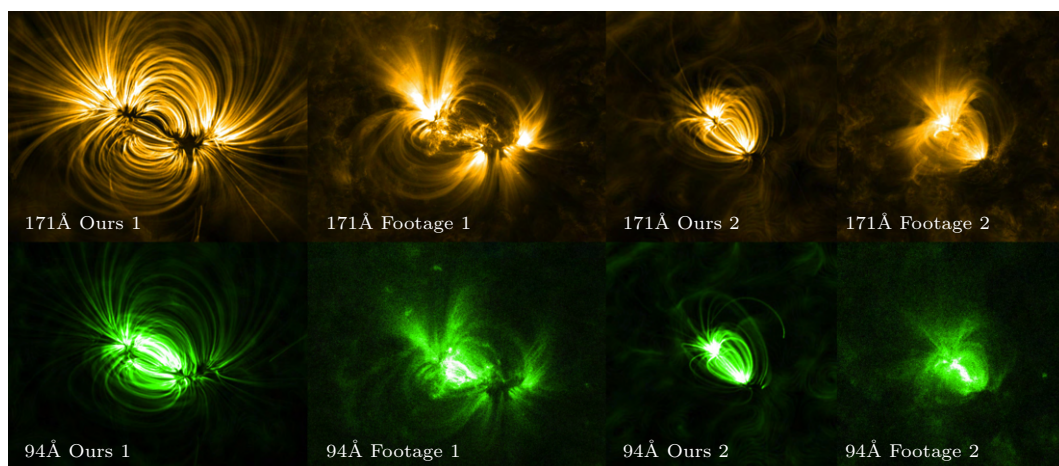

Figure 3.20: Comparisons of our output to images of [NASA Solar Dynamics Observatory(2023)] in extreme ultraviolet (171Å, gold) and X-ray (94Å, green). Left half: The region studied in [Williams et al.(2020)]. Right half: An active region on June 19th, 2010 (compare [Warren et al.(2018), Fig. 8]). 171Å images are sharper, while 94Å images can give more information about the areas of extreme heat.

We compare the results of our algorithm output and glow model with EUV 171Å and X-Ray 94Å footage in two cases in figure 3.20. We used the corresponding magnetograms and ran it as the input through our entire algorithm pipeline. For comparison purposes, we chose these two situations because they appear in the works of [Williams et al.(2020)] and [Warren et al.(2018), Fig. 8]. The difference between our 171Å and our 94Å output is that we simply swapped the temperature response function (as found in figure 3.5) and followed the different coloring convention (as found in figure 3.7). Both cases use exactly the same glow model. Evidently, figure 3.20 shows that in these cases the heat is substatially greater in the middle of the sunspot pair, a quality that our glow model captures too.

3.4.3   Varying Footpoint Density ρ_0

In the glow model of section 3.1.2 we fixed the density ρ_0 at the footpoints globally. We assume that this density varies on the surface, but we decided to fix it as a simplified approximation. One of the reasons we wanted to fix ρ_0 globally was because if we did not, it's spatially varying degree of freedom would allow us to specify any desired temperature T we want at the footpoints. This, in turn, would be too much freedom for the glow model and one might as well specify the temperatures first for a specific glow and then adjust the density to fit this requirement. We had also tried to establish a relation between the magnetic flux and good estimates of ρ_0, but with no reasonable dependency model was found.

We study the effects of varying ρ_0 in figure 3.21. Adjusting ρ_0 results in a shift of the temperatures, thus updating where the peaks of the temperature response functions (from figure 3.5) are met in the scene.
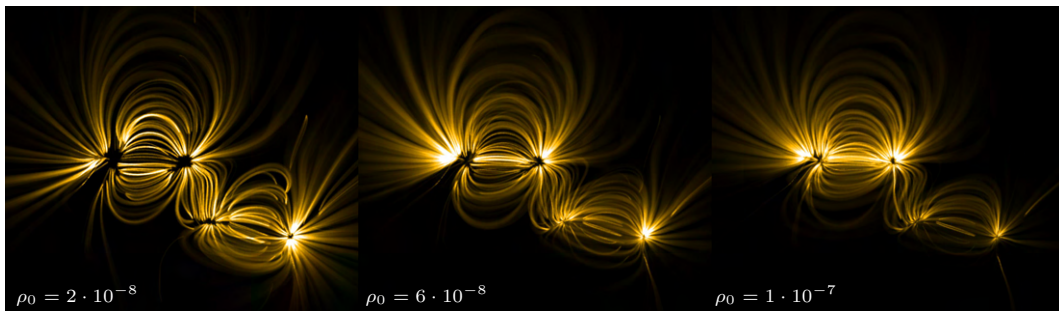

$\rho_0 = 2 \cdot 10^{-8}$ $\rho_0 = 6 \cdot 10^{-8}$ $\rho_0 = 1 \cdot 10^{-7}$

Figure 3.21: Glow of an active region from Apr. 19th, 2011 computed for $\rho_0 = 2 \cdot 10^{-8}$ (left), $\rho_0 = 6 \cdot 10^{-8}$ (middle) and $\rho_0 = 1 \cdot 10^{-7}$ (right). The same region was used in [Warren et al.(2018), Fig. 9] and the real footage is shown in the last column of figure 3.15. Adjusting ρ_0 shifts the temperature and thus it determines where the peak emission happens according to the temperature response function. No background layer was used in these images.

In the experiments in this work, we do not have a single fixed ρ_0 for all cases. In particular, the full sun shot like in figure 3.19 made us realize that there is no single ρ_0 that fits all the regions on the sun. In certain regions, a different ρ_0 yielded better results. The

close-up shots of figure 3.20 for example don't have the same ρ_0 in the two depicted events. The good news is that ρ_0 did not vary much in all of our examples.

Conclusion About the Glow Model

This entire dissertation was never set out to go into such detail about a glow model, but we realized on the way that it was a necessity to derive some functional approach in order to visualize the results. There is a lack of visualisation techniques for solar imagery. We have not yet seen any comparable model that results in images that can be compared to NASA's SDO footage with such level of detail.

We believe that the glow model has still plenty of space to be improved upon and hope that this dissertation can serve as inspiration to do so. This concludes the validation and testing section. We will now clarify where this dissertation stands, the contribution it makes and their applications.

3.5 Application: Magnetic Field Modeling

This dissertation provides a novel way to approach the modeling of the solar atmosphere using Lagrangian elements as primitives. We established discrete magnetic filaments as curves with thickness which allow us to concentrate all the computational effort into the region were we want more details. In a world full of grid based solvers, this alone makes our model a valuable addition.

We also tackled the magnetohydrostatic equation. Currently, many models still focus only on force-free fields, which is the case when the gas pressure is neglected. We believe that the gas pressure does have significant impact on the physics of the magnetic field, which we backed up in section 3.3.

Our framework may now be an additional tool for modeling the magnetic field of the sun. It is likely not the simplest to implement at the current state, but it opens up a new alley to explore results and our validation section 3.3 provides reassurance that this is a safe alley to go down in. This framework could be used as input for further experimentations, where a relaxed magnetic field is required as an initial condition. Or one could initialize complicated topologies and see where it goes in the relaxation process.

Speaking of topologies, we also tackled the matching problem, which is great for proposing a reasonable initial topology fast. This could be of great use in future research when requiring some initialization.

The quasi-Newton method for curve shortening is novel to the best of our knowledge. It itself could spark spin off projects, such as the stable computation of n-dimensional geodesics in any metric and the many applications thereof.

One could also augment the curve shortening algorithm to incorporate reconnection analogously to the vortex filament reconnection seen at [Weißmann and Pinkall(2010)]. In their work, fluid viscosity is dropped initially in the derivation for their dynamics. Later then,

reconnection is implemented by computing a weighted sum of kinetic energy differences and filament lengths. Vortex filament reconnection requires some vorticity to happen even though it was initially discarded. Similarly, we could justify our magnetic filaments to reconnect when they approach each other without having to reintroduced diffusivity. This could potentially allow us to start with a much more chaotic initialization that then ends up disentangling itself thanks to reconnection.

Another spin off project is a new approach for knot relaxations like the one done in the flux tori in figure 3.14. See *Plasma Knots* by [Gross et al.(2023)].

3.6   Application: A Full Visualization Pipeline
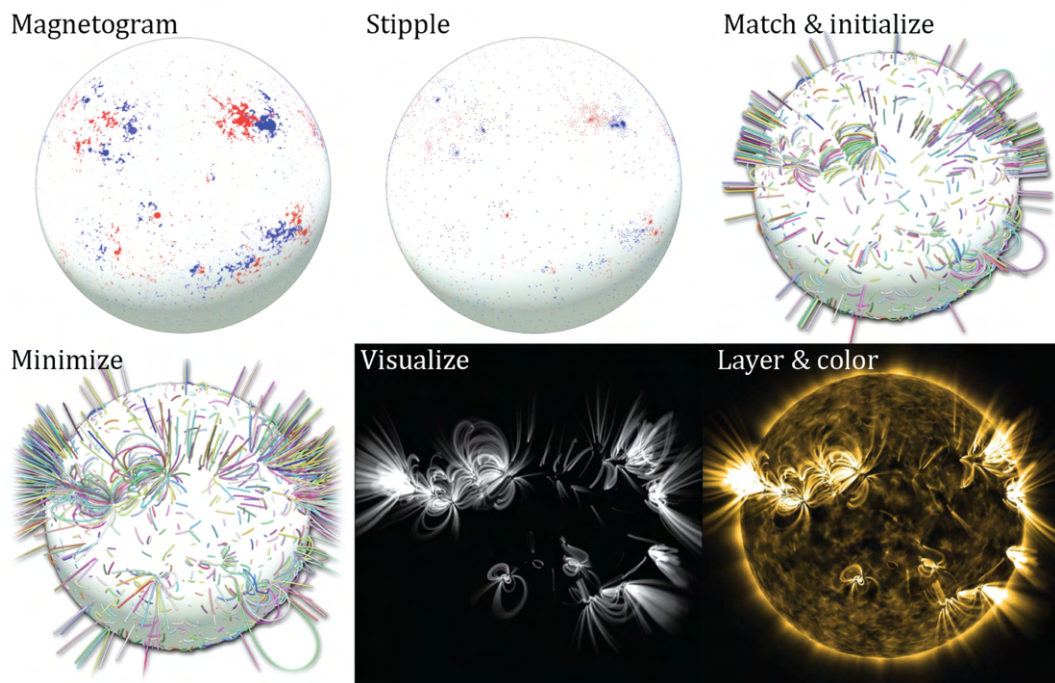

Figure 3.22:   The basic pipeline established in this dissertation. An initial magnetogram is stippled into points of equal flux. On these stipples we then solve the optimal matching problem to initialize discrete magnetic filaments on them. We then minimize the energy of these filaments and visualize the output using our glow model. We add background layers to the result and then color it according to common conventions.

Apart from proposing a magnetic field model, we also established a full pipeline that only requires a magnetogram as the input together with a few parameters that we will discuss here. Inside Houdini, we used python's *astropy* packages to import magnetograms onto meshes. From then on, the supplement material code provides the entire work automatically to generate solar images. The main steps of the pipeline (figure 3.22) are as follows:

- **Magnetogram:** The input is a magnetogram representing the solar surface's normal

flux. The magnetogram should have zero total flux.

- **Stipple:** The input magnetogram is stippled by points of equal flux.
- **Match and Initialize:** The stippled points are matched with each other by solving an optimal matching problem. Ideal filaments are created connecting the matched points to each other.
- **Minimize:** The filament set's MHS energy is minimized via the curve shortening flow according to the plasma metric.
- **Visualize:** Subfilaments are generated and the glow model is applied. The result is then rendered into a HDR image using floating points.
- **Layer:** We apply background layers for added detail by simply summing the resulting values into the HDR file.
- **Color:** The black and white output of the HDR file is then color mapped onto black-gold-white values in the case of 171Åimages.

3.6.1   Source Code

Our magnetic model was entirely implemented into SideFX's Houdini, a visual effects software that is widely used in the VFX industry for simulations. The *ytini* project [Naiman et al.(2017a)] has also created specific packages for astronomy visualisations in Houdini. We provide the source code to run some examples as supplementary material on the following github link:

https://github.com/marcelpadilla/Filament-Based-Plasma

3.6.2   Performance and Refinement Thereof

Table 3.2 displays the number of vertices and the computation times of some of our examples when executing our algorithms on a Ryzen 7 5800X CPU.

Application	Vertices	Initialization	Minimization of $\mathcal{E}$
Fig. 1	≈69k	0.98s	2:04min
Fig. 3.24	≈66k	2.86s	2:06min
Fig. 3.19 Ours	≈35k	2.1s	2:36min
Fig. 3.20 Left half	≈15k	0.073s	13.49s
Fig. 3.20 Right half	≈3k	0.082s	9.66s

Table 3.2: Computation times and parameters for our algorithm. Initialization refers to the combined computation time of stippling, matching and initializing curves. The last column shows the computation time of algorithm 5 [**Energy Minimization**].

As we can see, the initialization using the matching of stipples was relatively fast. This is because we turned the matching problem into a sparse matching problem (see section 2.5). Most of our computation time came though the energy minimization process. In it, we cycle between curve shortening steps and metric computations. The curve shortening is a local

and highly parallelizable operation, involving only the two neighbours of each point. Curve shortening imposed no computation hurdle. However, the real bottleneck comes from the way we compute our metric.

To compute the metric we need to make computations involving non-trivial neighbours. The two main instances are the computation of r_{opt} and grad u_{mag}.

- r_{opt} requires us to check the distance to neighbouring filaments to evaluate the closest distance for each point.
- grad u_{mag} requires us to sample u_{mag} in the neighbourhood in order to estimate the gradient.

The computations of these values themselves are not the problem, the problem lies in *determining the neighbours*. Each point needs to search for the nearest neighbours which are worth checking out for these computations. Determining such a list of neighbours is non-trivial and is by far the computationally most expensive operation in the entire algorithm.

To alleviate the computational cost, we resorted to simple tweaks for our algorithm. We reduced the search radius for candidate neighbours and avoid updating the list of neighbours in every single loop. This gave us a substantial performance boost, but we are well aware that more optimization is possible here.

Note that the objective of this work is the rigorous theoretical build up of this model and testing it. It was not made to compete computationally, nor was it optimized to its full potential for this reason. We believe that future optimization research will easily increase the performance. In table 3.3 we add the computation times of the highly optimized *pfsspy* package which was used to create all the PFSS examples in this work for comparison.

Table 3.3: Computation times for the PFSS field (*pfsspy* [Stansby et al.(2020)]) using data for Oct. 21, 2011 (figure 3.19) with different grid resolutions. *pfsspy* uses a curvilinear grid as its computation domain.

pfsspy resolution	Computation time
$720 \times 288 \times 50$	8.53s
$1440 \times 576 \times 50$	58.51s
$2160 \times 864 \times 50$	2:16min

Comparing table 3.2 with 3.3 exemplifies the differences between Lagrangian methods and Eulerian grid-based methods. Lagrangian methods can focus all of their computational primitives into the area of interest, saving a lot of computation time and enabling a significant increase in the amount of detail. Eulerian methods most of the time have to choose a static grid size. The desire to increase the amount of detail in one place requires the resolution of the entire computation domain to increase everywhere, which can easily be prohibitively expensive in a 3D environment.

3.6.3   Choosing Parameters

We concisely list the parameters and their use here:

- h: **The Flux Quantization**

  Description: The amount of magnetic flux per filament.

  Effect: One could call it the *strength* of each filament. Varying this parameter determines how many filaments are placed into the scene. A smaller value of h results in more, thinner filaments while a higher value of h results in fewer, thicker filaments.

- λ: **The Pressure Drop-Off**

  Description: The polynomial factor by which the pressure drops off by the height above the surface.

  Effect: It determines how strong the influence of the gas-pressure vanishes by height. A smaller value of λ means that the analytically derived ideal filaments can connect points on the surface that are farther away, thus increasing the computation time of the optimal matching problem (it becomes less sparse). λ also has a significant influence on the plasma metric and the optimal radius r_{opt}. A larger lambda will result in filaments that expand wider and thicker above the surface.

  For our sun, a value of $\lambda = 23$ works well. This values is closely related to the exact solution of the hydrostatic equilibrium of the solar corona of the sun if it were modeled by an exponential pressure model. Near the surface, the difference between the polynomial and exponential pressure model are small while the polynomial model blesses us with major analytical benefits (theorem 27). For general stars, λ is determined by the star's mass and radius.

- p_0: **The Base Pressure**

  Description: The pressure at the base of the solar corona.

  Effects: When extremely small values of p_0 are chosen the FCSS model approaches the potential field solution (theorem 40). In the high pressure limit of large values of p_0, we effectively inhibit the filaments from expanding radially at all ($r_{\mathrm{opt}} \approx 0$), making the global minimizer exactly that of the output of our optimal matching initialization (theorem 38). Thus, p_0 controls the influence of the gas pressure in our model and how much our magnetic filaments expand or compress.

- ρ_0: **The Footpoint Density**

  Description: The gas density at a footpoint used to determine the temperature of the glow model.

  Effect: Adjusting ρ_0 directly adjusts the footpoint temperature, which then determines the emission of the filaments according to the glow model. This is a visualization parameter that is only relevant in the glow model. When studying the magnetic field, ρ_0 is irrelevant.

We believe that a lot more can be improved about these parameters. For example, h is chosen to be the same value for all filaments. However, this was rather a convenience and

simplification. For the initialization, equal h makes the problem tractable. For the energy minimization however, this wouldn't be necessary.

Also, having a fixed footpoint density ρ_0 everywhere is pretty strict. This too was necessary to keep the problem tractable. For the glow model, one could vary ρ_0 just for visualization purposes by proposing relationships between ρ_0 and the magnetogram. We expect large amounts of follow up improvements possible to our novel and simple model.

3.7   Application: Visualization

A major motivation of this work was the visualisation of the solar corona by a physically based method. Here are some application notes regarding this.

3.7.1   Scientific Visualization

Scientific visualization serves multiple purposes. The main purpose is to compactly represent data in a way that allows the viewer to draw conclusions about it more easily. Another purpose is science communication, compiling complicated results into an intuitive understandable package for public accessibility and education.

In this work, we believe to have contributed to both of these purposes. In particular, the glow model is a much needed initial model to built the link between the naturally invisible magnetic field outputs to the visually attractive measurements from NASA's SDO publications.

3.7.2   Generating and Directing Solar Images

Apart from the use in scientific visualization, our set up also allows the generation and direction of solar-like imagery. Given our pipeline from the input magnetogram to the rendering output, a path for experimentation and artistic application becomes accessible.

One application example would be to generate magnetograms and test their visual output from this to study the EUV emissions at the limbs where magnetic flux data is unavailable, or to simply gain more insight on the visual properties in various scenarios. Our pipeline can also be the basis for basic experiments on field twisting as we will see in section 3.8.

Let's talk a little more about the input magnetograms. Where can we get magnetograms and how can we create our own?

3.7.3   Getting Real Magnetograms and Synoptic maps

Official magnetograms (HMI) and emission images (AIA) from NASA's SDO measurements are all available on the Joint Science Operations Center (JSOC) project hosted at Stanford:

http://jsoc.stanford.edu/

The site allows browsing every measurement taken in 45 second intervals since 2010. It is an amazing data base without which this dissertation would not have been possible. The data comes in form of matrices that need to be parsed using the python package *astropy*. Note that the magnetograms of these snapshots can only capture the line of sight component of the magnetic flux. The limbs and the back of the sun completely lack data (see figure 3.23 left). To eliviate this, JSOC also provides synoptic maps, which are the composition of 26 days worth of magnetograms (one solar rotation) to create one all-around map (see figure 3.23 right). They do however have a discontinuity in the back and do not correspond to any EUV image to compare with.
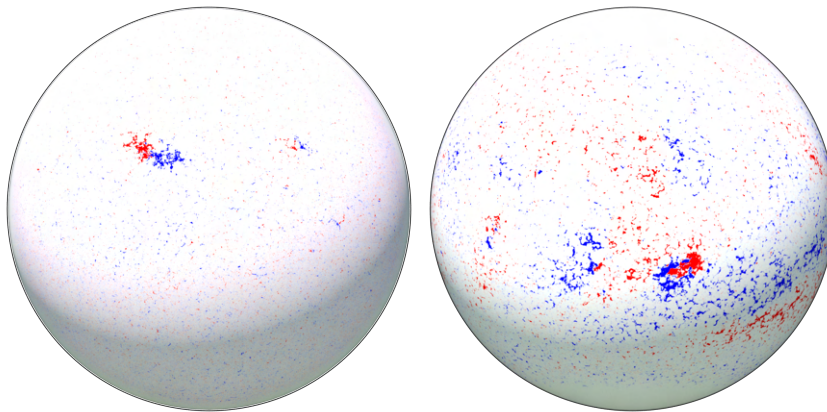
Figure 3.23: Left: A Real Magnetogram as downloaded from the JSOC project hosted at Stanford. Red areas indicate magnetic flux pointing outwards while blue areas indicate magnetic flux pointing inwards. Right: A synoptic map, a collection of 26 days of magnetogram latitude slices combined into one all-around map. It has a strong discontinuity on the back, and the differential rotation causes spatial shearing in this data. As with all magnetograms in this dissertation, the coloring displays the line-of-sight component of the magnetic field.

3.7.4 Crafting Magnetograms

Need to generate imagery of a sun with a physic-based system so that manual tweaking is minimal? Want to quickly control the amount of solar activity for dramatisation purposes? Just paint/generate a magnetogram onto a sphere and pick a value of h to balance out detail with computational costs. Then the magnetogram can be inserted into our pipeline to create an image of the sun. Figure 3.24 shows an example where we populated the surface of the sun with acm siggraph-logo like sunspot pairs. This type of application is artistically motivated.

3.7.5 Randomly Generating Magnetograms

We also provide a random magnetogram generation scheme. The distribution of sunspot pairs seems to be the sum of two Gaussians that have their mean slightly above and below the
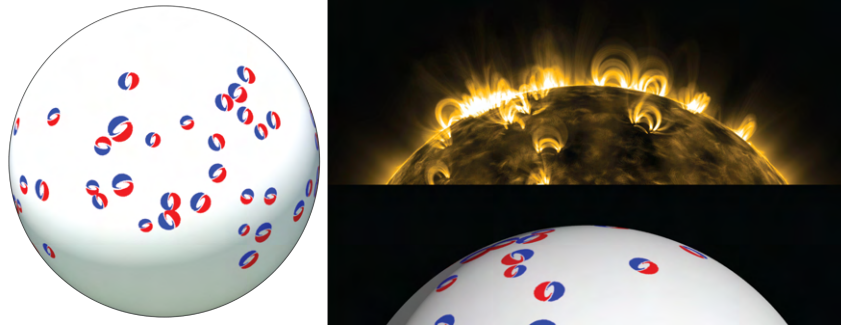
Figure 3.24: This magnetogram was crafted by us. We sampled points on the surface and then copied a sample sunspot pair inspired by the acm siggraph conference logo. Any magnetogram design is valid as long as the total flux is zero.

equator, as [Mandal et al.(2017)] have shown through data analysis. We use that information to sample sunspot pairs of equal strength across the sun and then apply noise masks to make these look far more natural. If, for any reason, the total magnetic flux is not zero, we can scale one of the two flux regions (positive or negative flux region) a little bit to create zero total flux.

By controlling the number of sunspot pairs we sample we can then generate stars that are as active as we want them to be. Figure 3.25 shows an example of this. The rendering with the glow model of this magnetogram can also bee seen in the teaser of this dissertation (figure 1 and figure 2). Figure 3.26 shows part of the visualisation pipeline and the filament usampling.
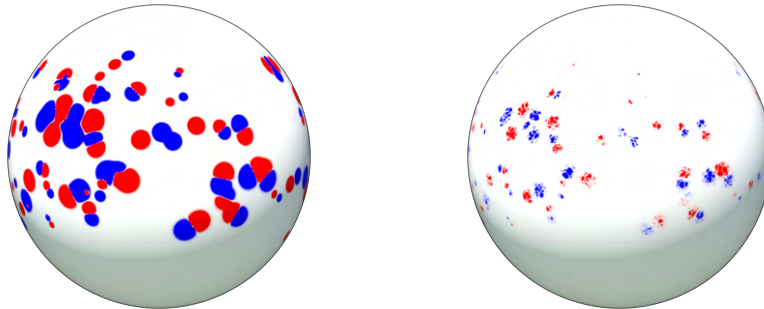

Figure 3.25: A randomly generated magnetogram. Left: We start by sampling random sunspot as gaussians pairs. We then multiply these gaussians with Manhattan cellular and Perlin noise masks to give them fine detail.

3.8 Experiment: Twisting Our Filaments

We also want to make space for a particularly interesting experiment that came to be thanks to our framework. Given that the magnetic field is frozen in the fluid (theorem 8), on the
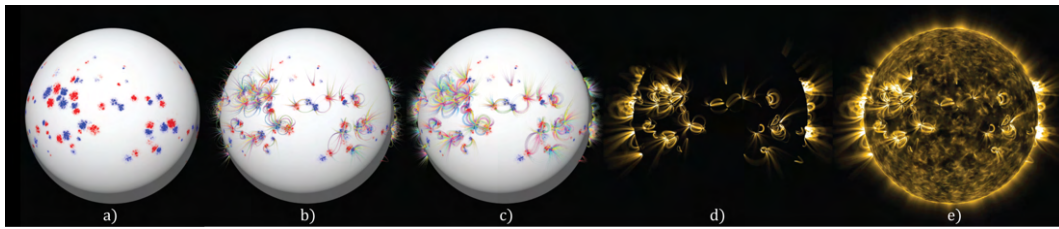
Figure 3.26: A randomly generated magnetogram (a) is used as input to be stippled and populated with curves. After energy minimization (b) filament upsampling is performed (c). These curves then serve as input in the glow model with some added glow variation (d) and the output of the glow model is then overlayed with the background layers (e).

surface of the sun where the magnetogram lies, one might assume that the ground truth magnetic field has to come with a time dependent topology that can't be extrapolated by a single magnetogram. While this is certainly the case, the impact of this is negligible in the majority of visible plasma filament structures. This is because the real life plasma obeys the non-ideal magnetohydrodynamic equations including diffusivity and magnetic resistivity which slowly dissipate topological twists and braids over time, simplifying the topology by reducing entanglements. However, some topologically twisting can still be found from time to time. Figure 3.27 shows two nice examples where the twist of the magnetic field structure becomes apparent through the plasma filaments.

Figure 3.27: Left: An image taken of twisted flux tubes (courtesy: Crimea Astrophysical Observatory). Right: an image of more twisted flux tubes by the TRACE Consortium (NASA). Twisted filament indicated twisted magnetic field structures.

Solar flares, explosive eruptions of plasma into the atmosphere, challenge the low twist assumption through their existence. Their dynamics are a still poorly understood as their energy build up is hard to analyse and measure. The basic theory is the following: viscous friction builds up heat inside the plasma, while magnetic resistivity causes the magnetic field lines to rearrange and release their energy in a process known as *magnetic reconnection*. On top of that surface flows cause twist in the topology, adding additional energy [Dixon

et al.(1989)]. This is however not the full story, as turbulent internal processes in the sun are also responsible for further energy build up. On top of that there seems to be a thermal instability cycle for plasma trapped inside filaments, causing plasma to move up and down in a process known as *coronal rain* [Antolin(2020)]. All in all, things are complicated, which is why the *coronal heating problem* is so difficult.

Despite this theoretical complexity, we decided to conduct an experiment to find out how the introduction of twist influences the MHS energy minimization. We will focus on the plasma filament's *footpoint motions as the main driver of this energy*. Due to the magnetic field being frozen into the plasma in ideal MHD (theorem 8) we can expect turbulent surface motions to distort the topology of the entire magnetic field. In our setting, this amounts to manipulating the footpoints of filaments. The hope is to highlight the role of twist in plasma filaments. We are motivated by related work proposing the surface twist to flare model [Prior and Yeates(2016b), Rachmeler et al.(2009)].

3.8.1   Twisting Experiment Set-up

How could we bring twists into our filament model? We will experiment on a simple scenario: a bundle of filaments connecting a sunspot pair. We could introduce twisting already at initialization, but that would require us to craft very complicated parametrizations of curves (figure 3.28).
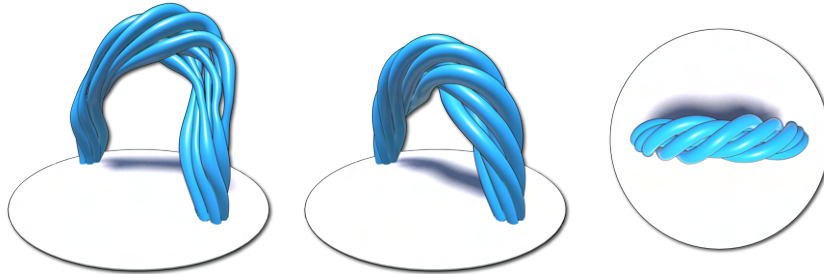

Figure 3.28: An initial configuration of twisted filaments is the input of our energy minimization. If the filaments are only slightly twisted, they end up in a stable configuration after energy minimization. In this set-up twist is not added continuously. Left: starting configuration that has some twist built in. Middle and right: after minimizing the energy we get a twisted and stable MHS solution.

We choose to start with an untwisted bundle of filaments and proceed to introduce the twist by only updating the boundary points. The idea is that our algorithm will automatically redistribute the twist along the whole curve through the energy minimization algorithm. This method of manipulating the input during the convergence of an algorithm is also known as *quasi-static viscosity evolution*. As a reminder, a *quasi-static evolution* is a sequence of solutions to varying input. If we adjust the magnetogram/boundary conditions and wait for complete convergence of the curve shortening flow at every input, we would end up with an

animation by quasi-static evolution. In contrast, a quasi-static viscosity evolution does not wait until full convergence before updating the boundary condition. The outcome is not mathematically sound as it depends on the convergence rate, but this approach is nevertheless used as a simple and computation efficient model which can still reveal basic properties about a system (see e.g. [Priest(2014), Sec. 1.9]). In our case the natural MHS energy minimization converges fast enough with respect to the boundary condition updates.
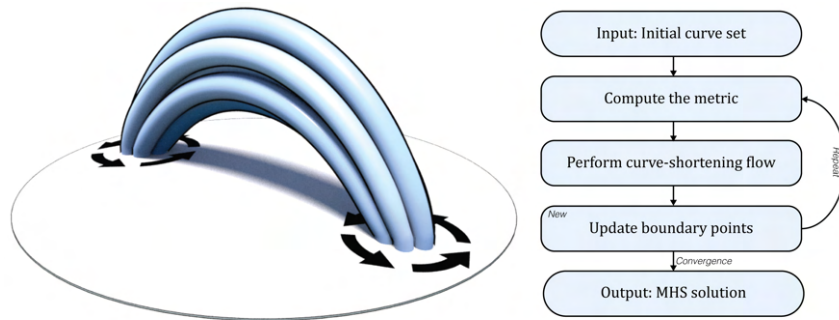

Figure 3.29: The basic experiment setup to introduce quasi-static viscosity evolution in order to study the effects of twist on the magnetic field. We twist a bundle of footpoints bit by bit and thus introduce topological twist, similarly to the way surface motion can distort the magnetic field of the sun. We revise our algorithm from section 2.4.4 to update the boundary points a little bit in the main loop.

The way we implement this is very simple. Algorithm 5 [**Energy Minimization**] iterates between computing the metric and performing a curve shortening step. We simply augment this loop with a call to slightly update the boundary condition. In our case we work directly with the filament footpoints and rotate them uniformly anti-clockwise with respect to the center of their sunspots. This is illustrated in figure 3.29. After reaching a certain amount of twist we stop updating the footpoints and keep the algorithm running as usual.

3.8.2 The Resulting Explosion

We run our energy minimization while twisting the filament bundle by its footpoints. Figure 3.30 shows a sequence of the resulting dynamics. At first, the twist evenly distributes throughout the filament bundles, but then the energy minimization causes the twisted filament bundle to rise higher and higher. The twist becomes more concentrated around the higher part of the filaments and the lower filaments appear untwisted. The higher part of the filaments is now outside of the visible domain of the solar corona and its magnetic field so expanded that its magnetic pressure becomes very weak. We are left with what looks like open field lines, field lines that exit the solar atmosphere before returning to the surface.

In figure 3.31 we track the MHS energy $\mathcal{E}$ during the quasi-static viscosity evolution. We see a rise in energy during the slow increase of the twist. After we stop twisting the footpoints we see an energy drop off after the already twisted filaments start moving upwards.
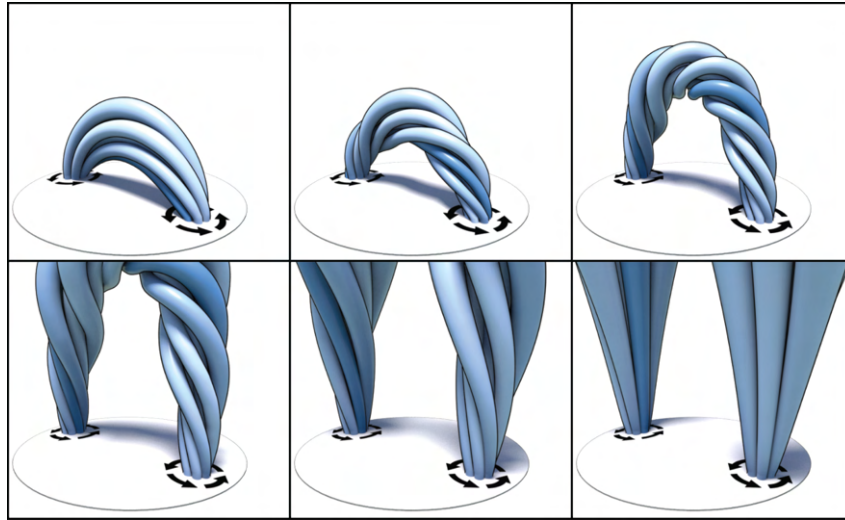
Figure 3.30: A sequence of our quasi-static viscosity evolution experiment. The initially untwisted filaments gradually build up more twist and thus more energy. At some point the twist becomes so big that the energy minimization causes the magnetic filaments to be lifted upwards rather than evenly distributing the twist.

The difference between this outcome and the result seen in figure 3.28 lies in the amount of twist added to the filament bundle. There is a critical amount of twist after which the filaments can no longer remain stable near the surface of the sun.

What makes this experiment so remarkable is that the sequence resembles a solar flare, the eruption of solar plasma into the upper atmosphere. We render these sequences too in figure 3.32 using the glow model (section 3.1.2). The energy difference of the twisted state and the erupted state is the amount of energy released by the solar flare. We see the match between the behaviour of our experiment and the proposed mechanism of solar flares through surface motion as further validation of the correctness and applicability of our theory and results.
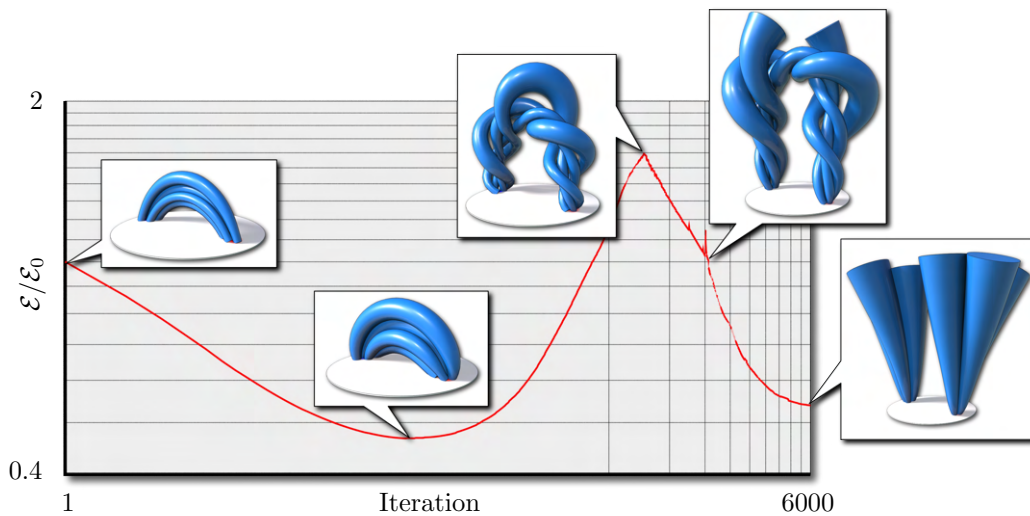
Figure 3.31: Time evolution and plot of MHS energy $\mathcal{E}$ (definition 34) of a *twisted* filament configuration over a single sunspot pair, obtained by moving the footpoints. This can be viewed as a model for a solar flare: in the twisted state the energy is larger than in the final erupted state—the difference being the amount of energy ejected into space.

Summary of Part 3:
Image Generation, Validation and Application

This concludes the third part of the dissertation. Let's have a quick recap of what happened.

- **Section 3.1, Physics Based Image Generation**
  We went through the entire process of using the discrete magnetic filaments to create physics-based images that are similar to the emission measures of the NASA SDO mission.

- **Section 3.2, Validation of Numerics**
  We proposed some theoretical predictions, performed some numerical experiments and verified that these experiments indeed match with the predicted outcome.

- **Section 3.3, Validation of FFCS Model Applicability**
  We compare the magnetic field output with related work as well as with predictions of the PFSS model.

- **Section 3.4, Validation of the Glow Model**
  We compared the output of our algorithm together with the glow model with captured data and studied some details of the glow model.

- **Section 3.5, Application: Magnetic Field Modeling**
  We highlight the use of the results for magnetic field modeling and give some performance data and possible refinements.

- **Section 3.6, Application: A Full Visualization Pipeline**
  We highlight that a result of this dissertation is the creation of a pipeline for solar
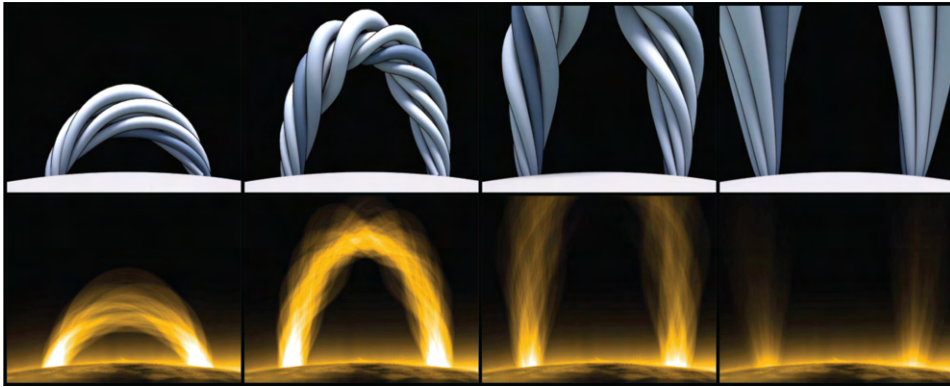
Figure 3.32: The twisting experiment side by side with it's glow model output. The build up of twist causes the magnetic filament bundle to rise, leading to the expulsion of solar plasma away from the sun. Twisting has been a suggested mechanism to explain solar flares [Prior and Yeates(2016a), Rachmeler et al.(2009)], and this experiment suggests that as well.

imagery creation given a magnetogram. We go through all the steps of this pipeline.

- **Section 3.7, Application: Visualization**

  We go through the different aspects of visualization and specify what types of input data can be used.

- **Section 3.8, Experiment: Twisting Our Filaments**

  We conduct an experiment where we twist filaments during the energy minimization process and observe that a solar flare like event occurs.

Part 4

Conclusion

This is the end of this dissertation. We now summarize the 3 parts of this dissertation and clarify its position in the world of research and applications.

4.1   Summary of this Dissertation

- **Part 1, The Mathematical Modeling of the MHS Equation**
  We introduced basic properties of solar physics and the magnetohydrostatic equation with some related work. We established the Force-Free Current Sheet model (FFCS) and analysed it. Most importantly, we established conditions when the FFCS model solves for a magnetohydrostatic field through a variational analysis of the magnetohydrostatic energy.
- **Part 2, The Discretization of the MHS Equation**
  A reformulation of the magnetohydrodynamic energy in terms of field lines was established. This motivated the definition of smooth magnetic filaments, which were then discretized into discrete magnetic filaments. The insights from part 1 were then used to express the energy geometrically as lengths and an energy minimization scheme was derived from that. We then also proposed a solution for the initialization of curves given a magnetogram.
- **Part 3, Image Generation, Validation and Application**
  A physics-based glow model is established to visualize the output. The results of this dissertation were then put through various tests to validate the outcome. Multiple application details were then discussed and an experiment involving twist was conducted.

4.2   Contributions

What are the take away results of this dissertation? We would like to clarify this here explicitly.

- **FFCS conditions to solve the MHS problem:**
  Theorem 6 [**FFCS MHS Theorem**] established the exact conditions for the FFCS model with its domain splitting to solve the MHS equation: the gas-flux pressure equilibrium at the gas and flux domain interface.

- **FFCS condition as MHS energy extrema:**
  In theorem 11 [**MHS Solutions are MHS Energy Extrema**] we show that the conditions required by theorem 6 are archived when the MHS energy reaches a local extremum. This opens up an approach to solve the MHS problem by energy minimization.

- **Geometric insight:**
  A geometric perspective of the solar magnetic field problem was established. The MHS energy was expressed in terms of field line lengths in theorem 14 [**MHS Energy Field Line Decomposition**].

- **Discretization using magnetic filaments:**
  Inspired by insights from solar physics, we established a Lagranian approach using discrete magnetic filaments (definition 31 [**Discrete Magnetic Filaments**]). We introduced them via smooth magnetic filaments and established their globally minimizing shapes in theorem 27 [**Energy Minimizer / Geodesics of Smooth Magnetic Filaments**].

- **Geometric algorithm:**
  The geometric insight was used to establish a conceptually simple algorithm 5 [**Energy Minimization**] to solve the MHS equation based on length shortening in the plasma metric. Explicit computational details were given.

- **Initialization problem:**
  An initialization method for curves with minimal twist from an input magnetogram was established by solving an optimal matching problem in theorem 38 [**Minimal Initialization**].

- **Visualizing the output:**
  We tackled the visualization problem with the focus on recreating images akin to the measured data from NASA's Solar Dynamics Observatory. At the core was the establishment of a glow model (definition 39 [**Filament Glow**]).

- **Validation through testing:**
  We went through a series of examples to test the numerics, applicability and visual fidelity of the output (sections 3.2 - 3.4).

- **A tool for solar physics and imagery:**
  The results here can be used to generate images from real or custom magnetograms with minimal parameter interventions. An entire pipeline was established and the results can be used for visualization as well as for further research purposes (sections 3.5 - 3.7).

4.3   Acknowledgements

Thank you for reading!

Bibliography

[Alissandrakis(1981)] CE Alissandrakis. 1981. On the computation of constant alpha force-free magnetic field. *Astronomy and Astrophysics* 100 (1981), 197–200.

[Altschuler and Newkirk(1969)] M. D. Altschuler and G. Newkirk. 1969. Magnetic Fields and the Structure of the Solar Corona. *Sol. Phys.* 9, 1 (1969), 131–149.

[Angelidis and Neyret(2005)] A. Angelidis and F. Neyret. 2005. Simulation of Smoke based on Vortex Filament Primitives. In *Proc. Symp. Comp. Anim.* ACM, New York, NY, USA, 87–96.

[Angles et al.(2019b)] Baptiste Angles, Daniel Rebain, Miles Macklin, Brian Wyvill, Loic Barthe, JP Lewis, Javier Von Der Pahlen, Shahram Izadi, Julien Valentin, Sofien Bouaziz, et al. 2019b. Viper: Volume invariant position-based elastic rods. *Proceedings of the ACM on Computer Graphics and Interactive Techniques* 2, 2 (2019), 1–26.

[Angles et al.(2019a)] B. Angles, D. Rebain, M. Macklin, B. Wyvill, L. Barthe, J. P. Lewis, J. von der Pahlen, S. Izadi, J. Valentin, S. Bouaziz, and A. Tagliasacchi. 2019a. VIPER: Volume Invariant Position-Based Elastic Rods. *Proc. ACM Comput. Graph. Interact. Tech.* 2, 2 (2019), 19:1–19:26.

[Antolin(2020)] Patrick Antolin. 2020. Thermal instability and non-equilibrium in solar coronal loops: from. (2020).

[Arnold and Khesin(1998)] Vladimir I. Arnold and Boris A. Khesin. 1998. *Topological Methods in Hydrodynamics.* Springer.

[Aschwanden(2006)] Markus Aschwanden. 2006. *Physics of the solar corona: an introduction with problems and solutions.* Springer Science & Business Media.

[Aschwanden et al.(2016)] M. J. Aschwanden, K. Reardon, and D. B. Jess. 2016. Tracing the Chromospheric and Coronal Magnetic Field with AIA, IRIS, IBIS, and ROSA Data. *Astrophys. J.* 826, 1 (2016), 61.

[Boerner et al.(2012)] P. Boerner, C. Edwards, J. Lemen, A. Rausch, C. Schrijver, R. Shine, L. Shing, R. Stern, T. Tarbell, C. J. Wolfson, et al. 2012. Initial Calibration of the

Atmospheric Imaging Assembly (AIA) on the Solar Dynamics Observatory (SDO). *Sol. Phys.* 275, 1-2 (2012), 41–66.

[Borkiewicz et al.(2019)] K. Borkiewicz, A. J. Christensen, D. Berry, C. Fluke, G. Shirah, and K. Elkins. 2019. Cinematic Scientific Visualization: The Art of Communicating Science. In *SIGGRAPH Asia 2019 Courses.* ACM, New York, NY, USA, Article 107, 313 pages.

[CADENS(2015)] CADENS. 2015. *Solar Superstorms.* Centrality of Advanced Digitally ENabled Science.

[Chern et al.(2017)] Albert Chern, Felix Knöppel, Ulrich Pinkall, and Peter Schröder. 2017. Inside fluids: Clebsch maps for visualization and processing. *ACM Transactions on Graphics (TOG)* 36, 4 (2017), 1–11.

[Chiu and Hilton(1977)] YT Chiu and HH Hilton. 1977. Exact Green's function method of solar force-free magnetic-field computations with constant alpha. I-Theory and basic test cases. *The Astrophysical Journal* 212 (1977), 873–885.

[Chodura and Schlüter(1981)] R. Chodura and A. Schlüter. 1981. A 3D code for MHD Equilibrium and Stability. *J. Comput. Phys.* 41, 1 (1981), 68–88.

[Clebsch(1859)] Alfred Clebsch. 1859. Ueber die Integration der hydrodynamischen Gleichungen. (1859).

[Contopoulos et al.(2011)] Ioannis Contopoulos, Constantinos Kalapotharakos, and MK Georgoulis. 2011. Nonlinear force-free reconstruction of the global solar magnetic field: methodology. *Solar Physics* 269, 2 (2011), 351–365.

[DeForest and Kankelborg(2007)] C. E. DeForest and C. C. Kankelborg. 2007. Fluxon Modeling of Low-Beta Plasmas. *J. Atmos. Sol.-Terr. Phys.* 69, 1 (2007), 116–128.

[Dixon et al.(1989)] A. M. Dixon, M. A. Berger, E. R. Priest, and P. K. Browning. 1989. A generalization of the Woltjer minimum-energy principle. *Astronomy and Astrophysic* 225, 1 (Nov. 1989), 156–166.

[Fage and Johansen(1928)] Arthur Fage and FC Johansen. 1928. XLII. The structure of vortex sheets. *The London, Edinburgh, and Dublin Philosophical Magazine and Journal of Science* 5, 28 (1928), 417–441.

[Gary(2001)] G Allen Gary. 2001. Plasma beta above a solar active region: rethinking the paradigm. *Solar Physics* 203 (2001), 71–86.

[Gent et al.(2013)] F. A. Gent, V. Fedun, S. J. Mumford, and R. Erdélyi. 2013. Magneto-hydrostatic Equilibrium – I. Three-Dimensional Open Magnetic Flux Tube in the Stratified Solar Atmosphere. *Mon. Notices Royal Astron. Soc.* 435, 1 (2013), 689–697.

[Gómez et al.(2017)] J. Gómez, J. Blinn, D. Em, and S. Rueff. 2017. History of the JPL Computer Graphics Lab. ACM SIGGRAPH 2017 Panel.

[Grad and Rubin(1958)] H. Grad and H. Rubin. 1958. Hydromagnetic Equilibria and Force-Free Fields. *J. nucl. Energy* 7, 3-4 (1958), 284–285.

[Gross et al.(2023)] Oliver Gross, Ulrich Pinkall, and Peter Schröder. 2023. Plasma knots. *Physics Letters A* 480 (2023), 128986.

[Hadap and Magnenat-Thalmann(2001)] S. Hadap and N. Magnenat-Thalmann. 2001. Modeling Dynamic Hair as a Continuum. *Comp. Graph. Forum* 20, 3 (2001), 329–338.

[Hathaway(2015)] David H Hathaway. 2015. The solar cycle. *Living reviews in solar physics* 12 (2015), 1–87.

[Janse et al.(2010)] Å. M. Janse, B. C. Low, and E. N. Parker. 2010. Topological Complexity and Tangential Discontinuity in Magnetic Fields. *Phys. Plasmas.* 17, 9 (2010), 092901.

[Klimchuk and Canfield(1994)] James A Klimchuk and Richard C Canfield. 1994. Photospheric magnetic field measurement errors and the inferred properties of coronal magnetic fields. In *Solar Active Region Evolution: Comparing Models with Observations*, Vol. 68. 233.

[Lionello et al.(2008)] R. Lionello, J. A. Linker, and Z. Mikić. 2008. Multispectral Emission of the Sun During the First Whole Sun Month: Magnetohydrodynamic Simulations. *Astrophys. J.* 690, 1 (2008), 902.

[Low(1973)] BC Low. 1973. Resistive diffusion of force-free magnetic fields in a passive medium. *The Astrophysical Journal* 181 (1973), 209–226.

[Low(1982)] B. C. Low. 1982. Magnetostatic atmospheres with variations in three dimensions. *Astrophys. J.* 263 (1982), 952–969.

[Luo(2004)] Feng Luo. 2004. Combinatorial Yamabe flow on surfaces. *Communications in Contemporary Mathematics* 6, 05 (2004), 765–780.

[Machado et al.(2012)] G. M. Machado, F. Sadlo, T. Müller, D. Müller, and T. Ertl. 2012. Visualizing Solar Dynamics Data. In *Vision, Modeling and Visualization*. The Eurographics Association, 95–102.

[Mackay and Van Ballegooijen(2006)] DH Mackay and AA Van Ballegooijen. 2006. Models of the large-scale corona. I. Formation, evolution, and liftoff of magnetic flux ropes. *The Astrophysical Journal* 641, 1 (2006), 577.

[Mandal et al.(2017)] Sudip Mandal, Bidya Binay Karak, and Dipankar Banerjee. 2017. Latitude distribution of sunspots: analysis using sunspot data and a dynamo model. *The Astrophysical Journal* 851, 1 (2017), 70.

[Metcalf et al.(2008)] Thomas R Metcalf, Marc L DeRosa, Carolus J Schrijver, Graham
    Barnes, Adriaan A van Ballegooijen, Thomas Wiegelmann, Michael S Wheatland,
    Gherardo Valori, and James M McTtiernan. 2008. Nonlinear force-free modeling of
    coronal magnetic fields. II. Modeling a filament arcade and simulated chromospheric and
    photospheric vector fields. *Solar Physics* 247, 2 (2008), 269–299.

[Mikić et al.(1999)] Zoran Mikić, Jon A Linker, Dalton D Schnack, Roberto Lionello, and
    Alfonso Tarditi. 1999. Magnetohydrodynamic modeling of the global solar corona.
    Physics of Plasmas 6, 5 (1999), 2217–2224.

[Moradi et al.(2010)] H. Moradi, C. Baldner, A. C. Birch, D. C. Braun, R. H. Cameron,
    T. L. Duvall, L. Gizon, D. Haber, S. M. Hanasoge, B. W. Hindman, J. Jackiewicz,
    E. Khomenko, R. Komm, P. Rajaguru, M. Rempel, M. Roth, R. Schlichenmaier, H.
    Schunker, H. C. Spruit, K. G. Strassmeier, M. J. Thompson, and S. Zharkov. 2010.
    Modeling the Subsurface Structure of Sunspots. *Sol. Phys.* 267, 1 (2010), 1–62.

[Nabizadeh et al.(2021)] M. S. Nabizadeh, A. Chern, and R. Ramamoorthi. 2021. Kelvin
    Transformations for Simulations on Infinite Domains. *ACM Trans. Graph.* 40, 4 (2021),
    97:1–97:15.

[Naiman et al.(2017a)] JP Naiman, Kalina Borkiewicz, and AJ Christensen. 2017a. Houdini
    for astrophysical visualization. *Publications of the Astronomical Society of the Pacific*
    129, 975 (2017), 058008.

[Naiman et al.(2017b)] J. P. Naiman, K. Borkiewicz, and A. J. Christensen. 2017b. Houdini
    for Astrophysical Visualization. *Publ. Astron. Soc. Pac.* 129, 975 (2017), 058008.

[Nakagawa and Raadu(1972)] Y Nakagawa and MA Raadu. 1972. On practical representation
    of magnetic field. *Solar Physics* 25, 1 (1972), 127–135.

[NASA Atmospheric Imaging Assembly(2023)] NASA Atmospheric Imaging Assembly. 2023.
    AIA LMSAL DATA.

[NASA Scientific Visualization Studio(2018)] NASA Scientific Visualization Studio. 2018.
    The Dynamic Solar Magnetic Field with Introduction.

[NASA Solar Dynamics Observatory(2023)] NASA Solar Dynamics Observatory. 2023.
    NASA AIA/HMI Data.

[Padilla et al.(2019)] M. Padilla, A. Chern, F. Knöppel, U. Pinkall, and P. Schröder. 2019.
    On Bubble Rings and Ink Chandeliers. *ACM Trans. Graph.* 38, 4 (2019), 129:1–129:14.

[Padilla et al.(2022)] Marcel Padilla, Oliver Gross, Felix Knöppel, Albert Chern, Ulrich
    Pinkall, and Peter Schröder. 2022. Filament based plasma. *ACM Transactions on
    Graphics (TOG)* 41, 4 (2022), 1–14.

[Parker(1994)] E. N. Parker. 1994. *Spontaneous Current Sheets in Magnetic Fields: With Applications to Stellar X-Rays.* Vol. 1. Ox. U. P., New York, NY.

[Pastor et al.(2003)] Oscar Meruvia Pastor, Bert Freudenberg, and Thomas Strothotte. 2003. Real-time animated stippling. *IEEE Computer Graphics and Applications* 23, 4 (2003), 62–68.

[Peter et al.(2012)] H. Peter, S. Bingert, and S. Kamio. 2012. Catastrophic Cooling and Cessation of Heating in the Solar Corona. *Astron. Astrophys.* 537 (2012), A152.

[Pevtsov et al.(1994)] Alexei A Pevtsov, Richard C Canfield, and Thomas R Metcalf. 1994. Patterns of helicity in solar active regions. *The Astrophysical Journal* 425 (1994), L117–L119.

[Priest(2014)] E. R. Priest. 2014. *Magnetohydrodynamics of the Sun.* Cam. U. P.

[Priest(2019)] E. R. Priest. 2019. Magnetohydrodynamics and Solar Dynamo Action. In *The Sun as a Guide to Stellar Physics.* Elsevier, 239–266.

[Prior and Yeates(2016a)] C. Prior and A. R. Yeates. 2016a. Twisted Versus Braided Magnetic Flux Ropes in Coronal Geometry – I. Construction and Relaxation. *Astron. Astrophys.* 587 (2016), 15.

[Prior and Yeates(2016b)] C. Prior and A. R. Yeates. 2016b. Twisted Versus Braided Magnetic Flux Ropes in Coronal Geometry – II. Comparative Behaviour. *Astron. Astrophys.* 591 (2016), 20.

[Purcell(1997)] Edward M Purcell. 1997. The efficiency of propulsion by a rotating flagellum. *Proceedings of the National Academy of Sciences* 94, 21 (1997), 11307–11311.

[Rachmeler et al.(2009)] L. A. Rachmeler, C. E. DeForest, and C. C. Kankelborg. 2009. Reconnectionless CME Eruption: Putting the Aly-Sturrock Conjecture to Rest. *Astrophys. J.* 693, 2 (2009), 1431–1436.

[Reale(2014)] F. Reale. 2014. Coronal Loops: Observations and Modeling of Confined Plasma. *Living Rev. Sol. Phys.* 11, 1 (2014), 1–94.

[Reale and Peres(1999)] F. Reale and G. Peres. 1999. TRACE-Derived Temperature and Emission Measure Profiles along Long-Lived Coronal Loops: The Role of Filamentation. *Astrophys. J. Lett.* 528, 1 (1999), L45.

[Reddiger and Poirier(2020)] M. Reddiger and B. Poirier. 2020. On the Differentiation Lemma and the Reynolds Transport Theorem for Manifolds with Corners. arXiv:1906.03330 [math-ph]

[Rieutord(2015)] Michel Rieutord. 2015. *Fluid Dynamics: An Introduction.* Springer.

[Rosner et al.(1978)] R. Rosner, W. H. Tucker, and G. S. Vaiana. 1978. Dynamics of the Quiescent Solar Corona. *Astrophys. J.* 220 (1978), 643–645.

[Sakurai(1979)] Takashi Sakurai. 1979. A New Approach to the Force-Free Field and Its Application to the Mag-netic Field of Solar Active Regions. *Publications of the Astronomical Society of Japan* 31 (1979), 209–230.

[Sakurai(1981)] Takashi Sakurai. 1981. Calculation of force-free magnetic field with non-constant α. *Solar physics* 69, 2 (1981), 343–359.

[Sakurai(1982)] T. Sakurai. 1982. Green's Function Methods for Potential Magnetic Fields. *Sol. Phys.* 76, 2 (1982), 301–321.

[Schrijver et al.(2005)] C. J. Schrijver, A. W. Sandman, M. J. Aschwanden, and M. L. De Rosa. 2005. Coronal Heating and the Appearance of Solar and Stellar Coronae. In *13th Cambridge Workshop on Cool Stars, Stellar Systems and the Sun*, Vol. 560. European Space Agency, 65.

[Springborn et al.(2008)] Boris Springborn, Peter Schröder, and Ulrich Pinkall. 2008. Conformal Equivalence of Triangle Meshes. In *ACM SIGGRAPH 2008 Papers* (Los Angeles, California) *(SIGGRAPH '08)*. Association for Computing Machinery, New York, NY, USA, Article 77, 11 pages. https://doi.org/10.1145/1399504.1360676

[Stansby et al.(2020)] D. Stansby, A. R. Yeates, and S. T. Badman. 2020. pfsspy: A Python Package for Potential Field Source Surface Modelling. *J. Open Source Softw.* 5, 54 (2020), 2732.

[Stern(1970)] David P Stern. 1970. Euler potentials. *American Journal of Physics* 38, 4 (1970), 494–501.

[Tadesse et al.(2014)] Tilaye Tadesse, T Wiegelmann, S Gosain, P MacNeice, and Alexei A Pevtsov. 2014. First use of synoptic vector magnetograms for global nonlinear, force-free coronal magnetic field models. *Astronomy & Astrophysics* 562 (2014), A105.

[Titov et al.(2018)] V. S. Titov, C. Downs, Z. Mikić, T. Török, J. A. Linker, and R. M. Caplan. 2018. Regularized Biot–Savart Laws for Modeling Magnetic Flux Ropes. *Astrophys. J. Lett.* 852, 2 (2018), L21.

[Wang(1993)] Jingxiu Wang. 1993. Analyses of Transverse Field. In *IAU Colloq. 141: The Magnetic and Velocity Fields of Solar Active Regions*, Vol. 46. 425.

[Warren et al.(2018)] H. P. Warren, N. A. Crump, I. Ugarte-Urra, X. Sun, M. J. Aschwanden, and T. Wiegelmann. 2018. Toward a Quantitative Comparison of Magnetic Field Extrapolations and Observed Coronal Loops. *Astrophys. J.* 860, 1 (2018), 46.

[Weißmann and Pinkall(2010)] S. Weißmann and U. Pinkall. 2010. Filament-based Smoke with Vortex Shedding and Variational Reconnection. *ACM Trans. Graph.* 29, 4 (2010), 115:1–12.

[Wheatland(2004)] MS Wheatland. 2004. Parallel construction of nonlinear force-free fields. *Solar Physics* 222, 2 (2004), 247–264.

[Wiegelmann(2007)] Thomas Wiegelmann. 2007. Computing nonlinear force-free coronal magnetic fields in spherical geometry. *Solar Physics* 240 (2007), 227–239.

[Wiegelmann et al.(2006)] Thomas Wiegelmann, Bernd Inhester, and Takashi Sakurai. 2006. Preprocessing of vector magnetograph data for a nonlinear force-free magnetic field reconstruction. *Solar Physics* 233, 2 (2006), 215–232.

[Wiegelmann and Solanki(2004a)] T. Wiegelmann and S. K. Solanki. 2004a. Similarities and Differences between Coronal Holes and the Quiet Sun: Are Loop Statistics the Key? *Sol. Phys.* 225, 2 (2004), 227–247.

[Wiegelmann and Solanki(2004b)] T. Wiegelmann and S. K. Solanki. 2004b. Why Are Coronal Holes Indistinguishable from the Quiet Sun in Transition Region Radiation?. In *SOHO 15 Coronal Heating*, Vol. 575. European Space Agency, 35.

[Williams et al.(2020)] T. Williams, R. W. Walsh, A. R. Winebarger, D. H. Brooks, J. W. Cirtain, B. De Pontieu, L. Golub, K. Kobayashi, D. E. McKenzie, R. J. Morton, H. Peter, L. A. Rachmeler, S. L. Savage, P. Testa, S. K. Tiwari, H. P. Warren, and B. J. Watkinson. 2020. Is the High-Resolution Coronal Imager Resolving Coronal Strands? Results from AR 12712. *Astrophys. J.* 892, 2 (2020), 134.

[Wilmot-Smith(2015)] AL Wilmot-Smith. 2015. An overview of flux braiding experiments. *Philosophical Transactions of the Royal Society A: Mathematical, Physical and Engineering Sciences* 373, 2042 (2015), 20140265.

[Winebarger et al.(2008)] A. R. Winebarger, H. P. Warren, and D. A. Falconer. 2008. Modeling X-Ray Loops and EUV "Moss" in an Active Region Core. *Astrophys. J.* 676, 1 (2008), 672.

[Woltjer(1958)] L. Woltjer. 1958. A THEOREM ON FORCE-FREE MAGNETIC FIELDS. *Proceedings of the National Academy of Sciences* 44, 6 (1958), 489–491. https://doi.org/10.1073/pnas.44.6.489 arXiv:https://www.pnas.org/doi/pdf/10.1073/pnas.44.6.489

[Yan(1995)] Yihua Yan. 1995. The 3-D boundary element formulation of linear force-free magnetic fields with finite energy content in semi-infinite space. *Solar Physics* 159, 1 (1995), 97–113.

[Yeates et al.(2018)] A. R. Yeates, T. Amari, I. Contopoulos, X. Feng, D. H. Mackay, Z. Mikić, T. Wiegelmann, J. Hutton, C. A. Lowder, H. Morgan, et al. 2018. Global

Non-Potential Magnetic Models of the Solar Corona During the March 2015 Eclipse. *Space Sci. Rev.* 214, 5 (2018), 99.

[Yu et al.(2021)] C. Yu, H. Schumacher, and K. Crane. 2021. Repulsive Curves. *ACM Trans. Graph.* 40, 2 (2021), 268:1–268:19.

[Zhu et al.(2022)] Junqiu Zhu, Sizhe Zhao, Lu Wang, Yanning Xu, and Ling-Qi Yan. 2022. Practical level-of-detail aggregation of fur appearance. *ACM Transactions on Graphics (TOG)* 41, 4 (2022), 1–17.

[Zhuleku et al.(2020)] J. Zhuleku, J. Warnecke, and H. Peter. 2020. Stellar Coronal X-ray Emission and Surface Magnetic Flux. *Astron. Astrophys.* 640 (2020), A119.